Oklahoma Department of Transportation
200 NE 21st Street, Oklahoma City, OK 73105-3204

FINAL REPORT ~ FHWA-OK-23-02

PROBABILISTIC APPROACH FOR DESIGN OF DRILLED SHAFTS SOCKETED IN WEAK ROCK IN OKLAHOMA

J.Erik Loehr, Ph.D., P.E.
Andrew Boeckmann, Ph.D., P.E.
Elgin Burton, M.S.
Dan Ding, Ph.D., P.E.

University of Missouri

May 2024

OKLAHOMA
Transportation

The Oklahoma Department of Transportation (ODOT) ensures that no person or groups of persons shall, on the grounds of race, color, sex, religion, national origin, age, disability, retaliation or genetic information, be excluded from participation in, be denied the benefits of, or be otherwise subjected to discrimination under any and all programs, services, or activities administered by ODOT, its recipients, sub-recipients, and contractors. To request an accommodation please contact the ADA Coordinator at 405-521-4140 or the Oklahoma Relay Service at 1-800-722-0353. If you have any ADA or Title VI questions email ODOT-ada-titlevi@odot.org.

The contents of this report reflect the views of the author(s) who is responsible for the facts and the accuracy of the data presented herein. The contents do not necessarily reflect the views of the Oklahoma Department of Transportation or the Federal Highway Administration. This report does not constitute a standard, specification, or regulation. While trade names may be used in this report, it is not intended as an endorsement of any machine, contractor, process, or product.

Probabilistic Approach for Design of Drilled Shafts Socketed in Weak Rock in Oklahoma

FINAL REPORT ~ FHWA-OK-23-02
ODOT SPR ITEM NUMBER 2279

Submitted to:
Office of Research and Implementation
Oklahoma Department of Transportation

Submitted by:
J. Erik Loehr, Ph.D., P.E.
Andrew Boeckmann, Ph.D., P.E.
Elgin Burton, M.S.
Dan Ding, Ph.D., P.E.

University of Missouri

OKLAHOMA
Transportation

May 2024

TECHNICAL REPORT DOCUMENTATION PAGE

1. REPORT NO.	2. GOVERNMENT ACCESSION NO.	3. RECIPIENT'S CATALOG NO.
FHWA-OK-23-02		

4. TITLE AND SUBTITLE	5. REPORT DATE
Probabilistic Approach for Design of Drilled Shafts Socketed in Weak Rock in Oklahoma	May 2024
	6. PERFORMING ORGANIZATION CODE
7. AUTHOR(S)	8. PERFORMING ORGANIZATION REPORT
J.E. Loehr, A. Boeckmann, E. Burton, and D. Ding	
9. PERFORMING ORGANIZATION NAME AND ADDRESS	10. WORK UNIT NO.
University of Missouri College of Engineering Columbia, MO 65211-2200	11. CONTRACT OR GRANT NO. ODOT SPR Item Number 2279
12. SPONSORING AGENCY NAME AND ADDRESS	13. TYPE OF REPORT AND PERIOD COVERED
Oklahoma Transportation Office of Research and Implementation 200 N.E. 21st Street, Rm. 3A7 Oklahoma City, OK 73105	Final Report Oct 2017 - Mar 2023
	14. SPONSORING AGENCY CODE

15. SUPPLEMENTARY NOTES

Click here to enter text.

16. ABSTRACT

This report documents the conduct and findings of a research program undertaken to evaluate alternative methods for design of drilled shafts founded in weak rock in Oklahoma, and to develop probabilistically calibrated resistance factors to achieve a target design reliability for recommended design methods. The report documents important background information, selection and characterization of two load test sites, construction of a total of eight test shafts, axial and lateral load testing of the construction shafts, and analyses conducted to interpret measurements for all field tests. Collective analysis of the axial load tests conducted for the project with additional load tests performed in Oklahoma and surrounding states was used to identify recommended relations for determining unit side and unit tip resistance for drilled shafts in weak rock. Three design relations are recommended for predicting unit tip resistance based on Texas Cone Penetration Test measurements, compressive strength measurements, and Standard Penetration Test measurements. Three additional relations are recommended for predicting unit side resistance based on similar measurements. Probabilistically calibrated resistance factors are also provided for the recommended design relations. Recommendations for design of drilled shafts in weak rock for lateral loads are also provided based on analysis of measurements from the lateral load tests.

17. KEY WORDS	18. DISTRIBUTION STATEMENT
Drilled shaft, Weak Rock, LRFD, Design, Load test, Calibration	No restrictions. This publication is available from the Office of Research and Implementation, Oklahoma DOT.

19. SECURITY CLASSIF. (OF THIS REPORT)	20. SECURITY CLASSIF. (OF THIS PAGE)	21. NO. OF PAGES	22. PRICE
Unclassified	Unclassified	202	N/A

Form DOT F 1700.7 (08/72)

SI* (MODERN METRIC) CONVERSION FACTORS

APPROXIMATE CONVERSIONS TO SI UNITS

SYMBOL	WHEN YOU KNOW	MULTIPLY BY	TO FIND	SYMBOL
		LENGTH		
in	inches	25.4	millimeters	mm
ft	feet	0.305	meters	m
yd	yards	0.914	meters	m
mi	miles	1.61	kilometers	km
		AREA		
in^2	square inches	645.2	square millimeters	mm^2
ft^2	square feet	0.093	square meters	m^2
yd^2	square yard	0.836	square meters	m^2
ac	acres	0.405	hectares	ha
mi^2	square miles	2.59	square kilometers	km^2
		VOLUME		
fl oz	fluid ounces	29.57	milliliters	mL
gal	gallons	3.785	liters	L
ft^3	cubic feet	0.028	cubic meters	m^3
yd^3	cubic yards	0.765	cubic meters	m^3
		NOTE: volumes greater than 1000 L shall be shown in m^3		
		MASS		
oz	ounces	28.35	grams	g
lb	pounds	0.454	kilograms	kg
T	short tons (2000 lb)	0.907	megagrams (or "metric ton")	Mg (or "t")
		TEMPERATURE (exact degrees)		
^oF	Fahrenheit	5 (F-32)/9 or (F-32)/1.8	Celsius	^oC
		ILLUMINATION		
fc	foot-candles	10.76	lux	lx
fl	foot-Lamberts	3.426	candela/m^2	cd/m^2
		FORCE and PRESSURE or STRESS		
lbf	poundforce	4.45	newtons	N
lbf/in^2	poundforce per square inch	6.89	kilopascals	kPa

APPROXIMATE CONVERSIONS FROM SI UNITS

SYMBOL	WHEN YOU KNOW	MULTIPLY BY	TO FIND	SYMBOL
		LENGTH		
mm	millimeters	0.039	inches	in
m	meters	3.28	feet	ft
m	meters	1.09	yards	yd
km	kilometers	0.621	miles	mi
		AREA		
mm^2	square millimeters	0.0016	square inches	in^2
m^2	square meters	10.764	square feet	ft^2
m^2	square meters	1.195	square yards	yd^2
ha	hectares	2.47	acres	ac
km^2	square kilometers	0.386	square miles	mi^2
		VOLUME		
mL	milliliters	0.034	fluid ounces	fl oz
L	liters	0.264	gallons	gal
m^3	cubic meters	35.314	cubic feet	ft^3
m^3	cubic meters	1.307	cubic yards	yd^3
		MASS		
g	grams	0.035	ounces	oz
kg	kilograms	2.202	pounds	lb
Mg (or "t")	megagrams (or "metric ton")	1.103	short tons (2000 lb)	T
		TEMPERATURE (exact degrees)		
^oC	Celsius	1.8C+32	Fahrenheit	^oF
		ILLUMINATION		
lx	lux	0.0929	foot-candles	fc
cd/m^2	candela/m^2	0.2919	foot-Lamberts	fl
		FORCE and PRESSURE or STRESS		
N	newtons	0.225	poundforce	lbf
kPa	kilopascals	0.145	poundforce per square inch	lbf/in^2

*SI is the symbol for the International System of Units. Appropriate rounding should be made to comply with Section 4 of ASTM E380. (Revised March 2003)

Table of Contents

Chapter 1 - Introduction

This report describes research conducted to evaluate the axial and lateral performance of drilled shafts in weak rock and to develop appropriate geotechnical design methods for the Oklahoma Department of Transportation (ODOT). This chapter describes the motivation and objectives for the research, the general scope of work, and the organization of this report.

1.1 MOTIVATION AND OBJECTIVE

Shale and other weak rock is generally well suited for supporting structures on drilled shafts (e.g., Brown, et al., 2018). Weak rock often has relatively high strength and stiffness, so that it can provide support for relatively large axial and lateral loads. The material can also often be easily excavated with common foundation tooling, often "in the dry" without the added complexity involved with support of shafts in softer clays and sands. However, design of drilled shafts in weak rock is also challenging for reasons that include:

- weak rock is often highly variable on site-specific, regional, and global scales;
- site characterization in weak rock is often challenging because materials may degrade quickly upon sampling;
- because of challenges with site characterization, numerous alternative design methods based on in situ testing have been proposed and used; however, the reliability of such methods is often unquantified or poorly characterized;
- the relative strength of weak rock poses challenges for purely empirical calibrations because it is often difficult to achieve failure in field load tests; as a result, many available field load test measurements are not completely suitable for calibration of resistance factors; and finally,
- the performance of drilled shafts in weak rock may be strongly affected by construction techniques that are difficult to account for in design.

The combined result of these challenges is that design methods for drilled shafts in weak rock have traditionally been very conservative. Fortunately, the degree of conservatism for design of drilled shafts in weak rock has gradually been reduced over time as more observations from load tests and field performance have been acquired. The work described in this report serves to continue improvement of design and construction of drilled shafts in weak rock.

Numerous methods have been proposed for design of drilled shafts in weak rock. Early design methods were often based on presumptive capacities or simple rules of thumb (e.g., Thorburn, 1966; Freeman, et al., 1972). Subsequent design methods (e.g., Horvath and Kenny, 1979; Williams and Pells, 1981; Rowe and Armitage, 1987; Kulhawy and Phoon, 1993; Zhang and Einstein, 1998) dramatically improved on these simple rules to produce methods that form the basis for design of drilled shafts in weak rock today. Most of these methods are based on empirical relations between compressive strength and the unit side and tip resistance for drilled shafts, although some also include provisions to account for shaft roughness and rock mass characteristics. Additionally, several alternative design methods that utilize in situ test measurements have been proposed because of the challenges listed above for site

characterization in weak rock. The most common of these methods are based on Standard Penetration Test (SPT) measurements (e.g., Hummert and Cooling, 1988; Abu-Hejleh, et al., 2005) and Texas Cone Penetration Test (TCPT) measurements (e.g., Nam and Vipulanandan, 2010; TXDOT, 2012). Each of these design methods have advantages and disadvantages, and each has different levels of uncertainty that impacts the reliability of resulting designs.

The primary objective for the proposed work is to evaluate current methods for design of drilled shafts in weak rock formations that are common in Oklahoma and, if appropriate, to develop new rational and practical Load and Resistance Factor Design (LRFD) methods. The initial focus of the research was on resistance to axial loading. However, the effort was subsequently expanded to include both axial and lateral loading considerations. This report documents efforts undertaken to achieve these objectives.

1.2 SCOPE OF WORK

An extensive scope of work was undertaken to accomplish the project objectives that included many overlapping tasks. The principal tasks in the scope of work included:

1. identifying, collecting, and analyzing results from previously conducted field load tests in weak rock formations similar to those commonly encountered in Oklahoma;
2. conducting additional full-scale load tests in appropriate site conditions to complement currently available load test measurements;
3. evaluating currently available site characterization measurements for load test sites and collecting, interpreting, and analyzing new site characterization measurements where needed to fulfill project objectives;
4. characterizing the reliability of new and/or existing methods for design of drilled shafts in weak rock based on the collected load test measurements;
5. probabilistically calibrating resistance factors for recommended drilled shaft design methods for implementation within an LRFD framework; and finally
6. developing practical and implementable design specifications that can be considered by ODOT for adoption and implementation.

The scope of work was generally completed as planned, with minor adjustments as the project progressed.

1.3 ORGANIZATION OF REPORT

The report is organized into nine chapters, including this introductory chapter. Chapter 2 describes important background information for the project including methods currently adopted by ODOT for design of drilled shafts in weak rock, methods adopted by the Missouri Department of Transportation (MoDOT) that motivated the current work, and other methods that have been proposed for design of drilled shafts in weak rock in surrounding states.

In Chapter 3, activities completed for selection of two field load test sites are described along with extensive site characterization activities that were completed to support load testing efforts. Interpretations of relevant design parameters based on collected site characterization measurements are presented for the selected load test sites, referred to throughout this report as the Edmond site and the Minco site. Similar interpretations

for sites where load tests have been previously conducted on drilled shafts in weak rock in Oklahoma are also described.

Construction and axial load testing of a total of eight full-scale drilled shafts at the Edmond and Minco sites are respectively described in Chapters 4 and 5. Chapter 5 also describes basic interpretation of the load test measurements that was conducted to establish interpreted values of unit side and unit tip resistance for each test shaft, and the observed load-transfer response in side and tip resistance. Interpreted values of unit side and unit tip resistance for other collected load tests in Oklahoma are also reported in Chapter 5.

Analyses conducted to evaluate and develop appropriate design methods for axially loaded drilled shafts in weak rock based on the collected measurements are described in Chapter 6. Recommended design relations are provided for predicting unit side and tip resistance based on Texas Cone Penetration Test (TCPT) measurements, based on measurements of compressive strength of weak rock, and based on Standard Penetration Test (SPT) measurements. Analyses performed to develop probabilistically calibrated resistance factors are also described and recommended resistance factors provided for each the recommended design relations.

Chapter 7 describes the lateral load tests performed for all test shafts at the Edmond and Minco test sites and interpretation of measurements from the lateral tests. Analyses conducted to develop recommendations for design of drilled shafts subjected to lateral loading are described in Chapter 8.

Finally, principal conclusions and recommendations from the entire projects are documented in Chapter 9. Conclusions and recommendations are provided for both axial and lateral loading of drilled shafts in weak rock.

[This page intentionally blank.]

Chapter 2 - Background

Several alternative methods developed for design of drilled shafts in shale and other weak rock are described in this chapter. Current methods used by the Oklahoma Department of Transportation (ODOT) for predicting unit side and unit tip resistance for drilled shafts in weak rock are first described. Design relations adopted for similar materials by the Missouri Department of Transportation (MoDOT), which served as motivation for the current research, are then described. Several other relevant methods for design of drilled shafts in weak rock are also described.

2.1 CURRENT ODOT DESIGN METHODS

ODOT currently designs drilled shafts using nominal unit side and tip resistance values established primarily from Texas Cone Penetration Test (TCPT) measurements. As described in more detail in Chapter 3, the TCPT is a dynamic penetration test performed in the bottom of boreholes using a special cone developed by the Texas Department of Transportation (TxDOT). For relatively stiff soil and weak rock conditions that are pertinent to the current work, TCPT measurements are reported as the penetration distance observed for 100 hammer blows in units of inches per 100 blows. Measured and nominal values for this penetration distance are denoted throughout this report as $MTCP$ values.

The nominal unit side resistance for current ODOT practice is determined as:

$$q_s = \begin{cases} \frac{39.2}{MTCP} & (\text{for } MTCP \leq 6.9) \\ \frac{9.4}{MTCP} + 4.4 & (\text{for } MTCP > 6.9) \end{cases} \leq 18 \text{ ksf} \qquad (2.1)$$

where q_s is the nominal unit side resistance in units of ksf, limited to be no greater than 18 ksf, and $MTCP$ is the nominal (interpreted) TCPT penetration value along the considered shaft segment in units of inches per 100 blows. A resistance factor of 0.45 is normally applied to the nominal side resistance from Equation 2.1 for design.

The nominal unit tip resistance, q_p, is similarly determined in units of ksf as:

$$q_p = \frac{248}{MTCP} \leq 120 \text{ ksf} \qquad (2.2)$$

where the predicted nominal unit tip resistance is limited to be no greater than 120 ksf. A resistance factor of 0.70 is normally applied to the nominal tip resistance from Equation 2.2 for design in current practice.

Equations 2.1 and 2.2 have been used in ODOT practice for many years without evidence of performance problems. Prior to the current work, few load tests had been performed within the state of Oklahoma to permit direct evaluation of current ODOT design methods. However, load tests performed in similar materials in nearby states suggest that unit tip resistance from Equation 2.2 is considerably conservative while unit

side resistance from Equation 2.1 is unconservative for $MTCP$ values greater than approximately 2 inches per 100 blows, and conservative for $MTCP$ values less than 2 inches per 100 blows. A primary objective of the work described in this report is to evaluate the appropriateness of Equations 2.1 and 2.2 for application in weak rock that is prevalent throughout much of Oklahoma.

2.2 MODOT DRILLED SHAFT DESIGN METHODS

MoDOT has adopted several alternative design relations for drilled shafts founded in weak rock (MoDOT, 2023) based on a comprehensive field test program conducted between 2008 and 2010, along with additional measurements from load tests conducted for specific bridges (Loehr, et al., 2011). The alternative methods allow for prediction of unit side and unit tip resistance from the compressive strength of weak rock, from $MTCP$ values, and from SPT N-values, among others.

2.2.1 MoDOT Design Methods based on Compressive Strength

When designing based on the compressive strength of weak rock, the nominal unit side resistance, q_s, in units of ksf is calculated as:

$$q_s = 0.76 \cdot \overline{q_u}^{0.79} \leq 30 \text{ ksf} \qquad (2.3)$$

where $\overline{q_u}$ is the representative mean compressive strength of rock core along the considered shaft segment and the nominal unit side resistance is limited to be no greater than 30 ksf. Equation 2.3 is plotted in Figure 2.1 along with the measured maximum unit side resistance values used to establish the relation, all of which were acquired from load tests in or near the state of Missouri.

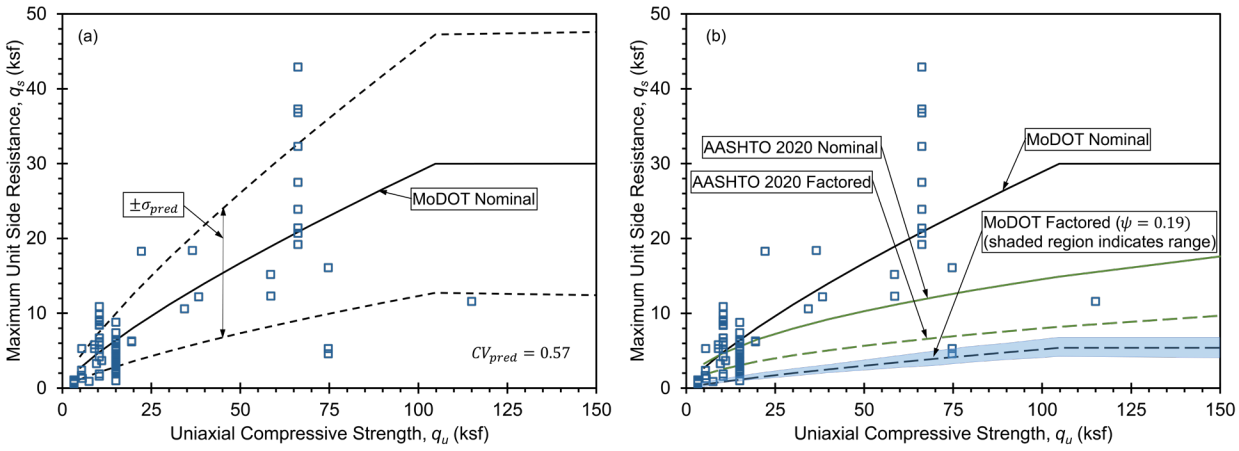

Figure 2.1 – MoDOT design relation for unit side resistance in weak rock from compressive strength of rock core: (a) nominal resistance showing prediction uncertainty and (b) nominal and factored unit resistance for MoDOT and AASHTO (2020) design methods.

Measurements shown in Figure 2.1 indicate considerable variability in unit side resistance for drilled shafts in weak rock (predominantly shale for the measurements

shown). Dashed lines in Figure 2.1a indicate prediction uncertainty bounds that are one standard deviation above and below the relation of Equation 2.3. These bounds correspond to a coefficient of variation for prediction uncertainty (the appropriate uncertainty for prediction of a new instance of a measurement), CV_{pred}, of 0.57, which is large compared to many other empirically established design methods for deep foundations. Probabilistically calibrated resistance factors for Equation 2.3 are therefore correspondingly lower than resistance factors for many other design methods.

A unique aspect of all MoDOT design methods described in this chapter is that resistance factors are specified to vary with both the uncertainty in design input parameters ($\overline{q_u}$ in this instance) and the importance of the supported structure. All resistance factors reported in this chapter are those adopted for structures on "major roads" for which the target reliability for foundations at strength limit states is taken to be 1 in 1500. This target reliability is similar to that used to develop resistance factors for the current AASHTO LRFD Bridge Design Specifications (AASHTO, 2020). Resistance factors calibrated for Equation 2.3 using this target reliability vary from a high of 0.22 for instances where $\overline{q_u}$ is perfectly characterized (no uncertainty) to a low of 0.14 when $\overline{q_u}$ is poorly characterized. The shaded region in Figure 2.1b indicates the corresponding range of factored values of unit side resistance from Equation 2.3, with the dashed line indicating the factored resistance for a resistance factor of 0.19 that is associated with "typical" levels of site characterization.

The nominal and factored unit side resistances prescribed in the current AASHTO design specifications, described subsequently in this chapter, are also plotted in Figure 2.1 for comparison. Comparison of the unit side resistances from the MoDOT and AASHTO design methods reveals that the MoDOT design method produces considerably greater values of nominal unit side resistance for q_u greater than about 20 ksf. However, the current AASHTO specifications adopt a considerably greater resistance factor ($\psi = 0.55$), which produces factored unit side resistance values that are approximately double that of the MoDOT design method for side resistance.

The nominal unit tip resistance, q_p, when designing based on the compressive strength of weak rock is similarly calculated in units of ksf as:

$$q_p = 14 \cdot \overline{q_u}^{0.71} \leq 400 \text{ ksf} \qquad (2.4)$$

where the nominal unit tip resistance is limited to be no greater than 400 ksf. Equation 2.4 is plotted in Figure 2.2 along with the measured maximum unit tip resistance values acquired from load tests in weak rock in or near the state of Missouri. Unlike measurements plotted in Figure 2.1, measurements plotted in Figure 2.2 are not universally associated with the ultimate tip resistance. Measurements of unit tip resistance that are deemed to have achieved failure are therefore indicated by boxes surrounding the respective data points as noted in the figure. Equation 2.4 was established considering only those measurements deemed to have achieved failure in tip resistance.

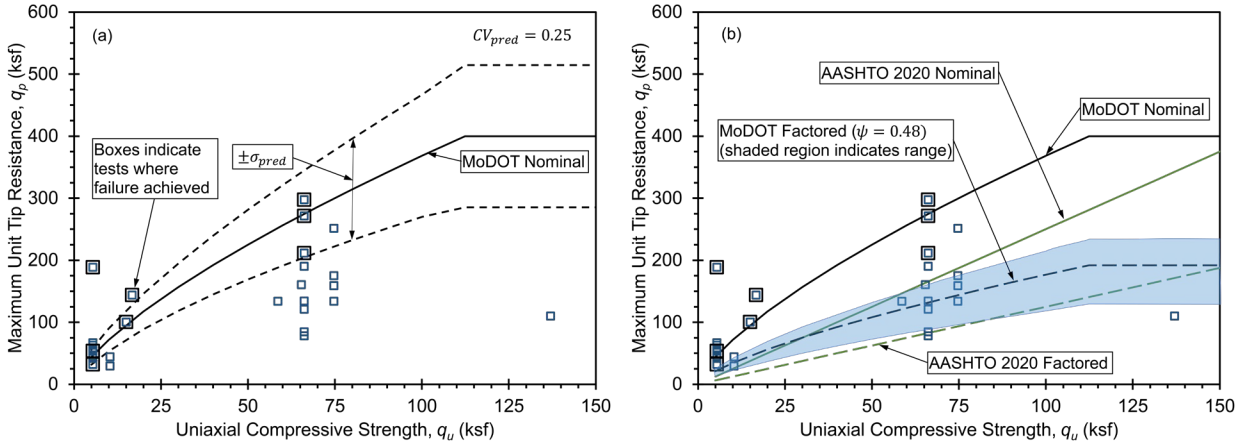

Figure 2.2 – MoDOT design relation for unit tip resistance in weak rock from compressive strength of rock core: (a) nominal resistance showing prediction uncertainty and (b) nominal and factored unit resistance for MoDOT and AASHTO (2020) design methods.

The observed variability of unit tip resistance for drilled shafts in weak rock in Figure 2.2 is considerably less than that observed for unit side resistance in Figure 2.1. Dashed lines in Figure 2.2a again indicate prediction uncertainty bounds one standard deviation above and below the relation of Equation 2.4. These bounds correspond to a coefficient of variation for prediction uncertainty, CV_{pred}, of 0.25, which is less than half of that determined for unit side resistance in similar materials. Probabilistically calibrated resistance factors for Equation 2.4 are therefore correspondingly greater than resistance factors for Equation 2.3 and vary from a high of 0.59 to a low of 0.32 depending on uncertainty in $\overline{q_u}$ as indicated by the shaded region in Figure 2.2b. The dashed line shown in Figure 2.2b reflects the factored resistance for typical levels of site characterization and is associated with a resistance factor of 0.48.

For comparison, Figure 2.2b also shows curves reflecting the nominal and factored unit tip resistances prescribed in the current AASHTO design specifications, which are described in Section 2.3. The current AASHTO design method produces nominal unit tip resistance values that are considerably less than those produced using Equation 2.4. Given that similar resistance factors are prescribed for both the AASHTO ($\psi = 0.50$) and MoDOT ($0.59 \geq \psi \geq 0.32$) design methods, the current AASHTO specifications produce factored unit tip resistance values that are considerably less than those prescribed by current MoDOT provisions.

2.2.2 MoDOT Design Methods based on Texas Cone Penetration Test Measurements

While not commonly utilized, MoDOT has also adopted design methods for drilled shafts based on TCPT measurements in weak rock. Using these methods, the nominal unit side resistance, q_s, can be established in units of ksf as:

$$q_s = 31.6 \cdot \overline{MTCP}^{-1.18} \leq 30 \text{ ksf} \quad (2.5)$$

where $\overline{MTCP}$ is the representative mean value of TCPT penetration for the soil or rock along the considered shaft segment in units of inches per 100 blows and the nominal unit side resistance is again limited to being no greater than 30 ksf. This design relation is plotted in Figure 2.3 along with the measured maximum unit side resistance values used to establish the relation. As observed in Figure 2.1, the measurements shown in Figure 2.3 indicate considerable variability in unit side resistance for drilled shafts in weak rock, with correspondingly wide prediction uncertainty bounds and a large coefficient of variation for prediction uncertainty ($CV_{pred} = 0.61$). Probabilistically calibrated resistance factors for Equation 2.5 range from 0.20 to 0.11 as represented by the shaded region in Figure 2.3b, with a resistance factor of 0.16 being associated with typical levels of site characterization as indicated by the dashed curve in the figure.

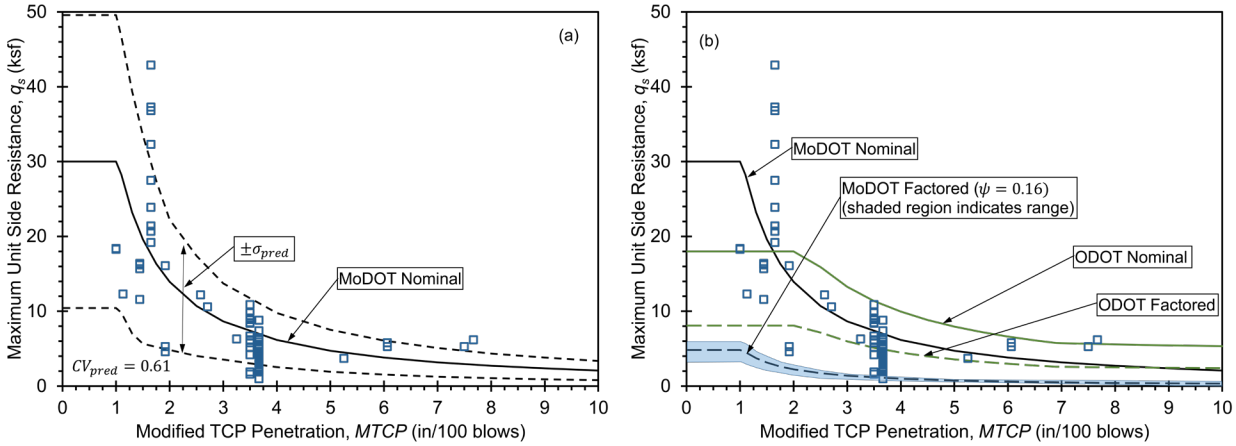

Figure 2.3 – MoDOT design relation for unit side resistance in weak rock from $MTCP$ penetration values: (a) nominal resistance showing prediction uncertainty and (b) nominal and factored unit resistance for MoDOT and current ODOT design methods.

Figure 2.3b also shows the nominal and factored unit side resistance from the current ODOT method (Equation 2.1) for comparison. As shown in the figure, the current ODOT method produces considerably greater values of nominal unit side resistance than the MoDOT TCPT-based method (Equation 2.5) for $\overline{MTCP}$ greater than approximately 1.6. The ODOT method produces considerably smaller values of nominal unit side resistance for $\overline{MTCP}$ less than approximately 1.6 because of differences in the upper limit placed on unit side resistance. Because of the much smaller resistance factors specified for the MoDOT TCPT-based method, factored unit side resistance values for the MoDOT method are considerably less than those associated with the current ODOT method for all values of $\overline{MTCP}$.

As shown in Figure 2.4, the nominal unit tip resistance, q_p, in units of ksf can be determined as:

$$q_p = 500 \cdot \overline{MTCP}^{-1.22} \leq 400 \text{ ksf} \qquad (2.6)$$

where the nominal unit tip resistance is again limited to being no greater than 400 ksf. As observed for design based on compressive strength, the measurements shown in

Figure 2.4 indicate significantly less variability in unit tip resistance for drilled shafts in weak rock compared to unit side resistance, with a coefficient of variation for prediction uncertainty equal to 0.25. Probabilistically calibrated resistance factors for Equation 2.6 range from 0.63 to 0.22, with a resistance factor of 0.45 being associated with typical levels of site characterization as respectively indicated by the shaded region and dashed curve in Figure 2.4b.

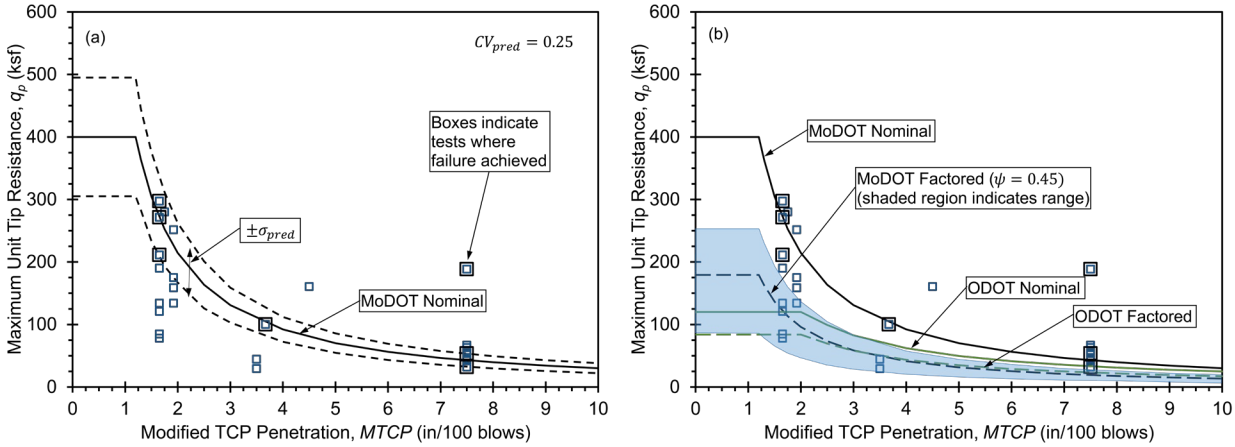

Figure 2.4 – MoDOT design relation for unit tip resistance in weak rock from $MTCP$ penetration values: (a) nominal resistance showing prediction uncertainty and (b) nominal and factored unit resistance for MoDOT and current ODOT design methods.

Comparison of nominal and factored unit tip resistances from the ODOT (Equation 2.2) and MoDOT (Equation 2.6) TCPT-based methods indicates that the MoDOT TCPT-based method produces considerably greater values of nominal unit tip resistance for all $\overline{MTCP}$ values. Values of factored unit tip resistance from the two methods are practically similar for $\overline{MTCP}$ values greater than about 2. However, the MoDOT TCPT-based method produces considerably greater values of factored unit tip resistance for $\overline{MTCP}$ values less than 2, both as a result of differences in the fundamental design relations (Equations 2.2 and 2.6) and as a result of differences in the upper limit specified for the two alternative methods.

2.2.3 MoDOT Design Methods based on Standard Penetration Test Measurements

Drawing from Colorado Department of Transportation (CDOT) practice, MoDOT developed and adopted SPT-based design methods for drilled shafts in weak rock. With these methods, the nominal unit side resistance, q_s, in units of ksf is predicted as:

$$q_s = \frac{\overline{N_{eq-60}}}{14} \leq 30 \text{ ksf} \qquad (2.7)$$

where $\overline{N_{eq-60}}$ is the representative mean of the equivalent N-value for the soil or rock along the considered shaft segment in units of blows per ft, determined as described in Chapter 3. In Equation 2.7, the nominal unit side resistance is again limited to being no

greater than 30 ksf. Equation 2.7 is plotted in Figure 2.5 along with the measured maximum unit side resistance values used to establish the relation, which again reveal considerable variability in unit side resistance for drilled shafts in weak rock and large prediction uncertainty bounds. The coefficient of variation for prediction uncertainty ($CV_{pred} = 0.64$) for Equation 2.7 is the largest coefficient of variation among the alternative MoDOT design methods for unit side resistance, indicating Equation 2.7 is the least reliable predictor of unit side resistance among the three methods. Probabilistically calibrated resistance factors for Equation 2.7 correspondingly range from 0.16 to 0.09 as represented by the shaded region in Figure 2.5b, with a resistance factor of 0.13 being associated with the dashed curve in the figure and representing typical levels of site characterization.

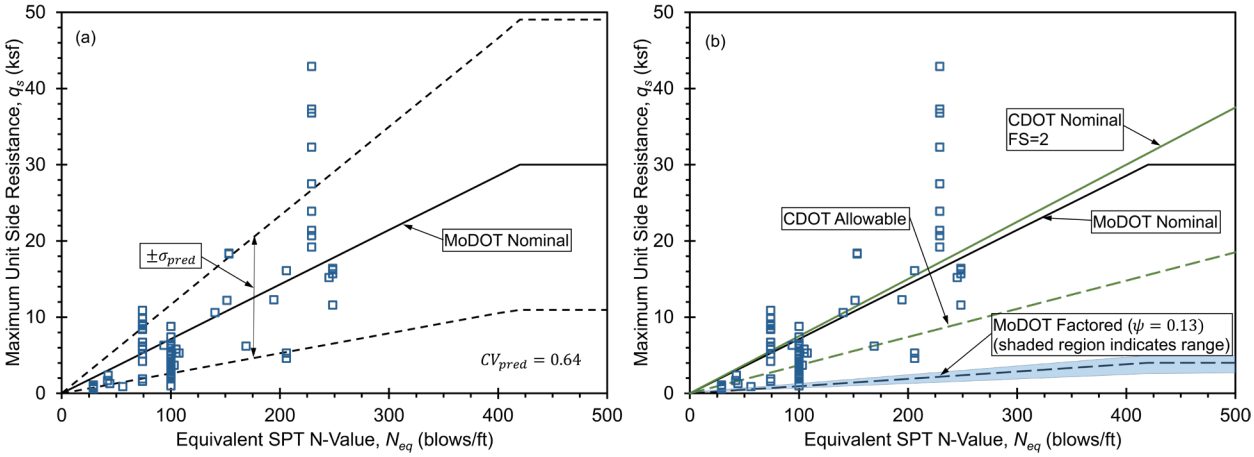

Figure 2.5 – MoDOT design relation for unit side resistance in weak rock from SPT equivalent N-values: (a) nominal resistance showing prediction uncertainty and (b) nominal and factored unit resistance for MoDOT design method and allowable and nominal unit resistance from CDOT design method.

Similar relations adopted by CDOT (Abu-Hejleh, et al., 2005) are also shown in Figure 2.5b and described in Section 2.6. The CDOT relation indicated as “CDOT Allowable” is fundamentally presented as an “allowable capacity”, which is analogous with a factored resistance. The relation indicated as “CDOT Nominal” is established based on the CDOT Allowable relation considering a presumed factor of safety equal to 2. Figure 2.5b shows that the CDOT Nominal relation is quite similar to the nominal unit side resistance predicted using Equation 2.7. In contrast, the factored unit side resistance from Equation 2.7 is considerably less than that produced using the CDOT Allowable relation, a result that follows directly from the large variability observed in load test measurements shown in Figure 2.5.

The nominal unit tip resistance, q_p, for the MoDOT SPT-based design method is similarly established as:

$$q_p = \frac{\overline{N_{eq-60}}}{1.6} \leq 400 \text{ ksf} \qquad (2.8)$$

where the nominal unit tip resistance is again in units of ksf and limited to being no greater than 400 ksf. Figure 2.6 shows Equation 2.8 plotted along with the measured maximum unit tip resistance values used to establish the relation. The variability of measured unit tip resistance values in the figure is considerably greater than that observed for the two alternative MoDOT design relations for unit tip resistance, which is reflected in the large prediction bounds and the coefficient of variation for prediction uncertainty ($CV_{pred} = 0.59$). As was observed for Equation 2.7, these observations indicate Equation 2.8 is also the least reliable predictor of unit tip resistance among the three MoDOT methods. Probabilistically calibrated resistance factors for Equation 2.8 range from 0.23 to 0.12 as depicted by the shaded region in Figure 2.6b, with a resistance factor of 0.19 being associated with the dashed curve in the figure and representing typical levels of site characterization. Comparison of the nominal and factored unit tip resistance values shown in Figure 2.6 for the MoDOT and corresponding CDOT methods reveals that Equation 2.8 produces nominal and factored unit tip resistances that are considerably less than the CDOT method.

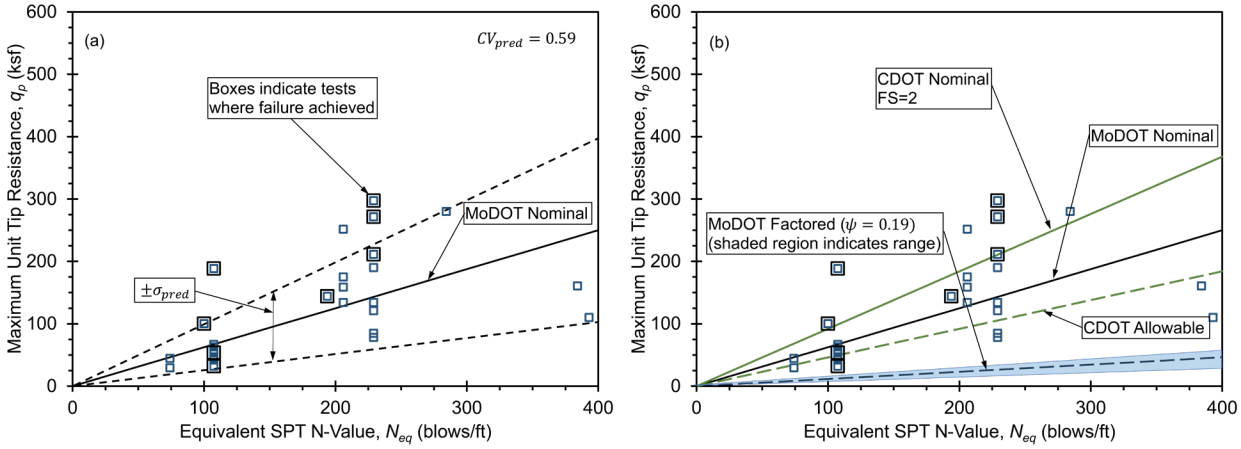

Figure 2.6 – MoDOT design relation for unit tip resistance in weak rock from SPT equivalent N-values: (a) nominal resistance showing prediction uncertainty and (b) nominal and factored unit resistance for MoDOT design method and allowable and nominal unit resistance from CDOT design method.

Subsequent to adoption of the methods described in this section, Pierce (2013) re-evaluated the same load test measurements and developed modifications to Equation 2.7 and 2.8 that have not yet been adopted by MoDOT. Pierce (2013) recommended that unit side resistance be predicted as:

$$q_s = \frac{\overline{N_{eq-60}}}{15} \tag{2.9}$$

while unit tip resistance be predicted as:

$$q_p = 0.95 \cdot \overline{N_{eq-60}} \tag{2.10}$$

where both q_s and q_p are in units of ksf. Pierce does not address the issue of requiring an upper limit for Equations 2.9 and 2.10. Equation 2.9 is only slightly different from

Equation 2.7 and, thus, previous observations regarding comparisons with the CDOT design relations generally apply. However, Equation 2.10 is markedly different from Equation 2.8. Figure 2.7 shows the relation of Equation 2.10 plotted with measured values of unit tip resistance used to develop the relation, along with prediction uncertainty bounds and comparisons with the CDOT design relations. The prediction uncertainty associated with Equation 2.10 is smaller than that associated with Equation 2.8. Figure 2.7 shows that the Pierce (2013) relation for nominal unit tip resistance (Equation 2.10) is quite similar to the CDOT nominal relation for unit tip resistance although the factored unit resistance from Equation 2.10 is still considerably less than the allowable unit tip resistance from the CDOT relation.

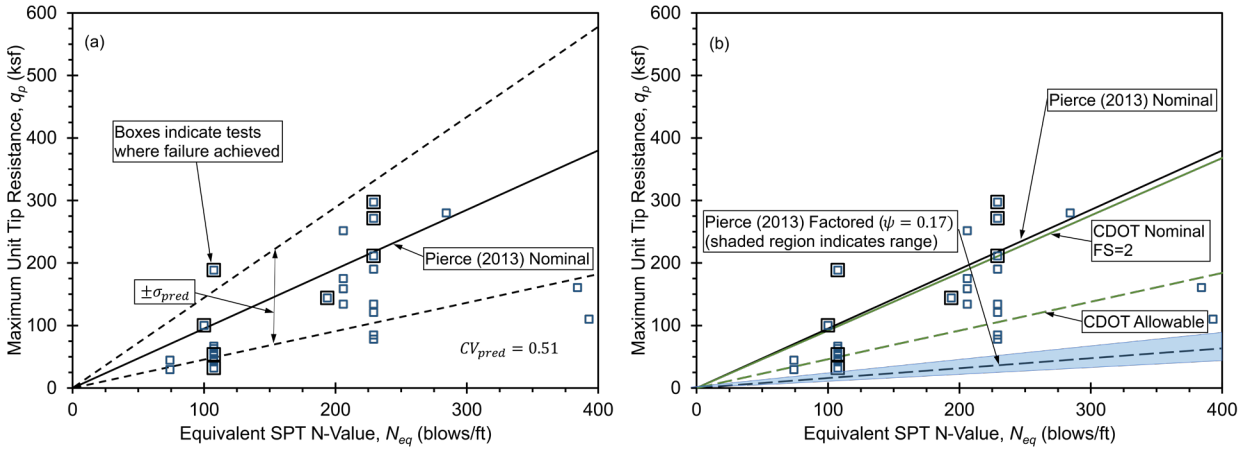

Figure 2.7 – Pierce (2013) design relation for unit tip resistance in weak rock from SPT equivalent N-values: (a) nominal resistance showing prediction uncertainty and (b) nominal and factored unit resistance for MoDOT design method and allowable and nominal unit resistance from CDOT design method.

2.3 AASHTO DESIGN METHODS BASED ON COMPRESSIVE STRENGTH

The current AASHTO LRFD Bridge Design Specifications (AASHTO, 2020) prescribe methods for design of drilled shafts in rock based on uniaxial compressive strength. The prescribed method for unit side resistance is based on recommendations by Kulhawy, et al. (2005) and, when considering units of ksf, can be written as:

$$q_s = 1.46 \cdot \sqrt{q_u} \leq 1.46 \cdot \sqrt{f_c'} \tag{2.11}$$

where q_u is the uniaxial compressive strength in units of ksf and f_c' is the compressive strength of concrete used for the drilled shaft. The prescribed AASHTO method for unit tip resistance is:

$$q_p = 2.5 \cdot q_u \tag{2.12}$$

The current AASHTO specification prescribes a resistance factor of 0.55 for Equation 2.11 and a resistance factor of 0.50 for Equation 2.12. Nominal and factored unit

resistance values from Equation 2.11 and 2.12 are respectively plotted in Figs. 2.1 and 2.2 for comparison with the MoDOT design methods based on compressive strength.

2.4 TEXAS DEPARTMENT OF TRANSPORTATION DESIGN METHODS BASED ON TEXAS CONE PENETRATION TEST MEASUREMENTS

TxDOT prescribes methods for prediction of unit side and tip resistance from TCPT measurements similar to methods described previously from ODOT and MoDOT but presented in design charts rather than as equations (TxDOT Geotechnical Manual, 2020). The design charts provide “allowable” values for unit side and tip resistance that are analogous to factored values for load and resistance factor design (LRFD) with a factor of safety of 3 being adopted for unit side resistance and a factor of safety of 2 being adopted for unit tip resistance. Figures 2.8 and 2.9 respectively show the nominal unit side and unit tip resistance determined from these charts by multiplying the provided allowable values by the specified factor of safety. Nominal resistances from the corresponding ODOT and MoDOT design methods are also plotted in the figures for comparison. These figures indicate the ODOT and TxDOT TCPT-based design methods produce similar values of nominal unit side and tip resistance, although TxDOT uses a slightly greater upper limit for unit side resistance.

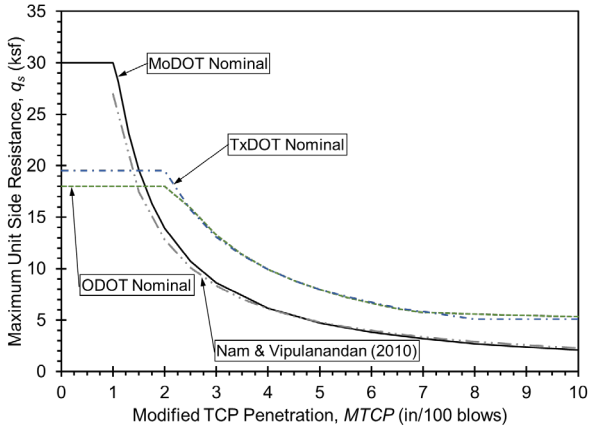

Figure 2.8 – Comparison of nominal unit side resistance from different TCP-based design methods.

2.5 NAM AND VIPULANANDAN METHODS BASED ON TEXAS CONE PENETRATION TEST MEASUREMENTS

Nam and Vipulanandan (2010) also proposed relationships for unit side and tip resistance from TCPT measurements based on several load tests in North Central Texas for drilled shafts socketed in weak rock. The proposed relations were reported in units of MPa for unit side and tip resistance and units of mm per 100 blows for $MTCP$. Converting these relations into units of ksf for unit resistance (q_s and q_p) and inches per 100 blows for $MTCP$, the relation for unit side resistance can be written as:

$$q_s = 27 \cdot \overline{MTCP}^{-1.07} \tag{2.13}$$

and the relation for unit tip resistance can be written as:

$$q_p = 200 \cdot \overline{MTCP}^{-0.79} \quad (2.14)$$

Equations 2.13 and 2.14 are also plotted in Figs. 2.8 and 2.9, respectively. The Nam and Vipulanandan relationship for unit side resistance (Equation 2.13) is seen to be similar to the MoDOT design relation for unit side resistance (Equation 2.5) whereas the Nam and Vipulanandan relationship for unit tip resistance is more similar to the ODOT and TxDOT design relations (Eqs. 2.2 and 2.14, respectively).

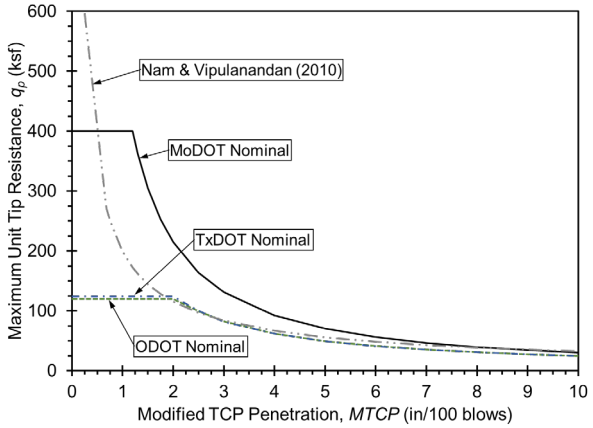

Figure 2.9 – Comparison of nominal unit tip resistance from different TCP-based design methods.

2.6 COLORADO DEPARTMENT OF TRANSPORTATION METHODS BASED ON STANDARD PENETRATION TEST MEASUREMENTS

CDOT has traditionally designed drilled shaft foundations socketed in weak rock using empirical methods and “rules of thumb” based on Standard Penetration Test (SPT) measurements since the 1960s. These historical practices were evaluated and updated based on a study by Abu-Hejleh, et al. (2005) based on load test measurements from several bridge projects to produce the “Updated Colorado SPT-based method”, or UCSB method. Similar to TxDOT, the UCSB method produces “allowable” values of unit side and tip resistance that are respectively determined as:

$$q_{s-allowable} = 0.037 \cdot N \quad (2.15)$$

$$q_{p-allowable} = 0.46 \cdot N \quad (2.16)$$

where $q_{s-allowable}$ is the allowable unit side resistance in units of ksf, $q_{p-allowable}$ is the allowable unit tip resistance in units of ksf, and N is the corrected SPT N-value in units of blows per ft. Studies by Abu-Hejleh, et al. (2003, 2005) concluded that the UCSB design methods predicts side and tip resistance values with an inherent factor of safety of approximately 2. Considering this value of the factor of safety, the nominal unit side and tip resistance for the UCSB methods can respectively be estimated as:

$$q_s = 0.075 \cdot N \quad (2.17)$$

$$q_p = 0.92 \cdot N \quad (2.18)$$

where q_s is the predicted nominal unit side resistance and q_p is the predicted nominal unit tip resistance (ksf), both in units of ksf.

Chapter 3 - Site Selection and Characterization

A signature component of the scope of work was field load testing of full-scale drilled shafts to allow for direct evaluation of existing design methods described in Chapter 2, or development of new design methods if justified by collected load test measurements. In order to accomplish this objective, devoted effort was given to selection of appropriate load test sites and subsequent characterization of subsurface conditions at the selected sites. This chapter describes important site selection and characterization activities conducted as part of the subject research. Probabilistic interpretations of important design parameters are also described for the selected test sites and several additional sites where load tests have been previously performed in weak rock formations in Oklahoma.

3.1 SITE SELECTION

Initial plans were to conduct load tests on replicate drilled shafts for at least two, or possibly three test sites to provide sufficient data to allow for evaluation and development of appropriate design methods for the Oklahoma Department of Transportation (ODOT). Substantial effort and attention were given to selection of sites for full-scale load testing in order to satisfy both technical requirements for the research and logistical requirements for load testing. General logistical requirements for site selection included having a safe working area of sufficient size to construct and test multiple drilled shafts at each site. Additionally, selected test sites needed to have good access for heavy equipment and be conveniently located near the Oklahoma City metro area to control site preparation, equipment mobilization, and general transport expenses so that the scope of testing could be maximized within the available budget. Finally, desired subsurface conditions to satisfy technical requirements needed to be located at reasonable depths to limit costs for construction of the test shafts so that the scope of testing could be maximized.

The fundamental technical requirement for site selection was to identify sites with subsurface conditions that would help to fill gaps in available load test data in weak rock materials that are present in Oklahoma and nearby states. Consideration of available data presented in Chapter 2 reveals significant differences among alternative design methods for relatively hard weak rock as well as a general lack of load test data in harder weak rock. Site selection activities therefore focused on identifying sites with relatively hard weak rock present at reasonable depths. Specifically, sites were desired to have weak rock formations with Texas Cone Penetration Test (TCPT) penetration values less than 3 inches per 100 blows, and preferably compressive strengths greater than approximately 75 ksf and Standard Penetration Test (SPT) N_{eq-60}-values greater than approximately 250 blows/ft. Site selection was also focused in central Oklahoma where subsurface conditions are predominantly composed of Permian-age or younger weak rock. The desire to select sites with Permian-age rock formations followed from the fact that Pennsylvanian-age rock formations found in eastern Oklahoma are at least generally similar to Pennsylvanian-age rock formations located in Missouri and Kansas where numerous load tests have been performed on drilled shafts. A relatively small

collection of load test measurements is also available in even younger rock formations located in north Texas and southeast Oklahoma; thus, there was strong desire to perform load tests in Permian-age rock formations to produce as robust of a collection of load test measurements as possible. Finally, it was deemed desirable to perform tests in both sandstone and shale formations because both types of rock are prevalent in Oklahoma and the lack of well-documented load tests in sandstone formations.

Preliminary screening was conducted for several dozen sites. Sites were initially evaluated and considered using historical boring information from ODOT records. Virtual and physical site visits were then conducted for the most promising sites to assess logistics and site access conditions. Project specific boring and testing was also conducted by ODOT for several promising sites. After several iterations of evaluation and assessment, two sites were finally selected for load testing. The first site is located at an ODOT facility in Edmond Oklahoma, which is referred to as the “Edmond site” throughout this report. The second site is located along US Highway 81 just north of the city of Minco Oklahoma, at a salt shed facility located at the intersection with State Highway 152/37. The second site is referred to as the “Minco site” in this report.

3.2 TESTING PROCEDURES

Subsurface conditions at each of the two selected test sites were thoroughly characterized using several different subsurface investigation methods. Conditions at both sites were characterized using both TCPT and SPT measurements conducted at alternating 2.5-foot intervals in several boreholes at each site. Rock core samples were collected from additional core borings at each site with core recovery (CR) and rock quality designation (RQD) being recorded for each 5-foot core run. Numerous confined compression (CC) and uniaxial compression (UC) tests were performed on specimens prepared from collected core samples and used to characterize the compressive strength of the rock formations present at each site. Point Load Index Tests (PLT) were also performed on collected specimens of rock core and several pressuremeter (PMT) tests were conducted in additional borings at each site. Procedures followed for performing TCPT, SPT, CC, UC, PLT, and PMT tests are described in this section.

3.2.1 Texas Cone Penetration Tests

The Texas Cone Penetration Test (TCPT) is employed by the Texas Department of Transportation (TxDOT) and ODOT for characterizing the relatively stiff soil and rock conditions that are commonly encountered in Texas and Oklahoma. The TCPT is a dynamic cone penetration test that utilizes a special 3-inch diameter cone specified in TxDOT Designation: TEX-132-E (TxDOT, 2020). The TxDOT procedure formally requires use of a special 170-lb hammer dropped from a distance of 24-inches for each hammer blow. However, since such hammers are not commonly available outside of Texas, the procedure is often performed using conventional SPT hammers with 140-lb hammers and 30-inch drops. Conventional SPT hammers theoretically impart similar hammer energy to that of the specified hammer (350 ft-lb per blow for conventional SPT hammers vs. 340 ft-lb per blow for the specified TCPT hammer) and, thus, are likely to produce similar measurements. However, because use of conventional SPT hammers

is not specified, TCPT measurements collected using conventional SPT hammers are referred to as “modified” TCPT measurements (Pierce, 2013).

In relatively soft materials, the TCPT procedure involves driving the cone to penetrate through two sequential 6-inch increments and measuring the number of blows required to penetrate the cone for each 6-inch increment. In such materials, the TCPT measurement is reported as a blow count calculated as the cumulative number of blows required to penetrate the cone for both 6-inch increments, in units of blows/ft similar to that reported for SPT measurements. In harder materials where the cone cannot be penetrated a distance of 12 inches in fewer than 100 blows, the TCPT procedure is changed to record the penetration distance for two sequential 50 blow increments. In such materials, the TCPT measurement is reported as a penetration distance calculated as the cumulative distance penetrated for the two sequential 50 blow increments, typically in units of inches per 100 blows. The TCPT penetration distance is generally appropriate for the materials involved in the present work, and is reported as “modified” penetration distance, $MTCP$, throughout this report to indicate the values were obtained using a conventional SPT hammer rather than the TxDOT-specified hammer.

3.2.2 Confined and Uniaxial Compression Tests

Confined compression (CC) and uniaxial compression (UC) tests were performed on core samples recovered from both load test sites. Tests were conducted for specimens from distributed depths and borehole locations at each site. Most CC and UC tests were conducted at a nearby lab facility as coring was being conducted such that testing was generally completed within a day of coring, and sometime within a few hours. A few additional CC and UC tests were conducted on remaining core in the laboratory at the University of Missouri in the days following coring, usually within a week of coring.

Confined compression tests were generally performed in accordance with ASTM D2850. Specimens approximately 4 inches in height were cut from intact lengths of the approximately 2-inch diameter core and placed into a triaxial cell within a rubber membrane. Specimens were then subjected to a confining stress approximately equal to the in-situ overburden stress for the specimen prior to applying axial load to produce an axial strain rate of approximately 1 %/min. The confined compressive strength, q_u, for each test was taken to be the maximum legitimate principal stress difference observed in each test ($\sigma_1 - \sigma_3$).

Uniaxial compression (UC) tests were performed in accordance with ASTM D2166. Specimens approximately 4 inches in height were again cut from intact lengths of rock core and loaded without confinement at an axial strain rate between 0.5 to 2 % per minute. The uniaxial compressive strength, q_u, was taken to be the maximum legitimate compressive stress observed in each test.

3.2.3 Standard Penetration Tests

SPT measurements were performed using a Standard split-barrel sampler and a conventional SPT hammer in general accordance with ASTM D1586. In the test, the

number of blows (up to 50) required to penetrate the sampler a distance of 6 inches at the base of a borehole is generally recorded for three successive 6-inch intervals. The measured SPT N-value, recorded in units of blows/ft and denoted as N_{meas}, is the sum of the blow counts for the second and third intervals, disregarding the first interval. However, when conducting SPT measurements in weak rock, it is common for 50 blows to be applied for a specific test interval prior to the sampler being penetrated the required distance of 6 inches. In such cases, testing is ceased, and the distance penetrated for the interval is reported along with blow counts for any previously completed test intervals. For the present work, the collected measurements were then used to establish an "equivalent" N-value denoted as N_{eq}.

Several potential scenarios exist for establishing N_{eq}-values. In instances where 50 blows are applied in the first test interval before the sampler penetrates a distance of 6 inches, the penetration achieved within those 50 blows is recorded and converted to an equivalent N-value as:

$$N_{eq} = 12 \cdot \left(\frac{N_{meas}}{p}\right) \quad (3.1)$$

where p is the measured penetration of the sampler (in inches) for the interval and N_{meas} is the number of blows imparted to produce that penetration (usually 50). In instances where the sampler is penetrated the full 6 inches at less than 50 blows during the first interval, but 50 blows are applied for the second interval before the sampler penetrates a distance of 6 inches, N_{eq} is calculated taking N_{meas} to be equal to the total number of blows for both intervals and p to be equal to the total penetration over both intervals. In instances when the sampler is successfully penetrated a distance of 6 inches for less than 50 blows during both the first and second intervals, but 50 blows are applied for the third interval before the sample penetrates a distance of 6 inches, N_{eq} is calculated taking N_{meas} to be equal to the total number of blows for the second and third intervals and p to be equal to the total penetration over the second and third intervals.

Finally, an energy correction was applied to N_{eq}-values established as described to account for the influence of different hammer efficiency and produce the N_{eq-60} values that are used as the basis for design methods described in Chapter 2, and in subsequent chapters. The correction is applied as (Test Method D4633 – from ASTM D1586):

$$N_{eq-60} = \left(\frac{E_f}{60}\right) \cdot N_{eq} \quad (3.2)$$

where E_f is the measured energy efficiency of the hammer system (in percent).

3.2.4 Point Load Index Tests

Point Load Index tests were performed on specimens of rock core from each test site in general accordance with ASTM D5731. Specimens approximately 1 inch in height were

saw cut from intact segments of core and loaded in an axial test orientation. Tests were performed for specimens taken from distributed locations along each core. Measured values were size corrected for a core diameter of 50 mm to produce size corrected values of the point load strength index, $I_{s(50)}$, as specified in the standard.

3.2.5 Pressuremeter Tests

Pressuremeter tests (PMT) were performed at 5-foot depth intervals in boreholes made specifically for pressuremeter testing near borings made for coring or in situ testing. Testing was performed using a G-AM II pressuremeter following procedures prescribed by the manufacturer. In most cases, PMT measurements were unable to reach the yield pressure of the formation; as such, only the pressuremeter modulus associated with the elastic range of PMT response was reported and interpreted for each site.

3.3 SITE CHARACTERIZATION FOR EDMOND SITE

The Edmond test site is located near the intersection of NE 122nd St and I-35 in Edmond, Oklahoma. The site is the location of several ODOT facilities, including a relatively large yard surfaced with asphalt millings that makes for a near ideal test site. Borings were made at four different boring locations shown in Figure 3.1, with up to three replicate borings being made at each boring location for different purposes. One boring at each location was used to acquire rock core for measuring compressive strength, point load strength index, core recovery, and RQD. A second boring was typically completed at each location for in situ testing, which was generally conducted by performing SPT and TCPT measurements at alternating 2.5-foot intervals. A third boring was completed at some locations for pressuremeter testing.

3.3.1 General Subsurface Characteristics

The Edmond test site is located within the central red-bed plains geomorphic province of Oklahoma that is generally composed of sedimentary rock deposited in the early Permian age. The predominant geologic formations in the area include shallow-marine, deltaic, and alluvial deposits of red Garber sandstone and Fairmont shale. Borings completed for the project only encountered the Garber sandstone. Sedimentary conglomerate was also sporadically observed in some borings that was most likely deposited during the Triassic Period as sediments deposited mainly in rivers and lakes drained from hills into the lowlands of Permian sedimentary strata (Johnson, 2008).

Figure 3.2 shows measurements of water content and total unit weight taken from core samples along with measured values of core recovery (CR) and rock quality designation (RQD) for the collected core. The observed stratigraphy at the boring locations consists of a thin layer of silty sand overlying sandstone throughout the entire depth of the borings. Several thin pockets of sedimentary conglomerate were observed at sporadic depths in three of the four core borings. Core recovery of the sandstone was generally observed to be between 60 to 100 percent throughout much of the boring depths, although little core was recovered for core runs conducted around elevation 1065. RQD was generally less than 50 percent throughout most of the depths investigated, with

very low RQD being observed above elevation 1085, around elevation 1065, and below elevation 1045.

Figure 3.1 – Aerial photo of Edmond test site showing boring locations.

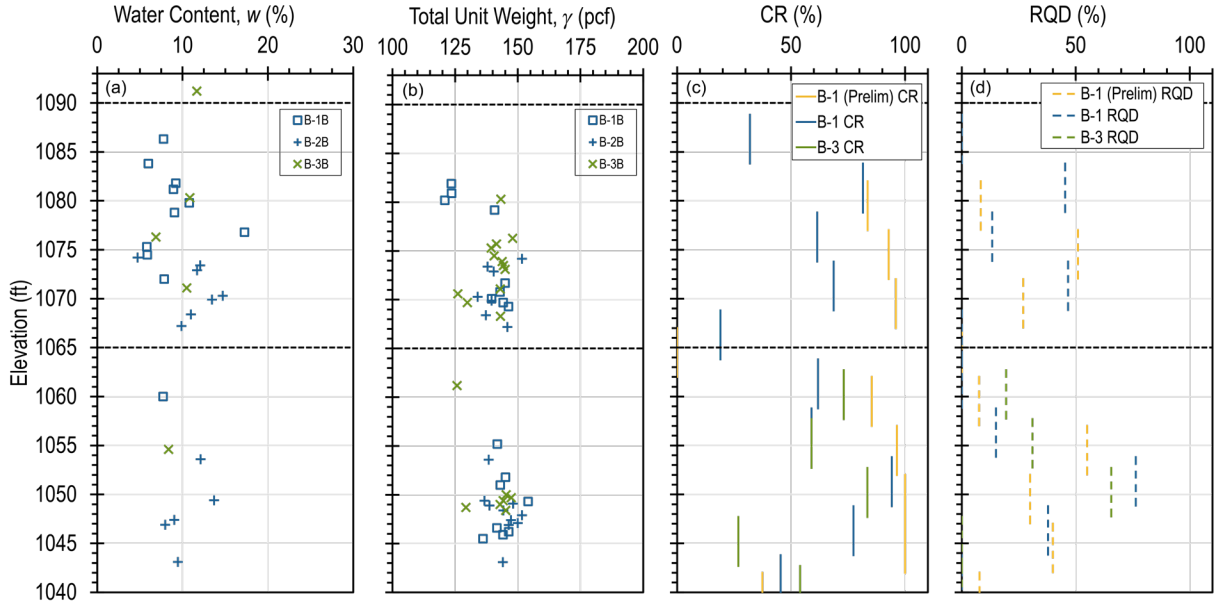

Figure 3.2 – Site characterization measurements for Edmond test site: (a) water content, (b) total unit weight, (c) core recovery, and (d) RQD.

For purposes of interpretation of load test measurements, the stratigraphy was divided into three separate strata based on all collected measurements. The uppermost stratum is a silty sand that is presumed to be weathered from the underlying sandstone

extending from the ground surface (approximate elevation 1093) to elevation 1090. The underlying sandstone is separated into two distinct strata: an upper sandstone stratum extending from elevation 1090 to elevation 1065, and a lower sandstone stratum extending below elevation 1065 to at least elevation 1040. Sedimentary conglomerate was sporadically observed within both of the sandstone strata.

Measurements of the compressive strength from rock core, TCPT penetration, SPT N-values, and the point load strength index from the Edmond site are respectively plotted versus elevation in Figure 3.3. The figure also shows probabilistic interpretations of the respective design parameters for the upper and lower sandstone strata as described in the following sections, with mean values of each parameter being indicated as solid vertical lines and the mean plus and minus one standard deviation being indicated using dashed vertical lines.

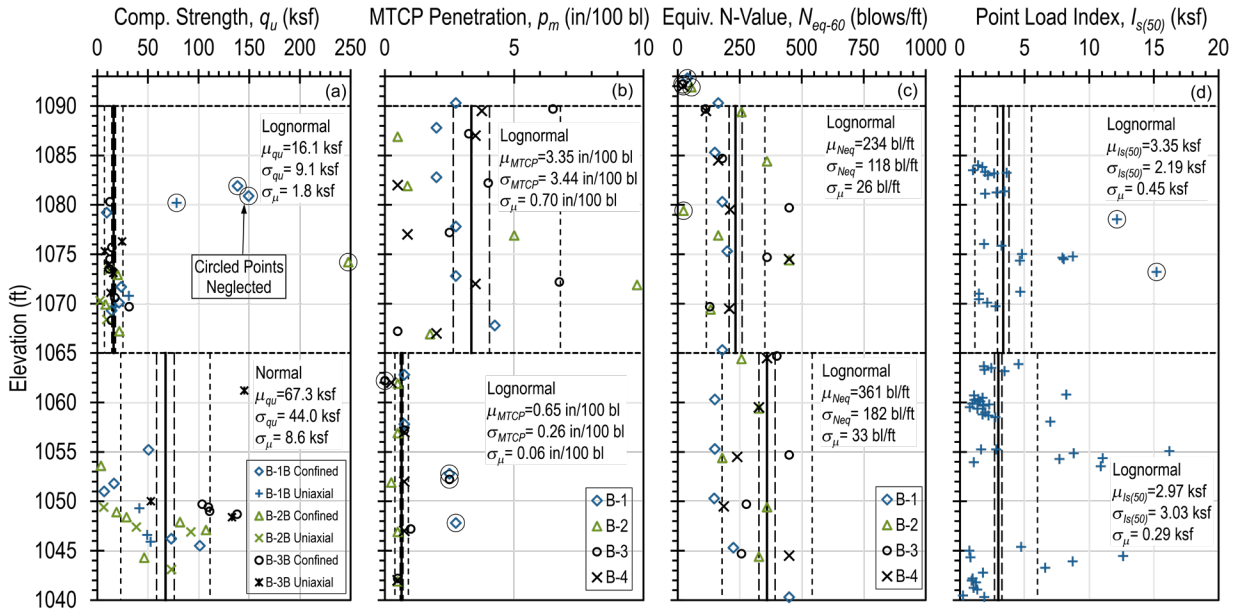

Figure 3.3 – Measurements of design parameters for the Edmond test site: (a) compressive strength, (b) TCPT penetration, (c) SPT N-values, and (d) point load strength index.

3.3.2 Compressive Strength

Measured values of compressive strength for rock core collected from three core borings at the site are plotted versus elevation in Figure 3.3a. Compressive strength could not be measured above elevation 1082 and between elevation 1055 and 1068 because of poor core recovery or rock quality. Measured values of compressive strength for sedimentary conglomerate samples are shown in Figure 3.3a but were neglected for interpretation of compressive strength for the two strata as indicated in the figure. As shown in the figure, no consistent differences were observed in measured values of compressive strength from confined and uniaxial compression tests; as such measurements from both types of tests were interpreted collectively.

Probabilistic interpretations of compressive strength were developed for the collected measurements using both spreadsheet calculations and MATLAB distribution fitting tools that allow one to interactively interpret the measurements. The resulting interpretations of compressive strength are shown in Figure 3.3a. Reported values from the probabilistic interpretations include the best-fit distribution type (lognormal or normal), the interpreted mean value from the best-fit distribution, μ_{q_u}, and two values of standard deviation, σ_{q_u} and σ_μ. The magnitude of σ_{q_u} represents so-called "prediction uncertainty" that reflects the likelihood of measuring a given value from a new test. In contrast, the magnitude of σ_μ represents "model uncertainty" (strictly the uncertainty in the mean value, μ_{q_u}) that reflects the degree of confidence in the interpreted model of compressive strength. The interpreted mean values of compressive strength are indicated by the solid lines in Figure 3.3a. Bounds indicating the mean value plus or minus the interpreted standard deviations are indicated using dashed lines with the outer dashed lines representing prediction uncertainty (σ_{q_u}) and the inner dashed lines representing model uncertainty (σ_μ), which is necessarily less than the prediction uncertainty.

As shown in Fig 3.3a, the upper sandstone stratum has a mean compressive strength of 16.1 ksf whereas the lower sandstone stratum has a mean compressive strength of 67.3 ksf. The upper sandstone is also seen to have less variability than the lower sandstone stratum based on comparison of the reported standard deviations.

3.3.3 Modified Texas Cone Penetration Test Penetration Resistance

Measurements of TCPT penetration values from four in-situ test borings for the Edmond Site are similarly plotted versus elevation in Figure 3.3b. No TCP tests were performed within the silty sand stratum. Measured $MTCP$ values in the upper sandstone stratum varied considerably, ranging from 0.5 to 9.75 inches per 100 blows, with no apparent trend in measurements for tests from a given borehole. The interpreted mean value of $MTCP$ for the upper sandstone is 3.4 inches per 100 blows. Measured $MTCP$ values within the lower sandstone stratum were much more consistent, even when considering measurements that were neglected. The interpreted mean value of $MTCP$ for the lower sandstone is 0.65 inches per 100 blows, which indicates significantly harder sandstone than observed for the upper sandstone stratum.

3.3.4 Standard Penetration Test N-values

Measured SPT N_{eq-60} values from the four in-situ test borings at the Edmond test site are plotted versus elevation in Figure 3.3c, and are qualitatively consistent with measurements of compressive strength and TCPT penetration. Measured SPT N_{60} values in the silty sand ranged from 20 to 56 blows/ft. Measured N_{eq-60} values in the sandstone produced a mean N_{eq-60} value of 234 blows/ft for the upper sandstone and a mean N_{eq-60} value of 361 blows/ft in the lower sandstone stratum. The variability of N_{eq-60} measurements within both the upper and lower sandstone strata was generally similar.

3.3.5 Point Load Strength Index

Measurements of the point load strength index, $I_{s(50)}$, from the three core borings are plotted versus elevation in Figure 3.3d. $I_{s(50)}$ measurements within the upper sandstone ranged from approximately 1 ksf to 9 ksf, with a calculated mean value of 3.35 ksf. Measurements within the lower sandstone stratum were more variable, ranging from less than 1 ksf to more than 16 ksf, but with a mean value of 2.97 ksf. The fact that the interpreted mean values of $I_{s(50)}$ for both the upper and lower sandstone strata are similar is inconsistent with measurements of compressive strength, MTCP penetration, and SPT, all of which indicate that the upper sandstone stratum has considerably lower strength than the lower sandstone stratum. This inconsistency raises questions about the appropriateness of point load strength index measurements in sandstone. As a result, point load strength index measurements were not considered as viable measurements for design of drilled shafts in sandstone.

3.3.6 Pressuremeter Modulus

Measured values of the pressuremeter modulus, E_{PMT}, obtained from two borings at the Edmond site are plotted versus elevation in Figure 3.4. The acquired measurements indicate dramatic variability in the pressuremeter modulus, with values ranging from approximately 600 psi to more than 50,000 psi with no apparent trend being observed with elevation.

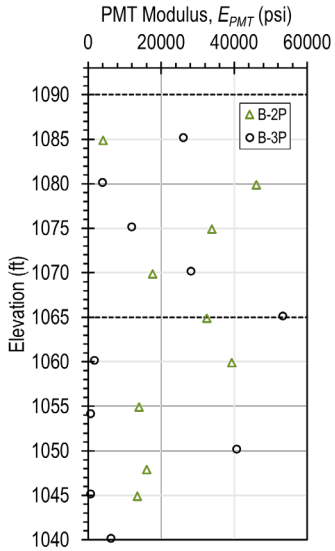

Figure 3.4 – Measurements of Pressuremeter Modulus for the Edmond test site.

Pressuremeter measurements were not considered further in this study, primarily because the yield stress of the sandstone could not be reached for any of the tests. While it is conceptually possible to relate measurements of the pressuremeter modulus to observations of side and tip resistance for the purpose of design, such use inherently involves considering pressuremeter modulus measurements as indirect measurements of rock strength that controls side and tip resistance. While some relationship between the strength and modulus of rock is often observed and logical (stronger rock is often

stiffer rock), such a relationship introduces considerable additional variability and uncertainty into a situation that is already subject to high levels of variability and uncertainty. When considered in combination with the observed scatter in measurements of pressuremeter modulus, the decision was made to not pursue development of a design method based on pressuremeter modulus because such efforts would be unlikely to produce a viable design method compared to the other approaches being considered.

3.4 SITE CHARACTERIZATION FOR MINCO SITE

The Minco test site is located at the intersection of State Highway 152/37 and US Highway 81 just north of Minco Oklahoma, about 40 miles southwest of Oklahoma City. The site is the location of an ODOT salt shed that has ample space for constructing and testing drilled shafts. Similar to investigations performed for the Edmond site, borings were made at four different locations shown in Figure 3.5, again with up to three replicate borings being made at some boring locations for different testing purposes.

Figure 3.5 – Aerial photo of Minco test site showing boring locations.

3.4.1 General Site Characteristics

The Minco test site is also located within the central red-bed plains geographic province of Oklahoma. The predominant geologic formation at the site is the Permian-age Fairmont shale, which includes occasional white gypsum deposits based on borings completed at the test site. The shale is overlain by Quaternary sand, silt, clay, and gravel deposited by the nearby Canadian River (Johnson, 2008).

Measurements of water content and total unit weight taken from core samples along with measured values of core recovery (CR) and rock quality designation (RQD) are plotted in Figure 3.6. The stratigraphy at the Minco site consists of approximately 18 feet of Quaternary sand overlying the Fairmont shale that included occasional thin lenses of gypsum at sporadic depths in three of the four core borings. Core recovery of the shale was generally quite good, with CR being close to 100 percent for most core runs. RQD measurements for the collected core was also generally quite good, and universally greater than 50 percent. RQD values for core collected above approximate elevation 1265 were slightly lower than values observed for deeper core.

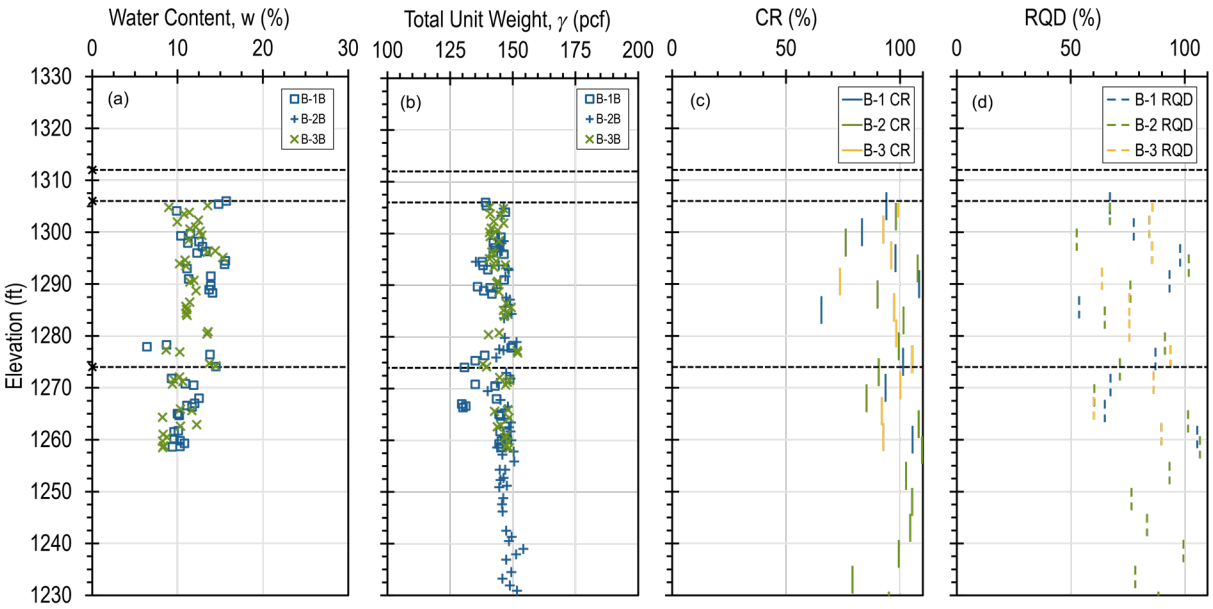

Figure 3.6 – Site characterization measurements for Minco test site: (a) water content, (b) total unit weight, (c) core recovery, and (d) RQD.

Stratigraphy at the Minco test site was divided into four separate strata based on all collected measurements. The uppermost stratum is the Quaternary sand that extends from the ground surface (approximate elevation 1329) to elevation 1312. The engineering properties of this stratum are not consequential to interpretation of the load tests because test shafts were isolated from the sand using dual casings as described in Chapter 4. The underlying shale was separated into three distinct strata that include a thin stratum of weathered shale, a thicker stratum of shale designated as the upper shale stratum, and another thick stratum of shale designated as the lower shale stratum. The weathered shale stratum extends from elevation 1312 to elevation 1306. The upper shale stratum extends from elevation 1306 down to elevation 1274 while the lower shale stratum extends from elevation 1274 to at least elevation 1230 where the deepest borings were terminated.

Measurements of the compressive strength from rock core, TCPT penetration, SPT N-values, and the point load strength index from the Minco site are respectively plotted versus elevation in Figure 3.7. The figure also shows probabilistic interpretations of the respective design parameters as described in the following sections.

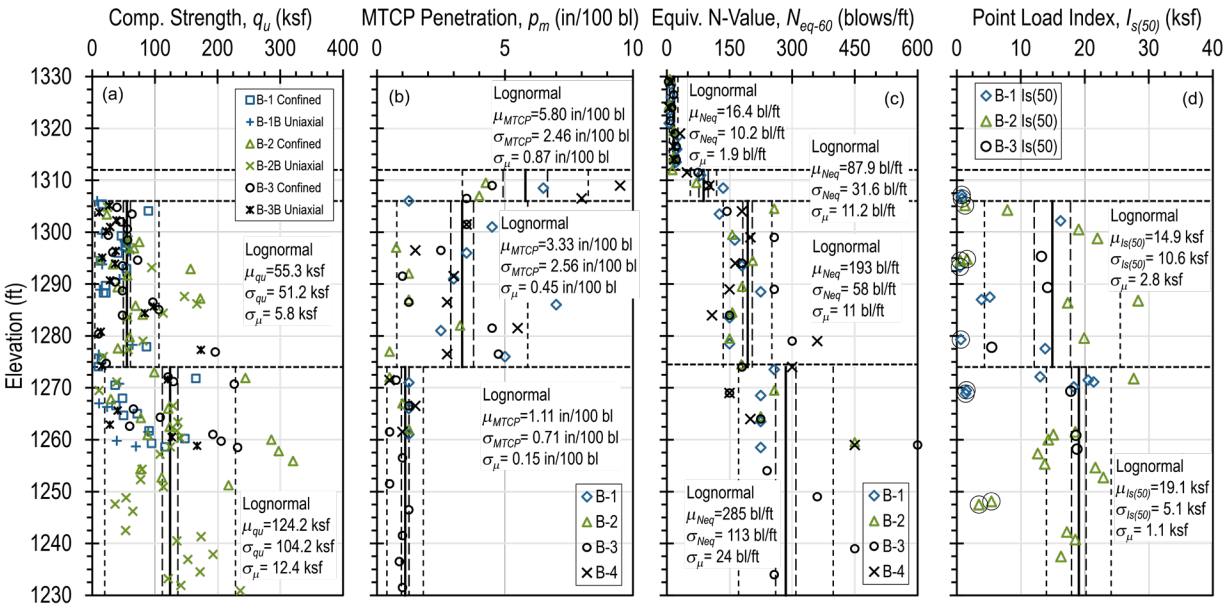

Figure 3.7 – Measurements of design parameters for the Minco test site: (a) compressive strength, (b) TCPT penetration, (c) SPT N-values, and (d) point load strength index.

3.4.2 Compressive Strength

Measured values of confined and uniaxial compressive strength are plotted versus elevation in Figure 3.7a. No compressive strength measurements were made in the Quaternary sand or the weathered shale stratum. Measurements from the upper shale stratum produced a mean compressive strength of 55.3 ksf whereas measurements from the lower shale stratum produced a mean compressive strength of 124.2 ksf. As is common for many shale formations, considerable variability is observed for compressive strengths, but without any consistent trend in the measurements.

3.4.3 Modified Texas Cone Penetration Test Penetration Resistance

TCPT measurements plotted in Figure 3.7b clearly indicate three distinct shale strata, which served as the primary basis for the selected interpretation of stratigraphy. Measured $MTCP$ values from the four in-situ test borings reflect decreasing TCPT penetration with depth, and to a lesser extent, decreasing variability. The mean $MTCP$ value for the weather shale stratum is 5.8 inches per 100 blows, while the upper shale stratum has a mean $MTCP$ equal to 3.33 inches per 100 blows and the lower shale stratum has a mean $MTCP$ equal to 1.11 inches per 100 blows. The variability observed in measured $MTCP$ values within the upper shale stratum is generally consistent with the variability in compressive strength values in the same stratum. However, the variability of $MTCP$ measurements within the lower shale stratum is noticeably less than observed for compressive strength in that stratum.

3.4.4 Standard Penetration Test N-values

SPT measurements from the four in-situ test borings at the Minco test site also support the selected stratification for the Minco test site and the observation of having generally increasing strength with increasing depth. SPT N-values measured within the Quaternary sand stratum produced an average N_{60} value of 16 blows/ft. SPT measurements conducted in the three shale strata produced mean N_{eq-60} values of 88 blows/ft for the weathered shale, 193 blows/ft for the upper shale, and 285 blows/ft for the lower shale. As observed for all measurements at both the Edmond and Minco test sites, considerable variability is observed among SPT measurements for the Minco site.

3.4.5 Point Load Strength Index

Point load strength index measurements plotted in Figure 3.7d are also highly variable but qualitatively consistent with the selected stratification based on all measurements. Notably, 11 of the 43 point load strength index measurements appear as outliers with exceptional low $I_{s(50)}$ values as indicated in the figure. These outliers were neglected when interpreting values for the respective strata. No point load strength index measurements were made within the weathered shale stratum. The mean value of $I_{s(50)}$ measurements for the upper shale stratum is 14.9 ksf while the mean value of $I_{s(50)}$ measurements for the lower shale stratum is 19.1 ksf. The variability of $I_{s(50)}$ measurements within the upper shale stratum is also considerably greater than the variability of $I_{s(50)}$ measurements for the lower shale stratum.

3.4.6 Pressuremeter Modulus

Measurements of pressuremeter modulus, E_{PMT}, from two borings made specifically for pressuremeter testing at the Minco site are plotted versus elevation in Figure 3.8. As experienced for pressuremeter testing at the Edmond site, most pressuremeter tests at the Minco site where not able to reach the yield stress of the shale. As such, only the pressuremeter modulus measurements are presented.

The interpreted mean values of pressuremeter modulus shown in Figure 3.8 are generally consistent with the interpreted stratigraphy from all measurements. The mean value of pressuremeter modulus for the upper shale stratum is 22.3 ksi while the interpreted mean value for the lower shale stratum is 117.5 ksi.

3.5 CHARACTERIZATION OF ADDITIONAL LOAD TEST SITES

In addition to load tests performed for the current work at the Edmond and Minco test sites, historical load tests performed in weak rock at three different sites in Oklahoma were identified and used for evaluation and development of design methods for ODOT. These tests included two bi-directional load tests performed in gypsum and shale at a bridge site in Harmon County Oklahoma, two bi-directional load tests performed in shale for a highway project in Broken Arrow Oklahoma, and two top-down load tests performed in shale at a power plant site hear Hugo Oklahoma. No new site characterization activities were carried out as part of the current work; however,

available measurements were interpreted to facilitate using the historical data for the present project as described in this section.

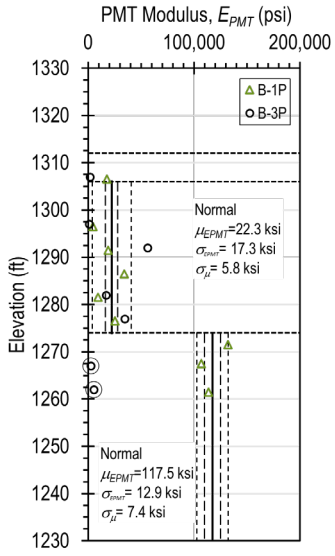

Figure 3.8 – Measurements of Pressuremeter Modulus for the Minco test site.

3.5.1 Harmon County Load Test Site

Two bi-directional load tests were performed for a bridge crossing of the Red River in Harmon County, Oklahoma. Subsurface conditions for the site generally consist of sand, clay, and gravel overburden materials overlying a gypsum stratum, which in turn overlies shale rock. Available site characterization measurements include core recovery and RQD measurements from rock core borings, uniaxial compressive strength measurements, TCPT measurements, and SPT measurements. Figure 3.9 shows the core recovery and RQD measurements plotted versus elevation. Both graphs in the figure indicate variable recovery and RQD, with a greater tendency for good recovery and RQD, but sporadic observations of low recovery and RQD, particularly in the shale stratum below elevation 1482. RQD values between approximate elevations 1480 and 1470 are consistently less than 50 percent, while most RQD values at greater depths are greater than 50 percent. Recovery and RQD measurements within the gypsum stratum between approximate elevations 1512 and 1482 also frequently indicate high recovery and RQD, but with sporadic observations of lower recovery and RQD.

Figure 3.10 shows graphs of available compressive strength, TCPT, and SPT measurements from the project site along with probabilistic interpretations of q_u, $MTCP$, and N_{eq-60} from these data. These interpretations indicate that the gypsum stratum has a mean q_u equal to 411 ksf, mean $MTCP$ value of 1.68 inches per 100 blows, and mean N_{eq-60} equal to 46 blows/ft. The underlying shale stratum that predominates the performance of the two test shafts has a mean q_u equal to 55.6 ksf, mean $MTCP$ equal to 3.0 inches per 100 blows, and mean N_{eq-60} of 97 blows/ft. It is noteworthy that measurements for the shale stratum for all three types of tests included several outliers that were neglected in the probabilistic interpretations of available measurements.

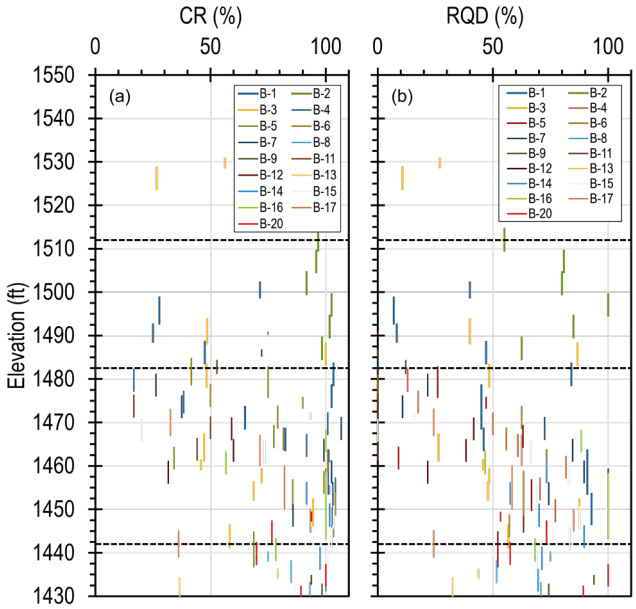

Figure 3.9 – Site characterization measurements for Harmon County test site: (a) core recovery, and (b) RQD.

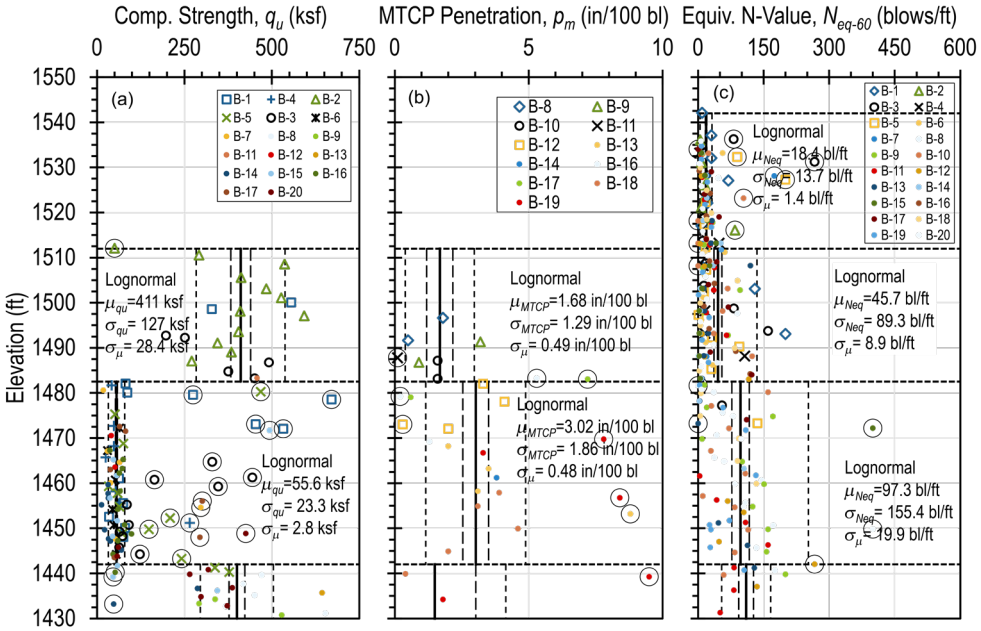

Figure 3.10 – Direct measurements of design parameters for the Harmon County test site: (a) compressive strength, (b) TCPT penetration, and (c) SPT N-values.

3.5.2 Broken Arrow Load Test Site

Two bi-directional load tests were conducted for a highway project in Broken Arrow Oklahoma. General subsurface conditions included silty clay extending from the ground surface at approximate elevation 636 to approximate elevation 613, overlying a thin layer of weathered shale down to approximate elevation 610, overlying more competent

shale extending to an undetermined depth. Available measurements for the project only included TCPT measurements within the shale stratum which are plotted versus elevation in Figure 3.11. Probabilistic interpretations were performed for these measurements similar to those described previously in this chapter, which produced a mean $MTCP$ value of 1.11 inches per 100 blows for the shale stratum.

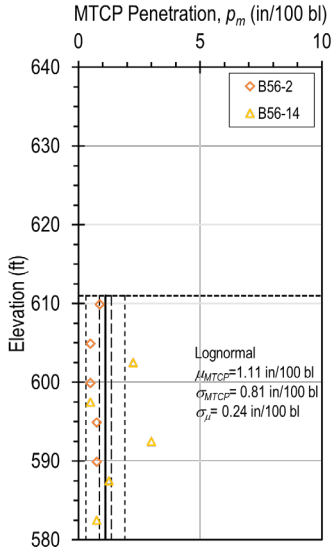

Figure 3.11 – TCPT penetration measurements for the Broken Arrow test site.

3.5.3 Hugo Load Test Site

The final two historical load tests collected for the project are two top-down load tests performed at a site near Hugo Oklahoma as reported by Goeke and Hustad (1979). Subsurface conditions at the location of the load tests consist of approximately 9 feet of silty clay extending from the ground surface at approximate elevation 484 to approximate elevation 475. Bedrock at the site includes a thin layer of limestone extending between approximate elevations 475 to 473, weathered shale between approximate elevations 473 and 470, competent gray shale between elevations 470 and 466, a thin limestone seam at approximate elevation 466, and more competent gray shale below elevation 466 to approximate elevation 445. Available measurements in the gray shale material included a dozen uniaxial compression tests and six SPT measurements, which are plotted in Figure 3.12. As shown in the figure, the available tests indicate variable compressive strength with a mean value of 16.8 ksf. The mean N_{eq-60} value is 55.3 blows/ft.

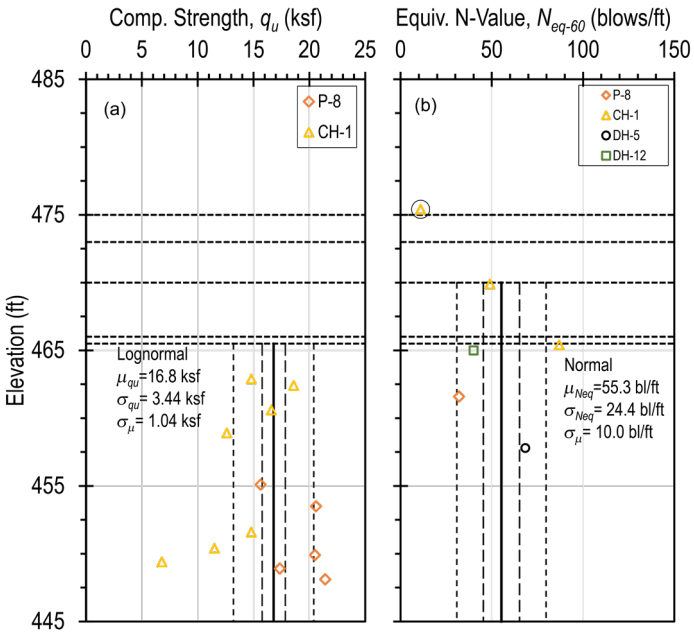

Figure 3.12 – Direct measurements of design parameters for the Hugo test site: (a) compressive strength and (b) SPT N-values.

[This page intentionally blank.]

Chapter 4 - Construction of Test Shafts

A total of eight full-scale drilled shafts were constructed and tested at the Edmond and Minco sites in order to acquire important measurements to allow for evaluation and development of appropriate design methods for ODOT. This chapter provides an overview of the field-testing program along with descriptions and schematic drawings of the test shafts including details regarding reinforcement and instrumentation. Construction of the test shafts at the Edmond and Minco test sites is also described.

4.1 FIELD TESTING PROGRAM

The field-testing program developed following completion of preliminary tasks included construction and testing of four test shafts at the Edmond site and four test shafts at the Minco site. As described in Chapter 3, the Edmond and Minco test sites were selected to provide important information regarding shaft performance in conditions that are not well represented in existing load test data. All test shafts were designed and instrumented for both axial and lateral load testing. All test shafts were constructed to have 48-inch nominal diameter with lengths ranging from approximately 45-ft to 70-ft. In order to allow for mobilizing considerable lateral load in the desired formations during lateral load tests, all test shafts were constructed with dual casings that included a 60- or 66-inch diameter, smooth-walled outer steel casing installed through the overburden soil combined with a 48-inch diameter, corrugated metal pipe (CMP) inner casing that extended from above the ground surface to just below the outer casing. The open annular space between the inner and outer casing served to isolate the test shafts from the overburden soils during both axial and lateral load testing, which importantly allowed for greater lateral load to be transferred to the top of the rock socket during the lateral load tests. Test shafts at each site were practically identical to provide for replicate measurements of shaft performance that allows for evaluation of within-site variability of shaft performance while also providing redundancy in the test program.

4.2 TEST SHAFTS AT EDMOND SITE

Tests shafts constructed at the Edmond site extended from several feet above the ground surface to approximately 45 feet below the ground surface. As shown in Figure 4.1, the test shafts were constructed near the crest of a small ridge line that passes through the Edmond site near the edge of a semi-paved area covered with asphalt millings. As shown in Figure 4.2 the test shafts were constructed in a single line, with center-to-center spacing equal to 24 feet, which is large enough to avoid potential interaction among adjacent shafts during lateral load testing.

4.2.1 Test Shaft Characteristics

Figures 4.3 and 4.4 show design details for the test shafts constructed at the Edmond site. All shafts were 48-inch nominal diameter shafts installed through a 60-inch diameter outer casing that extended several inches above ground to approximately 6 feet below existing ground surface. The inner 48-inch nominal diameter, 3-inch by 1-inch CMP casing extended from just below the tip of the outer casing to approximately 3

feet above existing ground, with the top elevation of all test shafts set to be consistent to allow for application of lateral load. O-Cell™ bi-directional loading devices were placed at the bottom of the reinforcing cage located just above the tip of each shaft.

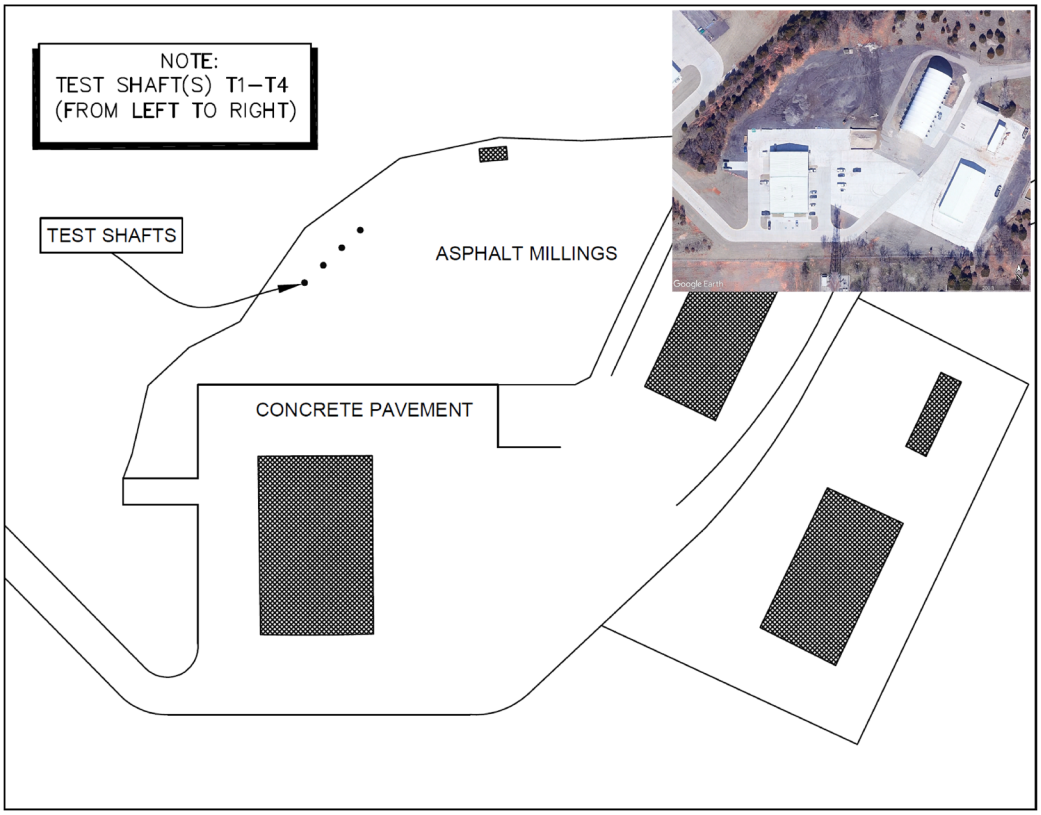

Figure 4.1 – Site plan for Edmond site showing locations of the four test shafts.

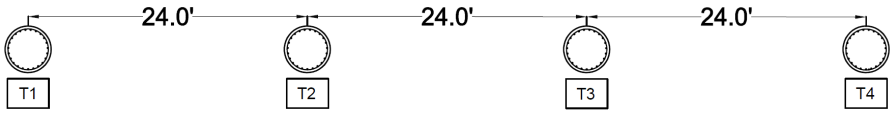

Figure 4.2 – Layout of test shafts at the Edmond site.

Reinforcement for the test shafts was designed to resist the maximum anticipated bending moment and shear forces during lateral load testing. As shown in Figure 4.4, reinforcement for each shaft included twenty-four #11 steel reinforcing bars extending along the entire length of each shaft. Reinforcing bars were placed in bundles of two bars distributed around the perimeter of the reinforcing cage to provide ample spacing for concrete to flow through the reinforcing cage. The shafts were additionally reinforced with 42-inch diameter, #5 steel stirrups placed at 6-in spacing along the entire length of the shaft to provide shear resistance for lateral load testing.

Instrumentation installed in each test shaft included eighteen vibrating-wire, sister-bar strain gages located along the length each test shaft as shown in Figure 4.3. Strain gages were installed in groups of four strain gages at elevations just above the bi-directional loading device and in two levels below the top of the rock socket where significant bending moments were expected during lateral load testing. Groups of two strain gages were installed in intermediate levels to allow for measurement of axial load

transfer at depths where significant bending moments were not expected during lateral load testing. Additional instrumentation in each shaft included five 0.5-inch diameter PVC telltale access tubes extending from the top of the shafts to the top and bottom plates of the bi-directional loading devices to provide for direct measurement of shaft compression and upward and downward movement of the top and bottom plates during axial load testing. Each shaft also included two 1-inch diameter PVC pipes extending along the full length of each shaft to allow for placement of shape-array inclinometers during lateral load testing. Removable vibrating-wire, laser, and analog devices were also used to measure displacement at the top of the shaft during axial and lateral load testing in addition to the instrumentation cast in each shaft during construction.

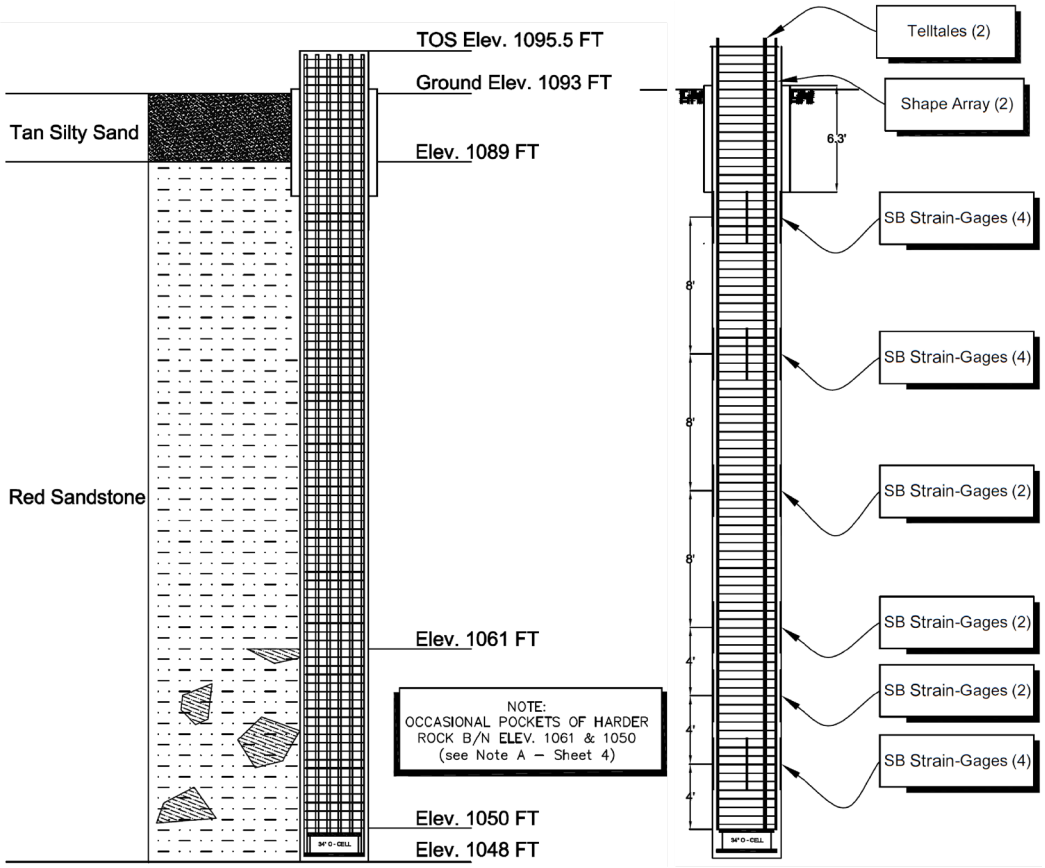

Figure 4.3 – Profile drawings of test shafts at Edmond site showing approximate depths of casing, bi-directional loading device, and instrumentation.

The sacrificial bi-directional loading device installed at the tip of each test shaft was a 34-inch diameter O-Cell™ device. These devices are rated to produce a minimum of 6000 kips of axial load in both the upward and downward directions, with a maximum total displacement of at least 4 inches. The devices were attached to 2-inch thick, steel upper and lower loading plates that extend across the entire area within the reinforcing cage.

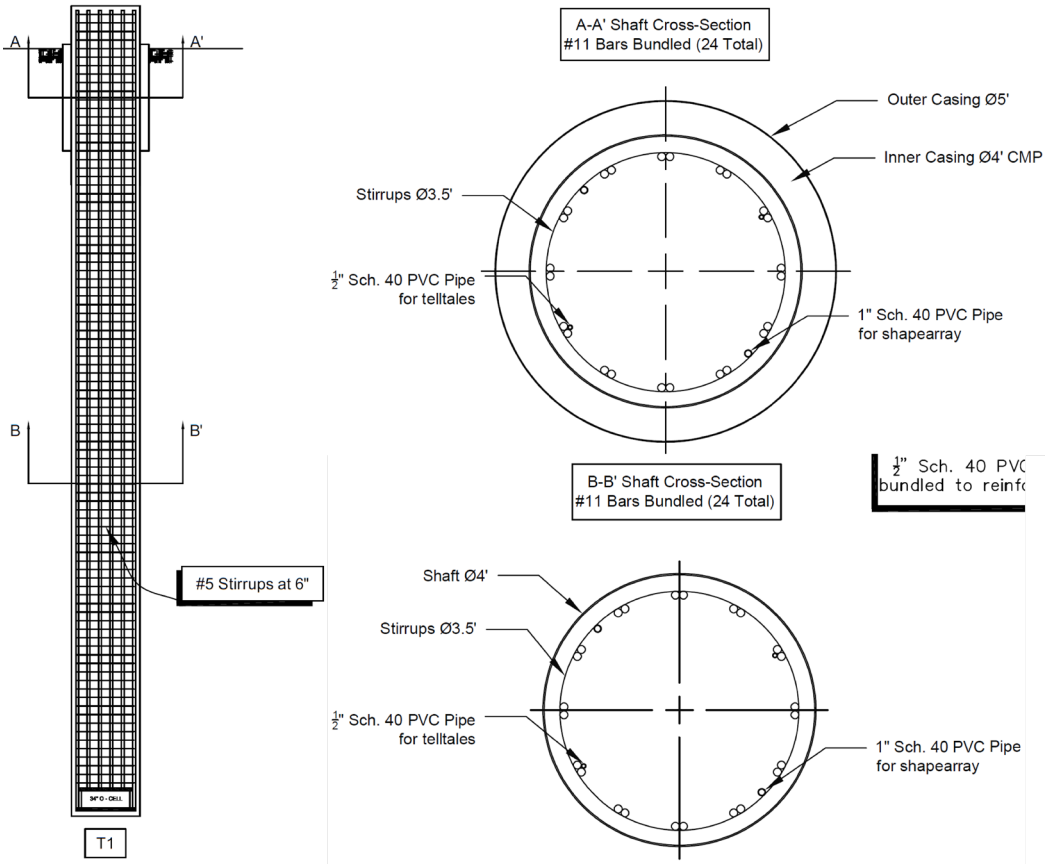

Figure 4.4 – Schematic drawings of test shafts at Edmond site showing reinforcement details.

4.2.2 Test Shaft Construction

All four test shafts at the Edmond site were constructed between January 13 and January 16, 2020, with each test shaft being drilled and concreted in a single day. All four test shafts were constructed using the “dry method” without the use of drilling fluid. Test shaft excavations were made using a Soil-Mec SR-45 drill rig following a common procedure for all four test shafts. The procedure began by using a 60-inch diameter auger to excavate to a depth of 6 feet below ground surface at which point the 60-inch diameter, outer casing was placed and seated. Drilling then continued using a 48-inch diameter auger, which was used to extend the excavation to a depth of approximately 44.5-ft below ground surface, just above the design finish depth. Prior to finishing the excavation, a reaming bit was attached to a 48-inch diameter core barrel to enlarge the diameter of the hole near the tip of the outer casing to allow for placement of the 48-inch diameter CMP inner casing. Following reaming, the inner casing was set into the excavation, extending approximately 2 feet beneath the tip of the outer casing. Seating of the inner casing was accomplished by a tight fit combined with burlap packing that was attached to the outside of the inner casing prior to placement as shown in Figure 4.5.

Figure 4.5 – CMP inner casing with burlap packing placed around tip.

Following placement of the inner casing, a 48-inch diameter cleanout bucket was used to clean the bottom of the excavation and extend the excavation to the final tip elevation. Small amounts of water were observed to seep into the excavations from perched water while placing the inner casings. The quantity of water, and the rate of inflow were both small enough to allow most of the water to be removed during cleanout. The small amount of remaining water was deemed to be inconsequential as long as concrete placement could proceed immediately following cleanout. Final cleanout of each excavation was therefore performed after concrete for each shaft had arrived on site. Final as-built depths of the constructed shafts varied slightly from a low of 44.6 feet to a high of 45.5 feet.

Concrete placement was somewhat complicated despite the fact that concrete was placed in the dry. The complication arose because the size of bi-directional cells needed to achieve the anticipated geotechnical resistance of the test shafts was so large as to prevent the concrete tremie pipe from extending past the bi-directional cell to ensure that the small volume of shaft beneath the cell was completely filled with sound concrete. This complication necessitated that a small amount of fresh concrete be placed into the bottom of the excavation prior to placement of the reinforcing cage so that the bi-directional cell could be “plunged” into the fresh concrete to ensure good contact across the entire shaft area. The procedure adopted involved first lifting the full-length reinforcing cage, without the bi-directional cell, to a vertical orientation using a boom truck while the bi-directional cell was welded to the interior of the cage as shown in Figure 4.6. The reinforcing cage with the bi-directional cell attached was then held vertically with the boom truck while approximately 1 to 1.5 feet of fresh concrete was placed in the bottom of the excavation using a concrete pump and tremie pipe. The reinforcing cage was then immediately lowered into the excavation and plunged into the fresh concrete until reaching the desired target elevation. Concreting was then continued by lowering the tremie pipe just above the bi-directional cell top plate and placing the remaining concrete normally following good tremie concreting practices.

Figure 4.6 – Attachment of bi-directional loading device to bottom of shaft reinforcement.

The concrete mix used for all test shafts was a tremie concrete mix classified as ODOT Class AA – Piers Underwater concrete, which uses ASTM aggregate gradation #67 with a maximum aggregate size of 0.5 inches. Concrete trucks generally arrived at the site with a slump of approximately 7 inches. Plasticizing admixture was added on site to increase the measured concrete slump to between 9 and 10 inches with a corresponding slump flow being between 16 to 22 inches. The minimum compressive strength of the concrete mixture used is 4,000 psi.

Once concreting was completed, the top of the shaft was rough finished to produce a consistent top of shaft elevation for all four test shafts (at approximate elevation 1096 feet). Figure 4.7 shows the completed test shafts at the Edmond site prior to axial and lateral load testing.

Figure 4.7 – Complete test shafts at the Edmond site.

4.3 MINCO LOAD TEST SITE

Tests shafts constructed at the Minco site extended from several feet above the ground surface to approximately 70 feet below the ground surface. The test shafts were constructed in square pattern located in an open area of the site as shown in Figure 4.8. As for test shafts at the Edmond site, the center-to-center spacing of the test shafts at the Minco site was set to be 24 feet as shown in Figure 4.9.

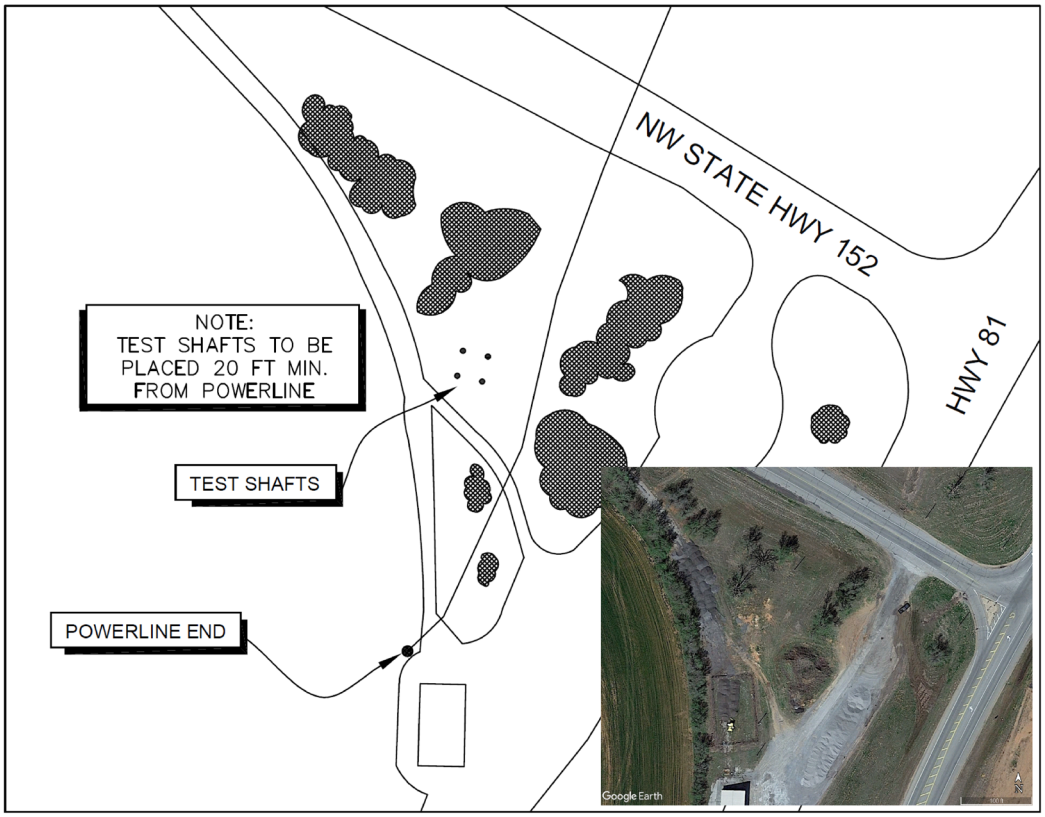

Figure 4.8 – Site plan for Minco site showing locations of the four test shafts.

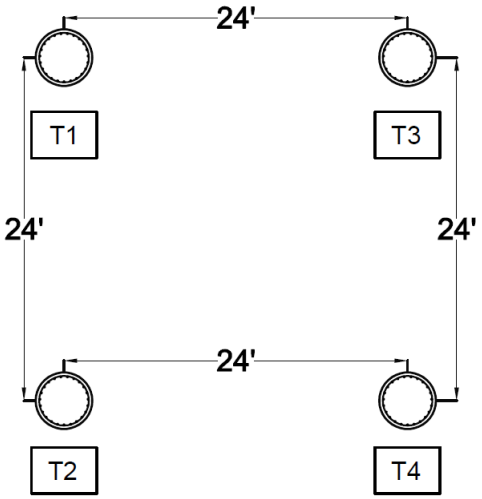

Figure 4.9 – Layout of test shafts at the Minco site.

4.3.1 Test Shaft Characteristics

Test shafts constructed at the Minco site share similarities with those constructed at the Edmond site, but with a few notable differences. Design details for the test shafts at the Minco site are shown in Figures 4.10 and 4.11. Like the Edmond test shafts, all test shafts at the Minco site were 48-inch nominal diameter shafts constructed with dual inner and outer casings extending through the overburden materials. However, subsurface conditions at the Minco site include a greater thickness of overburden materials (approximately 22 feet) compared to the Edmond site, which necessitated longer casing and produced a greater cantilevered length of the shafts for lateral load testing. The greater cantilever length, in turn, has two consequences for lateral load testing: (1) the greater cantilever length will produce greater bending moments in the shaft at the top of the rock socket for a given lateral load, and (2) the greater cantilever length will produce greater displacements of the top of the shafts for a given lateral load. The first consequence was addressed by including sufficient longitudinal and traverse reinforcement in the test shaft to resist the anticipated bending moments and shear forces. The second consequence was addressed by increasing the diameter of the outer steel casing to 66 inches to allow for 3 additional inches of lateral displacement during lateral load testing before the shaft would contact the outer casing. In order to balance the anticipated side and tip resistance for bi-directional load testing, test shafts at the Minco site also had considerably greater overall length, extending approximately 70 feet below ground surface. The inner casing used at Minco was again 48-inch diameter, 3-inch by 1-inch CMP casing extending from just below the tip of the outer casing to approximately 3 feet above existing ground, with the top elevation of all test shafts set to be consistent to allow for application of lateral load. The same O-Cell™ bi-directional loading devices used for test shafts at the Edmond site were used at the Minco site, and the devices where again placed at the bottom of the reinforcing cage just above the tip of each shaft. Instrumentation installed in each test shaft at the Minco site was also similar to that used for test shafts at the Edmond site as shown in Figure 4.10.

Longitudinal reinforcement for the test shafts at the Minco site included twenty-four #11 steel reinforcing bars for longitudinal reinforcement similar to what was used for the test shafts at the Edmond site. However, to avoid using lap splices, which would increase cage congestion and restrict concrete flow, 50-ft reinforcing bars (the maximum length available) were offset along the shaft length such that half of the bars extended from the shaft tip upwards and the other half of the bars extended from the top of shaft downwards. As shown in Figure 4.11, this produced a cage with four different sections of structural reinforcement: Section A-A’ with 12 longitudinal bars and the CMP casing; Section B-B’ with 24 longitudinal bars and the CMP casing; Section C-C’ with 24 longitudinal bars and no casing; and Section D-D’ with 12 longitudinal bars and no casing. Stirrup spacing was also varied along the shaft length with the 42-inch diameter, #5 steel stirrups placed at 12-inch spacings in Sections A-A’ and D-D’ and placed at 6-inch spacings in Sections B-B’ and C-C’. The resulting reinforcing cage placed sufficient steel reinforcement in locations with the greatest loading demands while controlling costs for steel and cage congestion. Longitudinal reinforcing bars in the overlapping

sections of the shafts (Sections B-B' and C-C') were placed in bundles of two bars provide ample spacing for concrete to flow through the reinforcing cage.

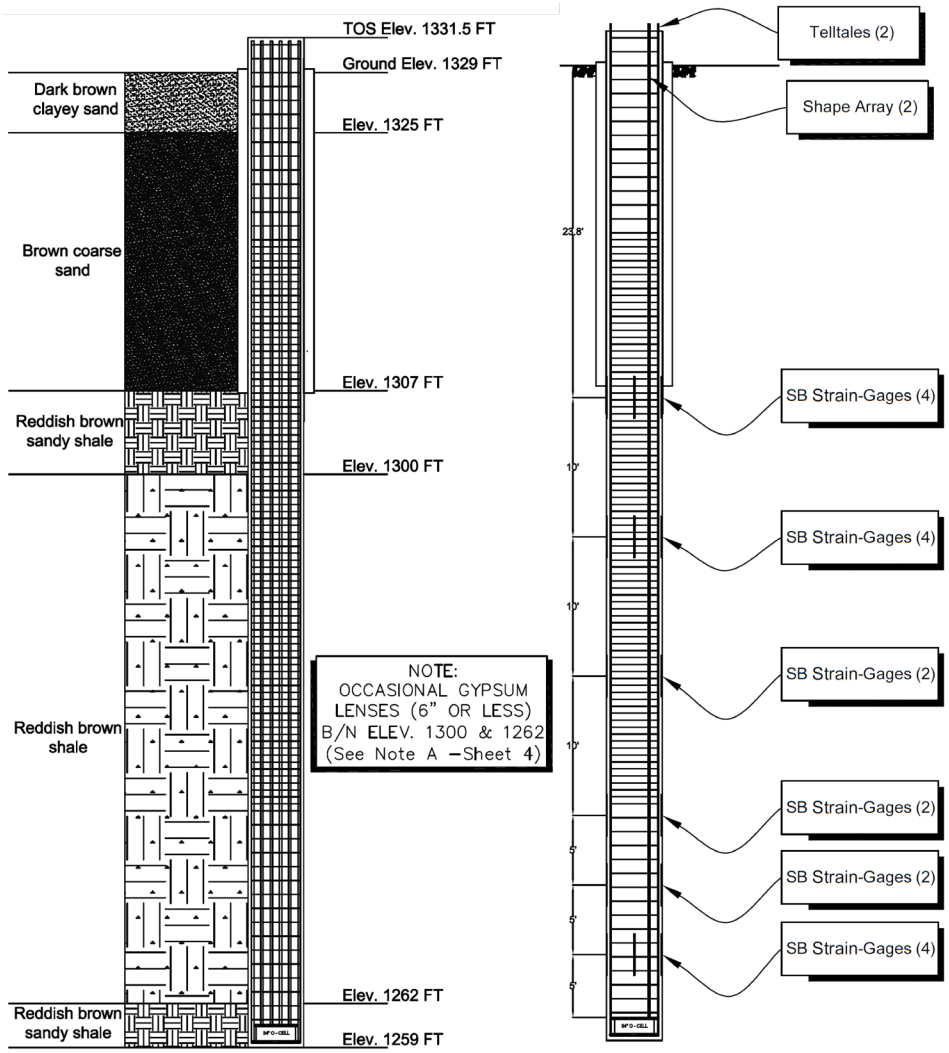

Figure 4.10 – Profile drawings of test shafts at Minco site showing approximate depths of casing, bi-directional loading device, and instrumentation.

4.3.2 Test Shaft Construction

Construction of test shafts at the Minco site began on January 20 and was completed on January 30, 2020. Construction initially began using the same Soil-Mec SR-45 drilling rig that was used to construct test shafts at the Edmond site. However, after drilling and placing the outer casings for test shafts T2 and T4, the Soil-Mec rig suffered electrical problems that rendered it unusable for the remainder of the project. An alternative IMT AF180d drilling rig was therefore mobilized to the site and used to complete construction of the test shafts at the Minco site.

A common procedure was used to construct all four test shafts at the Minco site, that differed from that used to construct test shafts at the Edmond site. Test shafts in Minco were initially drilled using "wet" excavation methods with a 66-inch diameter auger being

used to excavate through the sandy overburden materials while using polymer slurry to maintain the stability of the excavated shafts. Once the excavations reached competent shale at a depth of approximately 25 feet, the 66-inch diameter smooth, steel outer casings were set to seal off the excavation from groundwater inflow from the sandy overburden. With the outer casings set, the polymer drilling fluid was removed from the excavation and the remainder of the excavation was completed using “dry” excavation methods similar to that used at the Edmond site. A 48-inch diameter auger was used to extend the excavation to a depth just above the design finish depth. A reaming bit was then used to enlarge the diameter of the hole near the tip of the outer casing and the inner CMP casing was set into the excavation in a manner similar to that used at the Edmond site.

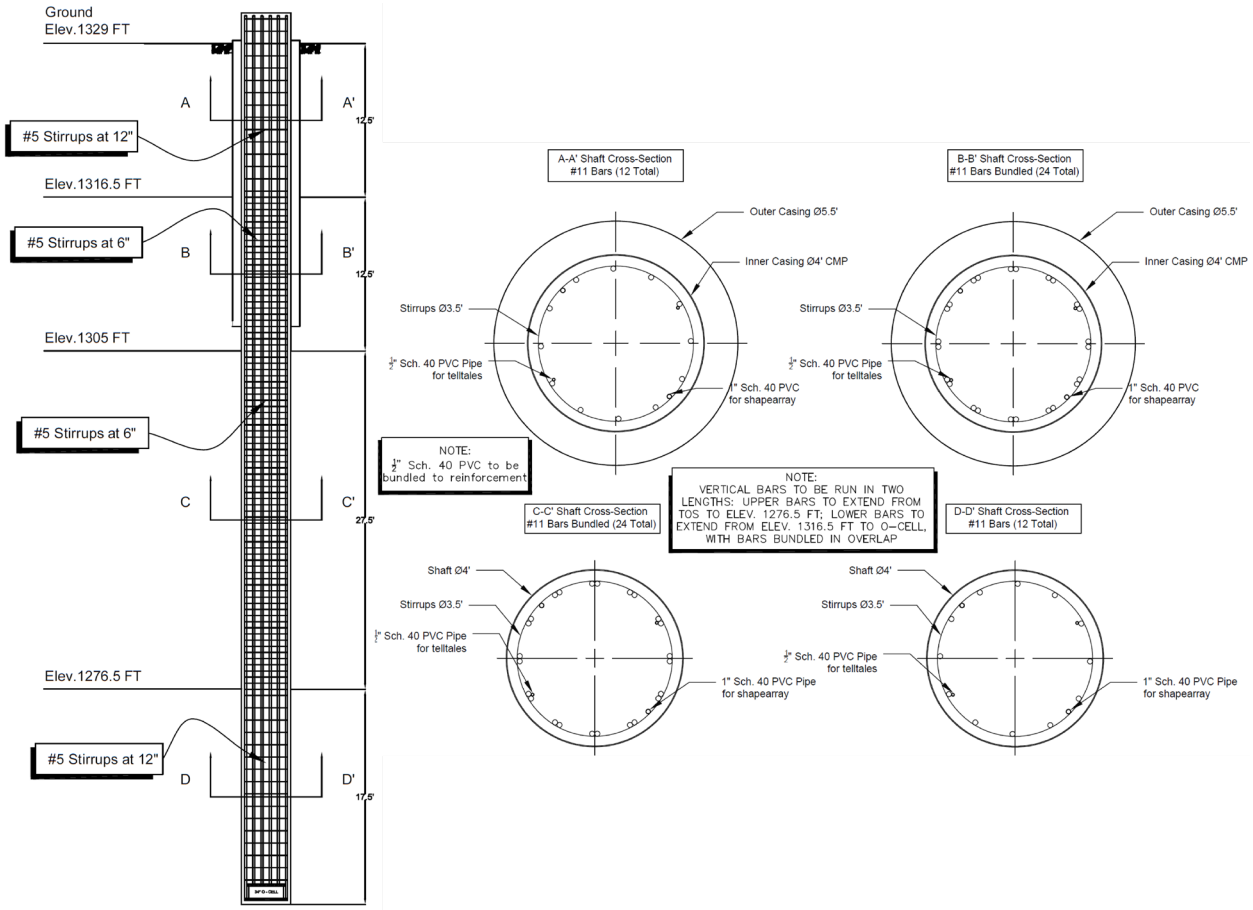

Figure 4.11 – Schematic drawings of test shafts at Minco site showing reinforcement details.

Similar procedures to those used at the Edmond site were followed for placing the reinforcing cage and concrete. The general sequence followed was lifting the reinforcing cage, attaching the bi-directional device to the cage, finishing the excavation using a clean-out bucket, placing 1 to 1.5 feet of concrete in the base of the excavation, lowering the reinforcing cage with the bi-directional cell to the appropriate elevation, and finally, placing concrete for the remainder of the shaft following good tremie placement practices. The concrete used to construct the test shafts at the Minco site was the same

mix design and was provided by the same supplier, but from a different batch plant. On-site quality control practices for the concrete were similar to those used for the Edmond site, including the addition of plasticizing admixtures to produce mixes with appropriate slump and slump flow. Figure 4.12 shows the completed test shafts at the Minco site.

Figure 4.12 – Complete test shafts at the Minco site.

[This page intentionally blank.]

Chapter 5 - Axial Load Tests

Bi-directional axial load tests were performed on test shafts at both the Edmond and Minco sites between February 24 and February 27, 2020, approximately one month after completing construction of the test shafts. This chapter describes the load testing procedure followed for the axial load tests, the measured axial load-displacement response for each test shaft, and the observed load transfer response for each test shaft. Measured values of unit side and unit tip resistance determined from the tests are also summarized along with similar values for other collected load tests performed in weak rock in Oklahoma.

5.1 AXIAL LOAD TEST PROCEDURE

Loading for all axial load tests was applied according to the ASTM “Quick Test” procedure (ASTM D8169, 2018), which is the most commonly adopted load testing procedure for axial load tests in general, and bi-directional load tests in particular. Bi-directional load was applied in constant increments of approximately 500 to 600 kips, with the load being held constant for a period of 8 minutes for each load increment. Load testing for each shaft was continued until the capacity of the bi-directional loading device was reached, until displacements exceeded the bi-directional device stroke, or until the applied load could not be maintained during a load increment because of excessive displacement of the drilled shaft. Following application of the maximum applied load, the shaft was unloaded in four approximately equal unloading increments, each of which was maintained for a period of 4 minutes. The number of loading increments ranged from 9 to 25 for the eight tests conducted for the current work, with each test also including four additional unloading increments.

Instrumentation readings were electronically acquired and logged every thirty seconds throughout testing; interpretations were made based on readings acquired at 1 minute, 2 minutes, 4 minutes, and 8 minutes after application of each load step. Instrumentation monitored during axial load testing included all vibrating-wire strain gages embedded in each shaft, vibrating-wire displacement transducers connected to the tell-tale rods to measure shaft compression and expansion of the bi-directional cell, vibrating wire pressure transducers to measure hydraulic pressure to the bi-directional device, and optical displacement devices for measuring the top-of-shaft displacement.

5.2 AXIAL LOAD TESTS AT EDMOND LOAD TEST SITE

The four test shafts at the Edmond site are referred to as Edmond-T1, Edmond-T2, Edmond-T3, and Edmond-T4 throughout this report. Tests performed for Edmond-T2, Edmond-T3, and Edmond-T4 all reached a maximum bi-directional load of approximately 9,000 kips, which is 50 percent greater than the rated capacity (6,000 kips) of the bi-directional cells used. The 9,000 kip bi-directional load is equivalent to a top-down load of 18,000 kips. The test performed for Edmond-T1 could only be loaded to approximately 5,000 kips because of excessive downward displacement at the shaft tip as described in more detail subsequently.

5.2.1 Axial Load-Displacement Response

Axial load, upward displacement, and downward displacement are directly measured in each load test, without requiring interpretation. The measured upward and downward load-displacement response for the four test shafts at the Edmond site are plotted in Figure 5.1. The upward and downward load-displacement responses for the Edmond-T2, Edmond-T3, and Edmond-T4 test shafts indicate consistent performance with each showing relatively balanced upward and downward displacements for a given load. The magnitude of downward displacement at the maximum load of approximately 9,000 kips was consistent among the three test shafts and equal to approximately 0.9 inches. The magnitude of upward displacement was less consistent, ranging from approximately 0.3 to 0.9 inches. The shape of the loading curves was mostly linear, albeit with clear indications of upward curvature for the upward (side resistance) loading and perhaps slight indications of downward curvature for the downward (tip resistance) loading. The load-displacement responses shown for Edmond-T2, Edmond-T3, and Edmond-T4 show no indications that failure was reached for any of the shafts despite exceeding the rated capacity of the bi-directional devices; the amount of additional load that could be resisted by the shafts is unknown. Upon rebounding to zero applied load, permanent upward and downward displacements of the test shafts were approximately 0.5 inches or less, which suggests some plastic behavior did occur.

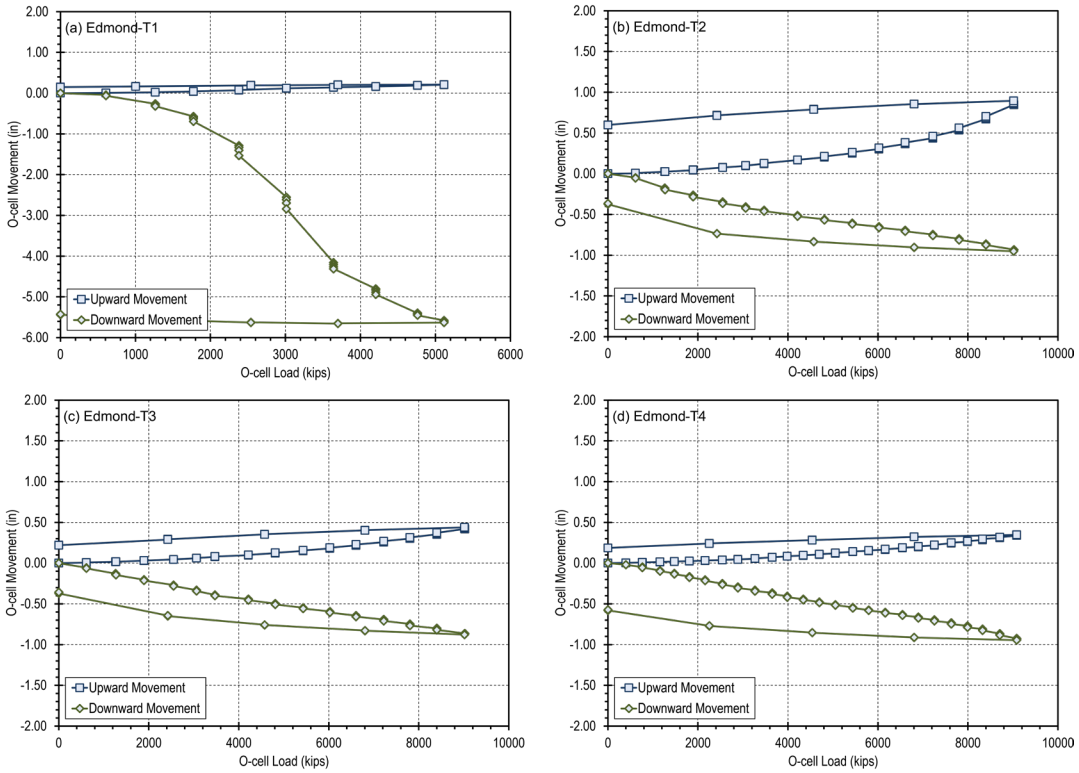

Figure 5.1 – Measured axial load-displacement response for Edmond test shafts: (a) Edmond-T1, (b) Edmond-T2, (c) Edmond-T3, and (d) Edmond-T4.

The observed load-displacement response for Edmond-T1 is clearly different. As shown in Figure 5.1a, the shaft experienced little upward movement above the bi-directional

device, but considerable downward displacement below the device. At the maximum applied load, downward displacement was approaching 6 inches, at which point the stroke of the bi-directional device was exceeded so the test had to be terminated. The shape of the downward load-displacement curve indicates initial downward curvature, which suggest that some form of failure (or at least plastic behavior) was occurring. However, at loads greater than about 3500 kips, the load-displacement response began to stiffen as reflected by the upward curvature of the load-displacement curve. While the cause of the observed response is not known, it is hypothesized that the concreting procedure described in Chapter 4 was unsuccessful in getting concrete uniformly distributed across the entire base of the shaft below the bi-directional cell. As a result, the area being loaded below the bi-directional cell was likely less than the theoretical area of the shaft tip, which led to the applied stresses being greater than assumed for a given load, and perhaps large enough to cause the large displacements. This hypothesis would also explain the observed stiffening of the load-displacement response at higher loads; if the observed displacement were sufficient to close up any gaps beneath the bi-directional device, the loaded area would increase along with the resistance provided below the device. Regardless of the cause of the unusual response, it seems clear that the observed response is not indicative of a well-constructed shaft. The measured response for Edmond-T1 was therefore disregarded for evaluation and development of design methods, which are described in Chapter 6.

It should be noted that the somewhat risky concreting procedure adopted for the test shafts, as described in Chapter 4, is only necessary when the size of the bi-directional cell covers most of the area of the shaft. The unusual response observed for the test shaft should therefore not be a concern for production shafts constructed without bi-directional devices or test shafts constructed to allow the tremie pipe to extend beneath the bi-directional device.

5.2.2 Load Transfer Response

The load transfer response of the test shafts in side and tip resistance can also be determined from instrumentation installed in all test shafts. However, determining the load transfer response requires considerable analysis along with informed judgement and interpretation. The required analyses are relatively straightforward mechanics calculations wherein the axial force, Q, as some point along the shaft can be determined from measured axial strains as:

$$Q = EA \cdot \varepsilon_a \tag{5.1}$$

where EA is the axial rigidity of the drilled shaft that can be determined from material Young's modulus, E, and cross-sectional area, A, and ε_a is the axial strain, both of which should reflect the location where Q is being determined. One challenge with application of Equation 5.1 is that the axial rigidity is not precisely known since the shaft area is potentially variable and, more significantly, the modulus of concrete varies with time, the magnitude of strain, and other factors. Application of Equation 5.1 is additionally complicated when strain gage measurements become questionable, in

which case judgment has to be used to decide whether questionable measurements should be considered or disregarded.

Interpretations of axial load along each of the test shafts at the Edmond site are plotted in Figure 5.2 for select load levels. The graphs naturally show increasing load along the shafts as the applied bi-directional load increases, with a maximum load observed at the location of the bi-directional devices near the shaft tip. The slope of the curves shown in Figure 5.2 are an indication of the magnitude of load transfer along specific segments of the test shafts, with steeper slopes indicating less load transfer than flatter slopes.

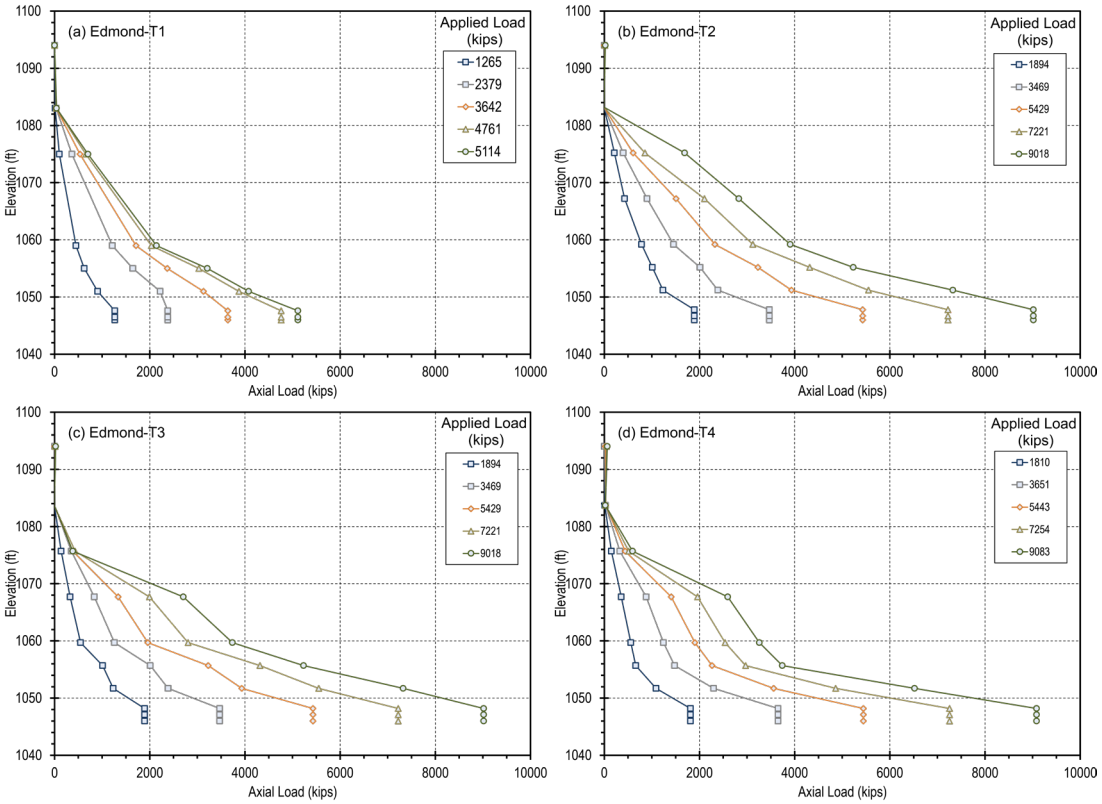

Figure 5.2 – Interpreted load transfer for Edmond test shafts: (a) Edmond-T1, (b) Edmond-T2, (c) Edmond-T3, and (d) Edmond-T4.

Looking at load transfer in Figure 5.2 for the largest applied loads, two distinct load transfer segments become apparent. The first extends from the shaft tips upwards to approximately elevation 1060, which falls within the stronger and stiffer sandstone stratum described in Chapter 3. The second extends from the bottom of the dual casing downward, which falls within the upper, weaker sandstone. A third segment extending between approximate elevations 1060 and 1070 is also apparent for Edmond-T3 and Edmond-T4, in which little load is being transferred. While potentially a result of misinterpretation of strain measurements, it is noteworthy that this segment falls between elevations where core recovery and RQD were very poor.

Given the distribution of load along a shaft, the difference in axial load between two points in the shaft is the load transferred in side resistance, which can in turn be used to determine unit side resistance, q_s, by dividing by the contact area of the shaft and the

surrounding ground between the two points. Unit tip resistance, q_p, is more simply determined by dividing the axial load at the shaft tip by the area of the shaft tip. Both q_s and q_p can be determined for any loading level, and then combined with calculated displacements to produce so-called t-z and q-z curves, where t is q_s and q is q_p.

Interpreted t-z and q-w curves for all four test shafts are respectively shown in Figures 5.3 and 5.4. Excepting interpretations for Edmond-T1, Figure 5.3 generally shows that the ultimate unit side resistance was mobilized for most shaft segments. The mobilized unit side resistance tends to be greatest for shaft segments located in the lower sandstone stratum, where the maximum unit side resistance ranges from 30 to 60 ksf. The maximum unit side resistance observed with the upper sandstone stratum is considerably lower, and generally less than 12 ksf. The variability of unit side resistance among the four test shafts and along each shaft is also significant, which is something that has been observed in previous load test programs with replicate test shafts.

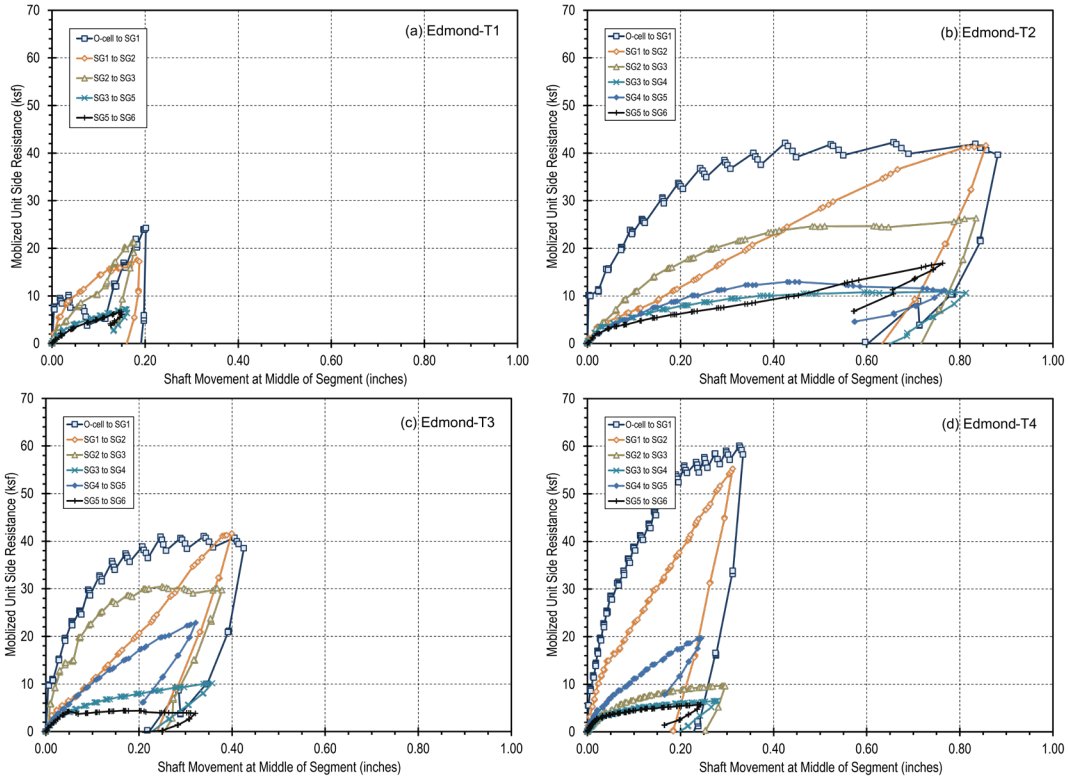

Figure 5.3 – Interpreted t-z response for Edmond test shafts: (a) Edmond-T1, (b) Edmond-T2, (c) Edmond-T3, and (d) Edmond-T4.

Again excepting measurements from Edmond-T1, Figure 5.4 shows consistent mobilization of tip resistance among test shafts Edmond-T2, Edmond-T3, and Edmond-T4. The q-z response shown in the figure for these three shafts are all near linear, with all three achieving downward displacement of approximately 0.9 inches for the maximum applied stress of approximately 700 ksf. The observed response suggests that none of the three shafts achieved failure in tip resistance. However, displacements occurring within individual loading increments were increasing at the highest loads, which provides some indication that the applied stress may be approaching failure.

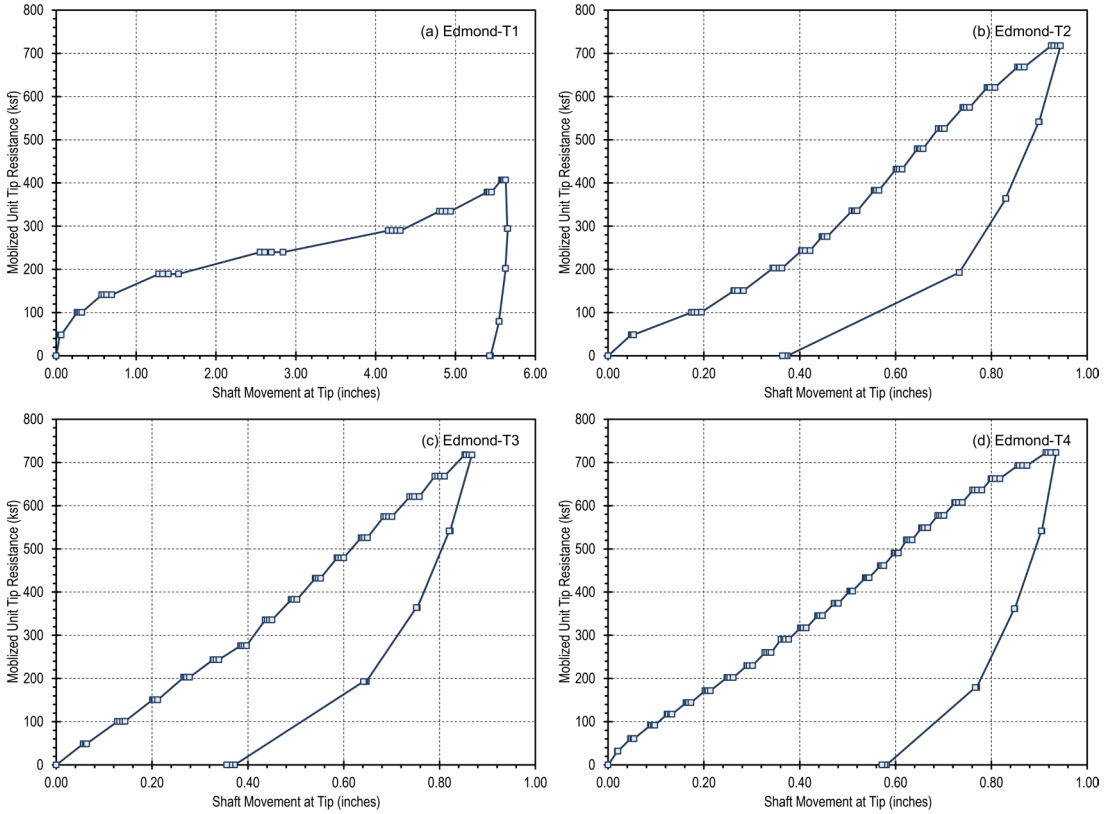

Figure 5.4 – Interpreted q-z for Edmond test shafts: (a) Edmond-T1, (b) Edmond-T2, (c) Edmond-T3, and (d) Edmond-T4.

5.2.3 Summary of Measured Unit Resistances

Tables 5.1 and 5.2 respectively summarize the maximum measured unit tip and unit side resistances from load tests on the four test shafts at the Edmond site. Unit side resistance values are provided for segments extending between strain gage levels (except for a few levels that were disregarded because of gage malfunctions) for each shaft. The tables additionally include notations of whether the individual reported unit resistances are associated with failure in side or tip resistance. Values provided in the tables, and especially those noted as having achieved failure, were used for evaluation of alternative design methods as described in Chapter 6.

Table 5.1 – Summary of unit tip resistance for test shafts at Edmond site.

Test Shaft	Tip Elev. (ft)	q_p (ksf)	Failure Observed
T1	1046	407	No
T2	1046	717.6	No
T3	1046	717.6	No
T4	1046	722.8	No

Table 5.2 – Summary of unit side resistance for test shafts at Edmond site.

Test Shaft	Max. Elev. (ft)	Min. Elev. (ft)	q_s (ksf)	Failure Observed
T1	1083	1075	6.6	No
	1075	1059	7.2	No
	1059	1055	21.1	No
	1055	1051	17.5	No
	1051	1046.5	24.2	No
T2	1083.2	1075.2	16.9	No
	1075.2	1067.2	13.0	Yes
	1067.2	1059.2	10.6	Yes
	1059.2	1055.2	26.3	Yes
	1055.2	1051.2	41.6	Yes
	1051.2	1046.7	41.9	Yes
T3	1083.7	1075.7	4.4	Yes
	1075.7	1067.7	22.9	No
	1067.7	1059.7	10.2	Yes
	1059.7	1055.7	30.5	Yes
	1055.7	1051.7	41.3	Yes
	1051.7	1047.1	41.0	Yes
T4	1083.7	1075.7	5.7	Yes
	1075.7	1067.7	19.7	No
	1067.7	1059.7	6.5	Yes
	1059.7	1055.7	9.7	Yes
	1055.7	1051.7	55.3	No
	1051.7	1047.1	60.1	Yes

5.3 AXIAL LOAD TESTS AT MINCO LOAD TEST SITE

The four test shafts at the Minco site are referred to as Minco-T1, Minco-T2, Minco-T3, and Minco-T4 throughout this report. Tests performed for Minco-T1, Minco-T2, and Minco-T4 were loaded to a maximum bi-directional load of approximately 8,000 kips, which is greater than the rated capacity (6,000 kips) of the bi-directional cells used but less than the 9,000 kip load that was reached during load tests at the Edmond site. The test performed for Minco-T3 was loaded to slightly more 6,000 kips when the upward displacement rate of the shaft increased to the point where additional load could not be sustained (indicating failure in side resistance above the bi-directional device).

5.3.1 Axial Load-Displacement Response

Figure 5.5 shows the measured upward and downward load-displacement response for the four test shafts at the Minco site. The load-displacement curves reflect generally balanced bi-directional loading with each shaft achieving greater than 1 inch of upward displacement and up to 2 inches of downward displacement. Upward displacements

during the last loading increment for each test were increasing significantly, which suggests that all four test shafts were failing in side resistance. Downward displacements were also significant, with three of the tests experiencing downward displacements of approximately 4 percent of the shaft diameter, which suggest these shafts were nearing failure in tip resistance as well. Permanent downward displacements following unloading ranged from 1 to 1.5 inches while permanent upward displacements ranged from approximately 0.75 to 1 inches, which indicates considerable plastic behavior.

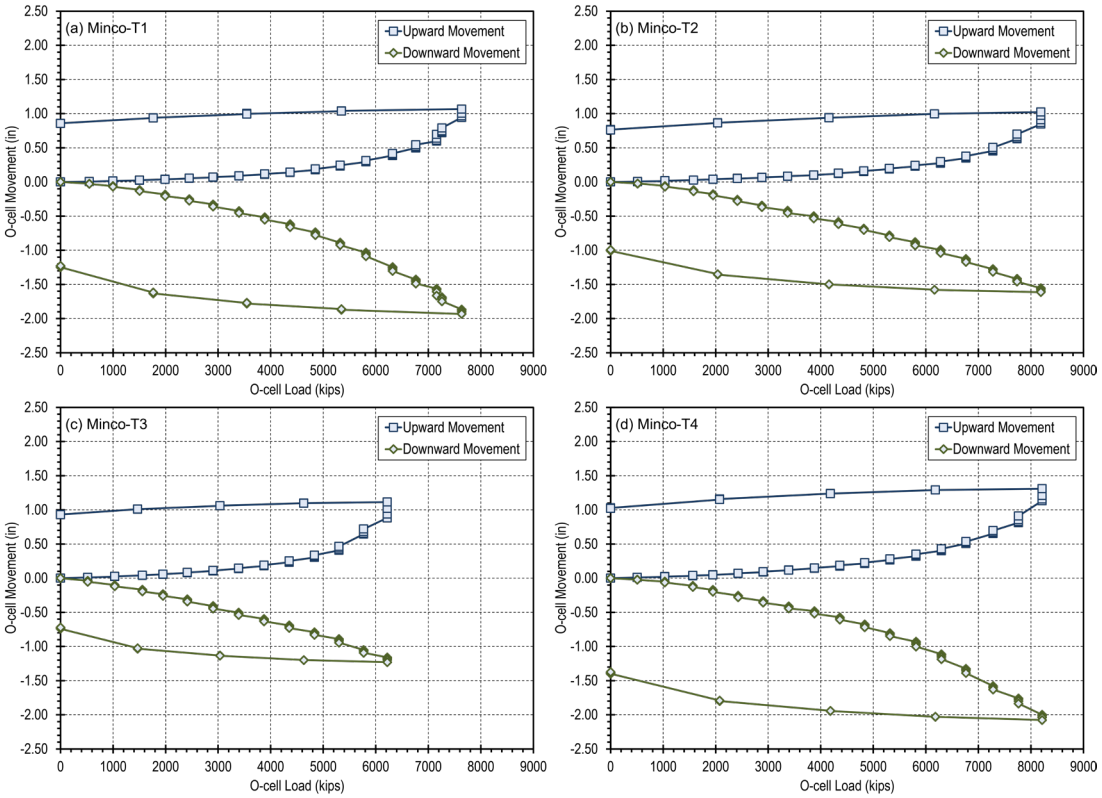

Figure 5.5 – Measured axial load-displacement response for Minco test shafts: (a) Minco-T1, (b) Minco-T2, (c) Minco-T3, and (d) Minco-T4.

5.3.2 Load Transfer Response

Figure 5.6 shows the interpreted axial load for select load levels plotted versus elevation for each of the test shafts at the Minco site. As was observed for interpreted axial load for tests at the Edmond site, the load distribution curves in Figure 5.6 suggest two shaft segments with distinct load transfer. The lower segment extending between approximate elevations 1260 and 1270 corresponds to the portion of the shaft founded in the lower shale stratum described in Chapter 3 and tends to have greater load transfer (flatter slope) than higher segments. The upper segment extends from the approximate bottom of the casing near elevation 1306 downward to approximate elevation 1275, which represents the approximate boundary between the upper and lower shale strata at the Minco site. Load transfer along this upper segment is notably less than that observed at greater depths along the shafts.

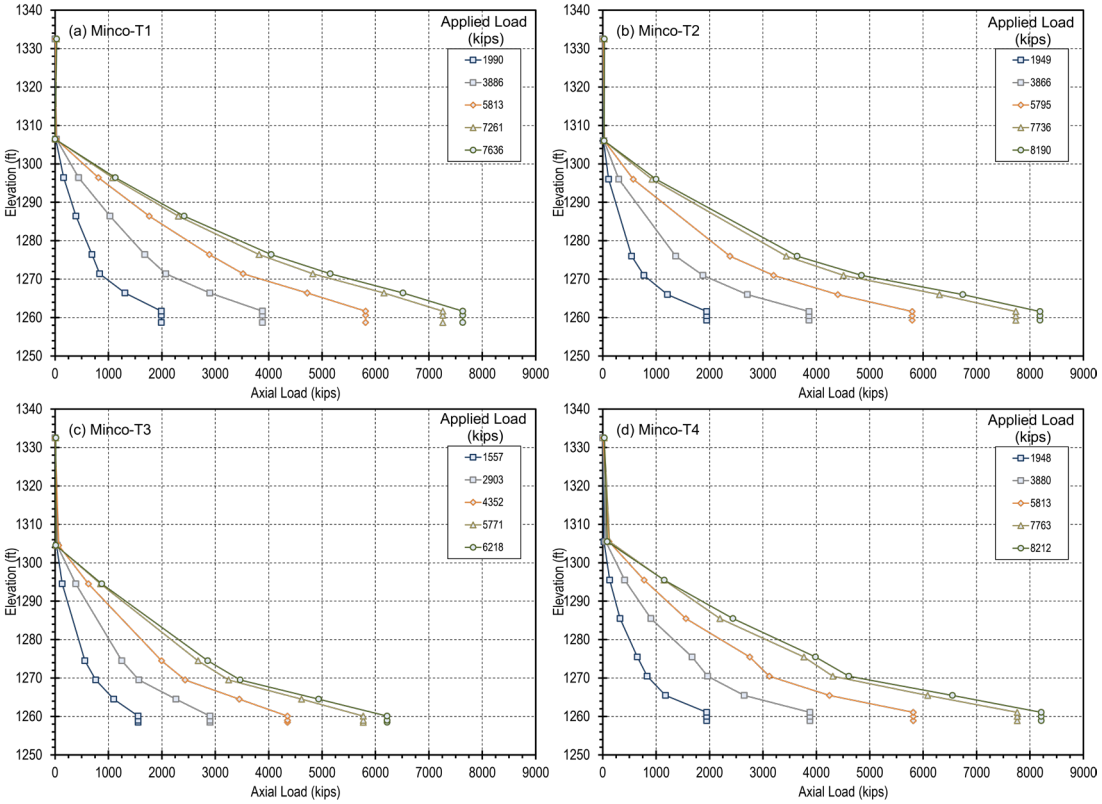

Figure 5.6 – Interpreted load transfer for Minco test shafts: (a) Minco-T1, (b) Minco-T2, (c) Minco-T3, and (d) Minco-T4.

Figure 5.7 shows interpreted t-z curves from load tests performed for the Minco test shafts. The figure consistently indicates similar load transfer response in side resistance for the lowest two shaft segments and different, but consistent response among the upper shaft segments. The interpreted response for the shaft segments extending between strain gage levels 2 and 3 is shown to fall between the observed response for the upper and lower segments for the Minco-T1 and Minco-T2 test shafts, which may be a result of inherent “averaging” of the responses for the upper and lower portions of the shaft. Figure 5.7 also clearly shows that the ultimate unit side resistance was mobilized for all shaft segments. The mobilized unit side resistance for the upper shaft segments that lie within the upper shale stratum range from approximately 7 to 13 ksf whereas the mobilized unit side resistance for segments within the lower shale stratum range from approximately 20 to 30 ksf.

Figure 5.8 shows the interpreted q-z responses for the four test shafts at the Minco site. As was observed for test shafts at the Edmond site, the interpreted q-z responses for the four Minco test shafts are quite consistent, with interpreted displacements for an applied stress of 500 ksf all falling between 1 and 1.2 inches. Figure 5.8 shows that none of the Minco shafts reached failure in tip resistance, but increasing displacements within individual load increments suggest that they were approaching failure. Because of these observations, the three tests that most distinctively show as approaching failure (Minco T1, Minco T2, and Minco T4) are subsequently considered to have reached failure for analyses presented in Chapter 6.

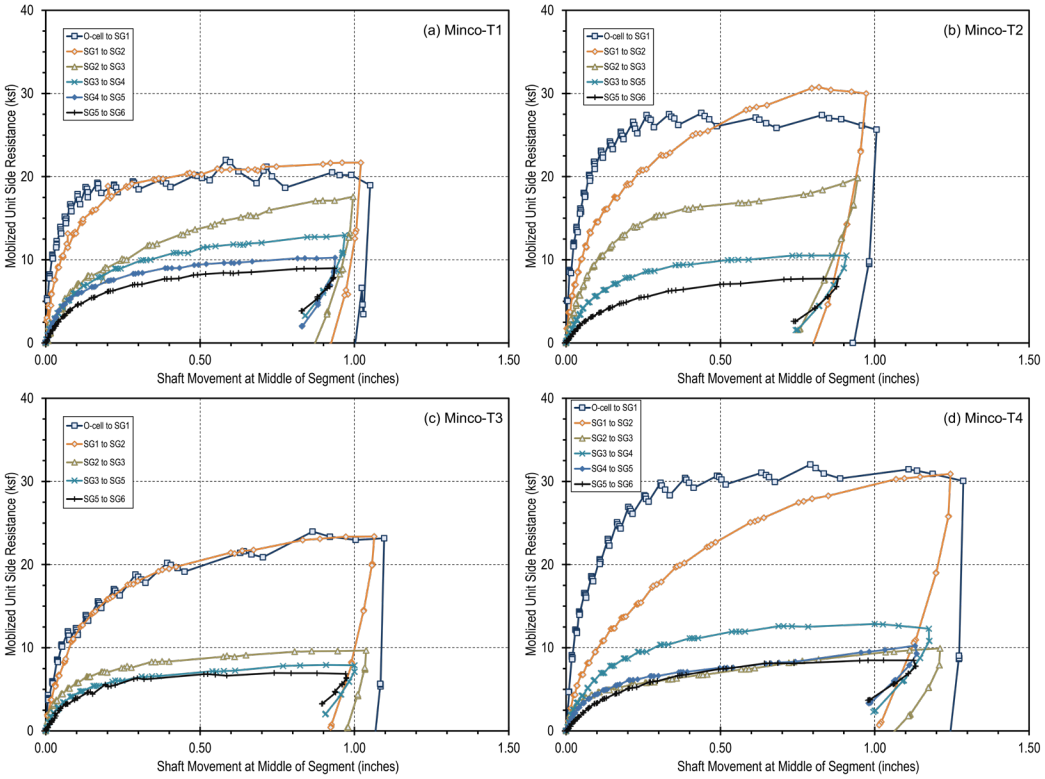

Figure 5.7 – Interpreted t-z response for Minco test shafts: (a) Minco-T1, (b) Minco-T2, (c) Minco-T3, and (d) Minco-T4.

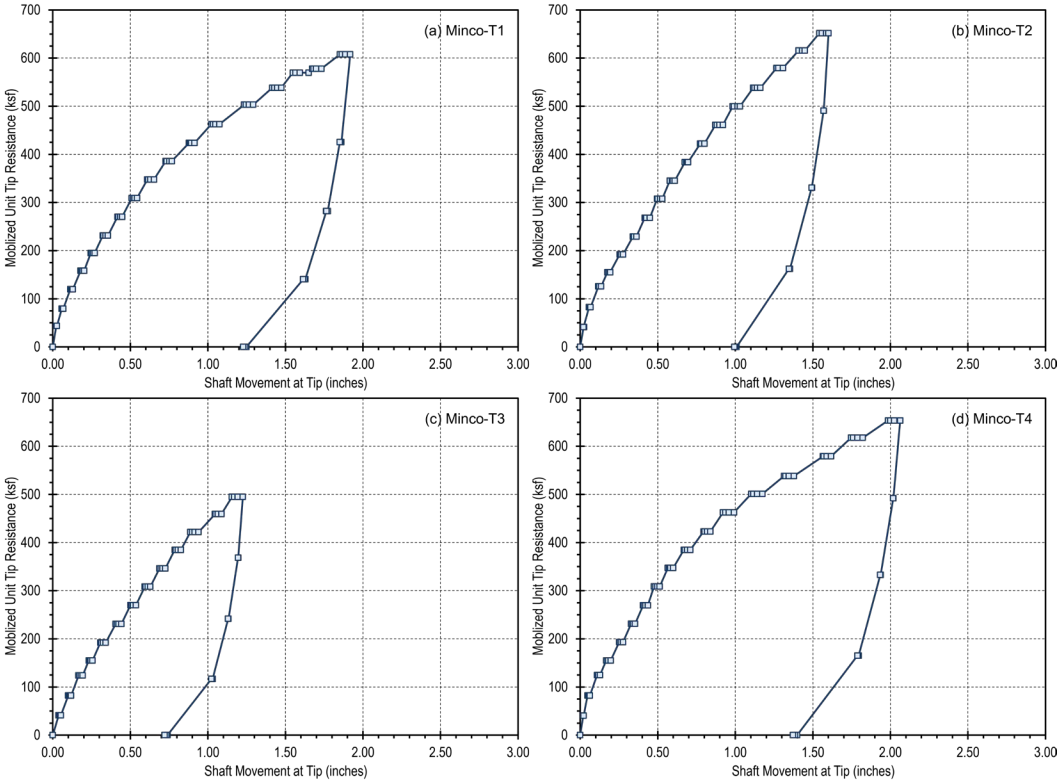

Figure 5.8 – Interpreted q-z response for Minco test shafts: (a) Minco-T1, (b) Minco-T2, (c) Minco-T3, and (d) Minco-T4.

5.3.3 Summary of Measured Unit Resistances

The maximum measured unit side and unit tip resistances from load tests on the four test shafts at the Minco site are respectively summarized in Tables 5.3 and 5.4. Values provided in the table were used for evaluation of alternative design methods as described in Chapter 6.

Table 5.3 – Summary of measured unit side resistance for test shafts at Minco site.

Test Shaft	Max. Elev. (ft)	Min. Elev. (ft)	q_s (ksf)	Failure Observed
T1	1306.4	1296.4	9.0	Yes
	1296.4	1286.4	10.3	Yes
	1286.4	1276.4	13.0	No
	1276.4	1271.4	17.6	Yes
	1271.4	1266.4	21.7	Yes
	1266.4	1260.6	22.0	Yes
T2	1306.0	1296.0	7.7	Yes
	1296.0	1276.0	10.5	Yes
	1276.0	1271.0	19.8	No
	1271.0	1266.0	30.7	Yes
	1266.0	1260.5	27.6	Yes
T3	1304.5	1294.5	7.0	Yes
	1294.5	1274.5	7.9	Yes
	1274.5	1269.5	9.7	Yes
	1269.5	1264.5	23.4	Yes
	1264.5	1259.0	24.0	Yes
T4	1305.5	1295.5	8.5	Yes
	1295.5	1285.5	10.2	Yes
	1285.5	1275.5	12.9	Yes
	1275.5	1270.5	9.9	Yes
	1270.5	1265.5	30.9	Yes
	1265.5	1260.0	32.0	Yes

Table 5.4 – Summary of measured unit tip resistance for test shafts at Minco site.

Test Shaft	Tip Elev. (ft)	q_p (ksf)	Failure Observed
T1	1258.7	607.7	Yes
T2	1259.3	651.7	Yes
T3	1258.5	494.8	No
T4	1258.9	653.5	Yes

5.4 OTHER COLLECTED LOAD TEST MEASUREMENTS IN OKLAHOMA

A few load tests have been performed in weak rock formations in Oklahoma. These tests include two top-down tests conducted near Hugo, two bi-directional tests conducted near Broken Arrow, and two bi-directional tests performed in Harmon County. Subsurface conditions for each of these sites are described in Chapter 3. Tables 5.3 and 5.4 respectively summarize the maximum unit side and unit tip resistances from the tests. While the site characterization parameters documented in Chapter 3 were independently analyzed and interpreted as part of this project, values provided for unit side and tip resistance were taken directly from documentation about the respective load tests. No independent analyses were performed for these tests.

Table 5.5 – Summary of measured unit side resistance for other collected load tests in Oklahoma.

Test Shaft	Max. Elev. (ft)	Min. Elev. (ft)	q_s (ksf)	Failure Observed
Hugo T1	464.1	461.1	4.8	Yes
	461.1	457.6	8.5	Yes
	457.6	455.1	10.6	Yes
Hugo T2	465.4	459.4	4.0	Yes
	459.4	454.4	7.0	Yes
	454.4	449.4	7.2	Yes
Broken Arrow T1	606.4	601.4	10.8	No
	601.4	595.7	9.1	No
Broken Arrow T2	601.7	593.2	8.9	No
Harmon County T1	1492.3	1481.3	0.0	No
	1481.3	1470.0	0.4	No
	1470.0	1463.3	4.8	Yes
Harmon County T2	1489.8	1456.8	1.6	No
	1456.8	1448.6	1.8	No
	1448.6	1440.5	4.6	Yes

Table 5.6 – Summary of measured unit tip resistance for other collected load tests in Oklahoma.

Test Shaft	Tip Elev. (ft)	q_p (ksf)	Failure Observed
Hugo T1	454.7	92.7	Yes
Hugo T2	447.3	122.2	No
Broken Arrow T1	593.9	99.1	No
Broken Arrow T2	592.9	74.5	No
Harmon County T1	1436.9	16.0	No
Harmon County T2	1457.2	14.0	No

Chapter 6 - Analysis and Recommendations for Axial Design

Interpreted values of unit side and unit tip resistance from load tests described in Chapter 5 were collectively analyzed with similar values determined from additional load tests performed in weak rock in Oklahoma and surrounding states. Analyses were performed to evaluate both new and existing design relations for predicting unit side and tip resistance from Texas Cone Penetration Test (TCPT) penetration, compressive strength, and Standard Penetration Test (SPT) equivalent N-values. This chapter describes the analyses conducted, recommended design relations for the Oklahoma Department of Transportation (ODOT) based on the collective analyses, and probabilistically calibrated resistance factors for use with the recommended relations.

6.1 GENERAL CONSIDERATIONS FOR ANALYSIS OF AXIAL DESIGN RELATIONS

The collective data set considered for the current work includes interpreted values of unit side resistance, q_s, and unit tip resistance, q_p, from load tests in weak rock in Oklahoma and surrounding states, including the values presented in Chapter 5. Additional data used for evaluating potential design relations included corresponding values of design parameters for each test, including compressive strength, q_u, TCPT penetration, denoted as $MTCP$, and equivalent SPT N-values, N_{eq-60}, determined as described for the Edmond and Minco test sites in Chapter 4. Evaluations conducted for the collective data set were primarily based on regression analyses performed considering paired values of q_s or q_p with corresponding values of relevant design parameters. Most of the analyses were performed using the ordinary least-squares (OLS) regression method, although some weighted least-squares (WLS) regression analyses were also conducted. Prediction uncertainty was quantified for all regression analyses and used as part of evaluations of alternative design relations.

The analyses performed were far more than just determining the “best fit” predictive functions for unit side and tip resistance. Considerable judgment was applied when conducting evaluations of alternative design relations. The alternative relations considered were restricted to reasonably simple functions that are practical for design, and strong preference was given to commonly adopted forms of design relations. Strong preference was also given to existing design relations that have been adopted by other state or federal transportation agencies, as long as those relations reasonably represent available measurements and can be effectively used. Changes to existing design relations are only recommended when such changes will produce considerably greater factored resistance for drilled shafts in weak rock, or significantly more accurate prediction of nominal unit resistance.

6.2 AXIAL DESIGN USING MODIFIED TCPT PENETRATION

Interpreted values of unit side resistance from load tests in weak rock are plotted versus corresponding interpreted values of $MTCP$ in Figure 6.1. The values plotted in the figure

represent load tests from Oklahoma, Missouri, and Texas, which are the only states with design methods that rely on TCPT measurements in weak rock. All plotted values represent measurements where the ultimate unit side resistance was achieved during the respective tests. The figure reveals that the load tests performed as part of the current work were successful in producing measurements in portions of the graph where data were previously limited, most notably for $MTCP$ values less than approximately 1.5 inches per 100 blows.

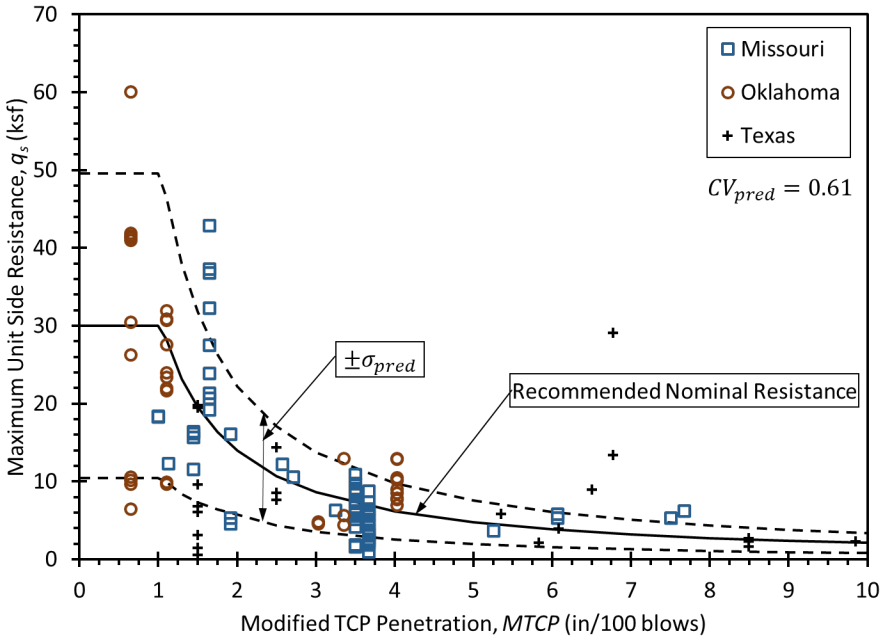

Figure 6.1 – Ultimate unit side resistance from collected load tests in weak rock with recommended relation for design from TCPT measurements.

The considerable variability of unit side resistance in weak rock is apparent from the collected measurements shown in Figure 6.1. Vertical clusters of measurements in the figure represent replicate measurements for a single stratum at a single site, which are indicative of so-called “within-site” variability. In extreme cases, these replicate values of interpreted unit side resistance vary by up to an order of magnitude (e.g., q_s values from one stratum at the Edmond site vary from 6.5 to 60 ksf). The fact that large within-site variability has now been observed for a considerable number of sites suggests that the variability is real, and representative of what can be expected for side resistance of drilled shafts in weak rock using common construction techniques. The overall variability of unit side resistance is also influenced by considerable “among-site” site variability, as evidenced by the fact that some vertical clusters of data points fall above the regression line shown while other vertical clusters fall below the regression line, and still others are approximately centered on the regression line.

Figure 6.1 also shows the recommended relation for prediction of unit side resistance from $MTCP$ values, along with bounds reflecting the prediction uncertainty associated with that relation. In this instance, the recommended relation is identical to the current MoDOT design relation given in Equation 2.5. The collected data from the current

project is consistent with both the MoDOT design relation and the prediction uncertainty for that relation. Plotted values from load tests performed at the Edmond and Minco sites also support the upper limit of 30 ksf that is currently adopted by MoDOT. Attempts to identify alternative practical functions for predicting unit side resistance from $MTCP$ values produced no practically superior relations. Adoption of the current MoDOT design relation for unit side resistance from $MTCP$ values, including the upper limit of 30 ksf, is therefore recommended.

Figure 6.2 shows interpreted values of unit tip resistance from the same load tests plotted versus corresponding interpreted values of $MTCP$. Plotted values represent the maximum value of unit tip resistance observed in the respective tests; values from tests where failure was achieved are indicated using surrounding boxes as noted in the figure. The interpreted values from load tests performed as part of the current work provide valuable evidence regarding the magnitude of unit tip resistance in weak rock with $MTCP$ less than 1.5 inches per 100 blows.

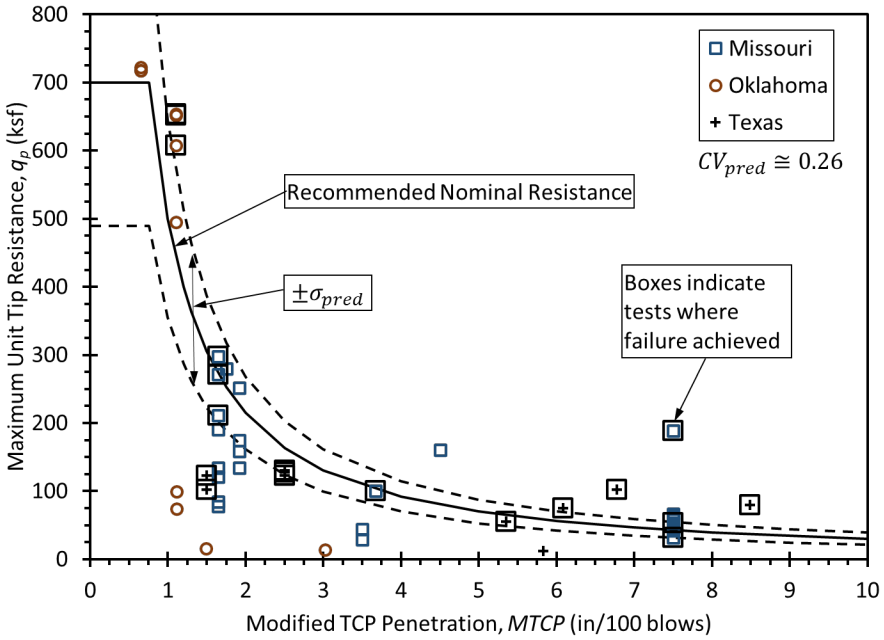

Figure 6.2 – Unit tip resistance from collected load tests in weak rock with recommended relation for design from TCPT measurements.

Despite the fact that failure was not achieved in several of the tests (failure in tip resistance was not achieved for any test at the Edmond site and only debatably achieved for three tests at the Minco site), the mobilized unit tip resistance from tests performed for the current project was more than double the maximum unit tip resistance observed in the other tests shown in Figure 6.2. The figure shows some scatter among the values plotted from different tests, which again provides indications of both among-site and within-site variability. However, when considering only tests where failure was achieved, the degree of scatter in the ultimate unit tip resistance is considerably less than that observed for side resistance for the same collection of tests, which demonstrates that tip resistance can be more reliably predicted than side resistance.

Comparing coefficients of variation for prediction uncertainty for side ($CV_{pred} = 0.61$) and tip ($CV_{pred} = 0.26$) resistance, predictions of unit tip resistance are roughly twice as reliable as predictions of side resistance.

Figure 6.2 also shows the recommended design relation for prediction of unit tip resistance from $MTCP$ values along with bounds indicating the magnitude of prediction uncertainty for the relation. The recommended relation is similar to that currently used by MoDOT, as given in Equation 2.6, but with a modified upper limit of 700 ksf as compared to 400 ksf that is currently prescribed in MoDOT design guidelines. Consideration of alternative functions for predicting unit tip resistance revealed that the fundamental MoDOT relation provides as good a representation of unit tip resistance as any practical alternative. However, measurements from both the Edmond and Minco sites clearly demonstrate that a greater upper limit is justified for $MTCP$ values less than about 1 inches per 100 blows.

The current MoDOT upper limit was subjectively established to limit the design relation to values that do not greatly exceed the maximum unit tip resistance that had been measured in weak rock at the time (approximately 300 ksf as shown in Figure 6.2), as well as based on considerations of the design compressive strength of concrete that is commonly used for drilled shafts on MoDOT projects (4,000 psi ≈ 575 ksf). While basing the upper limit of unit tip resistance on the compressive strength of concrete seems justified, such a limit should not be accomplished through the design relation for geotechnical resistance because different resistance factors apply to structural and geotechnical resistance. Instead, the factored geotechnical resistance determined from the recommended design relation should be compared to the factored structural resistance of the drilled shaft tip, and the lesser of the two factored resistances used when comparing factored loads and factored resistances for design of the shaft.

The interpreted unit tip resistances from load tests at the Edmond and Minco sites confirm that unit tip resistance increases dramatically for decreasing values of $MTCP$ and support adoption of the fundamental MoDOT design relation. However, maintaining some upper limit on the recommended design relation remains necessary to limit prediction of unjustified values for $MTCP$ values less than 1 inches per 100 blows. The necessity for such a limit primarily follows from the practical precision of TCPT measurements. The steep nature of the relation for $MTCP$ values less than 1 inches per 100 blows means that the relation predicts large changes in unit tip resistance for small changes in $MTCP$. For example, the nominal unit tip resistance from the recommended relation for $MTCP$ equal to 0.5 inches per 100 blows is equal to 1165 ksf while the nominal unit tip resistance for $MTCP$ equal to 0.4 inches per 100 blows is 1529 ksf, a 31 percent increase. The problem that arises is that the practical precision of $MTCP$ measurements is on the order of 0.25 inches given that the test is performed in the field, often in wet, messy conditions while exposed to the elements. Precision may be improved somewhat by taking the average of numerous measurements, but the fundamental issue of precision still remains. While the magnitude of the upper limit can be debated, a value of 700 ksf is recommended because this value reasonably represents the maximum unit tip resistance observed in weak rock formations to date.

Interestingly, the recommended upper limit is also approaching the upper limit for stress that can be applied using common bi-directional loading devices.

It is also important to emphasize that the weak rock at the Edmond site is sandstone while the weak rock for all other load tests shown in Figures 6.1 and 6.2 is argillaceous rock, primarily shale. The fact that interpreted unit side and tip resistances from load tests in sandstone are reasonably consistent with design relations established principally for argillaceous weak rock lends credence to the effectiveness of using TCTP measurements for design of drilled shafts in various types of weak rock.

6.3 AXIAL DESIGN USING COMPRESSIVE STRENGTH

Interpreted values of unit side resistance from collected load tests in Oklahoma, Colorado, Kansas, Missouri, and Texas are plotted in Figure 6.3 versus corresponding interpreted values of compressive strength. All plotted values again represent measurements where the ultimate unit side resistance was achieved. Load tests performed as part of the current work contributed important data for evaluation of design relations, particularly for compressive strengths greater than 50 ksf. Also shown in the figure is the recommended design relation based on compressive strength, with bounds indicating the magnitude of prediction uncertainty for the relation. The recommended relation for design based on compressive strength is identical to that currently adopted in MoDOT design provisions and given in Equation 2.3. Interpreted unit side resistances from load tests at the Minco site also support maintaining the upper limit of 30 ksf that is currently prescribed in MoDOT design provisions.

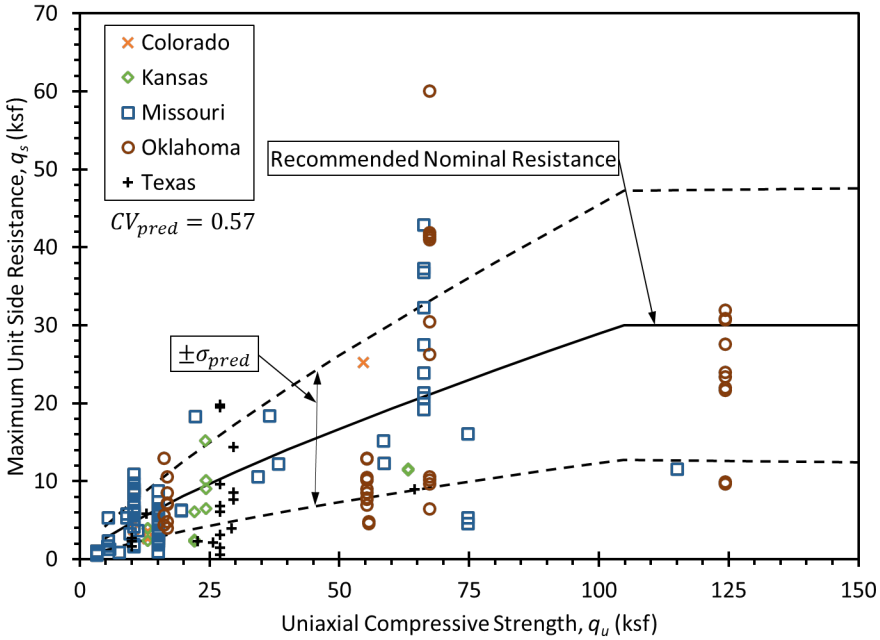

Figure 6.3 – Ultimate unit side resistance from collected load tests in weak rock with recommended relation for design from compressive strength measurements.

The scatter among unit side resistance values in Figure 6.3 is similar to that observed in Figure 6.1, which suggests that the scatter is principally a result of variability of side resistance rather than variability of interpreted design parameters used for the respective relations. The observed variability of unit side resistance from load tests in weak rock in Oklahoma is generally consistent with the variability of unit side resistance from load tests in other states, which supports collective interpretation of load tests in weak rock from different states. The magnitude of prediction uncertainty shown for the TCPT-based design relation in Figure 6.1 ($CV_{pred} = 0.61$) and the compressive strength-based relation in Figure 6.3 ($CV_{pred} = 0.57$) indicates that both design relations have similar reliability. Figure 6.3 also shows that the prediction uncertainty is produced by both within-site variability and among-site variability, with the within-site variability observed for load tests at the Edmond site being particularly large.

One caveat about the observed variability shown in Figures 6.1 and 6.3 is that the variability is derived from interpretation of side resistance along individual shaft segments extending between strain gage levels. Such segments are often approximately 5 to 10 feet in length. The variability of unit side resistance for longer shaft segments is likely to be less than that shown in the figures and considered for the present work because of inherent averaging of side resistance that takes place for longer shaft segments. While this phenomenon is widely understood and appreciated, it is difficult to take advantage of in formal design provisions for two reasons:

1. Little research has been conducted to measure the influence of “length-averaging” for drilled shafts or other deep foundation elements so that the magnitude of reduced uncertainty is not well defined.
2. Reductions in uncertainty with length are difficult to practically implement; some shafts inevitably have relatively short segments in weak rock while others may have longer segments in weak rock and developed design provisions must be appropriate for both.

As a result of these challenges, the potential benefits of inherent averaging of side resistance for long shaft segments has been conservatively neglected so that the recommended methods can be safely applied to shaft segments of any length.

Figure 6.4 shows interpreted values of unit tip resistance from the same load tests plotted versus the interpreted compressive strength for the respective tests, with values associated with failure again being indicated by surrounding boxes. Previous graphs in this chapter have demonstrated general consistency among resistances from load tests performed at the Edmond and Minco sites with resistances from other collected load tests. However, Fig, 6.4 shows that interpreted unit tip resistances from load tests at the Edmond and Minco sites fall considerably above the trend indicated from other tests, despite the fact that many of the load tests at Edmond and Minco did not achieve failure in tip resistance. The interpreted unit tip resistances from load tests at the Edmond site are obvious outliers that can be easily explained because the load tests were performed in sandstone rather than argillaceous rock. However, the considerable difference between the interpreted unit tip resistances from the Minco site and the relation show in the figure are more difficult to explain. It is possible that the shale at Minco is an

"exceptional shale" that produces tip resistance that simply falls at the upper extreme of the observed variability. However, it is also possible that the unexpected result could be a result other factors that are not understood.

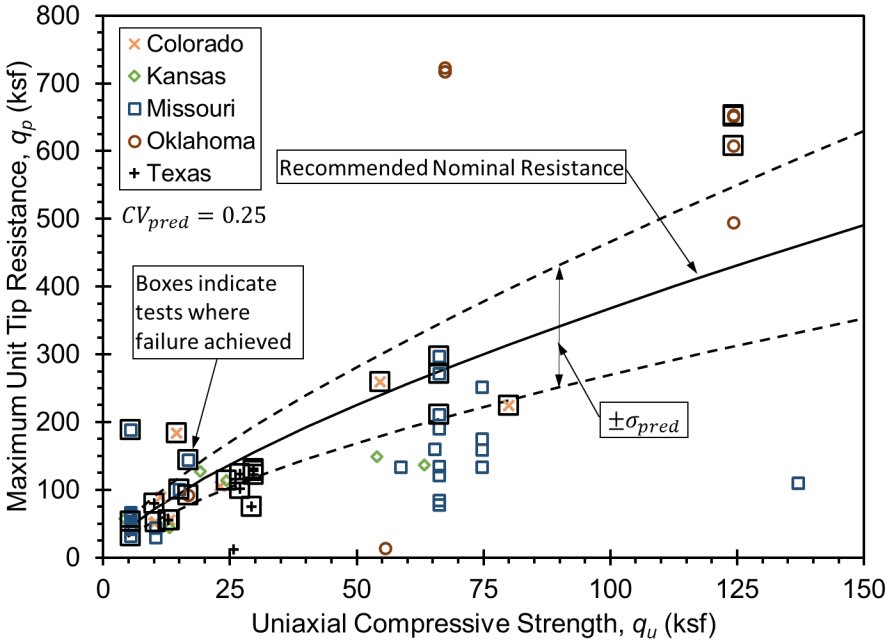

Figure 6.4 – Ultimate unit tip resistance from collected load tests in weak rock with recommended relation for design from compressive strength.

The recommended relation for prediction of unit tip resistance from compressive strength is also shown in Figure 6.4 with bounds representing prediction uncertainty for the relation. The recommended relation is a modification of the current MoDOT design relation given in Equation 2.4, with the upper limit being increased to 700 ksf for reasons described in Section 6.2. Other forms of design relations were also considered and evaluated. It is relatively easy to identify alternative functions that provide better fits to the values plotted in Figure 6.4, and especially to the values determined from load tests at the Minco site. Specifically, functions that have upward curvature provide better fits to the plotted values corresponding with failure. However, it is difficult to practically justify why unit tip resistance should follow a design relation with upward curvature and, given that it is tests from a single site (the Minco site) that suggest upward curvature, such functional relations were disregarded. Restricting considered functions to more commonly adopted linear and power functions, the fundamental MoDOT relationship that is shown in Figure 6.4 and recommended for use turns out to be as good or better than alternative relations that were considered. This result can be qualitatively understood by noting that increasing the magnitude of the relation to become closer to the measured resistance from the Minco site necessarily requires that the relation becomes a poorer predictor of other load test measurements, which acts to increase prediction uncertainty and lower the magnitude of required resistance factors. The magnitude of the factored tip resistance for the alternative relations considered was similar to or less than the factored resistance established for the current MoDOT design

relation. As a result, the modified MoDOT design relation with an upper limit of 700 ksf is recommended for adoption by ODOT.

While perhaps slightly conservative for weak, argillaceous rock formations with compressive strengths greater than 100 ksf, the recommended relation still predicts unit tip resistance values that are considerably greater than prescribed in the current AASHTO LRFD Bridge Design Specifications, and greater than predicted using another alternative method proposed by Zhang and Einstein (1998). While it is possible that additional load tests for weak rock with compressive strengths greater than 100 ksf could support and confirm the greater unit tip resistance observed for load tests at the Minco site, the recommended design relation represents the best relation for design of drilled shafts in argillaceous weak rock given available measurements.

The recommended design relation in Figure 6.4 is somewhat unsurprisingly a poor predictor of the unit tip resistance observed for load tests in sandstone at the Edmond site. By inference, the relation is also likely a poor predictor of unit tip resistance in sandstone more generally. Despite this observation, the recommended design relation in Figure 6.4 can still be justifiably used when it is necessary to predict unit tip resistance from compressive strength in sandstone since it is likely to produce conservative estimates of unit tip resistance. However, comparison of the design relations shown in Figures 6.2 and 6.4 reveals that the TCPT-based design relation is much more likely to produce accurate predictions of unit tip resistance in sandstone than the compressive strength-based design relation.

6.4 AXIAL DESIGN USING SPT N-VALUE

Figure 6.5 shows interpreted values of unit side resistance from load tests in weak rock in Oklahoma, Colorado, and Missouri plotted versus corresponding values of the equivalent SPT N-value, N_{eq-60}. Similar to Figures 6.1 and 6.3, Figure 6.5 demonstrates the considerable variability of unit side resistance in weak rock, but general consistency among interpreted values of unit side resistance determined from load tests for the current work with values of unit side resistance determined from other load tests. The recommended design relation shown in Figure 6.5 is identical to that recommended by Pierce (2013) as given in Equation 2.9. An upper limit of 30 ksf is recommended for the relation for consistency with other design relations for unit side resistance. The magnitude of prediction uncertainty for the recommended SPT-based relation is similar to that for prediction of unit side resistance from $MTCP$ and compressive strength.

Interpreted values of unit tip resistance from the same collected load tests are plotted in Figure 6.6 versus interpreted values of N_{eq-60}. As observed in Figure 6.4, interpreted values of unit tip resistance from the load tests performed at the Minco and Edmond sites are considerably greater than the recommended design relation, which is identical to that proposed by Pierce (2013). Potential modifications considered to increase the predicted nominal resistance for this relation so that it more closely predicts measured unit resistances from the Minco site simultaneously increases the prediction uncertainty, which in turn leads to decreases in calibrated resistance factors. These compensating effects produced little change in the factored resistance, which supports the

recommendation to use the Pierce (2013) for design based on SPT measurements. Increasing the design relation is also hard to justify given that the subject data points are from only a single site.

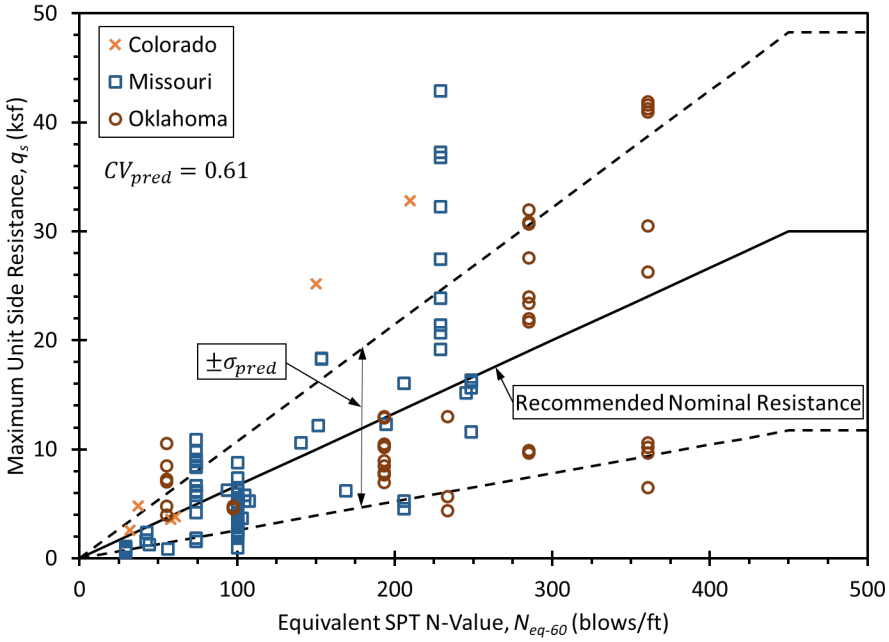

Figure 6.5 – Ultimate unit side resistance from collected load tests in weak rock with recommended relation for design from N_{eq-60}.

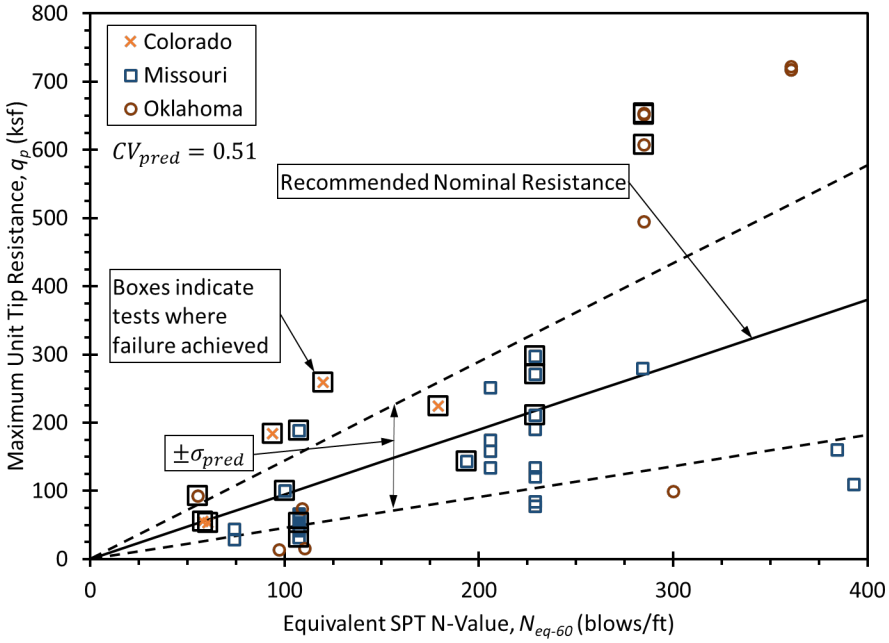

Figure 6.6 – Unit tip resistance from collected load tests in weak rock with recommended relation for design from N_{eq-60}.

The magnitude of prediction uncertainty for the recommended SPT-based design relations for side and tip resistance are roughly similar, and both quite large. The

prediction uncertainty for the SPT-based design relation for side resistance (Figure 6.5) is similar to that observed for both the TCPT- and compressive strength-based relations, which suggests that all three relations are similarly reliable. In contrast, the prediction uncertainty for the SPT-based design relation for tip resistance (Figure 6.6) is considerably greater than that observed for the TCPT- and compressive strength-based relations. This observation indicates that the SPT-based design relation for tip resistance is a poor predictor of unit tip resistance, and that preference should be given to using the other relations for tip resistance when possible.

6.5 RESISTANCE FACTORS FOR RECOMMENDED DESIGN METHODS

Probabilistically calibrated resistance factors were developed for many of the alternative design relations considered as part of evaluations described previously in this chapter. Resistance factors for all recommended design relations are presented in this section. Comparisons of the factored resistance for the recommended design relations with the factored resistance for comparable current design procedures are also described to provide context regarding the impact of adopting the recommended design methods.

6.5.1 Calibration Procedure

Recommended resistance factors were probabilistically calibrated to achieve a target probability of failure of 1 in 1000 for the strength limit state, which is generally consistent with the target probability of failure reported for foundation design in the current AASHTO Bridge Design Specifications (AASHTO, 2020). Probabilistic calibrations were performed using the Monte Carlo method, which is a numerical method for performing probability analyses that is commonly used for calibrating resistance factors for load and resistance factor design (LRFD). The Monte Carlo method utilizes simulations of performance with random sampling of probabilistic inputs to establish the probability distribution for a performance function. The probability analyses are iteratively repeated to develop a set of mean values for inputs that produce a probability distribution that just achieves the target probability of failure, given knowledge of uncertainty for probabilistic inputs. Resistance factors are then established based on these inputs and knowledge of nominal values for the inputs. A minimum of 10,000 simulations was used for all Monte Carlo simulations; simulations were repeated ten times to improve the precision of recommended resistance factors and ensure acceptable precision.

Probabilistic inputs for the calibrations include the magnitude of dead load effects and live load effects, a model factor that accounts for the prediction uncertainty of the respective design relations, and the uncertainty associated with the fundamental design parameter (i.e., $MTCP$, q_u, or N_{eq-60} depending on the design relation considered). The magnitudes of the mean dead load effect and mean live load effect were established by considering a dead load to live load ratio of 2.0 and varying the magnitude of the dead load effect to produce the target probability of failure. The coefficient of variation for the dead load effect was taken to be 0.10 while the coefficient of variation of the live load effect was taken to be 0.12 based on studies by Kulicki, et al. (2007). The mean value of the model factor was taken to be 1.0 since each of the recommended design relations produces unbiased estimates for the mean resistance. The uncertainty in the

model factor was set to reflect uncertainty in the design relation for the specific mean value of the considered design parameter (uncertainty for the recommended design relations vary with the value of the input parameter). Calibrations were repeated for mean values of the respective design parameters (i.e., $MTCP$, q_u, or N_{eq-60}) across the range of values for which the relation is considered appropriate, generally the range of values shown on the horizontal axes in Figures 6.1 through 6.6. The recommended resistance factors presented here are the average of the resistance factors determined for all mean values of the design parameters.

Recommended resistance factors were developed to be a function of the coefficient of variation representing uncertainty in the mean value of the relevant design parameter (i.e., $MTCP$, q_u, or N_{eq-60}). For situations where the design parameter can be considered uniform within a given stratum, this coefficient of variation is calculated as

$$CV_{\bar{d}} = \frac{\sigma_{\bar{d}}}{\bar{d}} = \frac{\frac{\sigma_d}{\sqrt{n}}}{\bar{d}} \tag{6.1}$$

where $CV_{\bar{d}}$ is the coefficient of variation representing uncertainty in the mean value for design parameter d, σ_d is the standard deviation of available measurements for design parameter d, n is the number of available measurements for design parameter d, $\bar{d}$ is the mean value for design parameter d, and $\sigma_{\bar{d}}$ is the standard deviation representing uncertainty in the mean value for design parameter d (i.e., $\sigma_{\bar{d}} = \sigma_d/\sqrt{n}$). In Equation 6.1, the variable d is intended to represent the relevant design parameter for each recommended relation (i.e., either $MTCP$, q_u, or N_{eq-60} depending on the relation). Resistance factors for each considered value of CV_d were determined by incorporating the associated uncertainty into the Monte Carlo simulations. It is important to emphasize that the coefficient of variation given in Equation 6.1 does not represent the variability of available measurements for a design parameter, but rather the level of confidence in the mean value of the parameter established from available measurements.

6.5.2 Resistance Factors for Tip Resistance Using Modified TCPT

The recommended nominal unit tip resistance established from interpreted values of $MTCP$ is calculated as:

$$q_p = 500 \cdot \overline{MTCP}^{-1.22} \leq 700 \text{ ksf} \tag{6.2}$$

where q_p is the nominal unit tip resistance in units of ksf and $\overline{MTCP}$ is the representative mean value of $MTCP$ for the weak rock beneath the shaft tip in units of inches per 100 blows. Calibrated resistance factors for Equation 6.2 are plotted versus the magnitude of $CV_{\overline{MTCP}}$ in Figure 6.7. The decreasing resistance factor for increasing uncertainty in $\overline{MTCP}$ (represented using $CV_{\overline{MTCP}}$ determined, for example, using Equation 6.1) reflects the influence of uncertainty in $\overline{MTCP}$ on the reliability of the foundation for satisfying the strength limit state. Calibrated resistance factors range from a high of 0.58 when $\overline{MTCP}$ is perfectly characterized (i.e., $CV_{\overline{MTCP}} = 0$) to a low of 0.22 when $\overline{MTCP}$ is very poorly characterized ($CV_{\overline{MTCP}} \geq 0.5$). “Typical” site characterization for historical practice often

produces $CV_{\overline{MTCP}}$ approximately equal to 0.25. The resistance factor associated with this value of $CV_{\overline{MTCP}}$ for Equation 6.2 is 0.41. Intensive site characterization programs similar to those described in Chapter 3 for the Edmond and Minco test sites will often produce $CV_{\overline{MTCP}}$ between 0.05 and 0.10. The resistance factor for design using Equation 6.2 with similar site characterization will often be approximately 0.54.

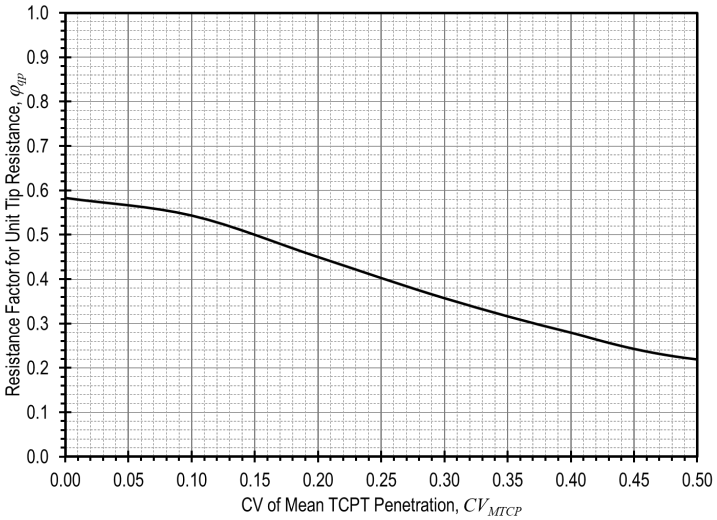

Figure 6.7 – Resistance factors for unit tip resistance from TCPT penetration for weak rock.

Figure 6.8 shows measurements of unit tip resistance presented previously with the recommended design relation of Equation 6.2 and the factored resistance established from Equation 6.2 with recommended resistance factors. The recommended design relation produces nominal unit tip resistances that are greater than produced using the current ODOT design relation (Equation 2.2) for all values of $MTCP$. Differences between the recommended and current ODOT relations are particularly dramatic for MTCP less than 2 inches per 100 blows, where the recommended relation produces unit tip resistance nearly six times greater than the current ODOT relation. The factored resistance produced by the recommended design procedure varies with site characteristics and the rigor of site characterization activities. However, for typical levels of characterization and $MTCP$ less than approximately 2 inches per 100 blows, the recommended design procedure will produce factored resistance that greatly exceeds the factored resistance from current ODOT procedures. The factored resistance from the recommended design procedure is similar to that produced using the current ODOT procedure for $MTCP$ greater than approximately 2 inches per 100 blows.

The shaded region shown in Figure 6.8 defines the range of factored resistance for design, which depends on uncertainty in the mean value of $MTCP$ (i.e., $CV_{\overline{MTCP}}$) and, in turn, the number of available $MTCP$ measurements and the variability of $MTCP$ throughout the considered stratum (as dictated by Equation 6.1, or similar equations appropriate for other situations). For a given site, factored resistance near the upper end of the range will apply for instances where large numbers of $MTCP$ measurements are available whereas factored resistance near the lower end of the range will apply when few $MTCP$ measurements are available. Importantly, the design reliability

achieved throughout the range will be similar regardless of the number of available measurements because the recommended resistance factors account for the level of uncertainty. This feature allows designers to seek to optimize costs for design and construction by comparing costs required to collect more measurements during design to cost savings that can be realized by constructing smaller foundations if greater numbers of measurements are collected. In general, overall costs for larger projects will often be reduced by collecting greater numbers of measurements while overall costs for smaller projects may be reduced by collecting fewer measurements. Similar concepts apply to other recommended design procedures described subsequently in this chapter, although ranges of factored resistance vary among the different design relations.

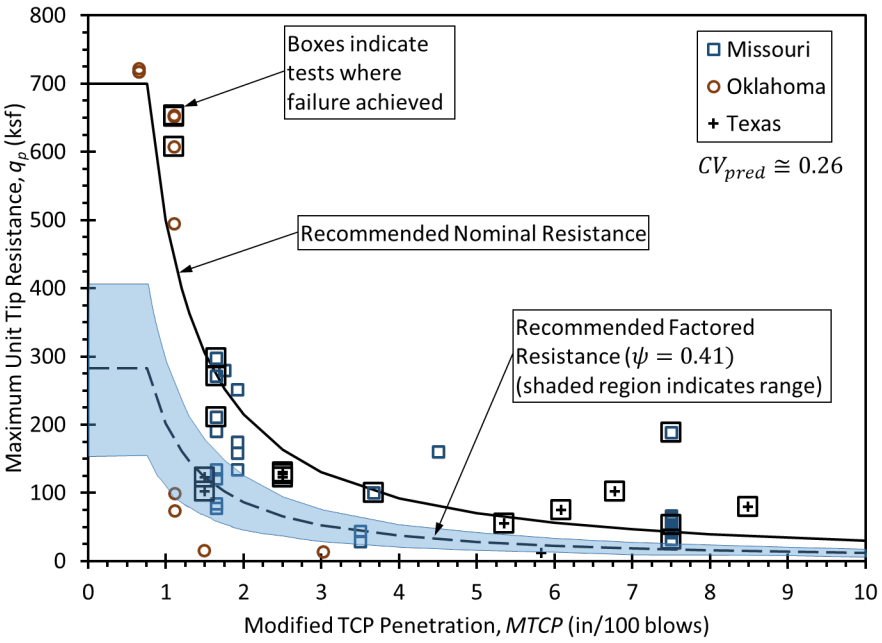

Figure 6.8 – Recommended nominal and factored unit tip resistance for recommended TCPT-based design relation.

While the absolute range of factored resistances shown in Figure 6.8 diminishes with increasing $MTCP$, the proportional range of factored resistance relative to the typical value shown by the dashed curve is actually constant across all values of $MTCP$. As a percentage of the typical values of factored resistance, the range shown reflects the potential to increase or decrease the factored resistance by up to 45 percent based on the quantity of available measurements.

6.5.3 Resistance Factors for Side Resistance Using Modified TCPT

The recommended nominal unit side resistance established from interpreted values of $MTCP$ is calculated as:

$$q_s = 31.6 \cdot \overline{MTCP}^{-1.18} \leq 30 \text{ ksf} \qquad (6.3)$$

where q_s is the nominal unit side resistance in units of ksf and $\overline{MTCP}$ is the representative mean value of $MTCP$ for the weak rock along the considered shaft segment in units of inches per 100 blows. Calibrated resistance factors for Equation 6.3 are provided in Figure 6.9, again as a function of $CV_{\overline{MTCP}}$. Calibrated resistance factors are again observed to decrease with increasing uncertainty in $\overline{MTCP}$ ($CV_{\overline{MTCP}}$) with calibrated resistance factors ranging from 0.21 to 0.12. The resistance factor associated with "typical" site characterization is approximately 0.18. These resistance factors are considerably lower than those for Equation 6.2 because of the considerable variability of unit side resistance observed in the collected load tests as described previously. The resistance factors are also considerably lower than the resistance factor currently adopted by ODOT for drilled shafts in weak rock, which means that current design practices are unlikely to produce the target reliability of 1 in 1000 that was used for calibrating resistance factors.

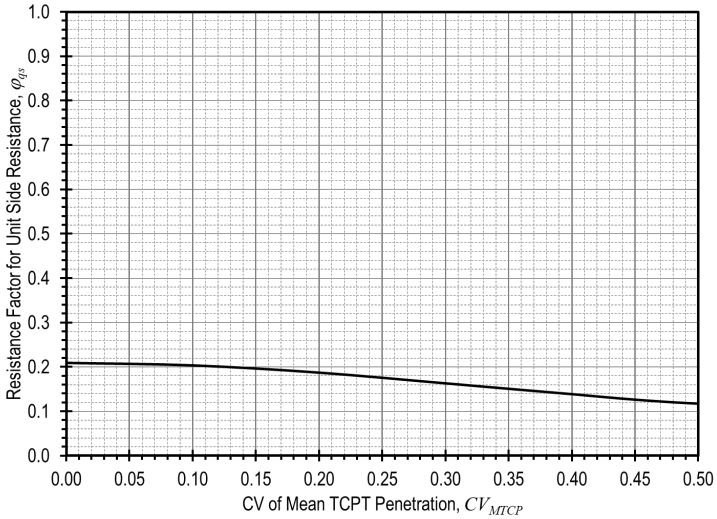

Figure 6.9 – Resistance factors for unit side resistance from TCPT penetration for weak rock.

Measurements of unit side resistance are plotted in Figure 6.10 along with the recommended design relation of Equation 6.3 and corresponding factored resistances produced using calibrated resistance factors from Figure 6.9. The recommended design relation produces nominal unit side resistance that is greater than the current ODOT design relation (Equation 2.1) for $MTCP$ less than approximately 1.5 inches per 100 blows, but less than the current ODOT relation for greater values of $MTCP$. Corresponding factored resistances produced by the recommended design procedure are considerably less than factored resistances from current ODOT design practices for all values of $MTCP$. The magnitude of the difference ranges from being approximately 40 percent less than current ODOT practice for $MTCP$ less than 1 inches per 100 blows to approximately 80 percent for $MTCP$ greater than 2 inches per 100 blows. The lower factored resistances are necessary to account for the considerable uncertainty associated with predicting unit side resistance in weak rock that is demonstrated by the load test measurements shown in the figure.

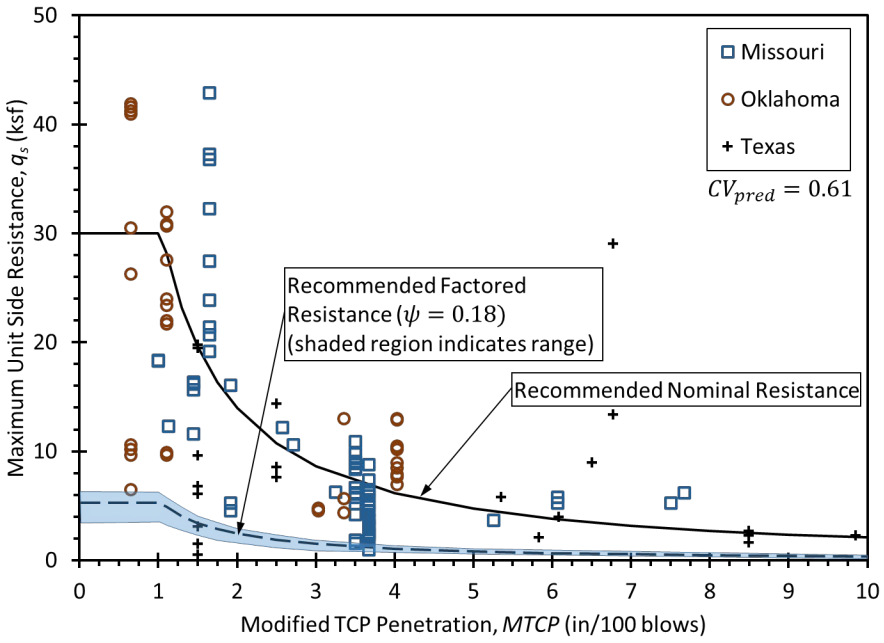

Figure 6.10 – Recommended nominal and factored unit side resistance for recommended TCPT-based design relation.

The large prediction uncertainty associated with Equation 6.3 also limits the influence of parameter uncertainty, $CV_{\overline{MTCP}}$, on the factored resistance as indicated by the relatively narrow shaded range in Figure 6.10. Relative to the factored resistance for typical numbers of $MTCP$ measurements represented by the dashed curve in the figure, collecting greater numbers of $MTCP$ measurements has the potential to increase the factored resistance by approximately 20 percent while collecting fewer $MTCP$ measurements has the potential to reduce the factored resistance by approximately 35 percent.

6.5.4 Resistance Factors for Tip Resistance Using Compressive Strength

The recommended design relation for establishing nominal unit tip resistance from interpreted values of q_u is:

$$q_p = 14 \cdot \overline{q_u}^{0.71} \leq 700 \text{ ksf} \qquad (6.4)$$

where q_p is the nominal unit tip resistance in units of ksf and $\overline{q_u}$ is the representative mean value of compressive strength for the weak rock beneath the shaft tip, also in units of ksf. Figure 6.11 shows calibrated resistance factors for Equation 6.4 plotted versus the magnitude of $CV_{\overline{q_u}}$. As consistently observed in similar figures presented previously, the magnitude of calibrated resistance factors decreases with increasing parameter uncertainty, $CV_{\overline{q_u}}$. Calibrated resistance factors range from a high of 0.60 to a low of 0.34 as $CV_{\overline{q_u}}$ increases from 0.0 to 0.5. The resistance factor for $CV_{\overline{q_u}}$=0.25, which is roughly representative of typical historical practice, is equal to 0.50.

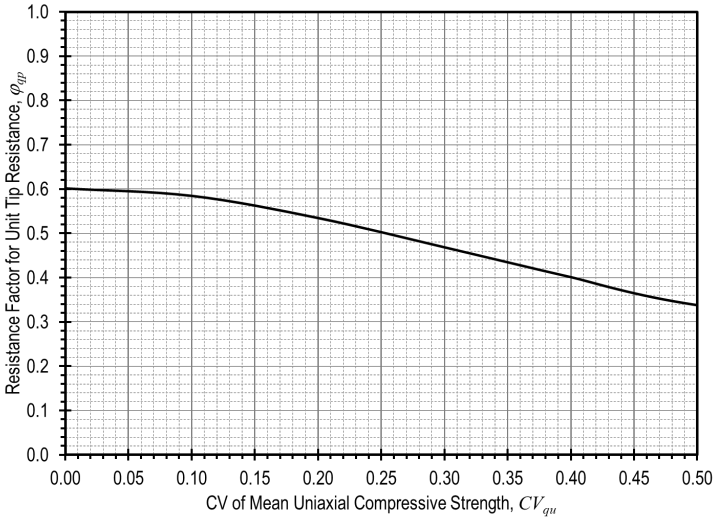

Figure 6.11 – Resistance factors for unit tip resistance from compressive strength for weak rock.

Figure 6.12 shows the interpreted measurements of unit tip resistance presented previously with the recommended design relation and associated values of factored resistance determined from the recommended design relation and resistance factors. The recommended design relation produces considerably greater values of both nominal and factored resistances compared with a similar method prescribed in the current AASHTO specifications (AASHTO, 2020), often by a factor of approximately 2. Similar comparisons apply for another method proposed by Zhang and Einstein (1998). The range of factored resistances defined by the shaded region in Figure 6.12 extend from approximately 20 percent above to 30 percent below the factored resistance associated with typical numbers of measurements, which provides considerable potential to optimize costs for design and construction for both large and small projects.

6.5.5 Resistance Factors for Side Resistance Using Compressive Strength

The design relation recommended for establishing nominal unit side resistance, q_s, in units of ksf from interpreted values of compressive strength is:

$$q_s = 0.76 \cdot \overline{q_u}^{0.79} \leq 30 \text{ ksf} \quad (6.5)$$

where $\overline{q_u}$ is again the representative mean value of compressive strength for the weak rock along in the considered shaft segment in units of ksf. Figures 6.13 and 6.14 respectively show calibrated resistance factors for Equation 6.5 and interpreted side resistance measurements with the recommended design relation and associated factored values of resistance.

As observed for the TCPT-based design relation for side resistance, calibrated resistance factors for side resistance based on compressive strength are quite low, ranging from 0.23 to 0.15. The nominal resistance predicted from Equation 6.5 is considerably greater than the nominal resistance prescribed in the current AASHTO specifications for drilled shafts in similar materials across the entire range of

compressive strengths considered in the current work. However, the low resistance factors associated with Equation 6.5 produce factored resistances that are consistently less than those produced according to the AASHTO specifications, despite the greater nominal resistance. However, the reduced factored resistance is justified by the large prediction uncertainty associated with predicting side resistance from compressive strength in weak rock. The large prediction uncertainty associated with Equation 6.5 also acts to limit the range of factored resistances that can be considered for different numbers of measurements for q_u, as was similarly observed for Equation 6.3.

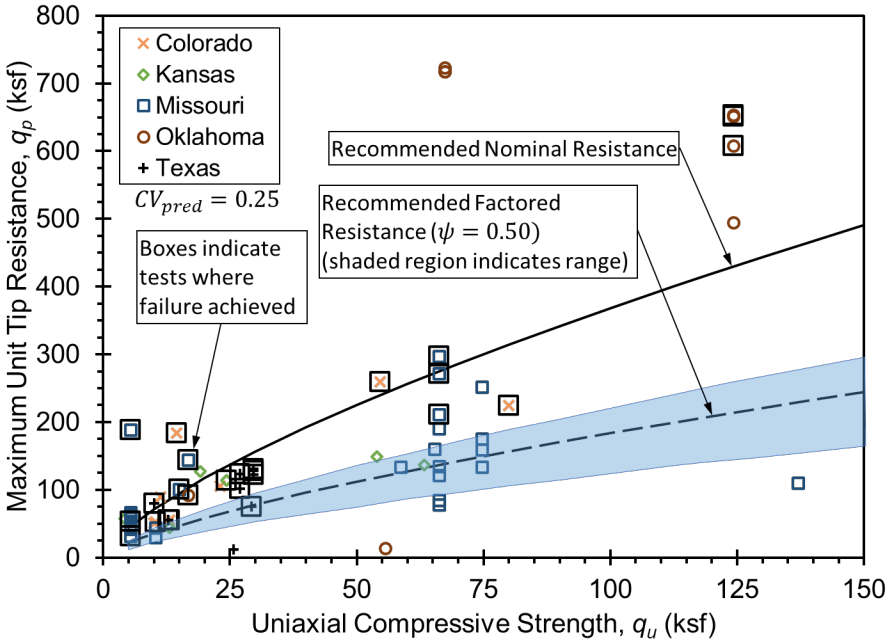

Figure 6.12 – Recommended nominal and factored unit tip resistance for recommended compressive strength-based design relation.

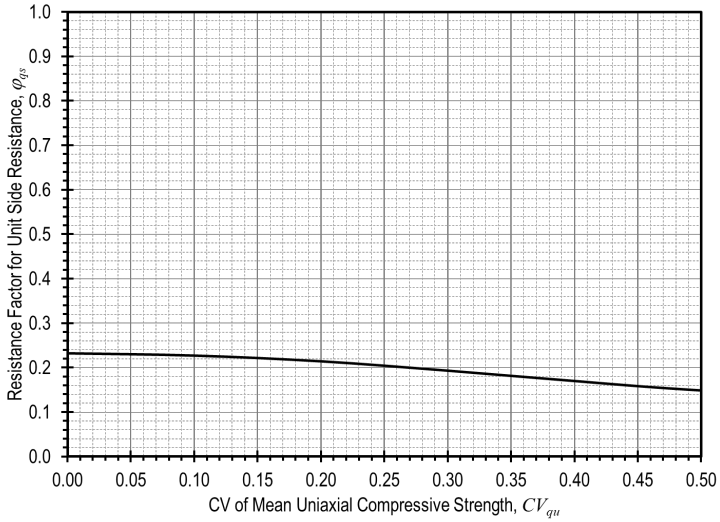

Figure 6.13 – Resistance factors for unit side resistance from compressive strength for weak rock.

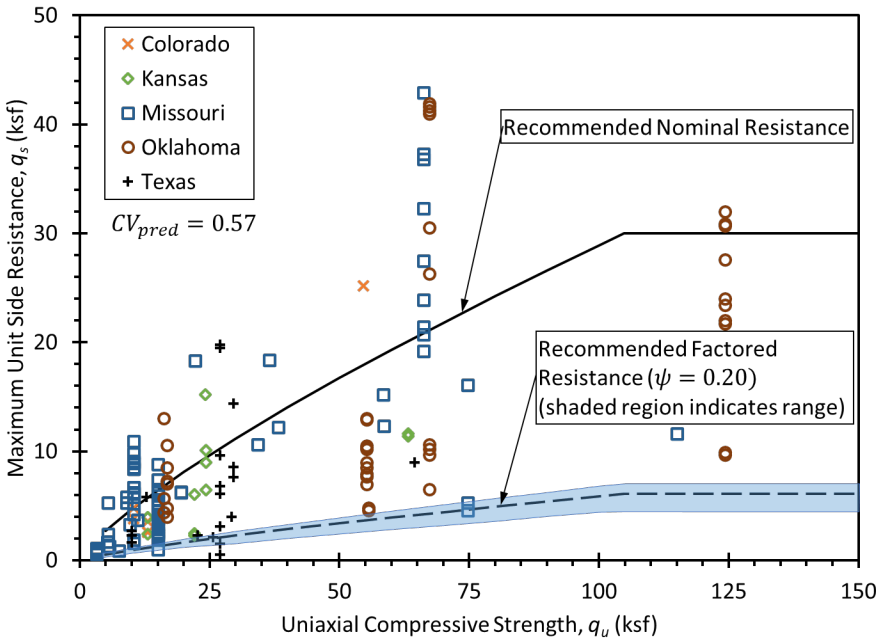

Figure 6.14 – Recommended nominal and factored unit side resistance for recommended compressive strength-based design relation.

6.5.6 Resistance Factors for Tip Resistance Using SPT

The recommended design relation for nominal unit tip resistance based on SPT measurements in weak rock is:

$$q_p = 0.95 \cdot \overline{N_{eq-60}} \leq 700 \text{ ksf} \quad (6.6)$$

where q_p is the nominal unit tip resistance in units of ksf and $\overline{N_{eq-60}}$ is the representative mean of N_{eq-60} values for the weak rock beneath the shaft tip in units of blows/ft. Calibrated resistance factors for Equation 6.4 shown in Figure 6.15 range from 0.28 to 0.14. These values are considerably less than resistance factors for other recommended design relations for tip resistance as a result of the considerably greater prediction uncertainty associated with Equation 6.6.

Nominal and factored resistances associated with Equation 6.6 are plotted in Figure 6.16 along with collected measurements of unit tip resistance for drilled shafts in weak rock. The factored resistance shown in the figure is considerably less than the "allowable resistance" associated with the Updated Colorado SPT-based design method described in Chapter 2. Both the nominal and factored resistances for Equation 6.6 are considerably greater than the relation currently adopted by MoDOT for determining unit tip resistance from SPT measurements in weak rock. While Equation 6.6 and the associated resistance factors in Figure 6.15 can be used for design of drilled shafts in weak rock that achieve the target reliability, more efficient designs will be produced using Equations 6.2 and 6.4 because of the significant differences in prediction uncertainty associated with the different relations. Equation 6.6 should therefore only be used when use of alternative relations for side resistance is not possible.

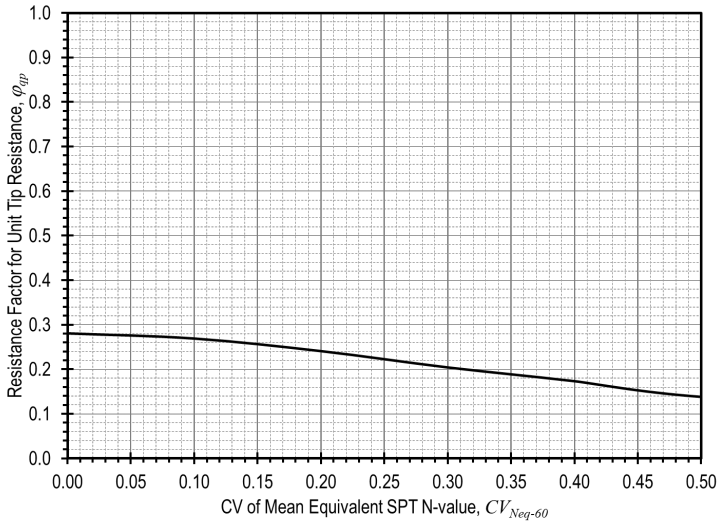

Figure 6.15 – Resistance factors for unit tip resistance from SPT N_{eq-60}.

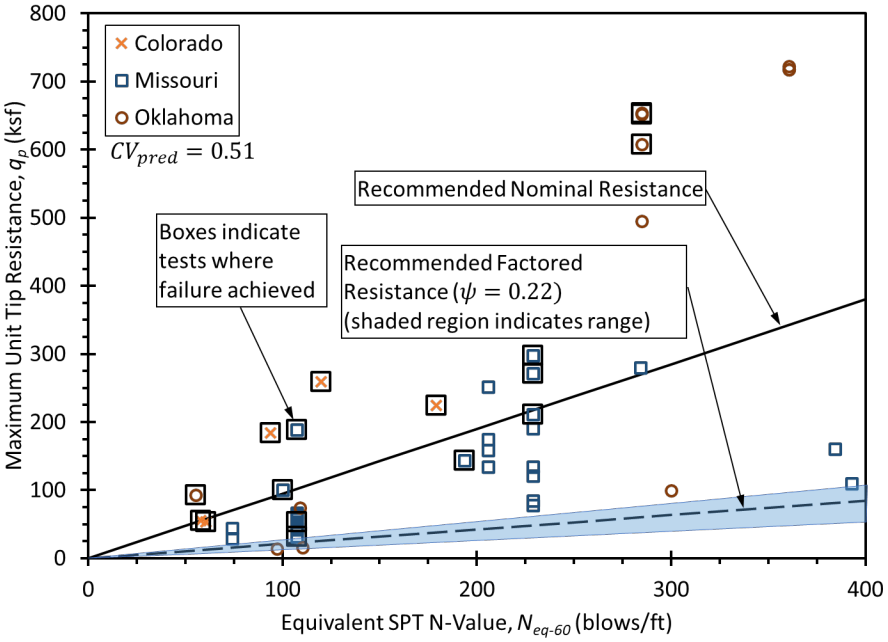

Figure 6.16 – Recommended nominal and factored unit tip resistance for recommended SPT-based design relation.

6.5.7 Resistance Factors for Side Resistance Using SPT

The recommended design relation for nominal unit side resistance, q_s, based on SPT measurements is:

$$q_s = \frac{\overline{N_{eq-60}}}{15} \leq 30 \text{ ksf} \quad (6.7)$$

where q_s is in units of ksf and $\overline{N_{eq-60}}$ is again the representative mean of N_{eq-60} along the considered shaft segment in units of blows/ft. As consistently observed for relations involving unit side resistance, calibrated resistance factors and the corresponding

factored unit side resistance for Equation 6.7 are quite low as shown in Figures 6.17 and 6.18.

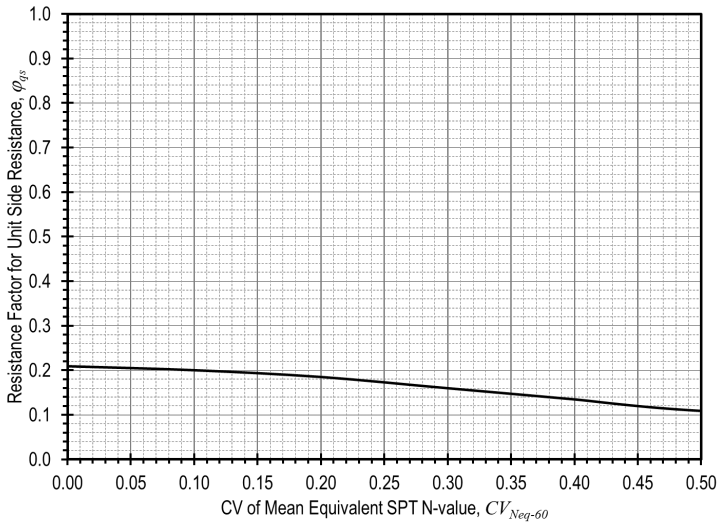

Figure 6.17 – Resistance factors for unit side resistance from SPT N_{eq-60}.

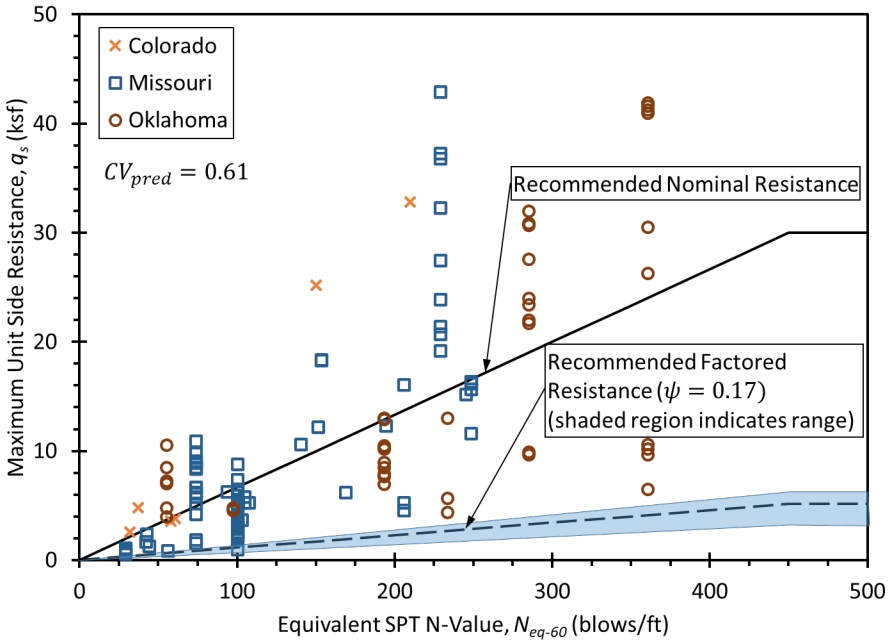

Figure 6.18 – Recommended nominal and factored unit side resistance for recommended SPT-based design relation.

As was observed for the SPT-based relation for unit tip resistance, the factored unit side resistance for Equation 6.7 is considerably less than the “allowable resistance” produced by the Updated Colorado SPT-based method for side resistance. The nominal unit resistance produced from Equation 6.7 is slightly less than that from the relation currently adopted by MoDOT. However, factored unit side resistances from Equation 6.7 and the current MoDOT method are similar.

6.6 PRACTICAL CONSIDERATIONS

All of the recommended design relations presented in this chapter are appropriate for design of drilled shafts in weak rock in Oklahoma. All of the recommended relations provide reasonable estimates for nominal resistance based on commonly available site characterization measurements. When used with the probabilistically calibrated resistance factors presented in this chapter, all of the methods appropriately account for the prediction uncertainty associated with the respective relations and, as such, will produce designs that achieve the target reliability that was used for calibration.

While all of the methods described can be used to achieve the target design reliability, some methods will do so with more efficient (shorter or smaller) drilled shafts than others. While the efficiency of the alternative methods cannot be quantified, it is likely that the recommended TCPT-based design relations given in Equations 6.2 and 6.3 will produce the most efficient shaft designs in the range of weak rock conditions and types that are commonly encountered in Oklahoma. The compressive strength-based design relations given in Equations 6.4 and 6.5 are likely to produce similar design efficiency in argillaceous weak rock, but less efficient designs in sandstone. The SPT-based design relations given in Equations 6.6 and 6.7 are likely to produce the least efficient designs among all of the recommended methods, but may be useful in instances where only SPT measurements are available for design.

Finally, it is important to note that the most efficient designs are likely to be achieved by performing site-specific load tests. While involving some costs, site-specific load tests will often produce more efficient designs for two fundamental reasons:

1. The resistance factor specified in the current AASHTO specifications for unit resistances determined from static load tests is 0.70, which is considerably greater than even the highest calibrated resistance factors recommended from the analyses described in this chapter.
2. There is a relatively high likelihood that the unit side and/or unit tip resistances measured in site-specific load tests will exceed the nominal resistance predicted using the design relations recommended in this chapter.

The greater resistance factor associated with site-specific load tests follows from the fact that site-specific load tests serve to reduce among-site variability that contributes to the prediction uncertainty observed for all of the recommended relations. The second reason follows from observations of measured unit side and tip resistance presented in graphs throughout this chapter. As shown in these figures, there are a considerable number of measurements that exceed those predicted by the different recommended design relations, sometimes by a relatively large amount. While it is difficult or impossible to know whether load tests for a specific site will fall above or below the recommended relations, even load tests producing measured resistances that fall near or slightly below the recommended relations will produce greater factored resistances, and therefore more efficient designs, because of the larger resistance factor associated with load tests. The likelihood of producing more efficient designs based on load tests is particularly high for drilled shafts in sandstone, as demonstrated by measurements from

the load tests performed at the Edmond site. Consideration of site-specific load testing for projects with costs that can justify the initial investment are therefore strongly encouraged, particularly for sites where drilled shafts will be founded in sandstone.

Chapter 7 - Lateral Load Tests

Lateral load tests were performed on all four test shafts at the Edmond site and all four test shafts at the Minco site. This chapter describes the load testing program, the lateral load testing apparatus and instrumentation, and the lateral load testing procedure. The observed load-displacement behavior at the top of each shaft and interpreted bending moment along the length of a representative shaft are also presented.

7.1 LATERAL LOAD TESTING PROGRAM

The goal of the load testing program was to measure the response of the foundations to static lateral loading. All tests were performed by pulling two shafts together, so that two foundations were loaded and monitored simultaneously.

7.1.1 Tests at Edmond Load Test Site

The arrangement of the two tests performed at the Edmond site is shown in Figure 7.1. Test shaft Edmond T1 was tested simultaneously with Edmond T2, and test shaft Edmond T3 was tested simultaneously with Edmond T4. The clear distance between shafts, 20 ft, is equal to the recommended clear distance of 5 shaft diameters in ASTM D3966 (2007).

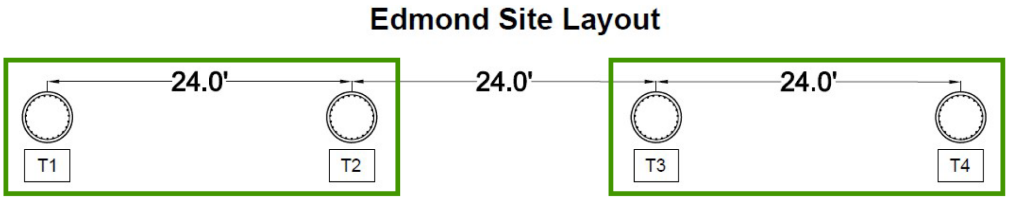

Figure 7.1 – Layout of test shafts at the Edmond site with rectangles indicating tested shaft pairs.

During performance of the first set of tests at Edmond in October 2021, limited test shaft displacement was achieved because of issues with the hydraulic system for testing of shafts T3 and T4, and the loading apparatus for testing of shafts T1 and T2. Lateral load testing at the Edmond site was therefore repeated in August 2022 in an attempt to achieve greater displacement. The second round of tests, which used the same shaft pairing shown in Figure 7.1, successfully achieved greater lateral load and displacement. Only measurements and interpretations from the second round of tests are presented in this report.

7.1.2 Tests at Minco Load Test Site

The arrangement of the two tests performed at the Minco site is shown in Figure 7.2. Test shaft Minco T1 was paired with Minco T3, and test shaft Minco T2 was paired with Minco T4. As for Edmond, the clear distance between shafts, 20 ft, is equal to the recommended clear distance of 5 shaft diameters in ASTM D3966 (2007).

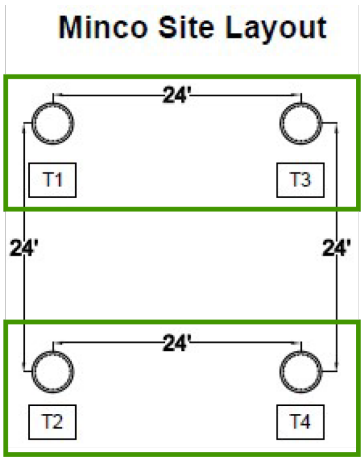

Figure 7.2 – Layout of test shafts at the Minco site with rectangles indicating tested shaft pairs.

7.2 LATERAL LOADING APPARATUS

Each test was performed by pulling paired shafts together using four hydraulic jacks as shown in Figure 7.3. The center-hole jacks (110 MP series 03) were provided by DYWIDAG-Systems International (DSI) and were used to apply tension to the Grade 150 steel threaded bars, also supplied by DSI. The bars were installed through the flanges of two beams, one behind each shaft as shown in Figure 7.3 and in the loading frame plan of Figure 7.4. Application of pressure to the jacks applied tension to the bars, which loaded the beams, which in turn applied load to seatings that were placed around each shaft, thereby loading the test shafts laterally.

Figure 7.3 – One side of lateral load test frame in place at the Minco site.

Together, the two beams, two seatings, and four bars comprise the loading apparatus, which is shown in plan set drawings in Figures 7.4 and 7.5. The beams are W24x131 sections with multiple stiffeners included to increase the shear resistance. In addition, bearing plates were placed between the jacks and beams to reduce stress concentrations at the points of load application. Each seating consists of three plates designed to transfer load from the beam to the shaft via a pipe section collared around the shaft. A photograph of the beam and collar is shown in Figure 7.6. The spherical

bearing shown in the plans was not used in any of the tests. Previous experience with the bearing indicates it introduces too much opportunity for misalignment (Boeckmann, et al., 2014).

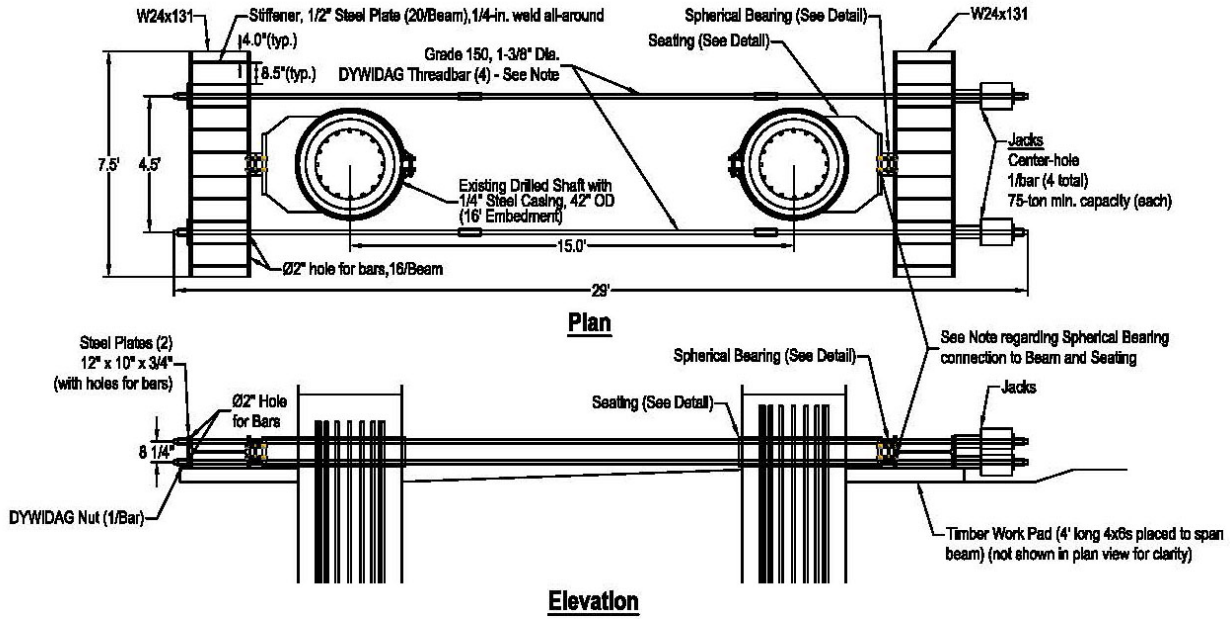

Figure 7.4 – Plan and elevation views of lateral load test frame.

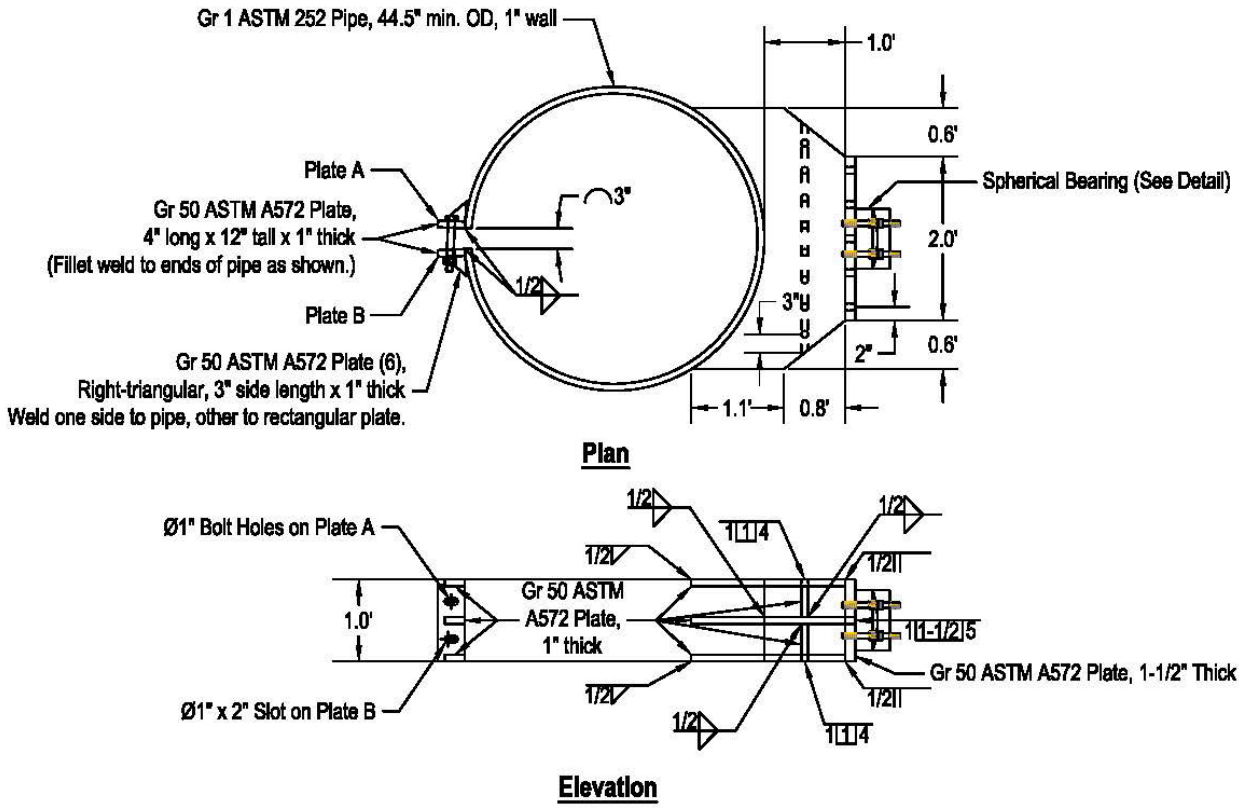

Figure 7.5 – Plan and elevation view of lateral load test frame seating detail.

Figure 7.6 – Beam and seating in place without bearing.

7.3 INSTRUMENTATION AND DATA ACQUISITION

Each test shaft was instrumented with one ShapeAccelArray (ShapeArray) inclinometer to measure deflection along the shaft length, vibrating wire strain gages to measure strain at discrete elevations, and vibrating wire displacement transducers and dial gages to measure displacement of the shaft head. In addition, the load applied to the shafts was measured by monitoring the hydraulic pressure supplied to the jacks. Each instrument is described in more detail in the sections that follow.

The DataTaker™ DT85G data logger shown in Figure 7.7 was used to record the vibrating wire displacement transducers and strain gages throughout each test. The ShapeArray inclinometer was connected directly to a laptop computer that recorded its readings, and the dial gage readings were recorded by hand along with the hydraulic pressure. As shown in Figure 7.8, the dial gages and displacement transducers were mounted to the drilled shafts via magnetic bases affixed to the corrugated metal pipe (CMP) casing. The rod end of each device was connected to the reference beam.

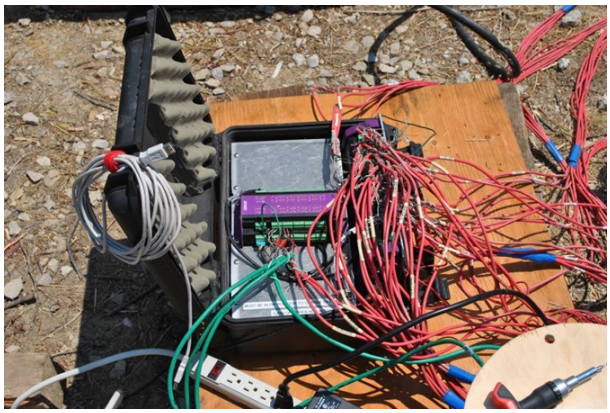

Figure 7.7 – DataTaker data acquisition system with vibrating wire strain gages and LVDTs connected to the multiplexer.

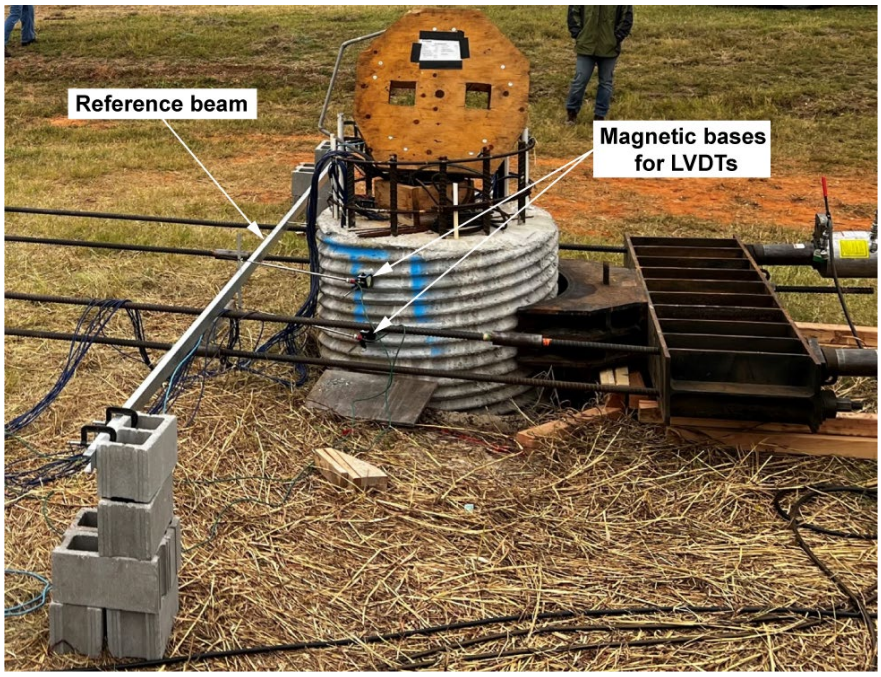

Figure 7.8 – LVDTs mounted to shaft and connected to reference beams.

7.3.1 Vibrating Wire Strain Gages

As described previously, six levels of vibrating wire strain gages were included in all test shafts. All vibrating wire strain gages were sister bar type, Geokon Model 4911 series. For lateral loading, the top two levels are most relevant, as significant load transfer below the top two levels was not anticipated. For all test shafts, the top two levels include four strain gages each.

7.3.2 Shape Array Inclinometers

ShapeAccelArray (ShapeArray) inclinometers were used to measure shaft deflection with depth. The ShapeArray inclinometer is a chain of rigid segments with sensors that use microelectromechanical systems (MEMS) technology to measure the tilt of each segment/joint (Measurand, 2012). The measuring principle of the ShapeArray inclinometer is therefore similar to that of traditional inclinometers. The deflection profile measured by the ShapeArray can be used to interpret bending moments within the test shaft, as described subsequently. Because the ShapeArray inclinometer provides measurements of deflection every 0.5 m (19.7 inch), it provides better spatial resolution than can generally be achieved with strain gages or conventional in-place inclinometers.

ShapeArray measurements were recorded continuously using the ShapeArray software program. Figure 7.9 shows the placement of the ShapeArray device on top of a drilled shaft during testing. The ShapeArray segment and joint are shown in Figure 7.10.

Figure 7.9 – ShapeArray resting atop Edmond T3 during testing.

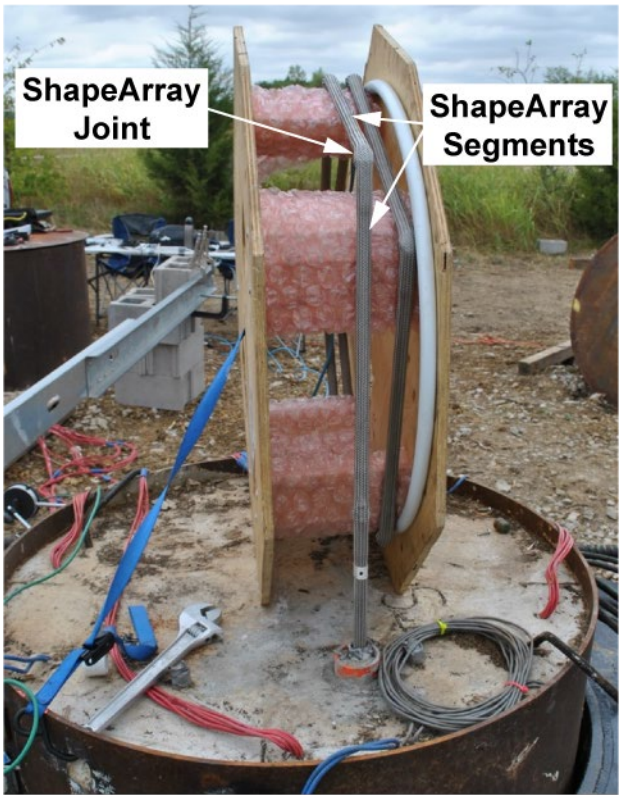

Figure 7.10 – ShapeArray segment and joint.

7.3.3 Vibrating Wire Displacement Transducers

The vibrating wire displacement transducers used were Geokon model 4450 transducers. As shown in Figure 7.8, the displacement transducers were connected between the CMP casing of the shaft via a magnetic base and the reference beam via a threaded rod and wing nut. Each shaft had two displacement transducers mounted at the top of the shaft, one above the other as shown in Figure 7.11. Mounting the transducers above one another allowed for interpretation of shaft head rotation and displacement at the ground surface. Measurements from the vibrating wire displacement transducers were recorded continuously by the DT85G data logger.

Figure 7.11 – Vibrating wire LVDTs attached to the reference beam.

7.3.4 Analog Dial Gages

One analog dial gage was mounted on each shaft during each test. Like the displacement transducers, the dial gages were mounted between the drilled shaft casing and the reference beam as shown in Figure 7.12. Dial gage measurements were recorded manually during testing to provide redundancy for displacement measurements.

7.3.5 Interpretation of Applied Load

The applied load was interpreted from the hydraulic pressure applied to each jack (Figure 7.13) by the pump (Figure 7.14) with the recorded pressure being converted to force via calibrations provided for each jack. Pressure readings were recorded manually for each load step using the pressure gage connected to the pump. The pressure gage was marked in 100-psi increments. The pressure supplied to each jack was also monitored using gages connected to the hydraulic manifold (“tree”) shown in Figure 7.15. The pressure supplied to each jack was generally consistent with the value at the pump. The total applied load is the sum of the forces applied by each jack.

Figure 7.12 – Dial gage mounted to the CMP casing and connected to the reference beam.

Figure 7.13 – Hydraulic jack on threaded bar applying load to beam through a bearing plate.

Figure 7.14 – Hydraulic pump with pressure gage.

Figure 7.15 – Hydraulic manifold with pressure gages for each of the four jacks.

7.4 LATERAL LOAD TESTING PROCEDURE

In general, the lateral load testing program followed procedures described in ASTM D3966 (2007). Lateral loads were applied for each test following the loading sequence of Procedure B for Static Excess Loading. During each load step, a near constant pressure was maintained until several consecutive dial gage readings were unchanged. For small loads, each load step lasted approximately 8 minutes. Loads were not increased if either shaft was still moving considerably. This resulted in longer load increments at higher loads, during which the pump was operated frequently to maintain a constant pressure as the shafts displaced. It was not uncommon for the final load increments for some of the tests to last 30 minutes. At the Edmond site, the tests were terminated when a constant hydraulic pressure could not be maintained because one or both shafts had reached an ultimate limit state. At the Minco site, the tests were terminated shortly after the test shafts contacted the isolation casing, at which point boundary conditions are significantly complicated as discussed in the next chapter.

Initial base readings for all instrumentation were recorded prior to loading. Readings from the dial gages were recorded 1, 2, 4, and 8 minutes after the start of a new loading increment. Subsequent readings were recorded as necessary for longer load steps toward the end of each test. The ShapeArray inclinometer, displacement transducers, and strain gages were recorded continuously with the data acquisition devices described in Section 7.3.

The displacement transducers, dial gages, and jacks were monitored to ensure they did not run out of stroke during loading. Due to the large amount of shaft displacement, this usually required resetting the reference beams once or twice during loading and again during unloading. The hydraulic jacks had to be reset more frequently since their stroke was consumed by displacement of both shafts as well as by elastic elongation of the threaded bars. During resetting of the jacks, the load was locked into the loading frame by tightening locking nuts housed within the neck of the center-hole jacks against the bearing plates. Any adjustments to the instrumentation or equipment were recorded in the test notes and accounted for accordingly during analysis of the test data.

A summary of the lateral load tests, including final loads and displacements, is presented in Table 7.1. As explained previously, the initial tests at Edmond achieved limited displacement, so they were repeated. The repeated tests achieved greater displacement. The Minco tests were terminated after the test shaft contacted the isolation casing. A photograph of a test shaft in contact with the isolation casing is shown in Figure 7.16.

Table 7.1 – Summary of field observations from lateral load tests.

Test Pair	Test Date	Number of Load Increments	Maximum Load (kips)	Maximum Displacement (in.)	Notes
Edmond T1-T2	10/29/2021	7	410	0.5 (T1) 0.5 (T2)	Terminated when T1 collar and beam began to lift significantly
Edmond T3-T4	10/28/2021	9	468	0.5 (T3) 0.8 (T4)	1.5-hour delay in test when inverter blew fuse; hydraulic system governor limited load application.
Edmond T1-T2 Retest	8/11/2022	11	613	2 (T1) 2.5 (T2)	
Edmond T3-T4 Retest	8/10/2022	19	672	3.5 (T3) 1.5 (T4)	Terminated when additional load could not be maintained due to test shaft displacement.
Minco T1-T3	11/2/2021	19	395	8 (T1) 8 (T3)	Both test shafts made contact with the isolation casing during application of the 220-kip load. (190 kips was the last load without contacting isolation casing.)
Minco T2-T4	10/31/2021	8	220	5 (T2) 6.5 (T4)	Both test shafts made contact with the isolation casing during application of the 190-kip load. (160 kips was the last load without contacting isolation casing.)

Figure 7.16 – Minco T1 in contact with isolation casing near the end of testing.

7.5 LATERAL LOAD-DISPLACEMENT RESPONSE

Displacement of the top of each shaft was measured with two LVDTs, one above the other, and with one dial gage. In addition, ShapeArray measurements provided a fourth measure of the displacement of the top of the shaft (using the displacement of the top joint of the ShapeArray). The total load applied to the shaft, which was interpreted from the pressure gage on the hydraulic pump, is plotted versus each of the measures of displacement of the top of the shaft in Figure 7.17 (Edmond T1-T2), Figure 7.18 (Edmond T3-T4), Figure 7.19 (Minco T1-T3), and Figure 7.20 (Minco T2-T4). Each of the four figures represents results from one paired test.

The shape of the load-displacement curves at Edmond suggests test shafts T1, T2, and T3 were at ultimate conditions, whereas T4 may or may not have reached ultimate conditions. The observation of ultimate conditions from the load-displacement curves is consistent with observations during performance of the tests. The shafts reached ultimate conditions at between 2 and 4 inches of displacement and applied loads between 600 and 700 kips.

Load-displacement curves at Minco are more difficult to interpret, likely because of the long stick-up of the shafts above the top of rock. Before the end of all tests, each test shaft had contacted the isolation casing, which results in a stiffening of the load-displacement response that is apparent in all of the Minco load-displacement curves, as called out in the figures. In addition to the stiffening, contact with the isolation casing greatly complicates the shaft response by introducing an uncertain reaction force from the isolation casing. The magnitude of the reaction force is uncertain, and its presence is difficult to model with conventional p-y techniques. Contact with the isolation casing generally happened at around 200 kips of applied load and with displacement of about 4 to 7 inches. For all four test shafts, there appears to be some softening of the load-displacement curve prior to contact with the isolation casing, but it is difficult to say for certain whether ultimate conditions were achieved. The interpretation of Chapter 8 investigates this further.

Finally, it is noteworthy that the displacement measuring system appears to be reliable. The independent measures of displacement are generally consistent with one another, but with slight differences that are consistent with rotation of the shaft, i.e., greatest displacement at the top joint of the ShapeArray; slightly greater displacement of the top LVDT compared with the bottom LVDT. The test of Edmond T1-T2 is an exception to these trends; the test setup resulted in dial gage and LVDT placement near the top of the shaft, resulting in ShapeArray displacement that is similar to LVDT and dial gage values. Also, at the end of the test for two shafts, Minco T1 and T2, less displacement is recorded for the top LVDT than the bottom LVDT. This is likely a result of displacement “lost” during shifting of the reference beams necessary to accommodate large displacements of the Minco shafts.

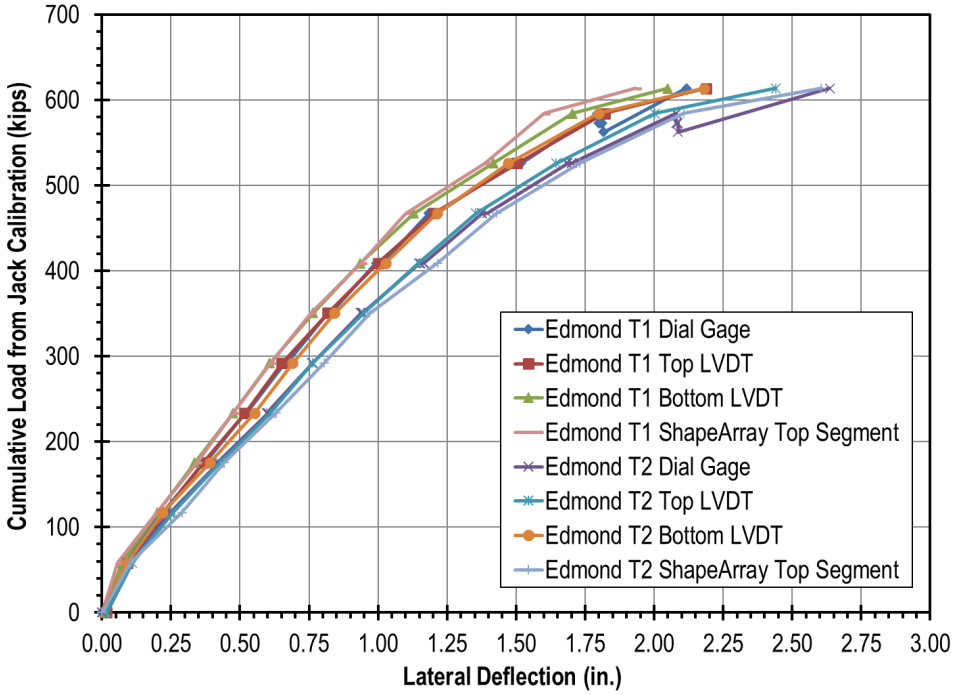

Figure 7.17 – Load-displacement curves for retest of Edmond shafts T1 and T2.

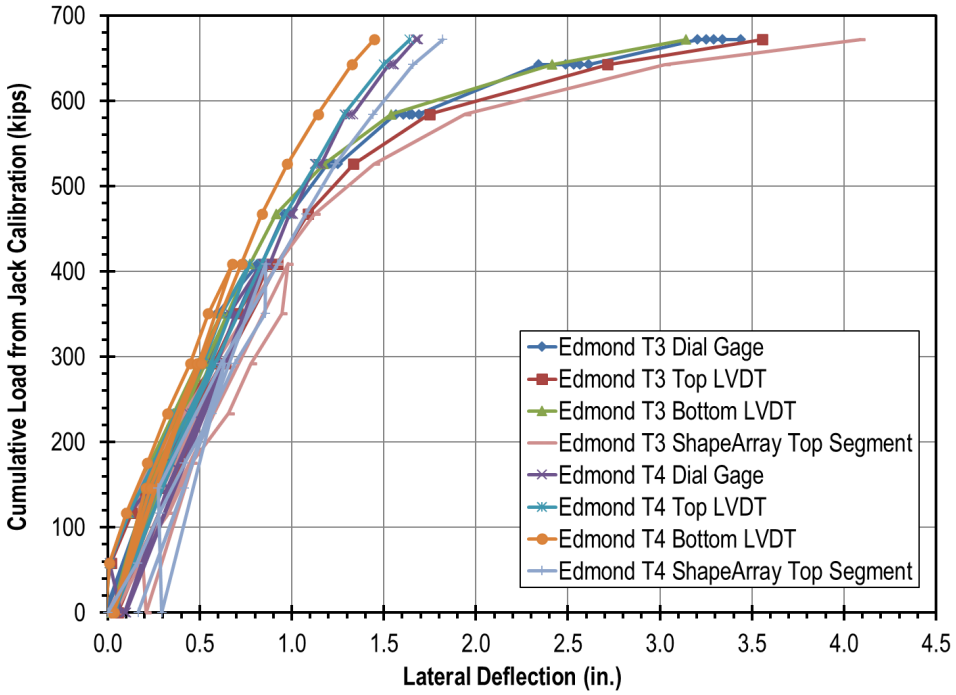

Figure 7.18 – Load-displacement curves for retest of Edmond shafts T3 and T4.

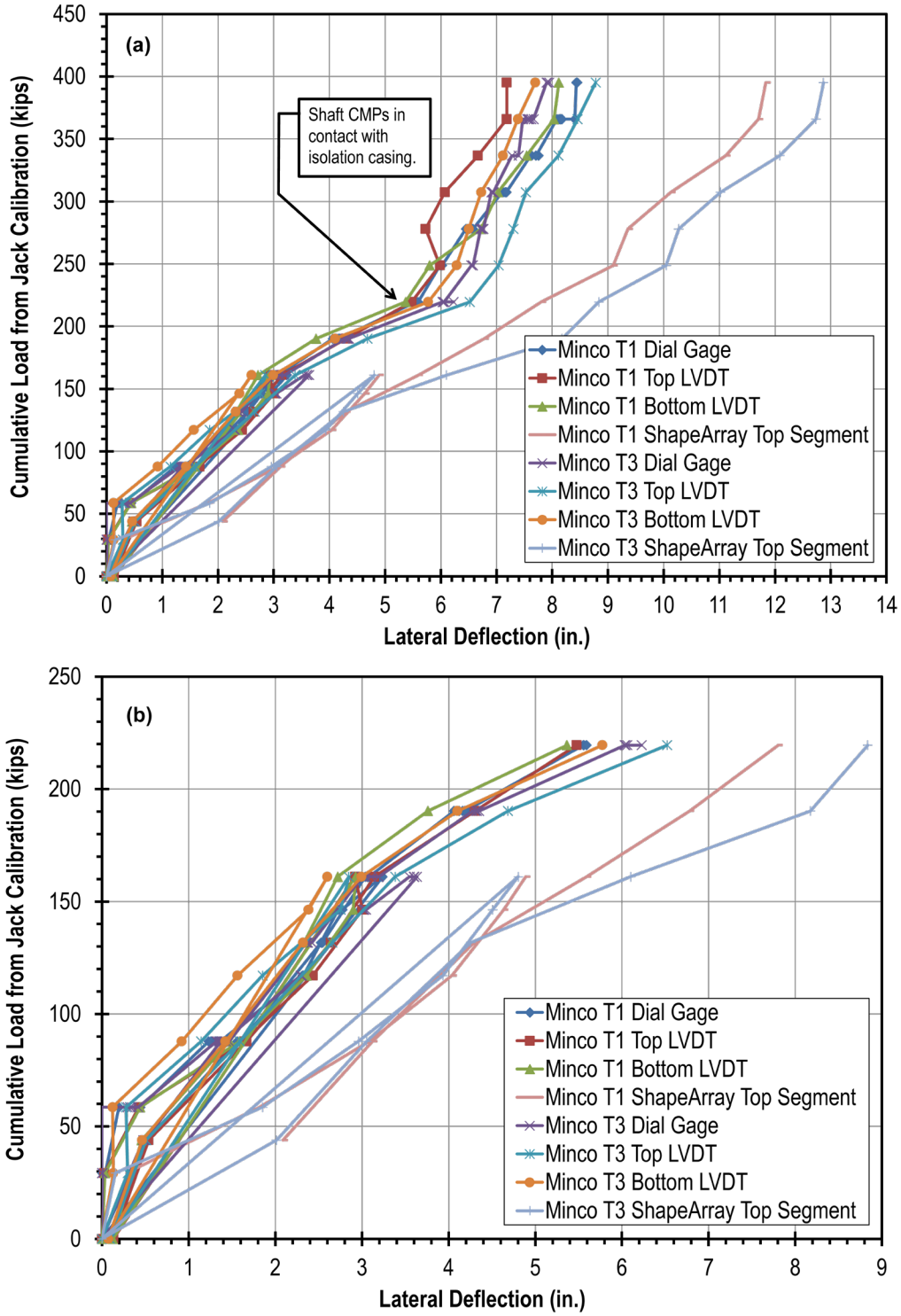

Figure 7.19 – Load-displacement curves for test of Minco shafts T1 and T3: (a) full test and (b) without load steps after shaft was clearly in contact with casing.

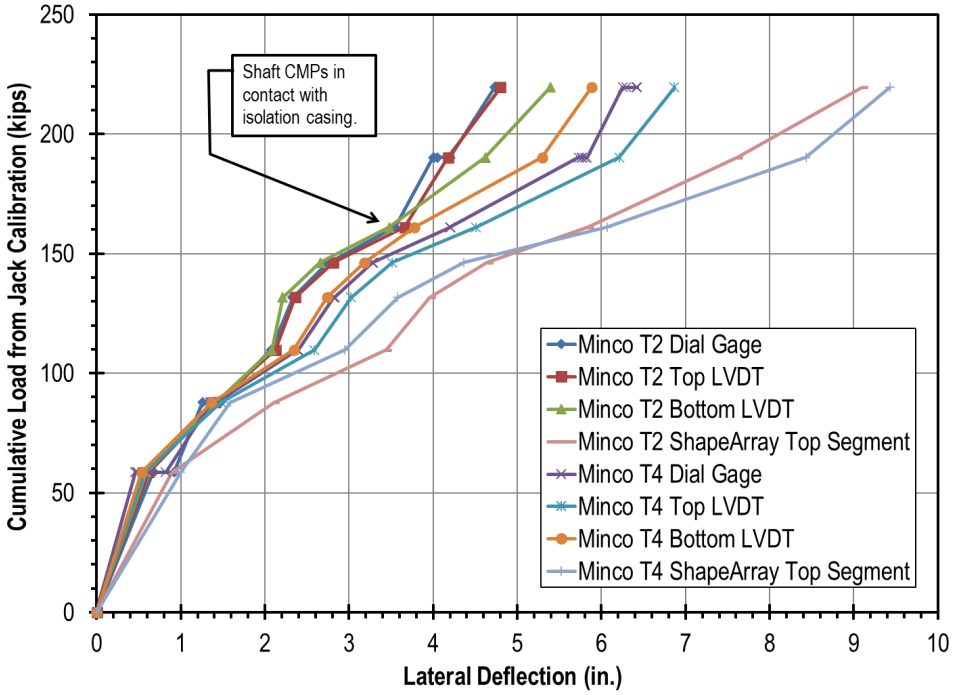

Figure 7.20 – Load-displacement curves for test of Minco shafts T2 and T4.

7.6 DISPLACEMENT PROFILES FROM SHAPEARRAY INCLINOMETERS

The ShapeArray inclinometers used during testing consist of a chain of 30 segments, each 500 mm (19.7 in.) in length. Position data for each joint between segments were recorded by the ShapeArray software in three dimensions, with the cross section of the shaft defined on the horizontal x and y axes and the vertical profile of the shaft on the z axis. Transverse displacement values at the end of each load increment were calculated from the differential movement in the x and y directions:

$$\delta_i = \sqrt{(x_i - x_{i0})^2 + (y_i - y_{i0})^2} \cdot \cos\left(\theta_{exp} - \theta_{obs}\right) \qquad (7.1)$$

where δ_i is the total transverse displacement of the i^{th} joint of the ShapeArray, x_i is the position of the i^{th} joint along the x-axis, x_{i0} is the initial (zero load) position of the i^{th} joint along the x-axis, y_i is the position of the i^{th} joint along the y-axis, and y_{i0} is the initial (zero load) position of the i^{th} joint along the y-axis, all in consistent units of length. The variable θ_{exp} in Equation 7.1 is the expected direction of movement (toward the opposite shaft) while θ_{obs} is the observed direction of movement. The first term of Equation 7.1 calculates the magnitude of total movement in the x-y plane. The second term projects the magnitude of total movement onto the plane of expected movement, which is toward the reaction shaft (i.e., the opposing shaft of the pair). The second term is necessary to capture the potential for negative movement (i.e., movement away from the reaction shaft) within the rock socket. The value of θ_{exp} was determined based on the observed direction of the top of the shaft near the end of testing. For most shafts, segments, and load steps, $\theta_{obs} \approx \theta_{exp}$, indicating movement was toward the reaction shaft and resulting in a value of $\cos\left(\theta_{exp} - \theta_{obs}\right)$ very near 1.0.

Profiles of displacement with depth for each load step were calculated according to Equation 7.1 for each shaft. The bottom of the ShapeArray ($i = 0$) is assumed to be stationary throughout the test, which is a reasonable assumption based on the results presented below. For most shafts, the full length of the ShapeArray could not be inserted in the casing. Segments above the top of shaft were neglected for development of the shaft displacement profiles. The resulting profiles of displacement are included in Appendix B. Each page of Appendix B presents results from one test shaft; the leftmost plot is the ShapeArray displacement profile.

For example, ShapeArray displacement profiles for the retest of Edmond T3 and T4 are shown in Figure 7.21. The figure includes one plot for T3 and one for T4. Each plot includes multiple lines, with each representing the displacement profile at the end of a different load step. As one would expect, the lines indicate greater displacement for greater loads. The results indicate greater displacement in Edmond T3 than Edmond T4, which is consistent with the load-displacement curves shown in Figure 7.18. The shape of all displacement profiles indicates displacement is greatest at the top of shaft, decreasing linearly with depth inside the isolation casing, and decreasing quickly to near zero within about 3 to 4 ft below the top of rock.

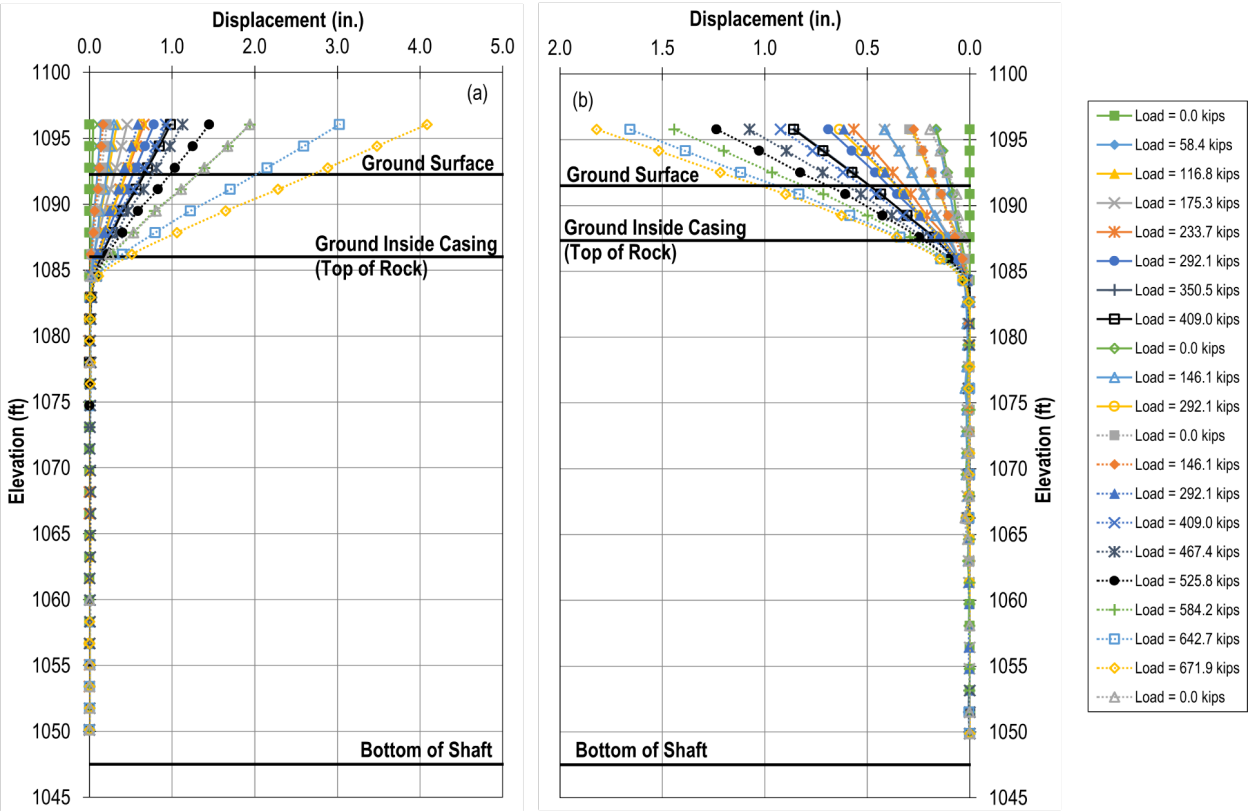

Figure 7.21 – ShapeArray displacement profiles for retest of Edmond shafts (a) T3 and (b) T4.

7.7 INTERPRETATION OF BENDING MOMENTS

Interpretation of bending moments from measurements of strain (via strain gages) and displacement (via ShapeArray) is a nontrivial exercise, primarily because the bending stiffness, EI, is nonlinear and greatly influenced by concrete cracking, which is difficult to predict. The procedure used here is to predict values of bending stiffness along the length of the shaft as a function of the bending curvature, which was calculated from measurements of strain for the strain gage interpretation and displacement for the ShapeArray interpretation. Values for bending stiffness as a function of curvature were computed using Ensoft LPILE v2022. The predicted values of bending stiffness were used to calculate bending moment profiles from ShapeArray data and from strain gage data. Each of these steps is described in more detail in the following paragraphs.

The displacement profiles interpreted from the ShapeArray data were differentiated using the central difference operator to calculate profiles of cross-sectional rotation of the shaft:

$$\theta_i = \frac{d\delta}{dz} \approx \tan^{-1}\left(\frac{\delta_{i+1}-\delta_{i-1}}{2L}\right) \tag{7.2}$$

where θ_i is the cross-sectional rotation of the i^{th} segment of the ShapeArray in radians and L is the ShapeArray segment length (500 mm = 19.7 in.). Profiles of cross-sectional rotation are also included in Appendix B, with rotation plotted just to the right of displacement for each shaft.

The rotation profiles were then differentiated, again using the central difference operator, to calculate profiles of bending curvature of the shaft:

$$\phi_i = \frac{1}{\rho_i} = \frac{d^2\delta}{dz^2} = \frac{d\theta}{dz} \approx \frac{\theta_{i+1}-\theta_{i-1}}{2L} \tag{7.3}$$

where ϕ_i is the bending curvature of the i^{th} segment of the ShapeArray in radians per unit length, ρ_i is the radius of curvature of the i^{th} segment of the ShapeArray in consistent units of length, and L is the ShapeArray segment length (500 mm = 19.7 in.). The values of bending curvature from differentiation of ShapeArray displacements (Equation 7.3) were used to estimate EI for interpretation of bending moments from ShapeArray data. For the separate interpretation of bending moment from strain gage data, bending curvature was estimated as the slope of the strain profile across the shaft cross-section. For depths with two strain gages, the slope is the difference in strain between the two gages divided by the distance between gages (i.e., the reinforcing cage diameter). For depths with four strain gages, strain was plotted versus cross-sectional location and least-squares regression was used to compute the slope.

For interpretation of bending moment from ShapeArrays and from strain gages, LPILE was used to estimate EI along the length of the shaft as a function of the bending curvature. The routine employed by LPILE is documented in the program's technical manual (Isenhower & Wang, 2011). In summary, LPILE iterates the location of the neutral axis until force equilibrium is satisfied, accounting for concrete cracking.

Cracking of the concrete is predicted as a function of the compressive strength of the concrete, which was estimated from compression tests performed on cylinders cast for each shaft. LPILE also accounts for yielding of the steel casing (if present) and longitudinal reinforcement.

The shaft bending stiffness predicted as a function of the bending curvature is shown in Figure 7.22 for the Minco test shafts. Four lines are included on the plot, each representing the EI-ϕ relationship for a different section of shaft:

- CMP casing, single bar bundles of No. 11 rebar (top)
- CMP casing, double bar bundles of No. 11 rebar (upper middle)
- No CMP casing, double bar bundles of No. 11 rebar (lower middle)
- No CMP casing, single bar bundles of No. 11 rebar (bottom)

The same four curves are applied for all shafts at Minco, but at different elevations depending on the length of casing and reinforcing cage sections. For all four sections, the bending stiffness decreases abruptly at small values of curvature, which corresponds to initial cracking of the concrete. After the concrete cracks, the decrease in stiffness is more gradual as the steel yields.

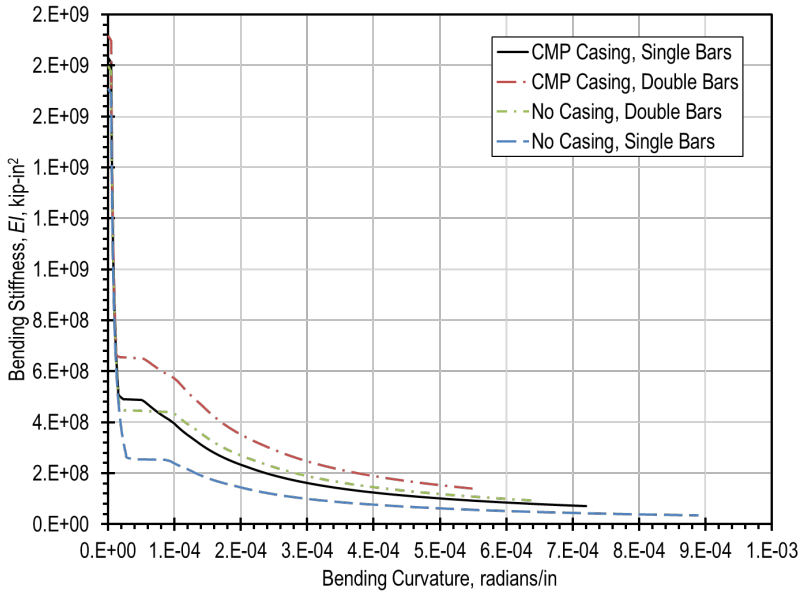

Figure 7.22 – Bending stiffness curve for Minco test shafts.

The EI-ϕ relationships shown in Figure 7.22 are not equal to those predicted by default using LPILE with the shaft geometry and material properties. The default EI-ϕ relationships are not used because for most of the test shafts, LPILE's structural model of the shaft does not converge for the maximum applied moment during testing. Instead, default values from LPILE were modified to increase the shaft bending moment capacity. The increase was achieved using user-input EI-M values. An example EI-M curve is shown in Figure 7.23. For uncracked concrete, the user-input model is equivalent to the default values predicted by LPILE. For cracked sections, the moment values were increased by a factor of 1.52 at Edmond and 1.4 at Minco. The factor

values are the minimum values that result in model convergence at the greatest applied moment. For both sites, the same factor was applied to all shafts.

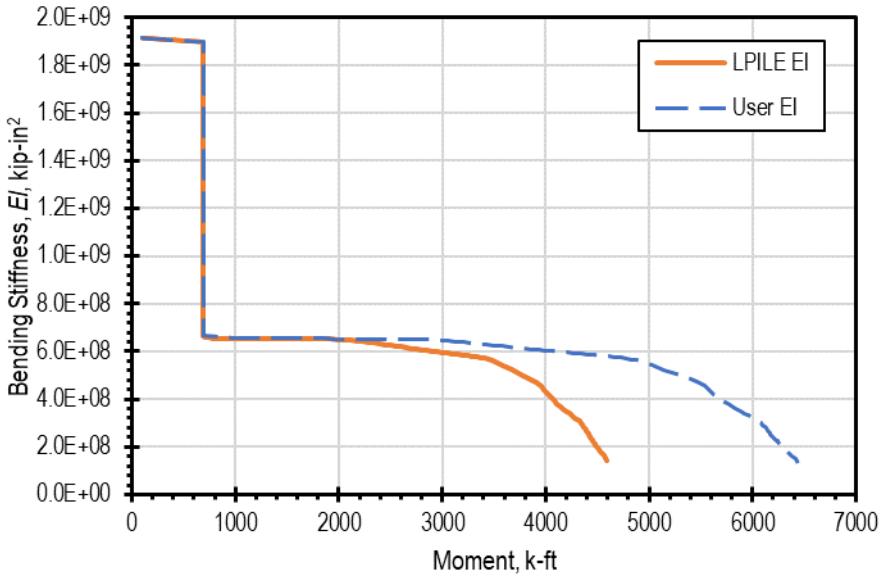

Figure 7.23 – Example user-input EI-M curve for Minco.

The estimated bending stiffness from LPILE was used to calculate two profiles of bending moment along the length of the shaft: one from ShapeArray measurements and another from strain gage measurements. Bending moment was calculated from ShapeArray measurements as:

$$M_i = \phi_i \cdot EI_i \tag{7.4}$$

where M_i is the bending moment of the i^{th} segment of the ShapeArray and EI_i is the shaft bending stiffness at the i^{th} segment of the ShapeArray. Bending moment from strain gage measurements was calculated as:

$$M_j = \phi_j \cdot EI_j \tag{7.5}$$

where M_j is the bending moment at the level of the j^{th} strain gage, ϕ_j is the bending curvature interpreted from the j^{th} set of strain gages, and EI_j is the shaft bending stiffness at the j^{th} strain gage. For all calculations, the bending stiffness at a particular depth was limited to its minimum historic value if the LPILE analysis indicated concrete cracking had ever occurred at that depth. For example, if the curvature at a depth of 10 feet was great enough to initiate concrete cracking for an applied lateral load of 100 kips, the bending stiffness used to calculate the bending moment for subsequent loads would be limited to the maximum value of the stiffness calculated for the 100-kip load, even if the bending curvature at a subsequent load was less than it had been at a load of 100 kips. This reasoning was extended to the shafts at Edmond that were tested twice.

7.8 OBSERVED BENDING MOMENT PROFILES

The full set of drilled shaft lateral load test results are presented in Appendix B. Each page of the appendix presents results for a different test shaft. Four profiles are shown on each page: displacement (left), rotation (middle left), bending moment from ShapeArray (middle right), and bending moment from strain gages (right). Example bending moment results for each site are presented in this section, with Figure 7.24 showing bending moment profile for Edmond T2 and Figure 7.25 showing bending moment profiles for Minco T1. Each figure is a plot of bending moment on the horizontal axis versus elevation on the vertical axis. Multiple lines are shown:

- A series of lines in color representing bending moments from strain gages at the end of various load increments;
- A single solid black line with open diamonds representing bending moments from the ShapeArray at the end of the maximum load increment;
- A dashed black line representing the applied moment in the free length of the shaft (above the isolation casing) at the maximum applied load; and
- Horizontal lines indicating the elevations of the top of shaft, ground within the isolation casing (top of rock), and bottom of shaft.

The shapes of the interpreted bending moment profiles are all consistent with expectations for the lateral load test setup, i.e., for an applied horizontal load atop a shaft cantilevered into rock. In addition, the magnitude of the interpreted bending moments from ShapeArray data are reasonably close to the applied moments in the cantilever sections, although the use of custom EI-M curves as described in the previous section makes this observation unsurprising. (No strain gages are present in the cantilever sections.) The progression of strain gage bending moments for increasing loads indicates the shape of the bending moment profile was consistent throughout testing, with increasing observed moments for increasing applied loads. Similar progression is observed in the ShapeArray bending moments (Appendix B).

Comparison of bending moments from strain gage and ShapeArray data indicates similar values for half the shafts (Edmond T2 and T3; Minco T1 and T3). For the others, ShapeArray bending moments are greater than strain gage moments by a factor of approximately 2. The exception is Minco T4, where one of the top-level strain gages was not functional during lateral load testing. Comparison of bending moments between the two measurement systems is challenging in this application, with only one level of strain gages present in the zone with significant bending moments. In addition, the gages subjected to bending are located just below the top of rock, where moments are diminishing significantly over short distances. The sharp decrease in bending moments further complicates the comparison. Nevertheless, the strain gage bending moments provide support for the bending moments interpreted from ShapeArray data, which offers the benefit of significantly greater spatial resolution.

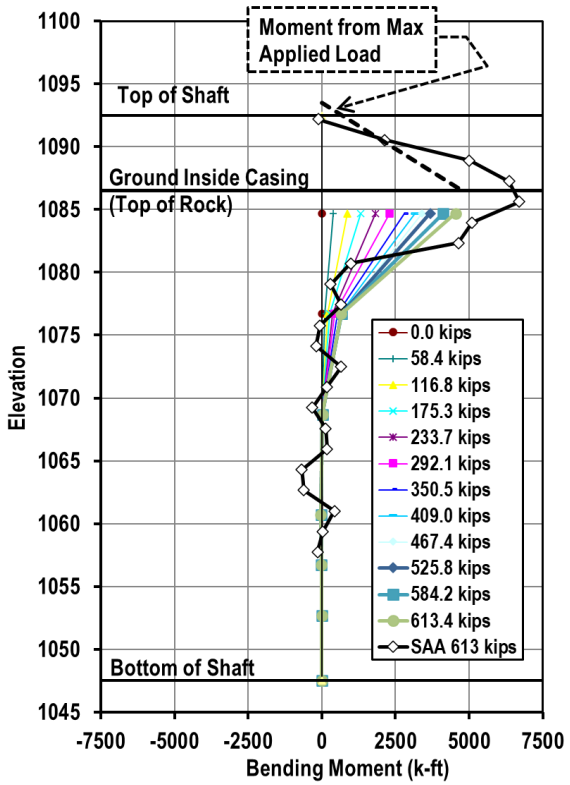

Figure 7.24 – Bending moment profile for Edmond T2.

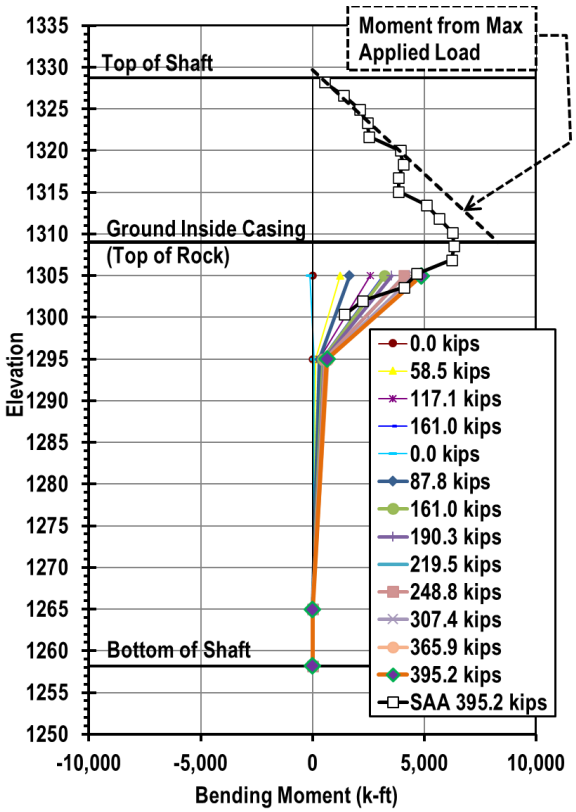

Figure 7.25 – Bending moment profile for Minco T1.

Chapter 8 - Analysis and Recommendations for Lateral Design

Analysis of the lateral load test results presented in the previous chapter consisted of three tasks: first, calibrating p-y values to the drilled shaft response observed for each loading increment; second, characterizing the collection of calibrated p-y data points resulting from the first task; and third, developing a p-y model for use in future applications. Details of each task are presented in this chapter. First, an introduction to the p-y method is presented; next, each of the three tasks is described with example results presented; finally, the proposed model is compared with existing models that are commonly applied to drilled shafts in shale and sandstone.

8.1 p-y METHOD

Interpretation of the lateral load test measurements employs the "p-y method" (e.g., Reese et al., 2006; Isenhower and Wang, 2011) to predict the response of a drilled shaft to lateral loading. The p-y method involves modeling the foundation element using beam elements and the surrounding soil or rock with a series of nonlinear springs as shown in Figure 8.1. Each spring is governed by a p-y curve, where p is the soil resistance on a unit length of the shaft (force/length) and y is the relative lateral deflection between the soil and the shaft (length). An example p-y curve is shown in Figure 8.2. An initial straight-line portion is connected by a curve to a final straight-line portion defined by the ultimate lateral resistance, p_{ult}.

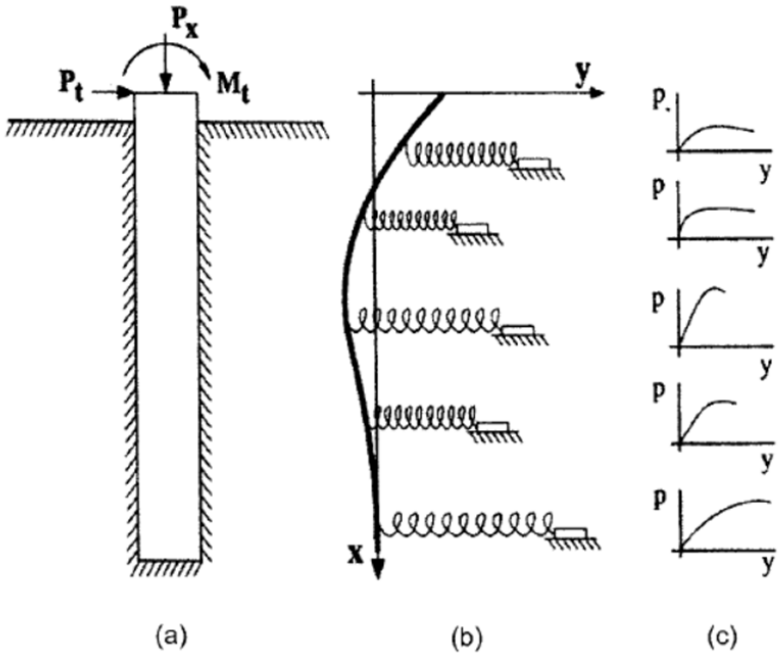

Figure 8.1 – Schematic representation of the p-y method: (a) deep foundation subjected to lateral loading, (b) soil modeled as a series of springs, and (c) p-y curves governing spring stiffness (Reese et al., 2006).

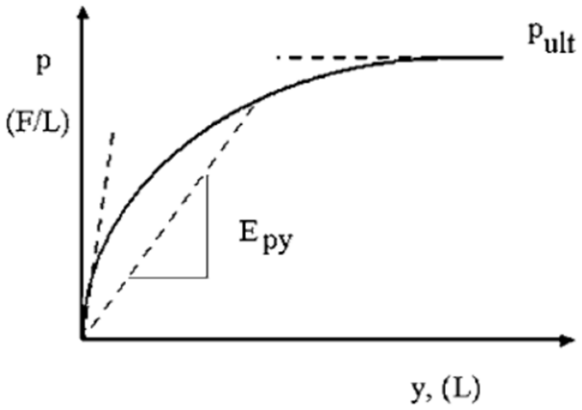

Figure 8.2 – Conceptual p-y curve (Reese et al., 2006).

8.2 CALIBRATION OF p-y CURVES

Calibration of p-y curves consistent with the observed shaft deflection is described in this section. First, the calibration methodology is explained, prior to presenting results of the calibration.

8.2.1 Methodology for Calibrating p-y Values to Observed Measurements

Calibration was performed using Ensoft L-PILE (v2022), a software program that analyzes laterally loaded foundations according to the p-y method. The mechanism for achieving calibration is the p-multiplier, an analytical tool that effectively scales the p-axis of the p-y curve. Examples of the effect of p-multipliers are shown in the p-y curves of Figure 8.3.

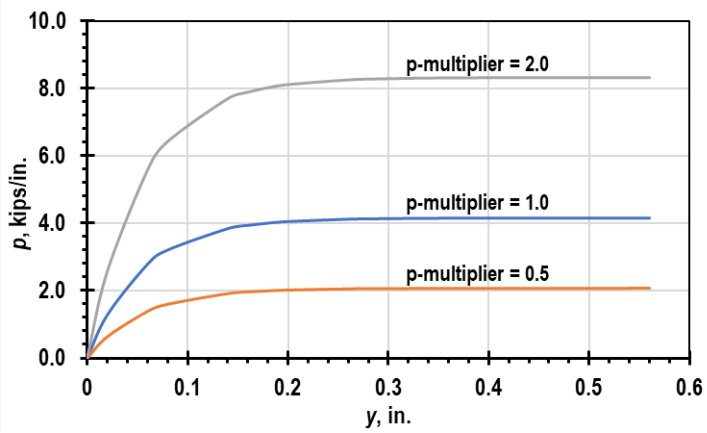

Figure 8.3 – Effect of p-multipliers.

In the calibration procedure, the p-multiplier was varied to produce the best fit of the observed shaft displacement profile data from ShapeArrays. The fit was evaluated using the square root of the sum of squared errors, $\sqrt{SSE}$, with smaller values of $\sqrt{SSE}$ interpreted as indicating better fit than larger values:

$$\sqrt{SSE} = \sqrt{\sum_{i=1}^{n}\left(y_{observed-i} - y_{predicted-i}\right)^2} \quad (8.1)$$

where n is the number of ShapeArray nodes used in calibration, $y_{observed-i}$ is the lateral displacement observed at i^{th} ShapeArray node, and $y_{predicted-i}$ is the lateral displacement predicted by the model at the i^{th} ShapeArray node.

The calibration procedure included the following steps:

1. Create an L-PILE model of the test drilled shaft. The structural component of each model is consistent with the discussion of EI in Section 7.3, including the use of different EI models along the shaft length to reflect changes in the casing and reinforcing cage, as well accounting for the effect of concrete cracking and steel yielding as bending moments increase. The geological component of each model is based on modeling the rock with the L-PILE stiff clay model as explained in the notes below these procedure steps. One value of undrained shear strength consistent with the uniaxial compressive strength values from the top of rock at each site was used for the base model (i.e., p-multiplier of unity).
2. Evaluate the L-PILE model for an initial load step using a p-multiplier of unity. Calculate $\sqrt{SSE}$ according to Equation 8.1.
3. Repeat Step 2 for a range of p-multipliers. Plot SSE versus p-multiplier and identify the value of p-multiplier that corresponds to the minimum value of $\sqrt{SSE}$. If necessary to better characterize the minimum $\sqrt{SSE}$ value, repeat Step 3 for additional values of p-multiplier. An example plot of $\sqrt{SSE}$ versus p-multiplier is shown in Figure 8.4. For the example in the figure, the calibrated p-multiplier is 1.7.

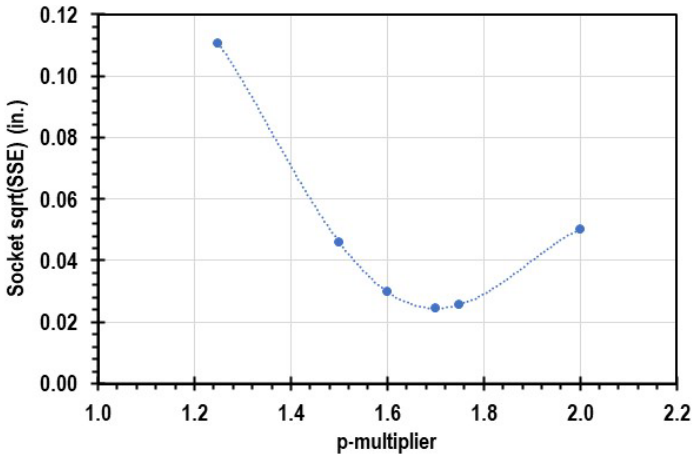

Figure 8.4 – Example plot of $\sqrt{SSE}$ versus p-multiplier (for Minco T2 at 161 kips applied load).

4. At each node included in the calibration (see notes below), a single p-y point results from the work of Step 3. The values of both p and y are from the L-PILE results with the value of p-multiplier that minimizes SSE. The y value from L-PILE is generally consistent with the value from the observation at the ShapeArray node, as can be seen from the results of the calibration presented below and in Appendix C.

5. Repeat Steps 2 through 4 for additional load steps. Each analysis produces an additional p-y data point for each node (depth). Continue repeating until a p-y curve has been sufficiently defined for each node. (Some intermediate load steps are not included.)
6. Repeat Steps 1 through 5 for all test shafts.

Completion of the calibration procedure outlined above results in one p-y curve per ShapeArray node, per shaft. Interpretable displacements were achieved in the top three nodes for each shaft, which corresponds to a length of approximately 5 ft. Accordingly, 24 p-y curves were interpreted during the calibration process (three for each of four test shafts at both sites).

Several other comments regarding the calibration procedure are noteworthy:

- Results from comprehensive analysis of the MoDOT test program results (Uong, 2018) indicate the effect of the initial p-y model on the resulting calibrated p-y model is limited. The results in Uong include similar p-y calibrations using a stiff clay model as the initial model compared to using an exponential model (as presented later in this chapter) as the initial model. Uong did find slightly greater p-values when a linear model is used as the initial model, but a linear model is likely unrealistic for large values of y, and the difference between using the linear model and the others was relatively small.
- The L-PILE model is created with approximately 500 nodes, which is the maximum permitted in L-PILE. A slightly smaller number was used in order to produce L-PILE nodes at the precise depths corresponding to ShapeArray nodes based on test records.
- The same value of p-multiplier was used along the entire length of the shaft in order to constrain the solution. While varying p-multipliers with depth would produce a better fit, the solution would not be unique.
- SSE was computed using only the nodes near the top of rock where non-negligible displacements were observed. Nodes in the shaft above the rock (i.e., in the free length of the shaft) were neglected because displacements in this region tend to be dominated by the structural model, and because the level of displacement is so much greater than within the rock that SSE tends to be uninfluenced by the portion of the shaft within the rock if the free length is considered. Nodes below the level of significant displacement are considered noise.
- Loading increments in which the permanent CMP casing was in contact with the outer isolation casing were not included in the calibration. There is no realistic way to model the resistance provided by the isolation casing and surrounding soil without introducing additional uncertainties that would greatly influence the calibration. The isolation casing interference occurred only at the end of load tests at the Minco site.

Finally, note that an alternative calibration procedure could be developed to optimize L-PILE output to fit the observed strain gage moments. Such an approach was not

pursued for two reasons. First, the ShapeArray data has better spatial resolution. For many load increments there is only one level of strain gages indicating measurable bending moments. Second, interpretation of the strain gage data to produce bending moment values produces uncertainties (Section 7.3); no similar interpretation uncertainty is present in the ShapeArray displacement data. Although the bending moment data were not explicitly included in the calibration routine described above, strain gage bending moments were compared to bending moments predicted by L-PILE in evaluation of the calibration results, as presented below.

Results of the p-y calibration for each test shaft and load step increment are presented in Appendix C. Example results for one shaft loading increment are presented below. The collection of calibrated p-y curves for both sites follows the example results.

8.2.2 Profiles of Shaft Response

Example calibration results for one loading increment of one shaft, 161 kips on Minco T2, are shown in Figure 8.5 and Figure 8.6. Figure 8.5 shows plots of displacement versus depth, with the plot on the left including displacement for the top 35 ft of the shaft and the plot on the right including only displacement near the top of rock (i.e., the zone in which the calibration fit was evaluated as described in Section 8.2.1). The displacement plots indicate reasonably strong agreement between the observed ShapeArray data and the calibrated L-PILE displacements, although L-PILE displacements in the free length of the shaft (above rock) are notably less than observed. Comparison of the results in Figure 8.5 with the other calibration results presented in Appendix C indicates the example of 161 kips on Minco T2 is representative, with similar quality fits observed for other loads and other shafts. The observation of under-predicted displacements above rock is consistent across the calibrations, especially for the free length at Minco.

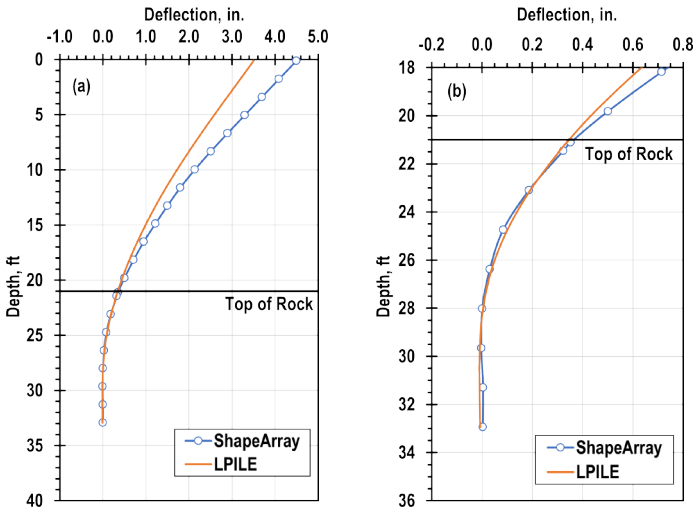

Figure 8.5 – Measured ShapeArray and calibrated L-PILE displacement values for Minco T2 at an applied load of 161 kips: (a) from top of shaft and (b) top of rock only.

Figure 8.6 shows a plot of bending moment versus depth. The plot displays reasonably close agreement between bending moments interpreted from strain gages and values predicted by the calibrated L-PILE model. Results from other calibrations (Appendix C) do not all indicate similarly close agreement, but the lack of multiple strain gage levels within the calibration zone makes such evaluations difficult.

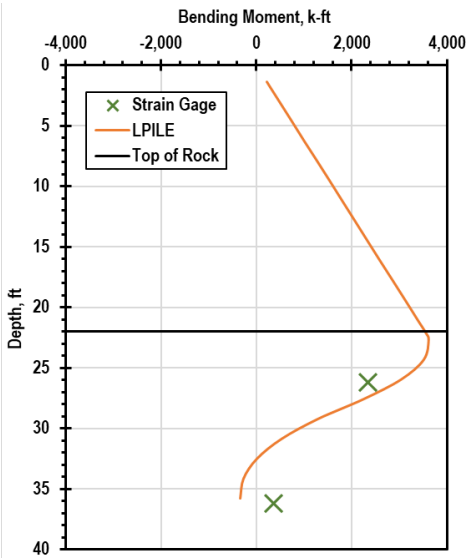

Figure 8.6 – Bending moments interpreted from strain gages and from calibrated L-PILE model for Minco T2 at an applied load of 161 kips.

8.2.3 Interpreted p-y Curves

As explained above, the p-y calibration process results in a p-y curve for each of three rock elevations (corresponding to ShapeArray node locations) per shaft. The resulting p-y curves are plotted in Figure 8.7 for Edmond and Figure 8.8 for Minco. The horizontal axis in both figures is identical, with values of y between 0 and 0.45 inch; the vertical axis is different, reflecting different values of p mobilized at each site. Each plot consists of three p-y curves for the top node in rock, three p-y curves for the middle node, and green p-y curves for the bottom node of the calibration. Different symbols are used to represent curves from each of the four test shafts at each site. Also shown in the plots are results of models commonly employed in L-PILE (stiff clay and weak rock) using inputs corresponding to site and shaft conditions. Comparison of the results with L-PILE models is discussed at the end of this chapter.

At Edmond, the calibrated p-y curves are remarkably consistent from shaft to shaft. For each elevation, the curves begin linearly, with a consistent slope among all four shafts. The initial portions of p-y curves calibrated at deeper nodes are stiffer (steeper p-y curve) than those at shallow nodes, an observation consistent with many published p-y models including the weak rock and stiff clay models used in L-PILE (Reese, et al., 2006). For shafts T1, T2, and T3, the final loading increments break from the linear portion toward a more horizontal slope, indicative of p_{ult} conditions. The curves for T4 are still linear at the final loading increment, but at smaller mobilized values of p than for

the other shafts. Perplexingly, the value of p at which the curves for T1, T2, and T3 appear to break toward p_{ult} conditions decreases with depth.

At Minco, the calibrated p-y curves are predominately linear, but with notable differences among the shafts. The p-y curves for T1 are linear from start to finish. In contrast, the final two points for each of the curves for T2 are suggestive of p_{ult} conditions; the same is true for T4, although the appearance of p_{ult} for T4 could be an artifact of the "hiccup" in the penultimate point. For T3, the curves follow an unusual, concave-up shape before breaking at the last loading increment calibrated. (Note each of the curves is terminated at the point at which the shaft made contact with the isolation casing.) As for Edmond, and consistent with literature, the stiffness increases with depth. The same perplexing trend of p_{ult} decreasing with depth is also observed at Minco.

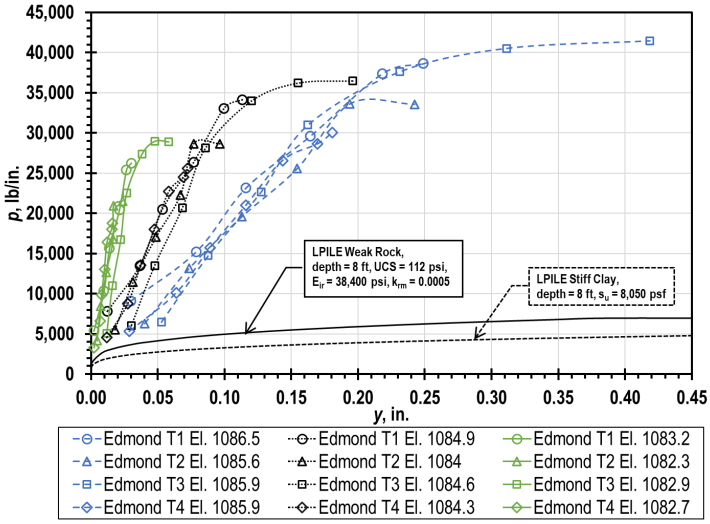

Figure 8.7 – Calibrated p-y curves for Edmond.

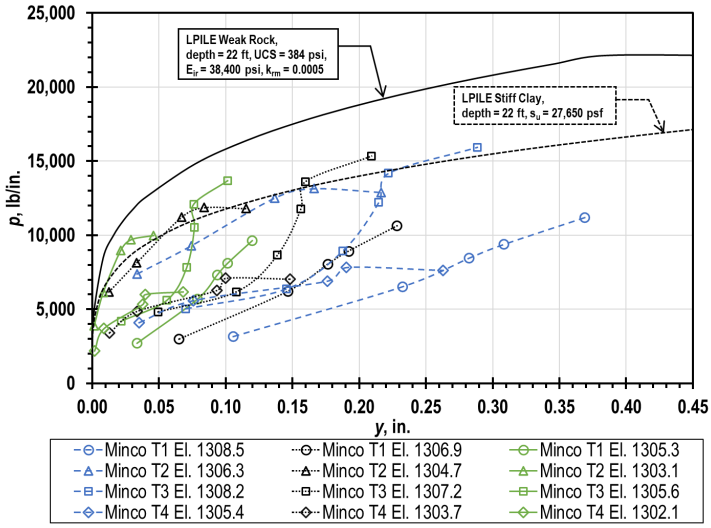

Figure 8.8 – Calibrated p-y curves for Minco.

8.3 CHARACTERIZATION OF CALIBRATED p-y VALUES

The p-y curves calibrated as described in the previous section were characterized by fitting curves of the same functional form to each curve. The functional form used, a scaled exponential function, is consistent with the approach used for the MoDOT lateral load test program (Uong, 2018).

8.3.1 General Form of Proposed p-y Model

The sets of p-y curves for each depth were fitted to a scaled exponential function shown in Equation 8.2. Uong (2018) presents an evaluation of several different functions fitted to p-y data from drilled shafts in shale and concluded the scaled exponential provides the best fit over a large range of observed displacements.

$$p = a\big(1 - \exp(-b * y)\big) \tag{8.2}$$

Another advantage of the exponential function is that its parameters are easily related to the more familiar terms p_{ult} and k_{py}, the initial slope of the p-y curve, as described by Equation 8.3 and Equation 8.4.

$$\begin{cases} p_{ult} = a \\ k_{py} = a * b \end{cases} \tag{8.3}$$

$$p = p_{ult}\left(1 - \exp\left(-\frac{k_{py}}{p_{ult}} * y\right)\right) \tag{8.4}$$

8.3.2 Fitted p-y Curves

One p-y curve conforming to Equation 8.4 was fit to each of the experimentally determined curves from the previous section (12 curves for each site). Uong (2018) presents an evaluation of different fitting approaches that included fitting one curve to all p-y data at a site, fitting one curve to data from all shafts at a particular depth, and fitting individual curves to each shaft-depth combination. The last approach, which is also used here, was found to provide the best relation between curve parameters (p_{ult} and k_{py}) and rock compressive strength. Relations with soil parameters are presented in the next section.

Values of the parameters p_{ult} and k_{py} were obtained using MATLAB's curve fitting tool to establish a best-fit to the calibrated p-y curves from the previous section. One constraint was imposed on the fit: values of p_{ult} were limited to the maximum value of p from the calibration, increased by a factor of 1.2. For evaluation purposes, additional curves were fit to the p-y calibrations using manually defined parameters: p_{ult} equal to the maximum value from the calibration and k_{py} based on calculation of the initial slope, with the points used in the slope calculation selected on a per-curve basis. For the shafts where p_{ult} was not achieved (Edmond T4, Minco T1 and T3), linear models

defined only by k_{py} were fit manually. (As explained in the next section, these shafts were also excluded from the p_{ult} versus compressive strength model.)

The resulting 24 p-y curves are presented in Appendix D. Examples are presented in Figure 8.9 for Edmond T1 at approximately 2 ft below the top of rock (the middle node) and in Figure 8.10 for Minco T1 at the same depth and node. The figures include the calibrated p-y data points (same points from Figure 8.7 and Figure 8.8), the MATLAB fit, and the curve based on manually defined parameters. Prediction intervals that bound values within which new observations are predicted to fall with 95 percent confidence are also shown for the MATLAB fit.

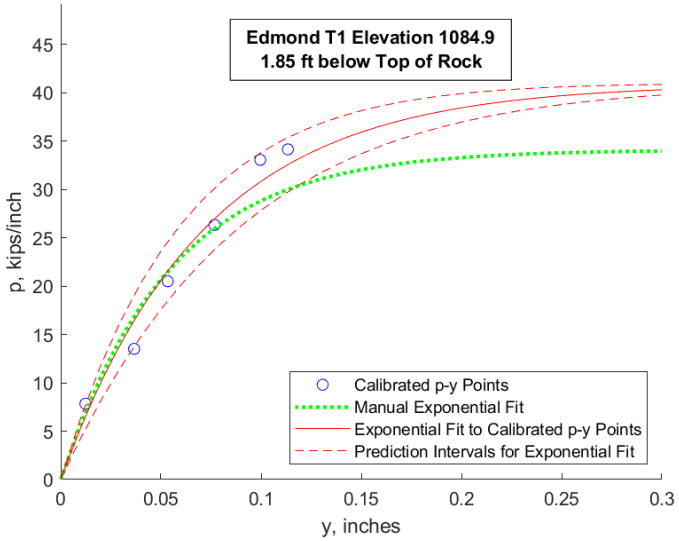

Figure 8.9 – Fitted p-y curve for Edmond T1, approximately 2 ft below the top of rock.

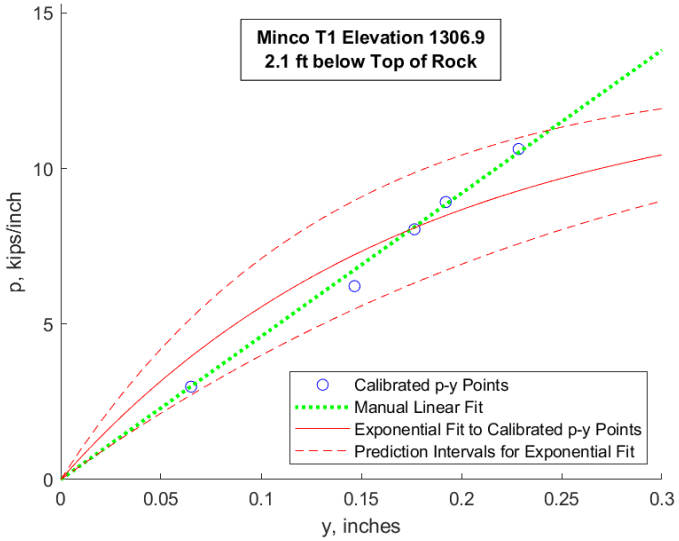

Figure 8.10 – Fitted p-y curve for Minco T1, approximately 2 ft below the top of rock.

In general, the scaled exponential model produces a good fit to the observed data. For the MATLAB fits, better fits are observed for the curves that achieved p_{ult} (e.g., Figure 8.9). As noted in the next section, curves that did not achieve p_{ult} (e.g., Figure 8.10) are excluded from the p_{ult} versus compressive strength model.

8.4 PROPOSED p-y MODEL FROM FITTED p-y CURVES

Models from the p-y curve characterization described in the previous section were used with rock compressive strength information from Chapter 3 to develop methods for predicting p_{ult} and k_{py} that can be applied to other shafts in shale and sandstone. The recommendations are based on models developed from the MoDOT load test program as presented in Uong (2018). The MoDOT model is used because there are only two test sites included in this program, and because the rock characteristics are generally similar for all of the MoDOT and ODOT sites: sedimentary rock with compressive strength between 5 and 100 ksf.

Parameters p_{ult} and k_{py} are plotted versus average compressive strength at the top of the rock layer in Figure 8.11 (p_{ult}) and Figure 8.12 (k_{py}). Both plots include the recommended model from Uong (2018), the data from Uong, and new data points for Edmond and Minco. Both plots also include results from a Kansas DOT study discussed in the next section.

The Uong models are based on a linear function for p_{ult} and an exponential function for the ratio of k_{py} to total overburden stress, as summarized in Equation 8.5 and Equation 8.6. Use of the ratio of k_{py}/σ_v rather than k_{py} is appropriate considering the consistent effect of depth observed in the collection of calibrated p-y curves.

$$p_{ult} = \frac{q_u}{6.5} + 1.8 \tag{8.5}$$

where p_{ult} is in kips per inch and q_u is in ksf and limited to be between 3 and 100 ksf.

$$\frac{k_{py}}{\sigma_v} = \exp\left(\frac{9.83 \cdot q_u - 201}{q_u + 31.1} + 11.9\right) \tag{8.6}$$

where k_{py} and q_u are in consistent units and q_u is again limited to be between 3 and 100 ksf.

For p_{ult}, results at Edmond are significantly greater than predicted by the Uong model for 16-ksf compressive strength. Since Edmond is the only site with sandstone bedrock, it is possible the sandstone provides greater ultimate lateral resistance than shale. The p_{ult} values for Minco are variable, but generally consistent with the Uong model.

For k_{py}, results at Edmond are consistent with the Uong model, but the Minco results suggest significantly less initial stiffness than predicted by the model. The Minco k_{py} values are believed to be an outlier. The Minco p-y curves are likely impacted by uncertainty in calibration inputs resulting from unknown concrete stiffness, changes in reinforcing cage stiffness with depth, and imprecision in the depth of the bottom of the

permanent CMP casing. Each of these effects is also likely exacerbated by the long unsupported lengths of the Minco shafts.

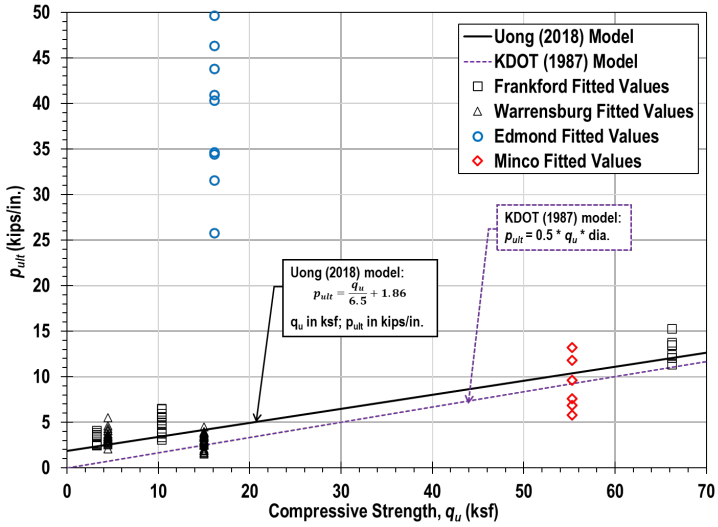

Figure 8.11 – Proposed relationship between p_{ult} and compressive strength.

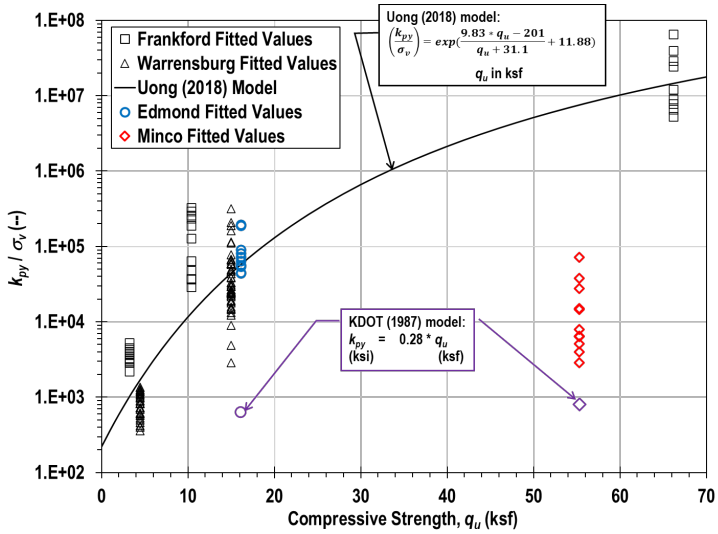

Figure 8.12 – Proposed relationship between k_{py} and compressive strength.

Based on the generally favorable comparison of the Minco and Edmond test results with MoDOT test results, the model represented by Equations 8.4, 8.5, and 8.6 is recommended for use in design of drilled shafts in shale and sandstone with q_u between 3 and 100 ksf.

More data, especially from material with q_u between 15 and 50 ksf, would likely improve the model. The recommended range for the models, q_u between 3 and 100 ksf, is representative of the materials for which p-y curves were developed, including shale at Minco and both MoDOT sites, sandstone at Edmond, and stiff clay at one MoDOT site. The models should not be applied outside the stated range of compressive strength.

It is important to note the model for p_{ult} does not include any effect of diameter. Because all of the test shafts at the ODOT sites are the same diameter, and a similar diameter to the MoDOT test shafts, isolating any effect of diameter in the results is not possible. Results in literature suggest diameter can have a significant effect on p_{ult}. Reese, et al. (2006) note a linear relationship between diameter and p_{ult} for deep foundations in clay, but perhaps no effect for deep foundations in sand. As discussed below, previous research for the Kansas DOT found a linear relationship between p_{ult} and diameter for small-diameter piles in shale and sandstone. Because the test shafts are on the small end of the range of diameters typically employed for transportation structures, use of the recommended model may be conservative for larger shafts.

8.5 COMPARISON OF PROPOSED MODEL WITH EXISTING MODELS

The p-y curves fitted from the test measurements and the model for p_{ult} and k_{py} are compared to published values in this section. First, p-y curves are presented for common L-PILE models; second, the relationships for p_{ult} and k_{py} are compared to results from the Kansas DOT study (Frantzen and Stratton, 1987).

8.5.1 Comparison with Common L-PILE Models

Drilled shafts in shale and sandstone are commonly modeled using L-PILE's stiff clay and weak rock models. As shown in Figure 8.7 (Edmond) and Figure 8.8 (Minco), p-y curves were generated in L-PILE using both the stiff clay model and the weak rock model, with input parameters corresponding to average rock strength and depth as well as test shaft geometry. At Edmond, the interpreted p-y curves represent significantly greater lateral resistance than would be predicted using either the stiff clay or weak rock model. Both L-PILE models predict similar resistance; the interpreted values from the p-y calibration are nearly an order of magnitude greater.

At Minco, the interpreted p-y curves are slightly less than the L-PILE model predictions. The greatest p-y values from the calibration are generally slightly greater than the stiff clay model, which is approximately 30 percent less than the weak rock model.

8.5.2 Comparison with KDOT's p-y Model for Sandstone and Sandy Shale

The Kansas Department of Transportation published a report (Frantzen and Stratton, 1987) that proposed p-y curves derived from a series of lateral load tests on 8-inch pipe piles installed in weak rock at four sites in the Kansas City area. Based on results for shallow depths (up to 2 ft), the authors recommended a p-y model with an initial linear region, a less steeply inclined linear transition region, and a constant ultimate region. The initial stiffness was defined as 80 times the undrained strength of the material (consistent units), and the ultimate resistance was defined as the diameter of the pile times the undrained strength (also consistent units). These recommendations are plotted with the proposed models from Uong (2018) in Figures 8.11 and 8.12.

The KDOT values of p_{ult} for a diameter of 4 ft (like the shafts at Edmond and Minco) are slightly less than those proposed in Equation 8.5, with a similar slope with respect to

material strength but no y-intercept. The initial stiffness, k_{py}, of the KDOT model is also significantly less than that proposed in Equation 8.6, as can be seen in Figure 8.12. Scale effects (8-in. piles for KDOT vs. 3- to 4-ft shafts for the MoDOT and ODOT shafts) may account for much of the observed difference.

[This page intentionally blank.]

Chapter 9 - Conclusions and Recommendations

Numerous conclusions and recommendations can be drawn from the research effort described in this report. Many such conclusions and recommendations are provided throughout the body of this report. This chapter summarizes the most significant and consequential conclusions and recommendations developed from the research program, especially focusing on those that are important to implementation.

9.1 GENERAL CONCLUSIONS

The completed load testing program was successful. The selected load test sites proved to be appropriate and effective for filling notable gaps in axial and lateral load test measurements for drilled shafts in weak rock that existed prior to the project. Axial load tests were generally loaded well beyond the rated capacity for the bi-directional loading devices used, which are the largest cells available for shafts with the diameter of the test shafts. The ultimate unit side resistance was mobilized along the entire length of the shaft for most test shafts. The ultimate unit tip resistance was not mobilized for load tests at the Edmond site, despite axial loads “maxing out” the bi-directional loading devices. Loading for test shafts at the Minco site was judged to be near failure in tip resistance. Collectively, the axial load tests conducted provide important Oklahoma-specific data that enabled informed evaluation of alternative design methods when combined with additional load tests from Oklahoma and surrounding states. More generally, interpretations of the axial load tests additionally contribute valuable data about the performance of drilled shafts in weak rock that, in turn, enabled broadly applicable conclusions and recommendations to be developed.

Lateral load tests were also successful. The applied loads produced significant displacement at the top of the shaft and the test set up allowed the applied lateral load to be effectively transferred to the weak rock strata located at depth. Interpretations of the lateral response of the test shafts contributed significantly to the relatively sparse collection of measurements of the lateral response for drilled shafts in weak rock.

9.2 CONCLUSIONS AND RECOMMENDATIONS FOR TIP RESISTANCE

Interpreted values of unit tip resistance from load tests at the Edmond and Minco sites dramatically exceed values determined for other load tests on drilled shafts in weak rock in Oklahoma and surrounding states despite the fact that failure in tip resistance was not achieved for many of the tests. The interpreted values of unit tip resistance from both sites are reasonably predicted using the fundamental design relation adopted by MoDOT for design based on Texas Cone Penetration Test (TCPT) penetration measurements. However, interpreted values of unit tip resistance from both sites tend to be considerably greater than predicted using the fundamental relations adopted by MoDOT for design based on compressive strength and equivalent Standard Penetration Test (SPT) N-values. The surprisingly large values of unit tip resistance from load tests at the Edmond site are easily explain by the fact that the test shafts at Edmond were founded in sandstone rather than argillaceous rock that is associated with all other load tests considered. The large values of unit tip resistance from load tests at the Minco site

are more difficult to explain since those shafts are founded in shale that is at least qualitatively similar to the weak rock for the other load tests that were considered.

Despite differences between interpreted unit tip resistance values from load tests at the Edmond and Minco sites and current MoDOT design procedures, evaluations described in Chapter 6 demonstrate that the fundamental design relations adopted by MoDOT are the most appropriate relations for design of drilled shafts in weak rock. Recommended design relations for ODOT are therefore similar to provisions currently adopted by MoDOT for design based on compressive strength and TCPT penetration, albeit with dramatically increased upper limits based on the load tests at the Edmond and Minco sites. A third relation for design based on equivalent SPT N-values is also recommended based on findings from Pierce (2013).

Prediction uncertainties associated with the recommended TCPT-based design relation and the compressive strength-based design relation are similar, and generally consistent with many other design methods for drilled shafts in different materials. The recommended TCPT-based design relation for unit tip resistance produces considerably greater values of nominal unit tip resistance than the current ODOT design method for all weak rock, with dramatic differences existing for TCPT penetration ($MTCP$) less than 2 inches per 100 blows. Associated resistance factors for the recommended TCPT-based design relation produce factored resistances that are much greater than current ODOT design practices for $MTCP$ less than 2 inches per 100 blows and similar to current ODOT practices for $MTCP$ greater than 2 inches per 100 blows. The recommended compressive strength-based design relation also produces considerably greater nominal and factored unit tip resistances than comparable design methods based on compressive strength.

The prediction uncertainty associated with the recommended SPT-based design relation is considerably greater than the prediction uncertainty for the recommended TCPT- and compressive strength-based design relations. The greater prediction uncertainty indicates that the SPT-based design relation is less reliable than the alternative recommended relations, which necessitates lower resistance factors. The SPT-based design relation produces nominal unit tip resistances that are similar to those estimated for a similar method developed for the Colorado Department of Transportation (CDOT). However, the low calibrated resistance factors for the recommended SPT-based method result in the method producing considerably lower factored values of unit tip resistance than the CDOT method.

Both the recommended TCPT-based design relation and the recommended compressive strength-based design relations for unit tip resistance are recommended for routine use by ODOT. The TCPT-based relation is likely to produce greater factored resistance among the two alternatives because the relation more closely predicts the considerable tip resistance observed in load tests at the Edmond and Minco test sites. The recommended SPT-base design relation for unit tip resistance can be used to design foundations with appropriate design reliability; however, the relation is likely to require considerably larger drilled shafts to satisfy design requirements and, therefore,

is not recommended for use unless the alternative methods cannot be used (e.g., if TCPT or compressive strength measurements are not available).

9.3 CONCLUSIONS AND RECOMMENDATIONS FOR SIDE RESISTANCE

Interpreted values of unit side resistance from load tests at the Edmond and Minco sites confirm previous observations that side resistance for drilled shafts in weak rock is highly variable. In contrast with observations regarding tip resistance, interpreted values of unit side resistance from these and other load tests in Oklahoma are generally consistent with interpreted values of unit side resistance from load tests in similar materials from surrounding states. Collectively, interpreted values of side resistance from load tests in Oklahoma and surrounding states are also consistent with both the trend and prediction uncertainty for design relations currently adopted by MoDOT for side resistance for drilled shafts in weak rock. These findings, in turn, support the recommendation to adopt current MoDOT design relations for unit side resistance in weak rock as described in Chapter 6.

The recommended design relations produce values of nominal unit side resistance that are lower than produced using current ODOT design procedures. Probabilistically calibrated resistance factors for the recommended design relations for unit side resistance are also lower than currently being used by ODOT as a result of the large prediction uncertainty associated with the recommended design relations. The magnitude of factored resistance for the recommended design relations is, therefore, considerably less than the factored unit side resistance being currently used by ODOT. Given that the recommended nominal side resistance is consistent with available measurements and the probabilistically calibrated resistance factors are those that are necessary to achieve the adopted target reliability, it is apparent that the target reliability of side resistance is not likely being achieved with current ODOT practices. Other factors (e.g., conservative loads, conservative tip resistance, conservative interpretation of design parameters) may potentially compensate for this practice.

It is not strictly possible to explicitly determine which of the three recommended design relations for unit side resistance will produce more efficient designs since there are no well-established relations among compressive strength, TCPT penetration, and equivalent SPT N-values. However, it is likely that all three methods will produce similar design efficiency given that all three relations were developed from many of the same load tests, that all three relations produce unbiased estimates for the nominal side resistance, and that the prediction uncertainty for the three relations are similar. Selection among the different methods is therefore a matter of preference.

9.4 CONCLUSIONS AND RECOMMENDATIONS FOR LATERAL LOADING

Calibrated p-y curves for the Edmond tests shafts indicate notable consistency in initial lateral stiffness values among all four test shafts with three of the four test shafts achieving p_{ult} conditions. Considerably greater variability was observed among test shafts at the Minco site, with two of four shafts likely achieving p_{ult} conditions.

Interpreted p-y curves for the Edmond test shafts indicate lateral resistance an order of magnitude greater than would be predicted using common LPILE models (stiff clay and weak rock) with the average compressive strength. Calibrated p_{ult} values for the Edmond test shafts are also significantly greater than predicted by the Uong (2018) model that was developed based on a similar load testing program. Calibrated k_{py} values for the Edmond test shafts are consistent with Uong's model.

In contrast, the calibrated p-y curves for the Minco test shafts indicate slightly lower resistance than predicted with common LPILE models using the average compressive strength. While calibrated p_{ult} values for the Minco test shafts are consistent with Uong's model, calibrated k_{py} values are considerably less.

Despite the conflicting evidence, evaluations based on the lateral load tests conducted suggest that analysis of laterally loaded shafts in weak rock in Oklahoma be based on the p-y model developed by Uong that is presented in Chapter 8. While imperfect, the Uong model predicts significantly greater resistance to lateral loading than the resistance predicted by an alternative model developed for the Kansas Department of Transportation by Frantzen and Stratton (1987) for slender deep foundations in shale.

Calibrated p-y curves for both sites demonstrate increasing initial stiffness with depth, a trend consistent with other published p-y curves. Perplexingly, the value of p_{ult} from the calibrations decreased with depth for the shafts that achieved p_{ult} conditions.

9.5 ADDITIONAL RECOMMENDATIONS

Deliberate consideration should be given to performing site- and project-specific axial load tests for projects where drilled shafts will be founded in weak rock, particularly for drilled shafts founded in sandstone and drilled shafts founded in argillaceous rock with compressive strength greater than 100 ksf. While project-specific load tests involve up-front costs, considerable overall cost savings can be anticipated for most projects because there is high likelihood that site-specific measurements of side and/or tip resistance may exceed the nominal resistances predicted using the recommended design relations. Additionally, a greater resistance factor can be used when site-specific load tests are performed, which will usually result in greater factored resistance and considerable construction cost savings. When possible, site-specific load tests should preferably be loaded to failure, or at least to applied loads that significantly exceed the calculated nominal resistance for the constructed shafts.

Once project-specific load tests are performed on a handful of projects, additional research should be conducted to compare measurements from the load tests with the recommended design relations provided in this report to evaluate whether updated relations are justified. Such efforts would be particularly valuable for drilled shafts in sandstone, where available measurements are extremely limited and suggest that the recommended relations may underestimate the likely magnitude of tip resistance.

Additional study of the performance of laterally loaded drilled shafts in weak rock is also needed. Such studies would particularly benefit from additional testing in weak rock with

compressive strength between 15 and 50 ksf. Alternative models for p_{ult} and k_{py} with parameters predicted as a function of TCPT penetration rather than compressive strength should also be developed and evaluated.

[This page intentionally blank.]

References

AASHTO (2012), *AASHTO LRFD Bridge Design Specification: Customary U.S. Units*, American Association of State Highway and Transportation Officials, 6th Edition with 2013 Interim Revisions.

Abu-Hejleh, N.M., M.W. O'Neill, D. Hanneman, and W.J. Attwooll (2005), "Improvement of the Geotechnical Axial Design Methodology for Colorado's Drilled Shafts Socketed in Weak Rocks," *Transportation Research Record: Journal of the Transportation Research Board*, Transportation Research Board of the National Academies, No. 1936, pp. 100-107.

ASTM Standard D3966 (2007), "Standard Test Methods for Deep Foundations Under Lateral Load," ASTM International, West Conshohocken, PA, 2007, DOI: 10.1520/D3966-07, www.astm.org.

Boeckmann, A., S. Myers, M. Uong, and J.E. Loehr (2014), *Load and Resistance Factor Design of Drilled Shafts in Shale for Lateral Loading*, Report for the Missouri Department of Transportation, 300 p.

Brown, D.A., J.P. Turner, and R.J. Castelli (2010), *Drilled Shafts: Construction Procedures and LRFD Design Methods*, FHWA-NHI-10-016.

Brown, D.A., J.P. Turner, R.J. Castelli, and J.E. Loehr (2018), *Drilled Shafts: Construction Procedures and Design Methods*, FHWA NHI-18-024, 754 pp.

Frantzen, J. and F.W. Stratton (1987), *P-Y Curve Data for Laterally Loaded Piles in Shale and Sandstone*, Report No. FHWA-KS-87-2 by Kansas Department of Transportation.

Freeman, C.F., D. Klajnerman, and G.D. Prasad (1972), "Design of Deep Socketed Caissons Into Shale Bedrock," *Canadian Geotechnical Journal*, Vol. 9, pp. 105-114.

Horvath, R.G., and T.C. Kenney (1979), "Shaft Resistance of Rock-socketed Drilled Piers," *Proceedings of Symposium on Deep Foundations*, ASCE National Convention, Atlanta, GA, ASCE, pp. 182-214.

Hummert, J.B., and T.L. Cooling (1988), "Drilled Pier Load Test, Fort Collins, Colorado," *Proceedings of the 2nd International Conference on Case Histories in Geotechnical Engineering*, St. Louis, Missouri, pp. 1375-1382.

Isenhower, W.M. and S-T Wang (2011), *Technical Manual for LPILE, Version 6*.

Johnson, K.S. (2008), *Geologic History of Oklahoma*, Educational Publication 9, Oklahoma Geological Survey, 8 pp.

Kulhawy, F.H., and K.K. Phoon (1993), "Drilled Shaft Side Resistance in Clay Soil to Rock," *Design and Performance of Deep Foundations: Piles and Piers in Soil and Soft Rock*, ASCE, pp. 172-183.

Measurand Inc. (2013), *ShapeAccelArray Manual*, Rev. 0.

Missouri Department of Transportation (2023), *Engineering Policy Guide*, LRFD Bridge Design Guidelines for Drilled Shafts, EPG 751.37.

Nam, M.S., and C. Vipulanandan (2010), "Relationship between Texas Cone Penetrometer Tests and Axial Resistances of Drilled Shafts Socketed in Clay Shale and Limestone," *Journal of Geotechnical and Geoenvironmental Engineering*, ASCE, Vol. 136, No. 8, pp. 1161-1165.

Pierce, M.D. (2013), *Load and Resistance Factor Design of Drilled Shafts in Shale Using SPT and TCP Measurements*, M.S. Thesis, University of Missouri, 174 pp.

Reese, L.C., W.M. Isenhower, and S-T Wang (2006), *Shallow and Deep Foundations*, John Wiley & Sons, Hoboken, New Jersey.

Rowe, R.K., and H.H. Armitage (1987), "A design method for drilled piers in soft rock," *Canadian Geotechnical Journal*, Vol. 24, pp. 126-142.

Texas Department of Transportation (2012), *Geotechnical Manual*, Texas Department of Transportation.

Thorburn, S. (1966), "Large diameter piles founded on bedrock," *Large Bored Piles: Proceedings of the Symposium Organized by the Institution of Civil Engineers and the Reinforced Concrete Association*, Institution of Civil Engineers, Chapter 5, pp. 121-129.

Uong, M.D. (2018), *Load and Resistance Factor Design of Drilled Shafts Subjected to Lateral Loading at Service Limit State*, Dissertation presented to the Faculty of the Graduate School of the University of Missouri.

Williams, A.F., and P.J.N. Pells (1981), "Side resistance rock sockets in sandstone, mudstone, and shale," *Canadian Geotechnical Journal*, Vol. 18, pp. 502-513.

Zhang, L., and H.H. Einstein (1998), "End Bearing Capacity of Drilled Shafts in Rock," *Journal of Geotechnical and Geoenvironmental Engineering*, ASCE, Vol. 124, No. 7, pp. 574-584.

Appendix A – As-Built Shaft Information

Abbreviations used in this Appendix

BOS	Bottom of Shaft
BPC	Bottom of Permanent Casing
BTC	Bottom of Temporary Casing
SG	Strain Gage
TOC	Top of Concrete
TPC	Top of Permanent Casing
TTC	Top of Temporary Casing

A-2

Site Plan

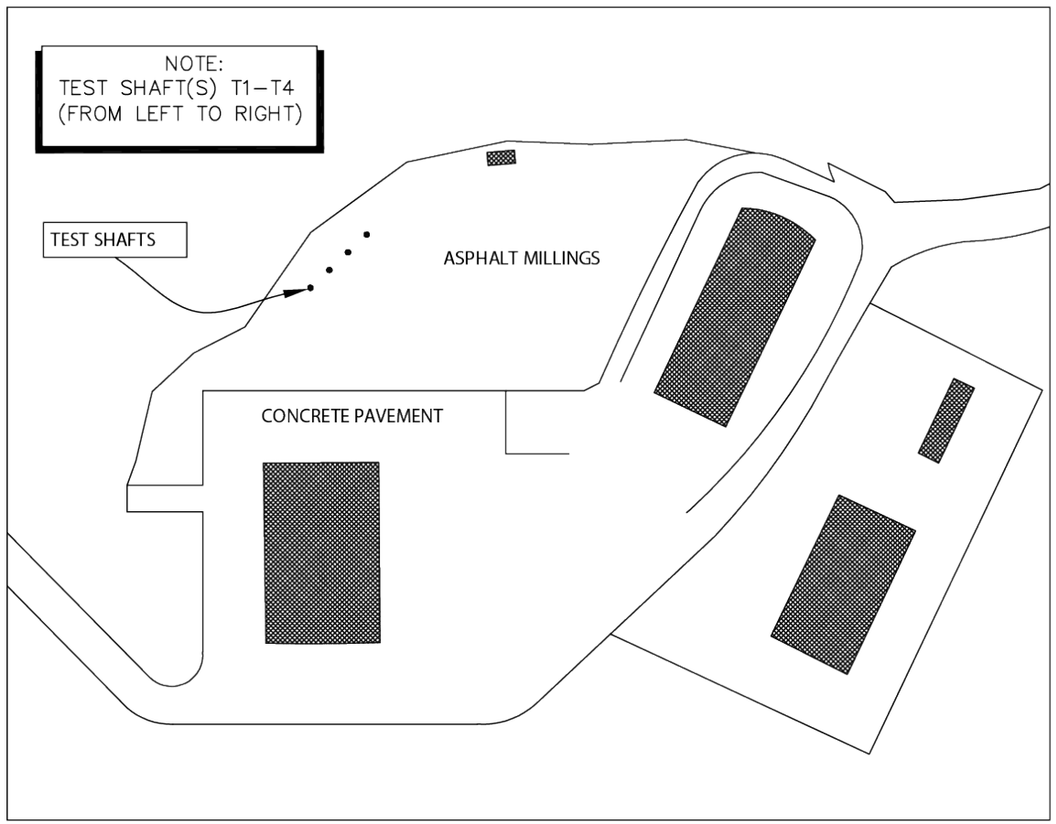

Shaft Cross-Section

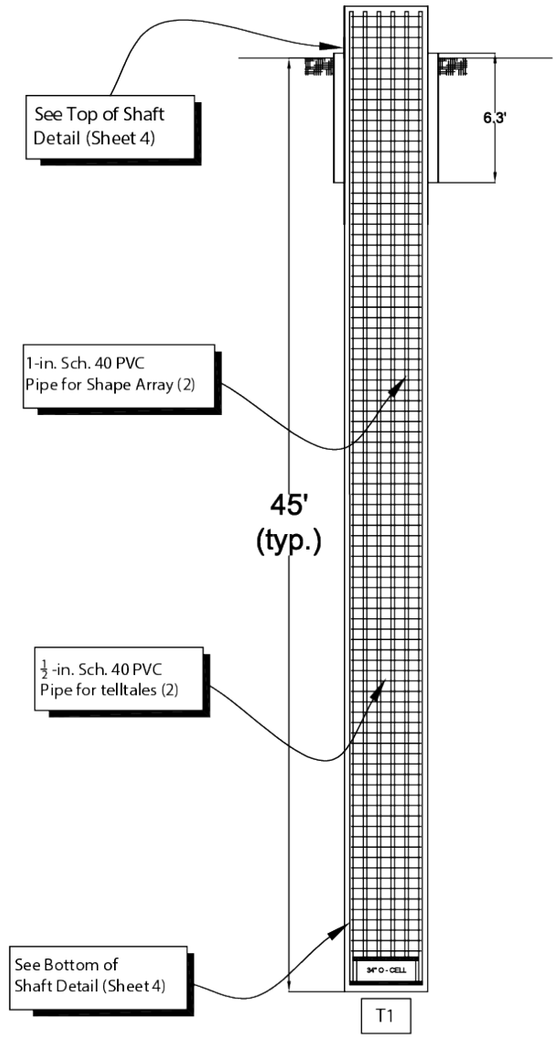

Edmond Site Layout

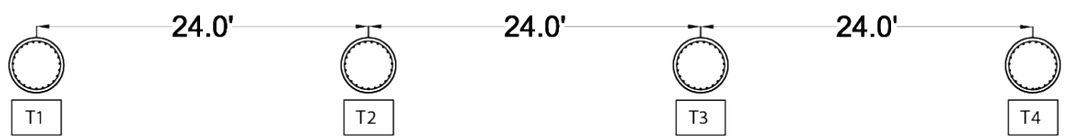

University of Missouri
Civil and Environmental Engineering

ODOT DRILLED SHAFT

Edmond, Oklahoma: Shaft Profile

Scale:	*VARIES*	Dwn: E.Q.B.	Date: 11/25/19	1/4

A-3

Soil Profile

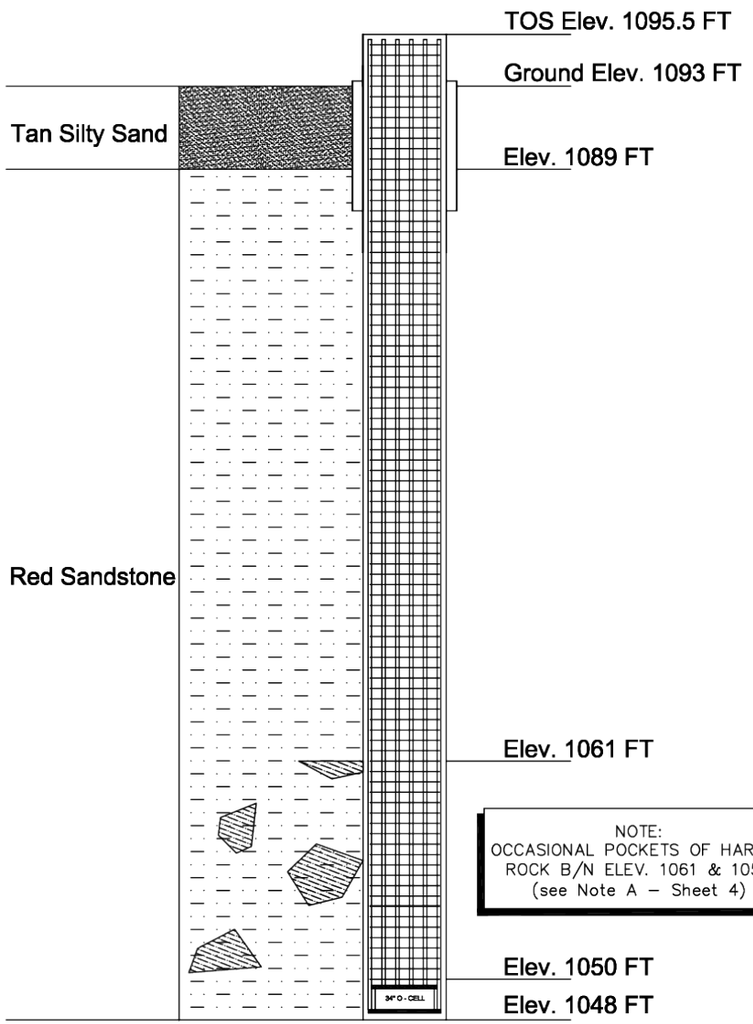

Instrumentation

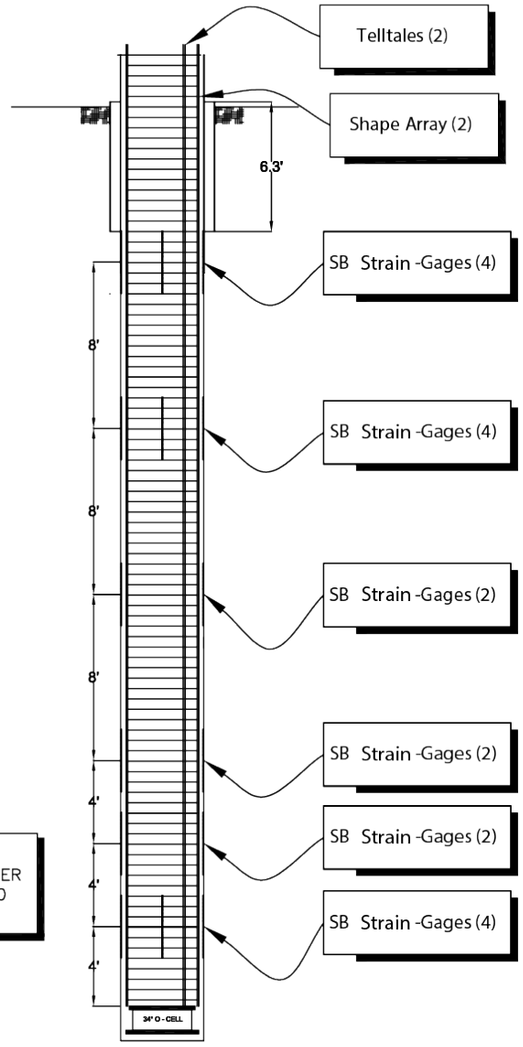

Strength Measurements

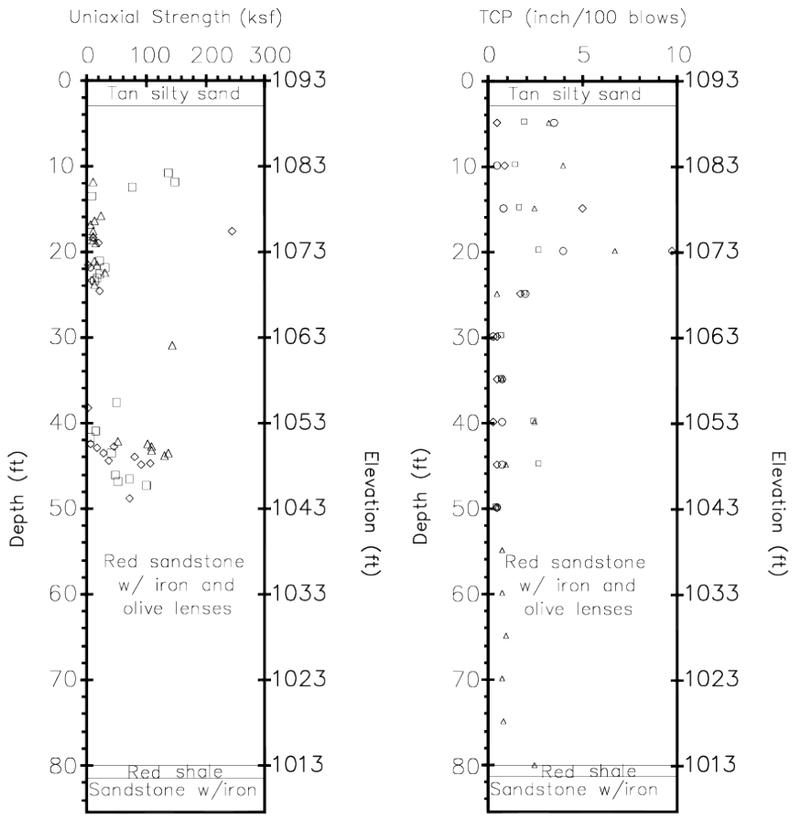

University of Missouri
Civil and Environmental Engineering

ODOT DRILLED SHAFT

Edmond, Oklahoma: Shaft Profile

Scale:	*VARIES*	Dwn: E.Q.B.	Date: 11/25/19	2/4

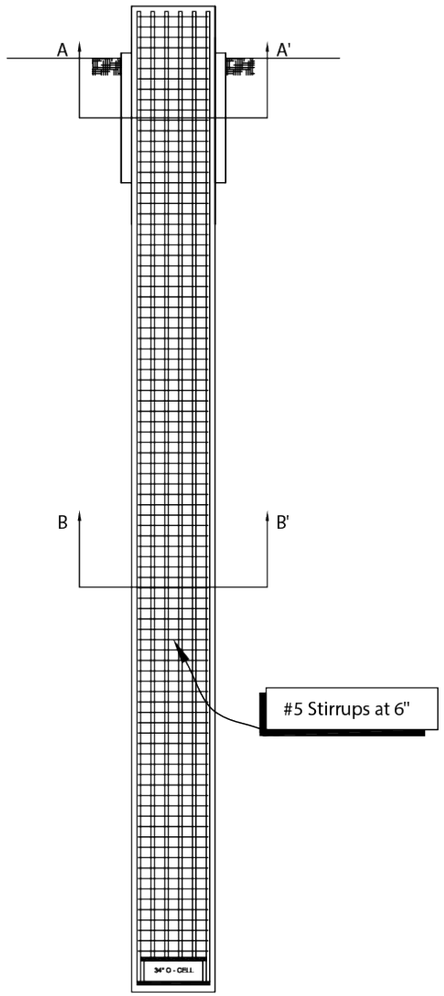

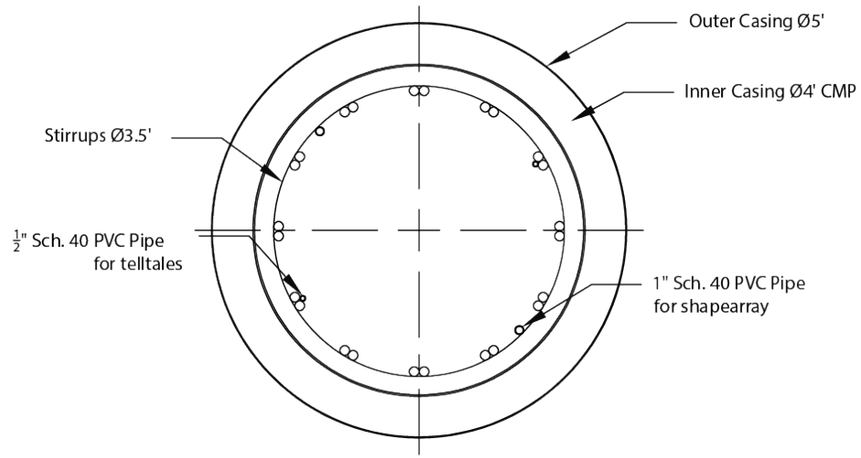

NOTE:
½" Sch. 40 PVC to be bundled to reinforcement

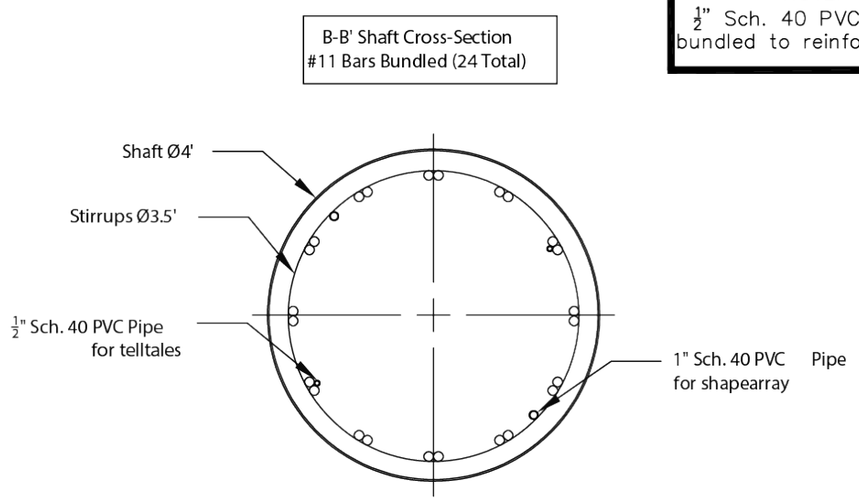

A-4

University of Missouri
Civil and Environmental Engineering

ODOT DRILLED SHAFT

Edmond, Oklahoma: Shaft Profile

Scale:	*VARIES*	Dwn: E.Q.B.	Date: 11/25/19	3/4

Top of Shaft

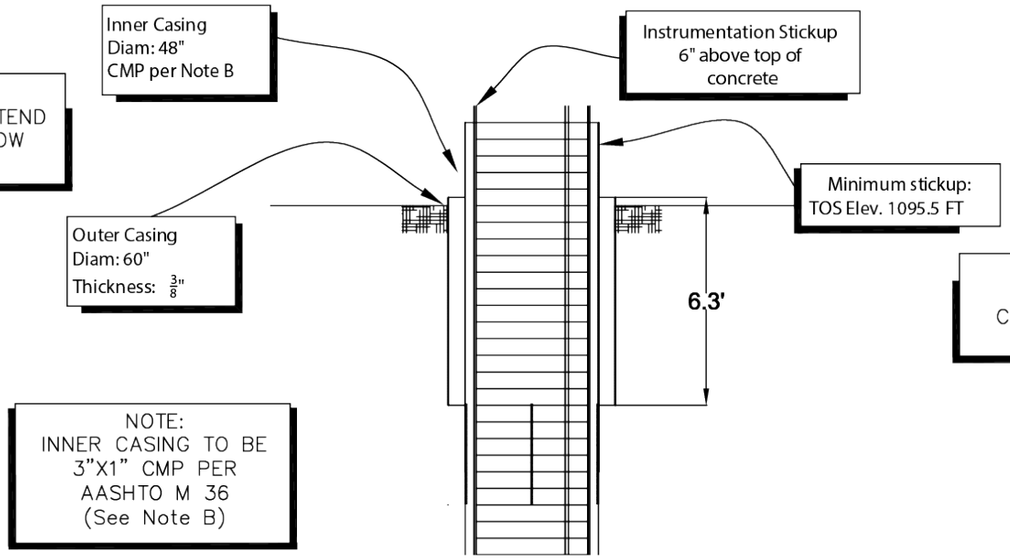

NOTE:
TOS ELEV. TO BE
CONSISTENT FOR ALL
SHAFTS

NOTE:
SISTER BARS TO BE
PLACED ON STIRRUPS

NOTE:
TOP O-CELL PLATE TO BE
WELDED TO REINFORCING CAGE
AS DIRECTED ON-SITE BY
LOADTEST

NOTE:
REFER TO LOADTEST O-CELL
ASSEMBLY DRAWINGS FOR
FURTHER O-CELL AND LOAD
PLATE INSTRUCTION

NOTE:
SISTER BARS LOCATED
4 FT ABOVE O-CELL TOP PLATE

Note	
A	Hard conglomerate exhibiting strengths ranging from 5000 to 9000 psi between elevations 1061 FT and 1050 FT
B	For interior casings, use round corrugated galvanized steel pipe with 3 in x 1 in [75 mm x 25 mm] corrugations in accordance with AASHTO M 36. Ensure the pipe gauge stays round and can withstand the concrete pressure.

Bottom of Shaft

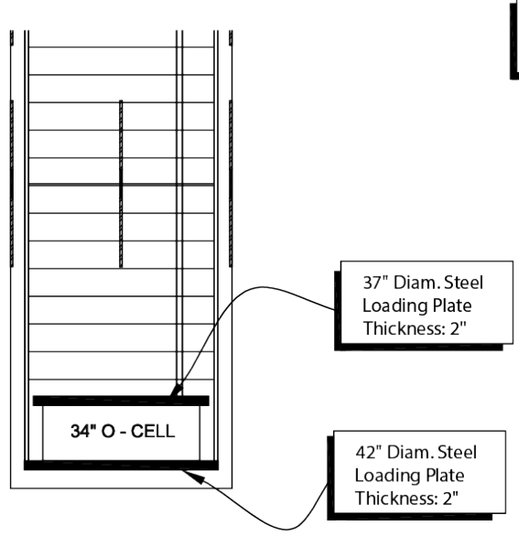

Edmond: Estimated Resistance (kip)		
Design Method	Estimated Side Resistance (kips)	Estimated Tip Resistance (kips)
UCS	7,200	3,500
TCP	14,700	11,700

University of Missouri
Civil and Environmental Engineering

ODOT DRILLED SHAFT

Edmond, Oklahoma: Shaft Profile

Scale: *VARIES* | Dwn: E.Q.B. | Date: 11/25/19 | 4/4

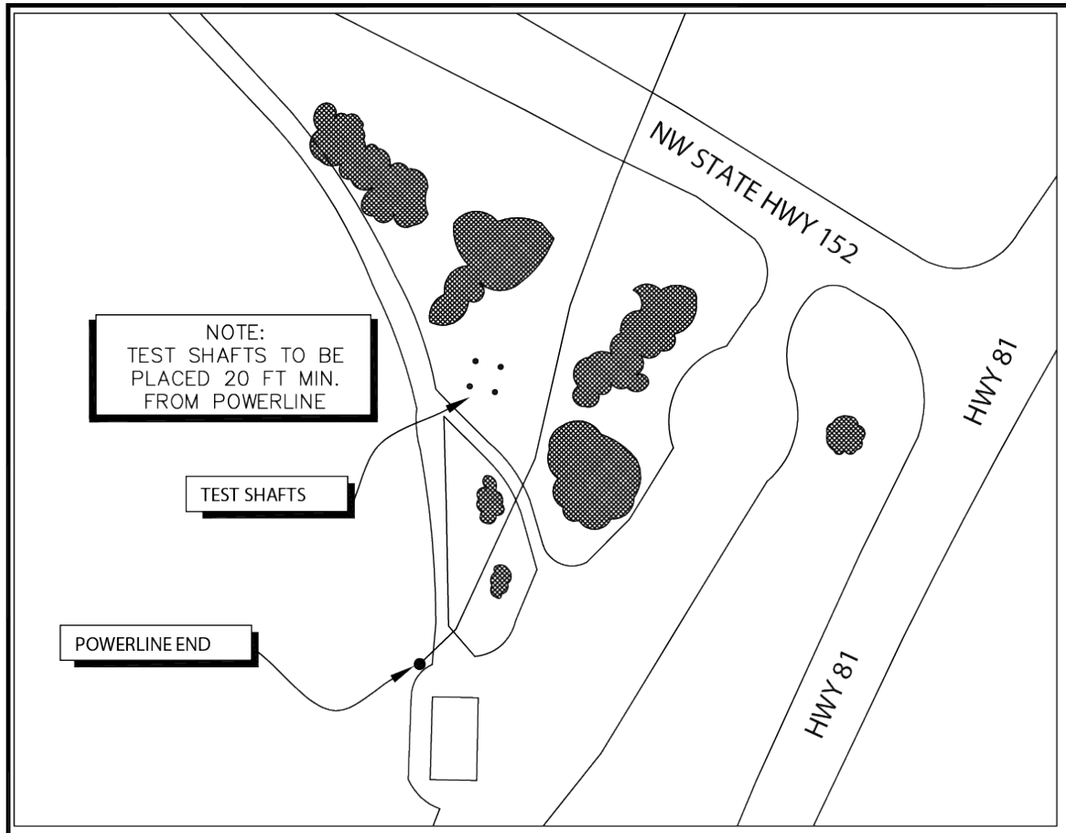

Minco Site Layout

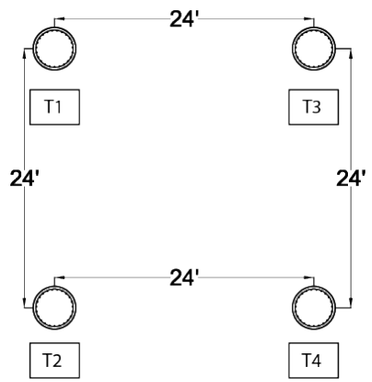

Shaft Cross-Section

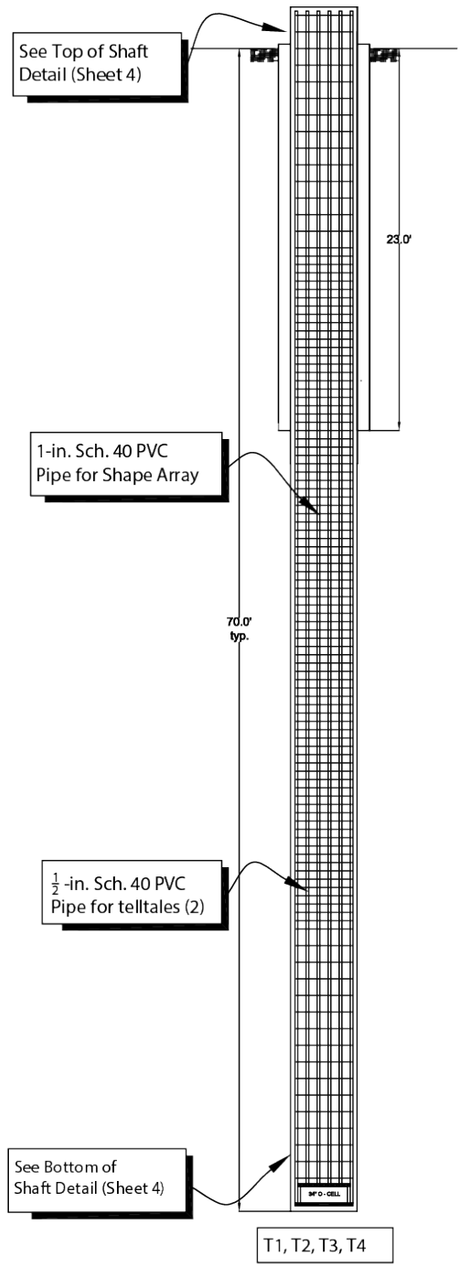

A-6

University of Missouri
Civil and Environmental Engineering

ODOT DRILLED SHAFT

Minco, Oklahoma: Shaft Profile

Scale:	*VARIES*	Dwn: E.Q.B.	Date: 11/25/19	1/4

Soil Profile
Depth: 70 FT

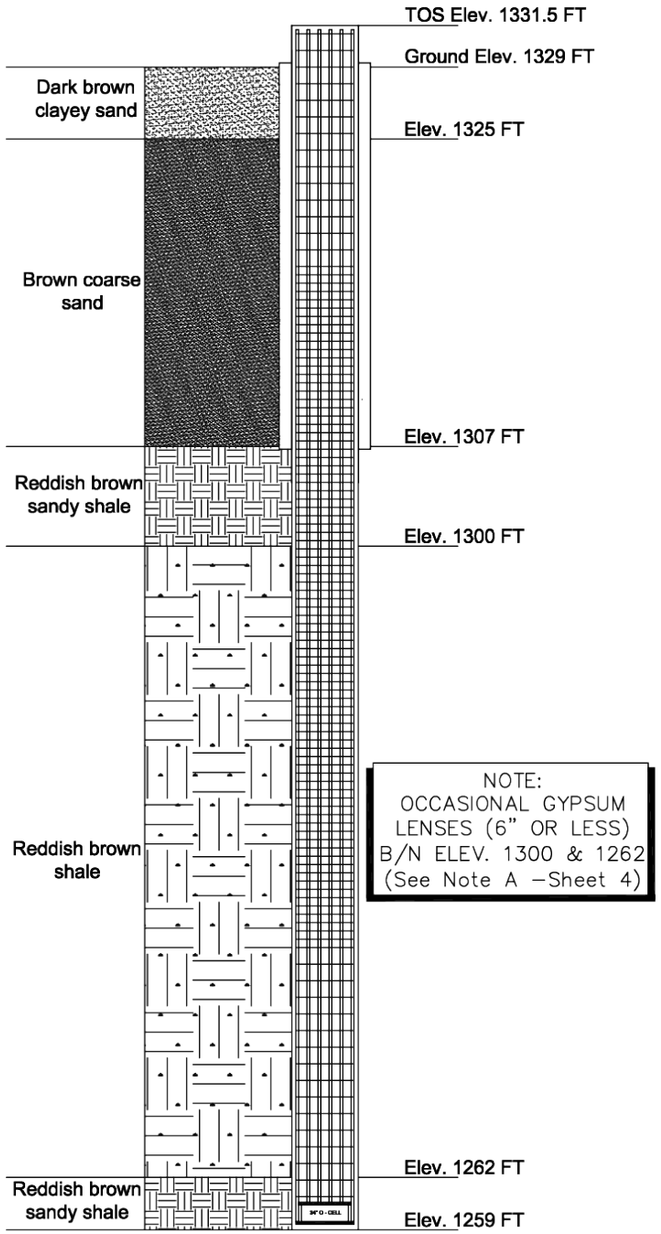

Instrumentation
Depth: 70 FT

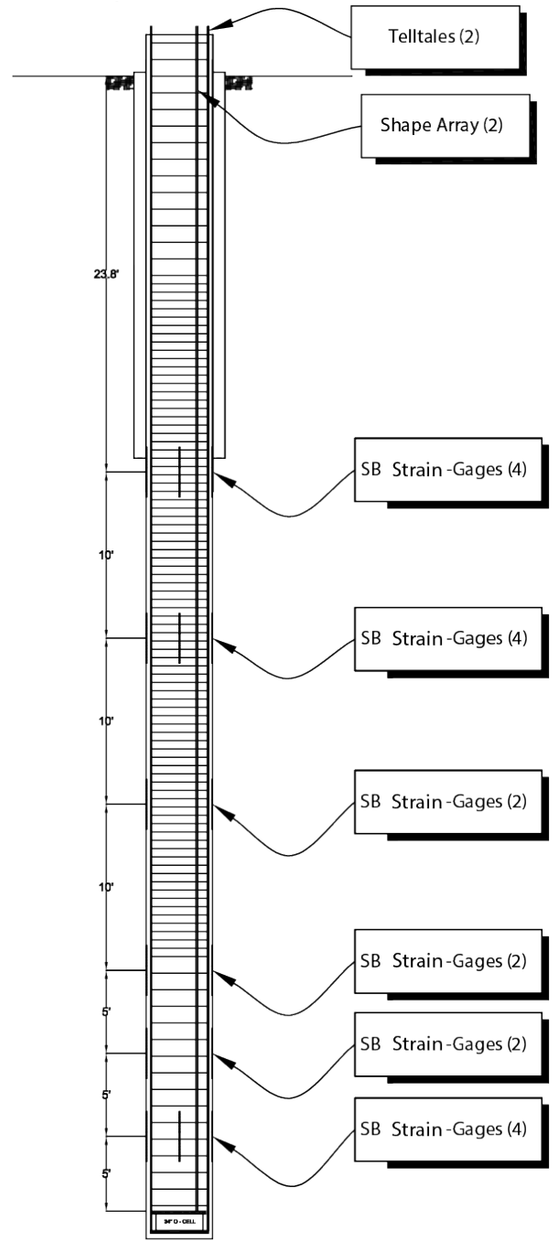

Strength Measurements

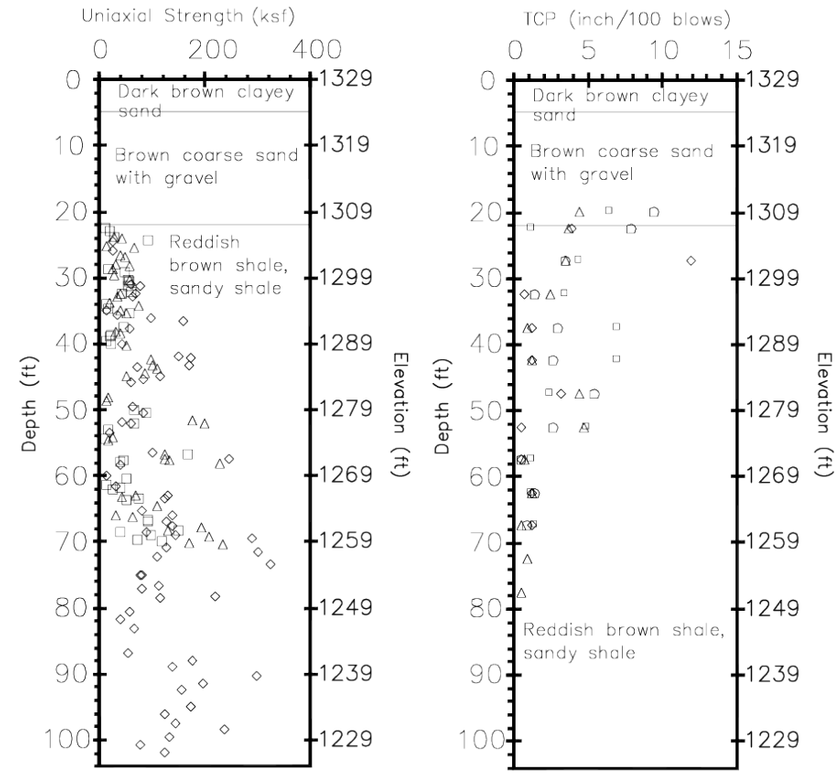

A-7

University of Missouri
Civil and Environmental Engineering

ODOT DRILLED SHAFT

Minco, Oklahoma: Shaft Profile

Scale:	*VARIES*	Dwn: E.Q.B.	Date: 11/25/19	2/4

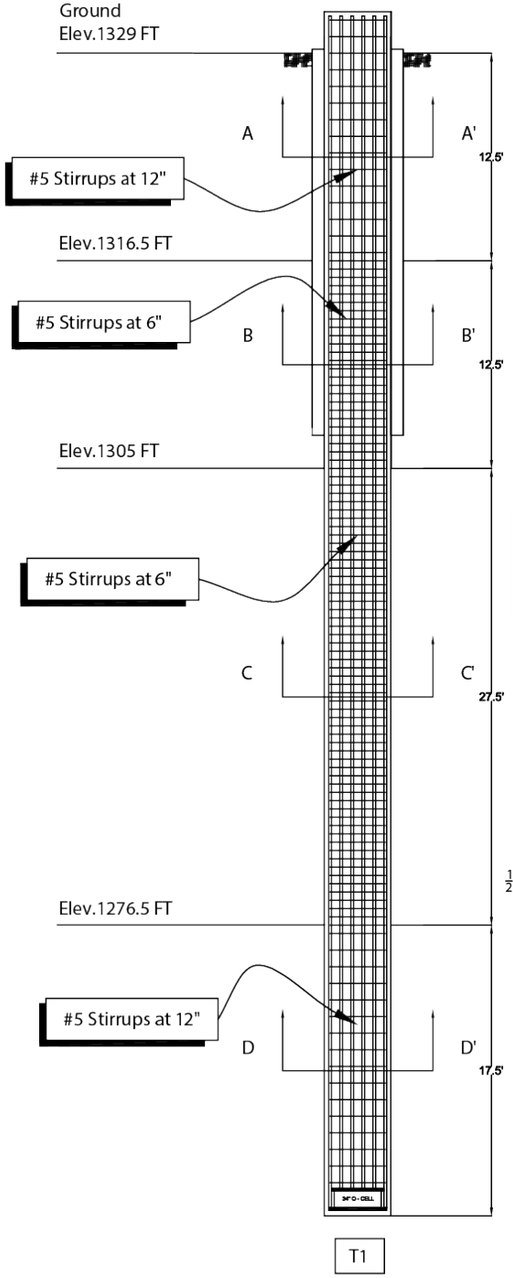

A-A' Shaft Cross-Section
#11 Bars (12 Total)

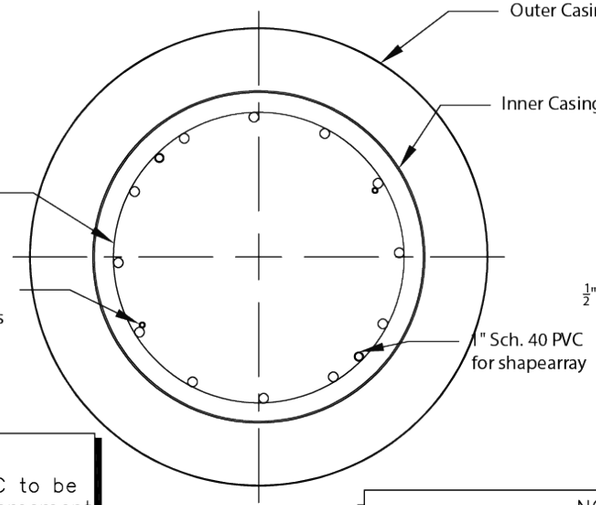

B-B' Shaft Cross-Section
#11 Bars Bundled (24 Total)

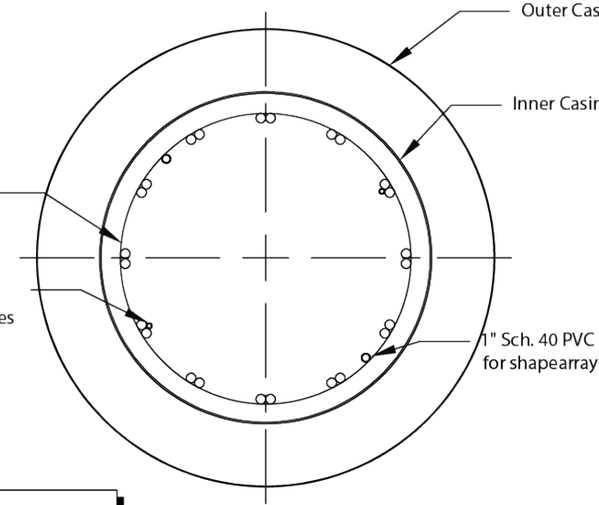

NOTE:
½" Sch. 40 PVC to be bundled to reinforcement

NOTE:
VERTICAL BARS TO BE RUN IN TWO LENGTHS: UPPER BARS TO EXTEND FROM TOS TO ELEV. 1276.5 FT; LOWER BARS TO EXTEND FROM ELEV. 1316.5 FT TO O-CELL, WITH BARS BUNDLED IN OVERLAP

C-C' Shaft Cross-Section
#11 Bars Bundled (24 Total)

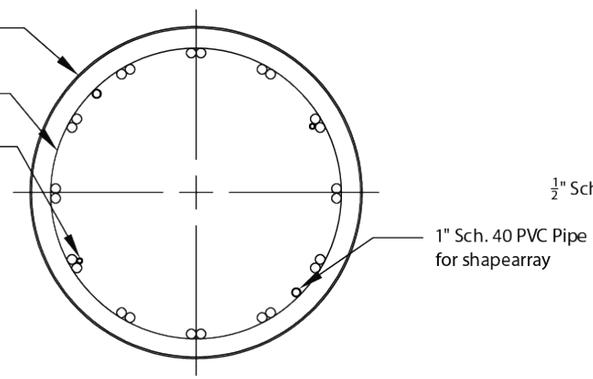

D-D' Shaft Cross-Section
#11 Bars (12 Total)

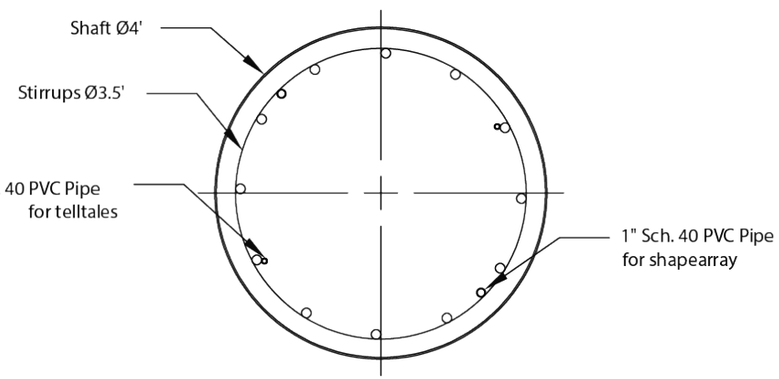

University of Missouri
Civil and Environmental Engineering

ODOT DRILLED SHAFT

Minco, Oklahoma: Test Shafts

Scale:	*VARIES*	Dwn: E.Q.B.	Date: 11/25/19	3/4

Top of Shaft

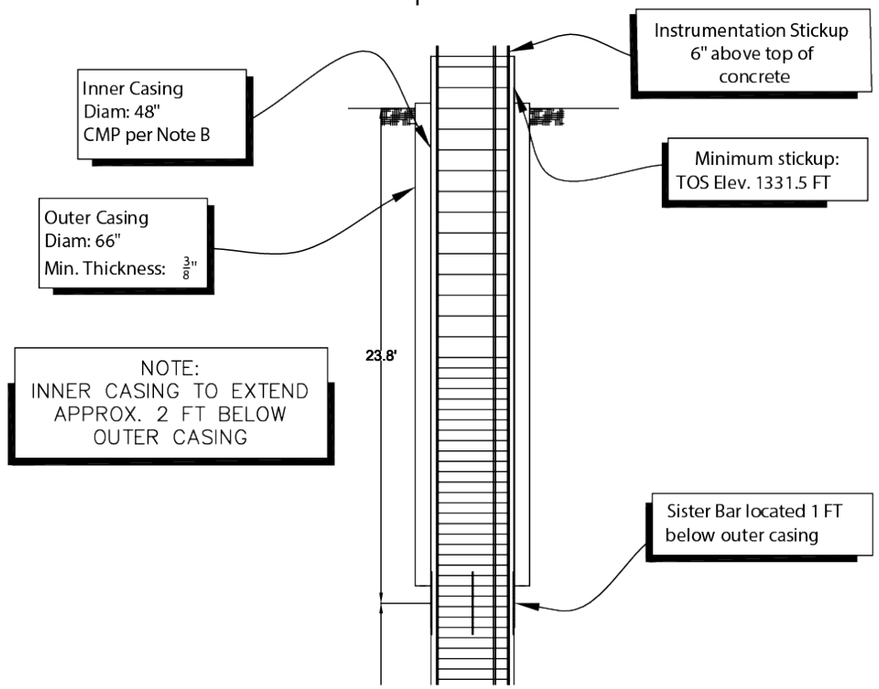

NOTE:
TOS ELEV. TO BE
CONSISTENT FOR ALL
SHAFTS

NOTE:
SISTER BARS TO BE
PLACED ON STIRRUPS

NOTE:
TOP O-CELL PLATE TO BE
WELDED TO REINFORCING CAGE
AS DIRECTED ON-SITE BY
LOADTEST

NOTE:
REFER TO LOADTEST O-CELL
ASSEMBLY DRAWINGS FOR
FURTHER O-CELL AND LOAD
PLATE INSTRUCTION

NOTE:
SISTER BARS LOCATED
5 FT ABOVE O-CELL TOP PLATE

Bottom of Shaft

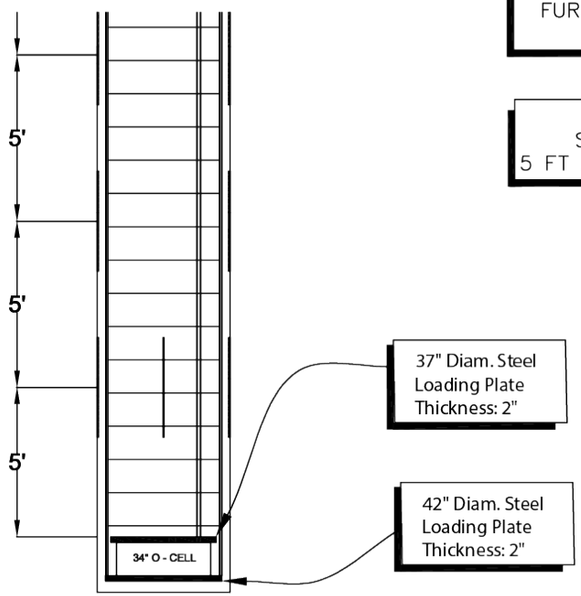

Note	
A	Gypsum lenses (6" or less) exist between elevations 1300 Ft and 1262 FT. There is a potential for loss of drilling fluid between these depths.
B	For interior casings, use round corrugated galvanized steel pipe with 3 in x 1 in [75 mm x 25 mm] corrugations in accordance with AASHTO M 36. Ensure the pipe gauge stays round and can withstand the concrete pressure.

Minco - 70 FT: Estimated Resistance (kip)		
Design Method	Estimated Side Resistance (kips)	Estimated Tip Resistance (kips)
UCS	13,700	5,200
TCP	8,600	6,300

University of Missouri
Civil and Environmental Engineering

ODOT DRILLED SHAFT

Minco, Oklahoma: Shaft Profile

Scale: *VARIES* | Dwn: E.Q.B. | Date: 11/25/19 | 4/4

Appendix B – Measured Drilled Shaft Response Profiles

ShapeArray Displacement, Rotation, and Bending Moments

Strain Gage Bending Moments

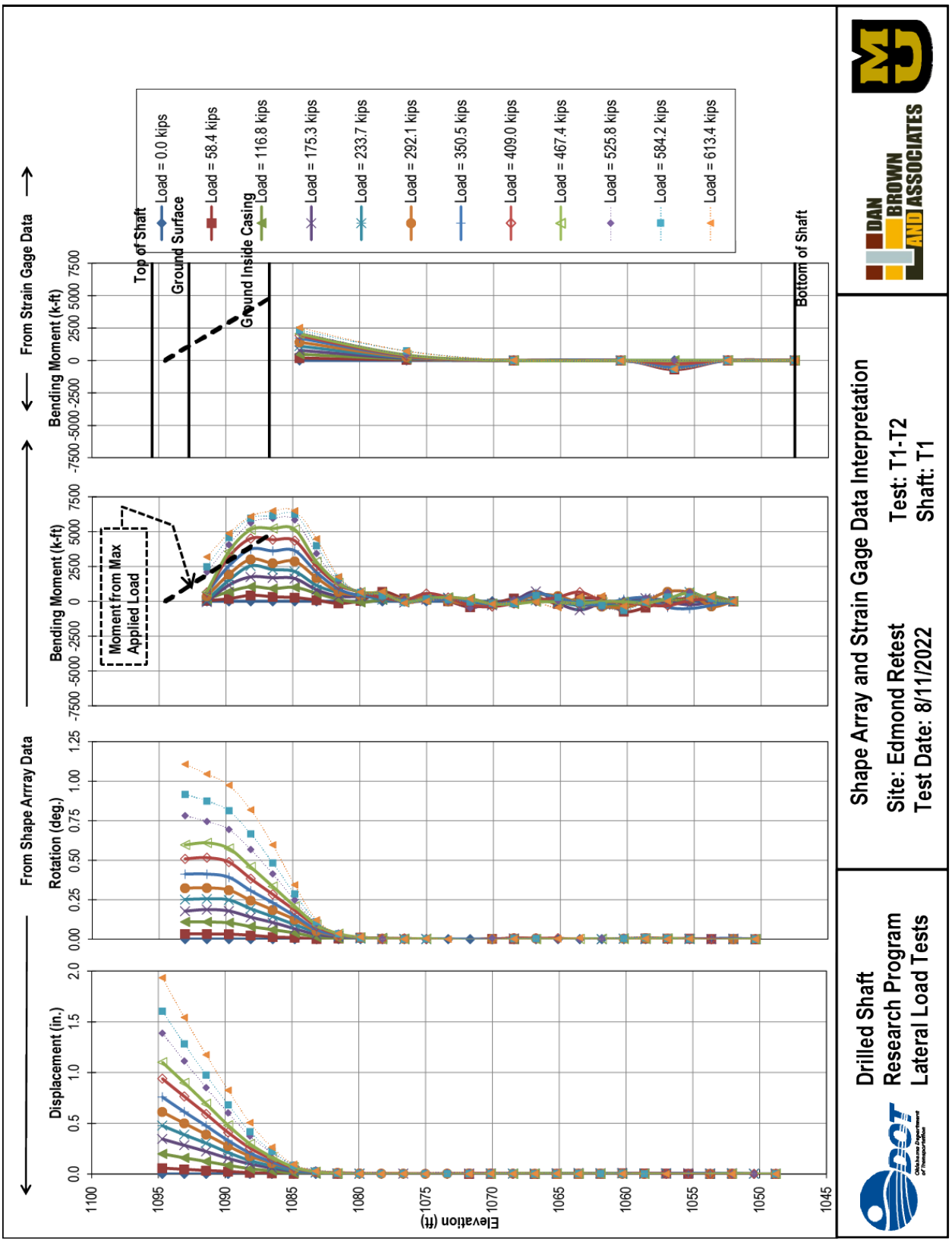
Drilled Shaft
Research Program
Lateral Load Tests
Shape Array and Strain Gage Data Interpretation
Site: Edmond Retest
Test Date: 8/11/2022
Test: T1-T2
Shaft: T1
DAN BROWN AND ASSOCIATES
From Shape Array Data
From Strain Gage Data
Displacement (in.)
Rotation (deg.)
Bending Moment (k-ft)
Moment from Max Applied Load
Bending Moment (k-ft)
Top of Shaft
Ground Surface
Ground Inside Casing
Bottom of Shaft
Load = 0.0 kips
Load = 58.4 kips
Load = 116.8 kips
Load = 175.3 kips
Load = 233.7 kips
Load = 292.1 kips
Load = 350.5 kips
Load = 409.0 kips
Load = 467.4 kips
Load = 525.8 kips
Load = 584.2 kips
Load = 613.4 kips
Elevation (ft)

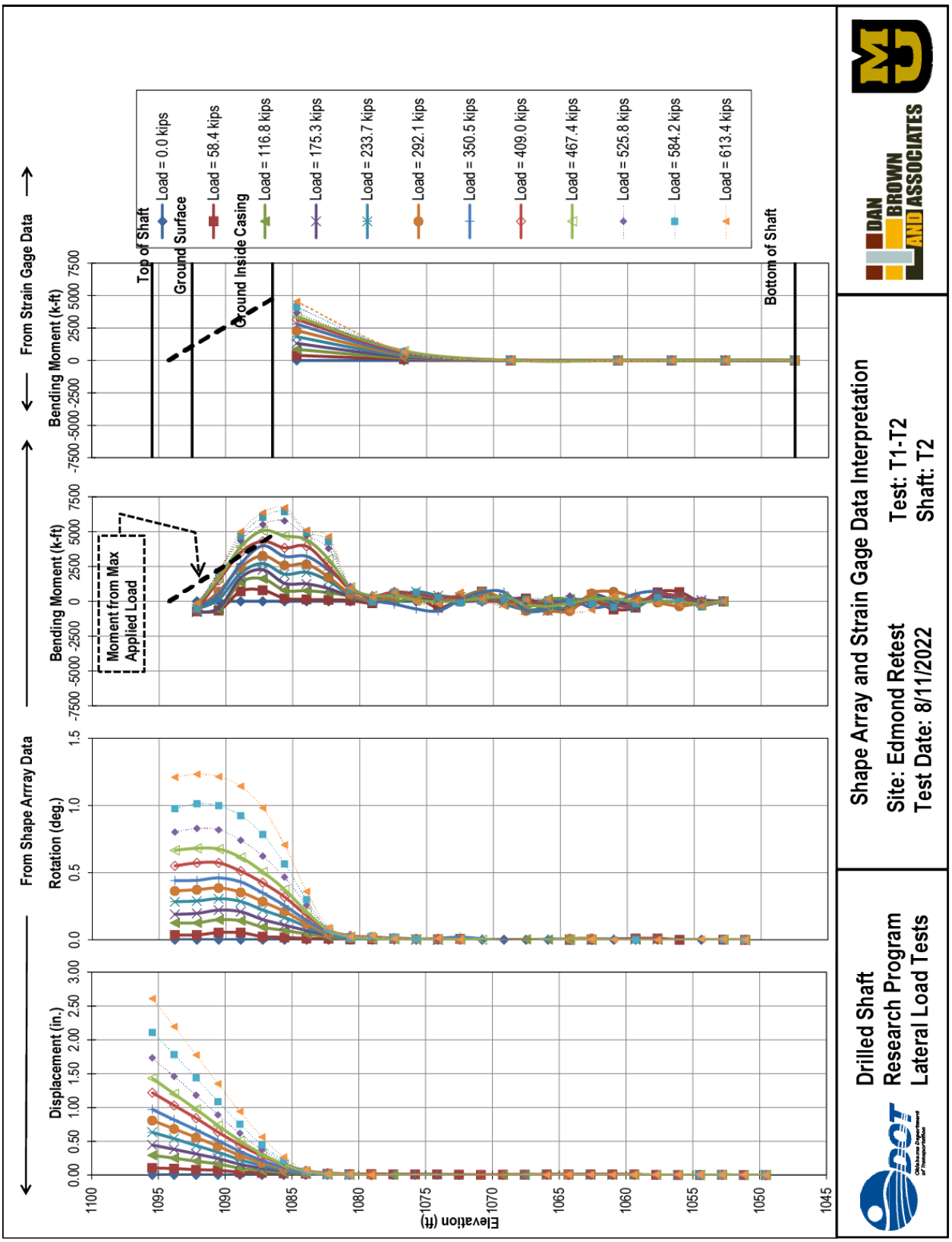
From Shape Array Data
From Strain Gage Data
Displacement (in.)
Rotation (deg.)
Bending Moment (k-ft)
Moment from Max Applied Load
Bending Moment (k-ft)
Top of Shaft
Ground Surface
Ground Inside Casing
Bottom of Shaft
Load = 0.0 kips
Load = 58.4 kips
Load = 116.8 kips
Load = 175.3 kips
Load = 233.7 kips
Load = 292.1 kips
Load = 350.5 kips
Load = 409.0 kips
Load = 467.4 kips
Load = 525.8 kips
Load = 584.2 kips
Load = 613.4 kips
Elevation (ft)
Drilled Shaft
Research Program
Lateral Load Tests
Shape Array and Strain Gage Data Interpretation
Site: Edmond Retest
Test Date: 8/11/2022
Test: T1-T2
Shaft: T2
DAN BROWN AND ASSOCIATES

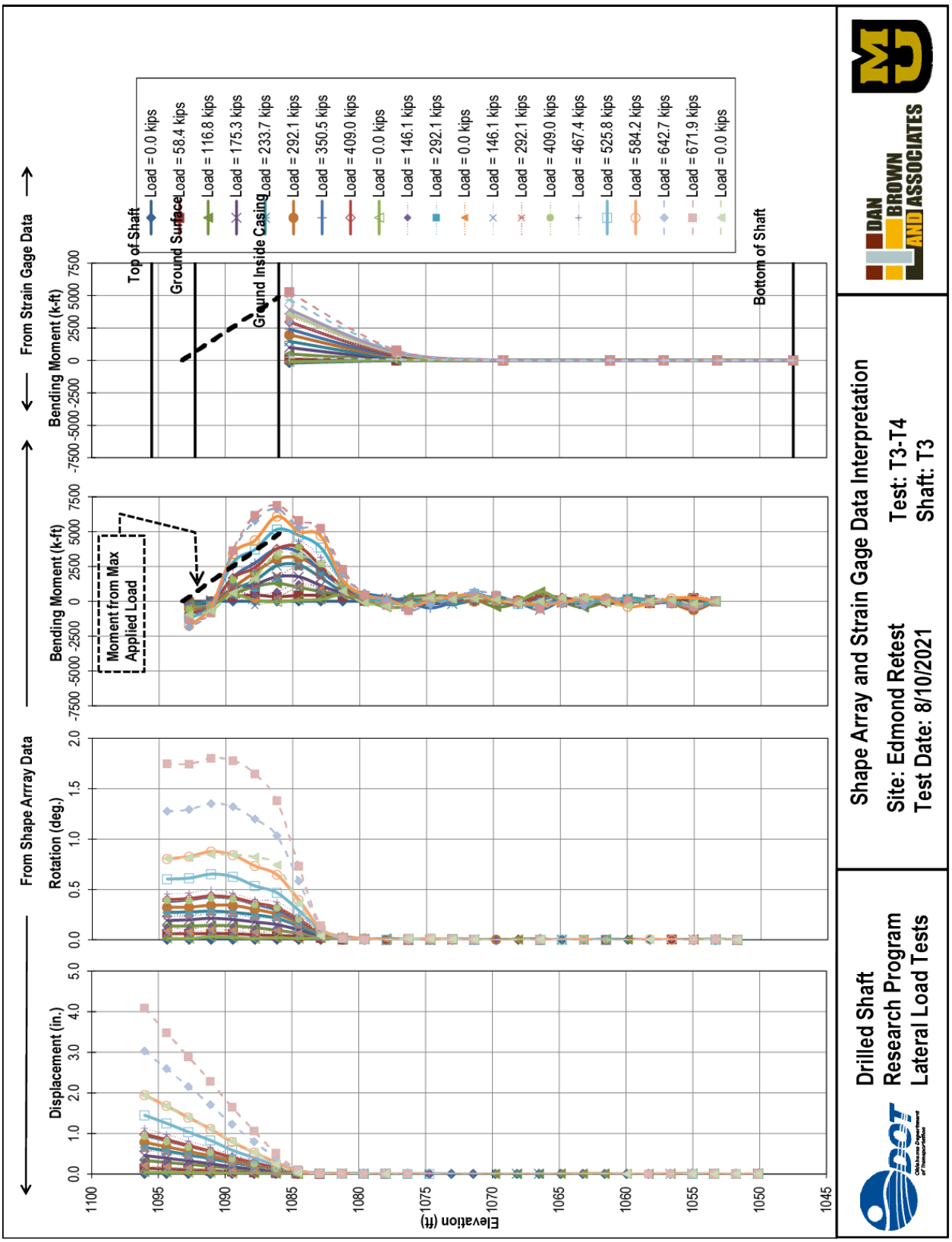
From Shape Array Data
From Strain Gage Data
Displacement (in.)
Rotation (deg.)
Bending Moment (k-ft)
Moment from Max Applied Load
Bending Moment (k-ft)
Top of Shaft
Ground Surface
Ground Inside Casing
Bottom of Shaft
Load = 0.0 kips
Load = 58.4 kips
Load = 116.8 kips
Load = 175.3 kips
Load = 233.7 kips
Load = 292.1 kips
Load = 350.5 kips
Load = 409.0 kips
Load = 0.0 kips
Load = 146.1 kips
Load = 292.1 kips
Load = 0.0 kips
Load = 146.1 kips
Load = 292.1 kips
Load = 409.0 kips
Load = 467.4 kips
Load = 525.8 kips
Load = 584.2 kips
Load = 642.7 kips
Load = 671.9 kips
Load = 0.0 kips
Elevation (ft)
Drilled Shaft
Research Program
Lateral Load Tests
Shape Array and Strain Gage Data Interpretation
Site: Edmond Retest
Test Date: 8/10/2021
Test: T3-T4
Shaft: T3
DAN BROWN AND ASSOCIATES

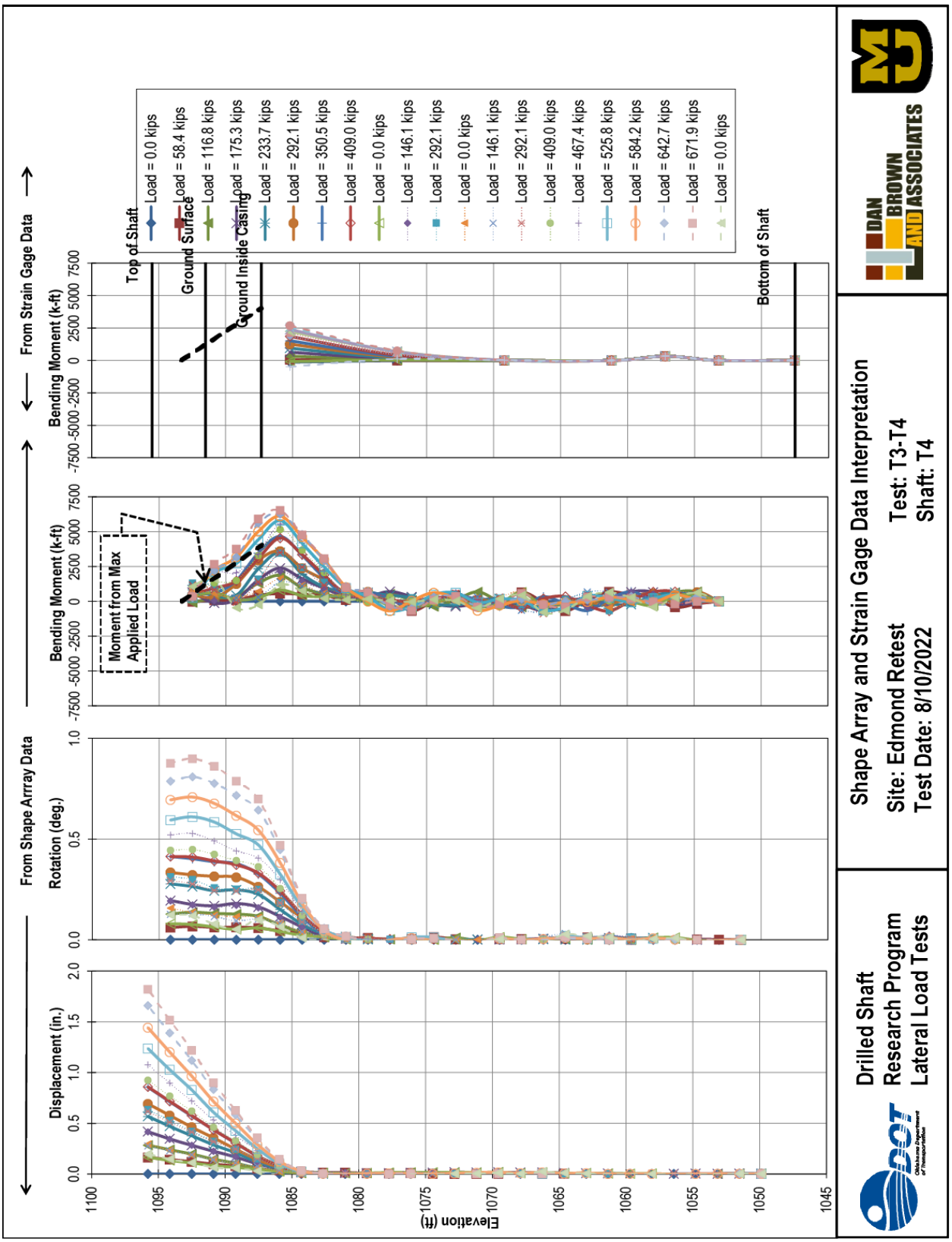
From Shape Array Data
From Strain Gage Data
Displacement (in.)
Rotation (deg.)
Bending Moment (k-ft)
Moment from Max Applied Load
Bending Moment (k-ft)
Top of Shaft
Ground Surface
Ground Inside Casing
Bottom of Shaft
Load = 0.0 kips
Load = 58.4 kips
Load = 116.8 kips
Load = 175.3 kips
Load = 233.7 kips
Load = 292.1 kips
Load = 350.5 kips
Load = 409.0 kips
Load = 0.0 kips
Load = 146.1 kips
Load = 292.1 kips
Load = 0.0 kips
Load = 146.1 kips
Load = 292.1 kips
Load = 409.0 kips
Load = 467.4 kips
Load = 525.8 kips
Load = 584.2 kips
Load = 642.7 kips
Load = 671.9 kips
Load = 0.0 kips
Elevation (ft)
Drilled Shaft Research Program Lateral Load Tests
Shape Array and Strain Gage Data Interpretation
Site: Edmond Retest
Test Date: 8/10/2022
Test: T3-T4
Shaft: T4
DAN BROWN AND ASSOCIATES

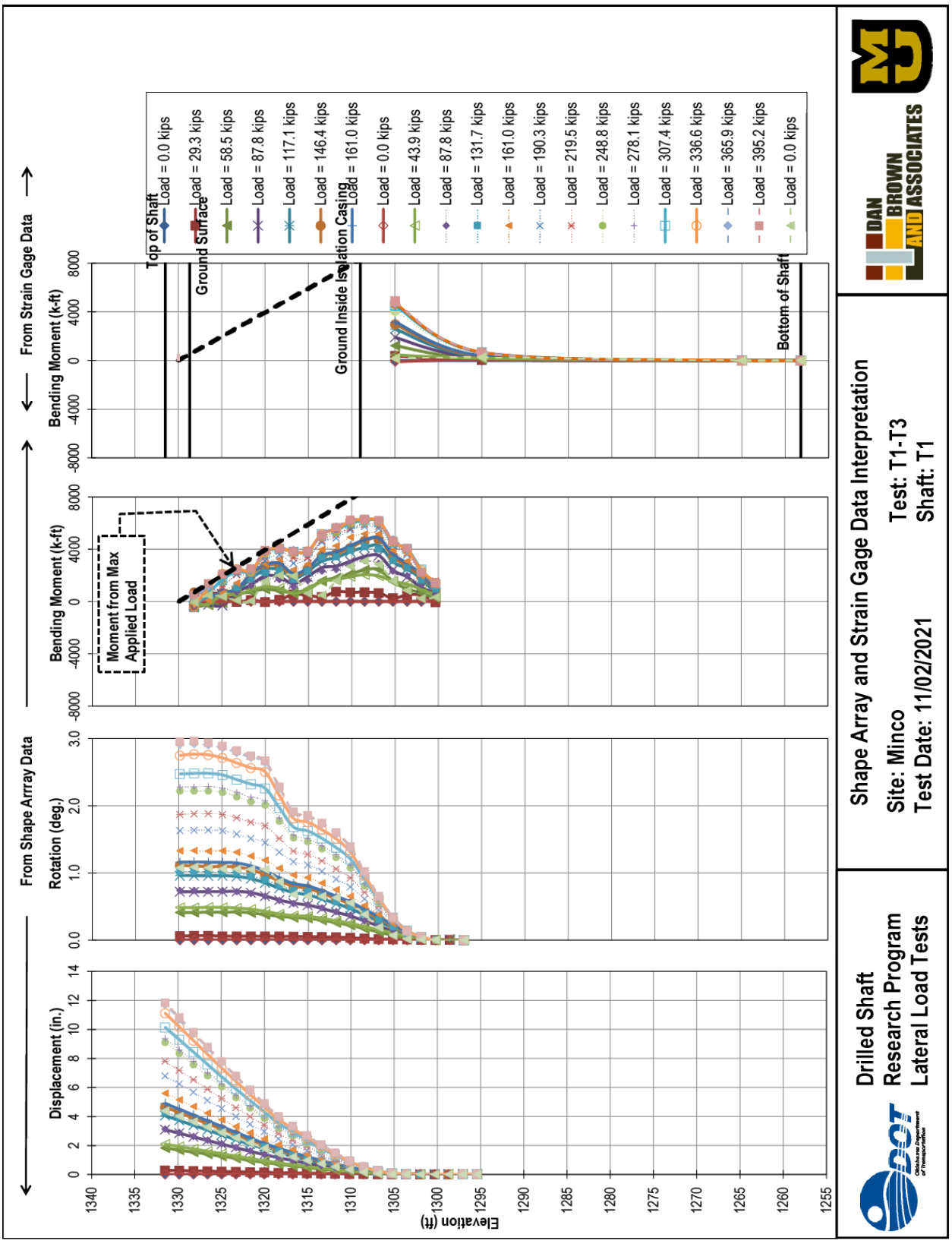
Drilled Shaft
Research Program
Lateral Load Tests
Shape Array and Strain Gage Data Interpretation
Site: Minco
Test Date: 11/02/2021
Test: T1-T3
Shaft: T1
DAN BROWN AND ASSOCIATES
From Shape Array Data
From Strain Gage Data
Displacement (in.)
Rotation (deg.)
Bending Moment (k-ft)
Moment from Max Applied Load
Elevation (ft)
Top of Shaft
Ground Surface
Ground Inside Isolation Casing
Bottom of Shaft
Load = 0.0 kips
Load = 29.3 kips
Load = 58.5 kips
Load = 87.8 kips
Load = 117.1 kips
Load = 146.4 kips
Load = 161.0 kips
Load = 0.0 kips
Load = 43.9 kips
Load = 87.8 kips
Load = 131.7 kips
Load = 161.0 kips
Load = 190.3 kips
Load = 219.5 kips
Load = 248.8 kips
Load = 278.1 kips
Load = 307.4 kips
Load = 336.6 kips
Load = 365.9 kips
Load = 395.2 kips
Load = 0.0 kips

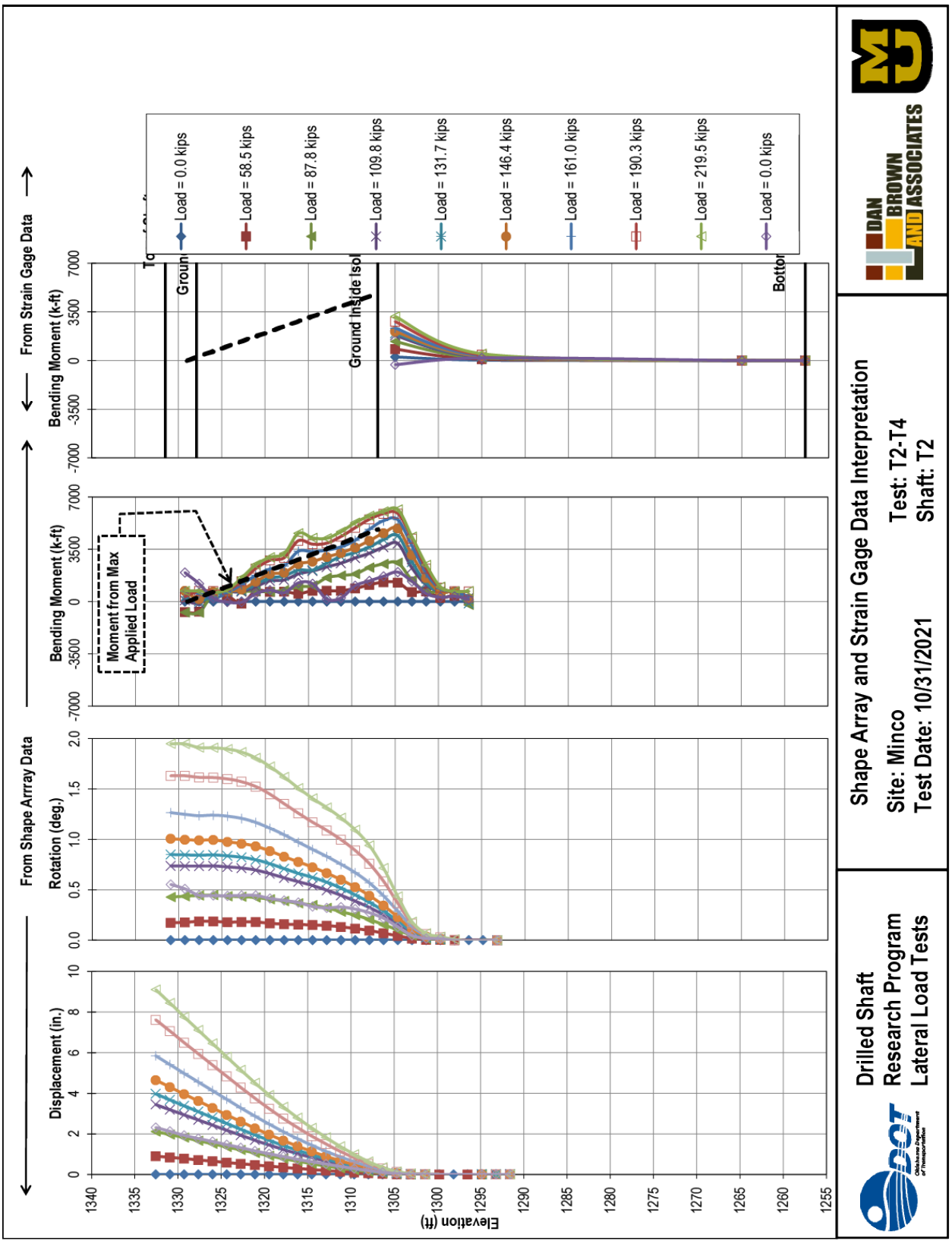
Drilled Shaft
Research Program
Lateral Load Tests
Shape Array and Strain Gage Data Interpretation
Site: Minco
Test Date: 10/31/2021
Test: T2-T4
Shaft: T2
DAN BROWN AND ASSOCIATES
From Shape Array Data
From Strain Gage Data
Displacement (in.)
Rotation (deg.)
Bending Moment (k-ft)
Moment from Max Applied Load
Ground Inside Isol
Load = 0.0 kips
Load = 58.5 kips
Load = 87.8 kips
Load = 109.8 kips
Load = 131.7 kips
Load = 146.4 kips
Load = 161.0 kips
Load = 190.3 kips
Load = 219.5 kips
Load = 0.0 kips
Elevation (ft)

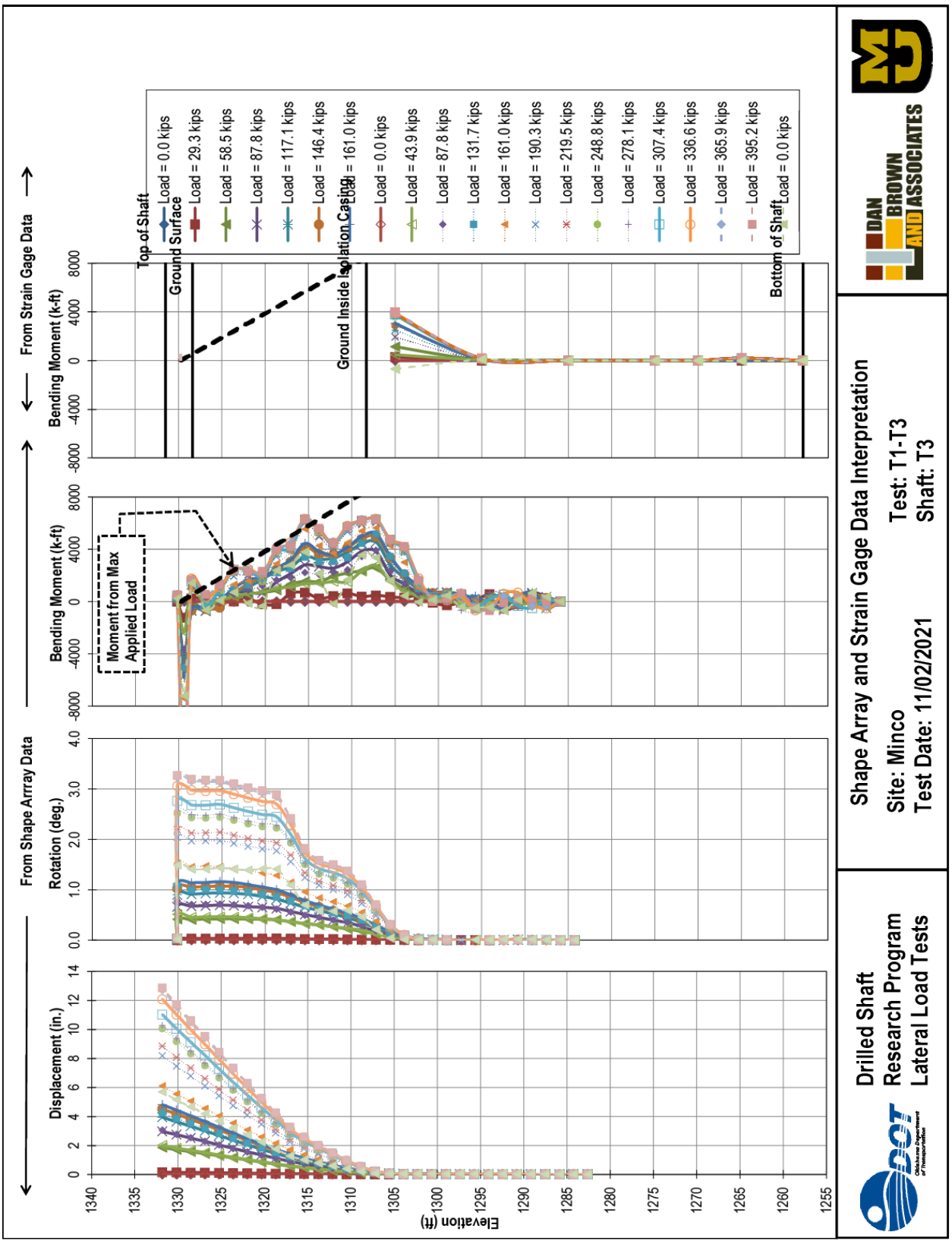
Drilled Shaft
Research Program
Lateral Load Tests
Shape Array and Strain Gage Data Interpretation
Site: Minco
Test Date: 11/02/2021
Test: T1-T3
Shaft: T3
DAN BROWN AND ASSOCIATES
From Shape Arrray Data
From Strain Gage Data
Displacement (in.)
Rotation (deg.)
Bending Moment (k-ft)
Moment from Max Applied Load
Bending Moment (k-ft)
Elevation (ft)
Top of Shaft
Ground Surface
Ground Inside Isolation Casing
Bottom of Shaft
Load = 0.0 kips
Load = 29.3 kips
Load = 58.5 kips
Load = 87.8 kips
Load = 117.1 kips
Load = 146.4 kips
Load = 161.0 kips
Load = 0.0 kips
Load = 43.9 kips
Load = 87.8 kips
Load = 131.7 kips
Load = 161.0 kips
Load = 190.3 kips
Load = 219.5 kips
Load = 248.8 kips
Load = 278.1 kips
Load = 307.4 kips
Load = 336.6 kips
Load = 365.9 kips
Load = 395.2 kips
Load = 0.0 kips

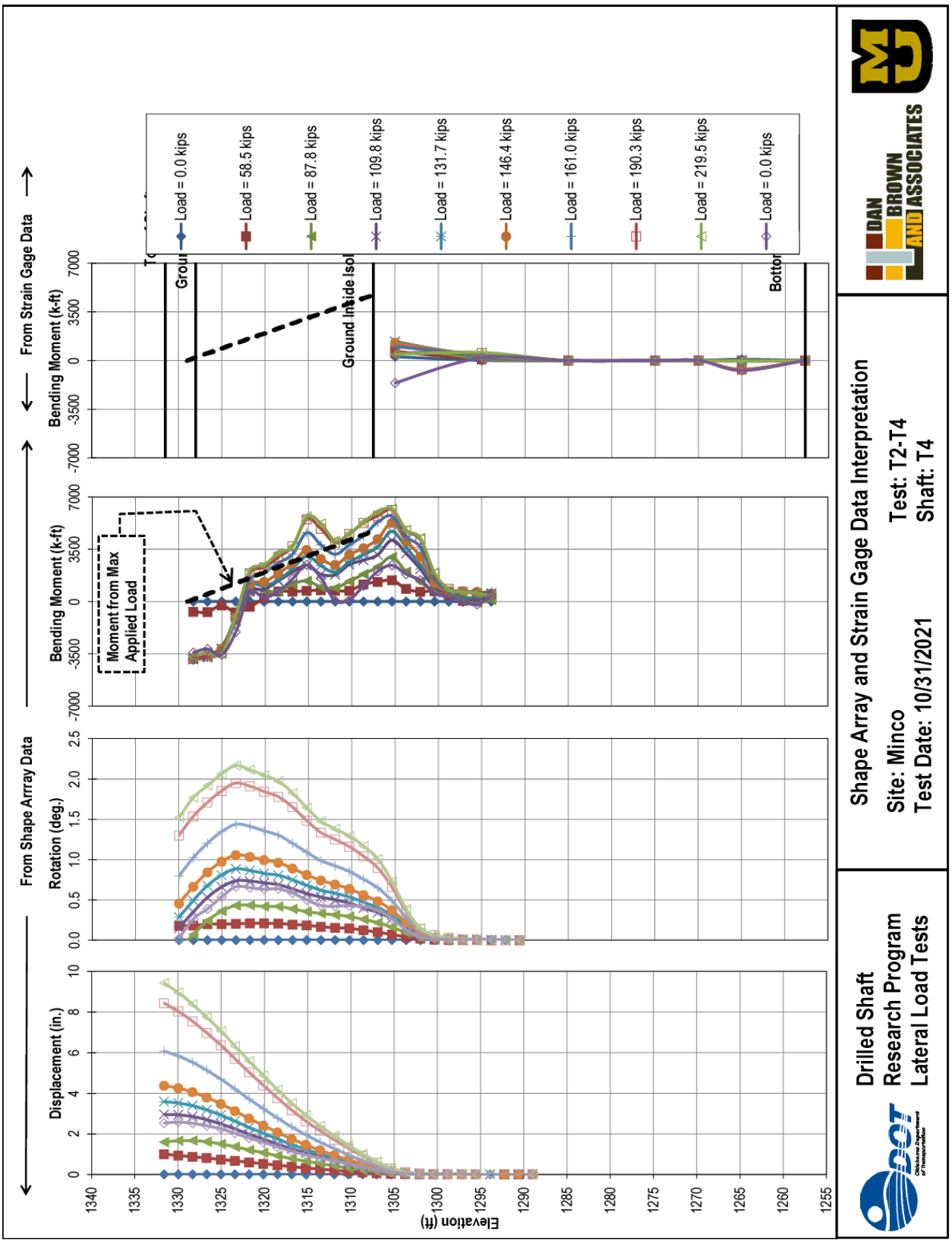
From Shape Array Data
From Strain Gage Data
Displacement (in.)
Rotation (deg.)
Bending Moment (k-ft)
Moment from Max Applied Load
Bending Moment (k-ft)
Load = 0.0 kips
Load = 58.5 kips
Load = 87.8 kips
Load = 109.8 kips
Load = 131.7 kips
Load = 146.4 kips
Load = 161.0 kips
Load = 190.3 kips
Load = 219.5 kips
Load = 0.0 kips
Ground Inside Isol
Elevation (ft)
Drilled Shaft Research Program Lateral Load Tests
Shape Array and Strain Gage Data Interpretation
Site: Minco
Test Date: 10/31/2021
Test: T2-T4
Shaft: T4
DAN BROWN AND ASSOCIATES

Appendix C – *p-y* Calibration Results for All Load Increments

Edmond, T1 Retest, 117 kips

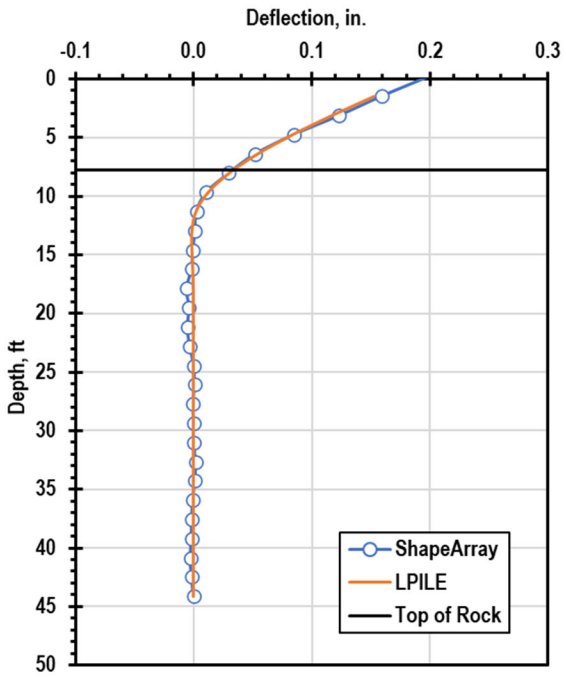

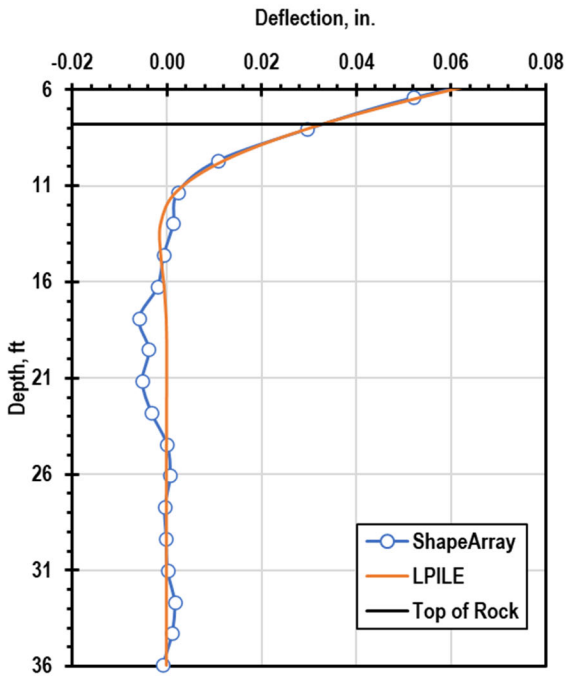

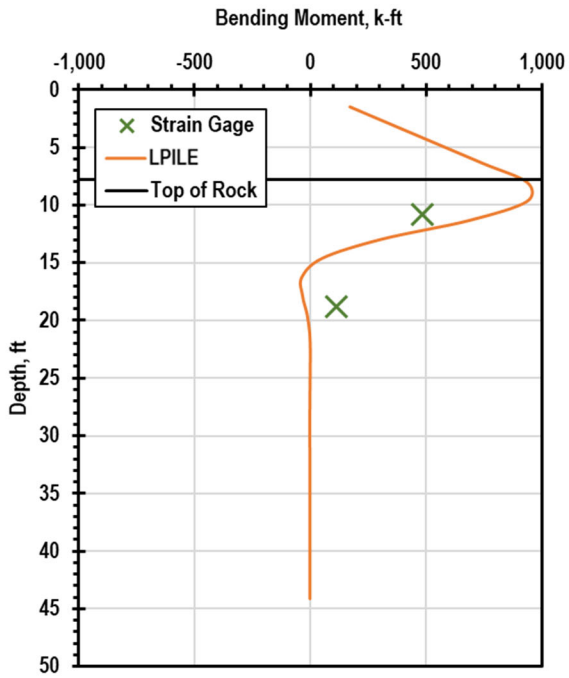

Edmond, T1 Retest, 234 kips

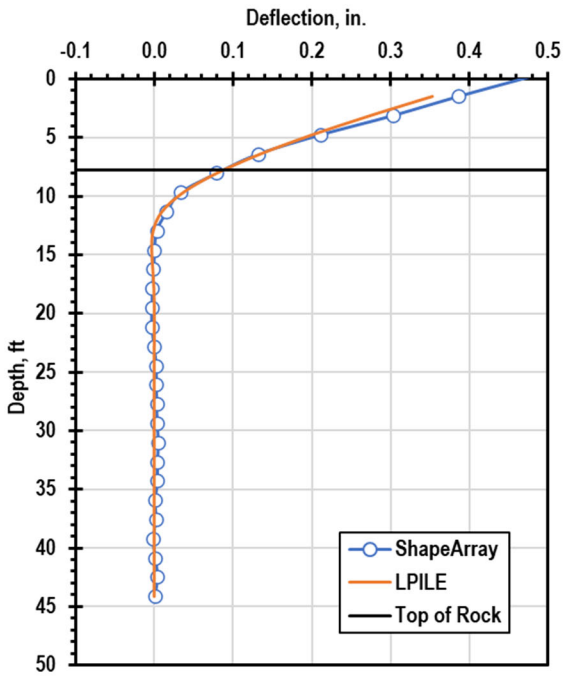

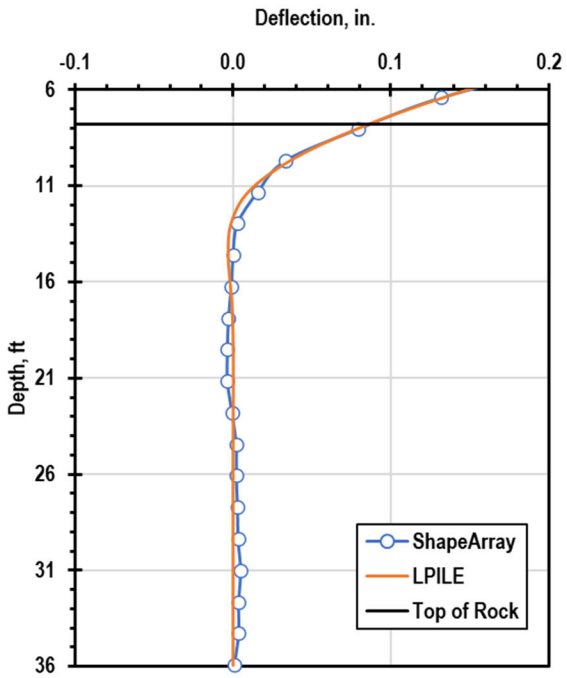

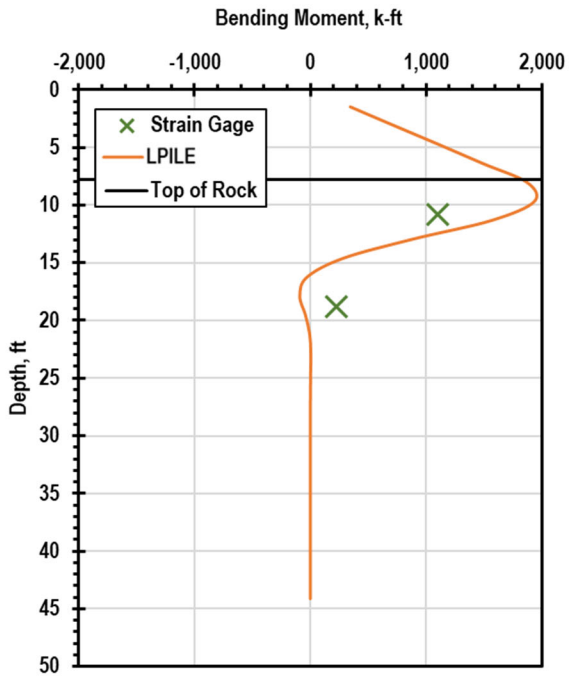

Edmond, T1 Retest, 351 kips

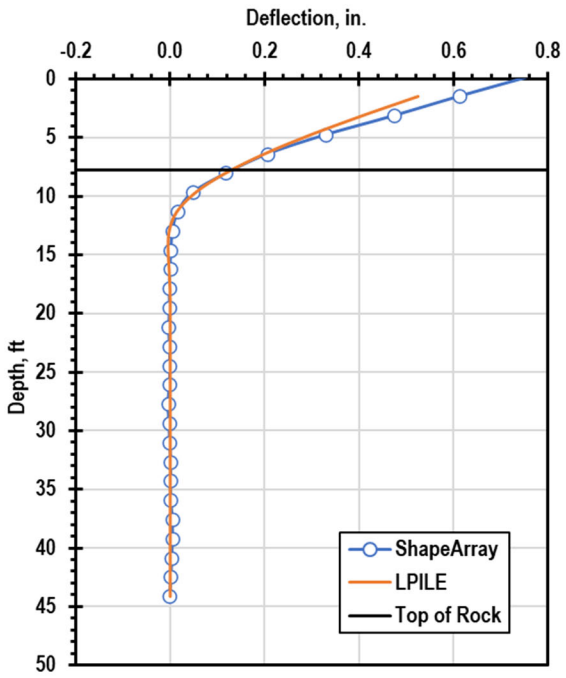

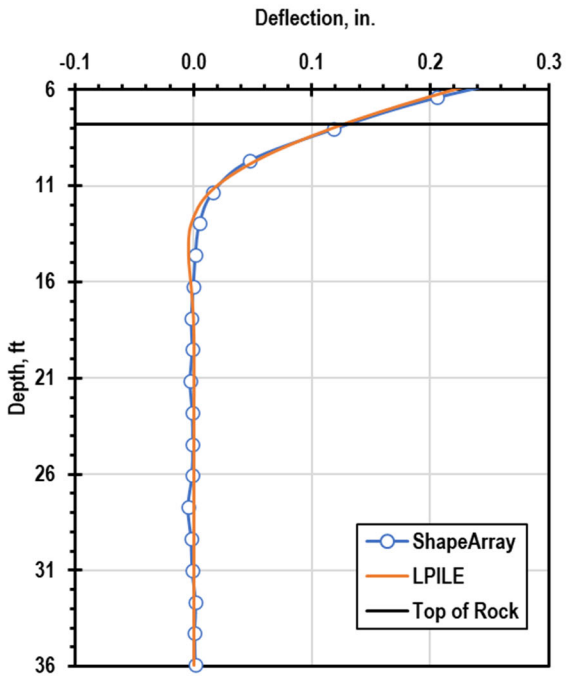

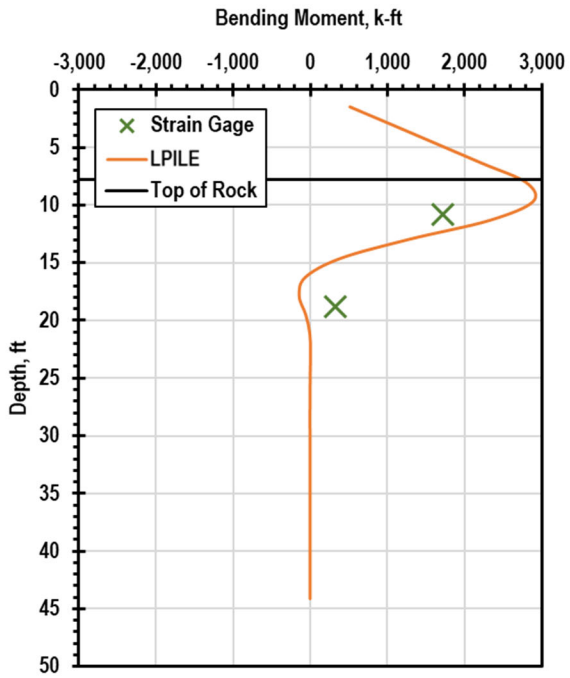

Edmond, T1 Retest, 467 kips

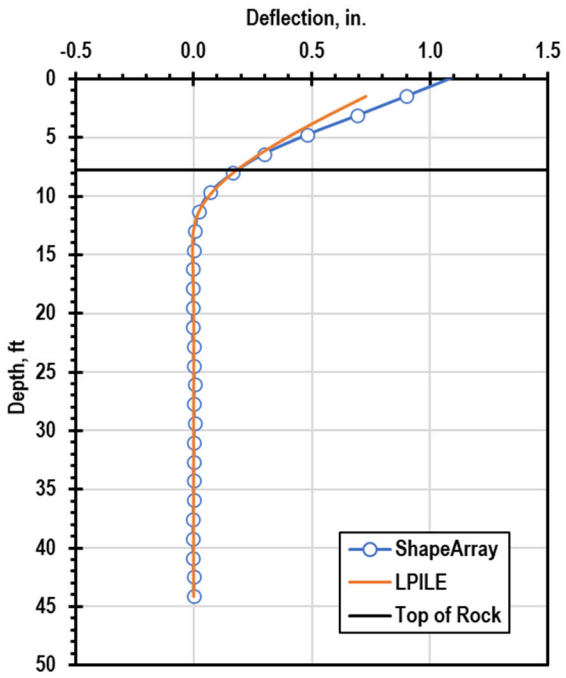

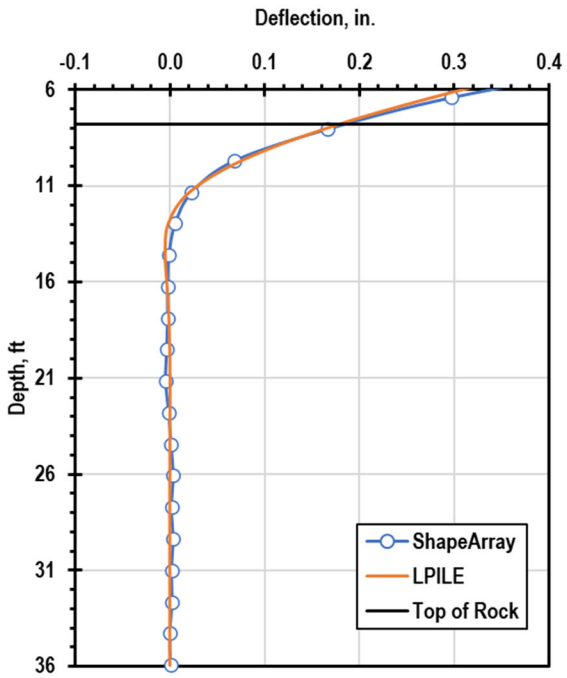

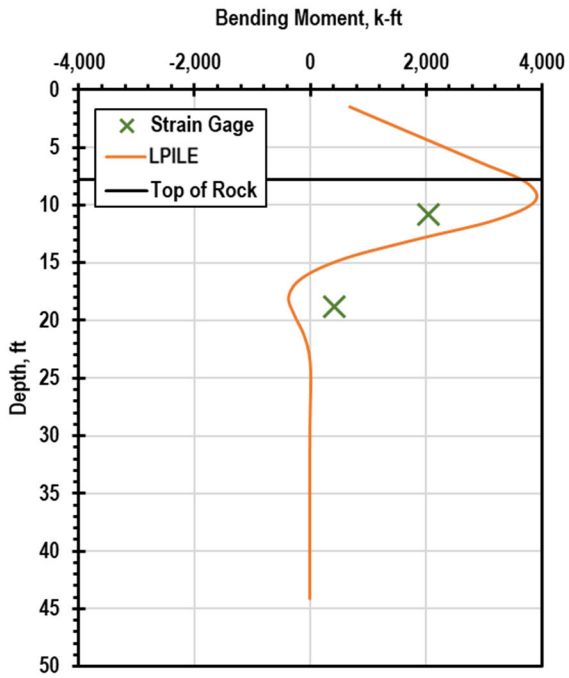

Edmond, T1 Retest, 584 kips

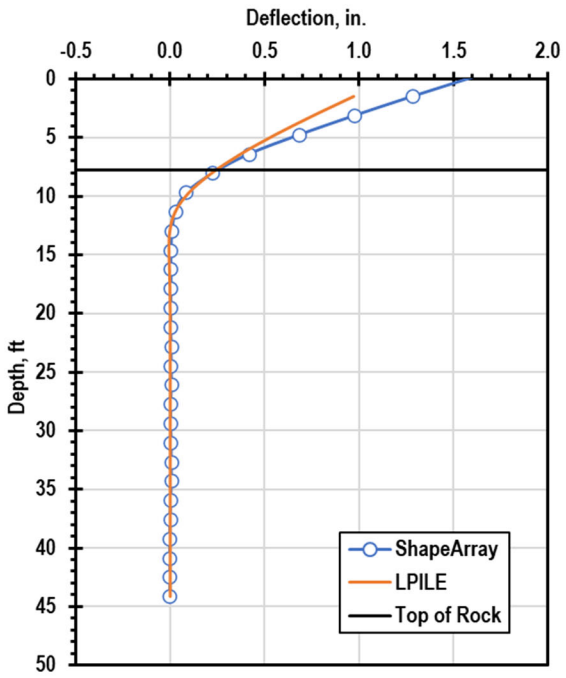

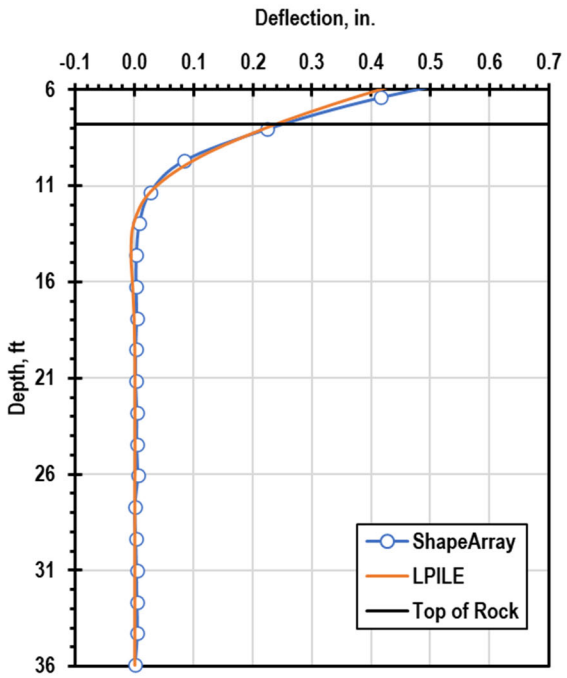

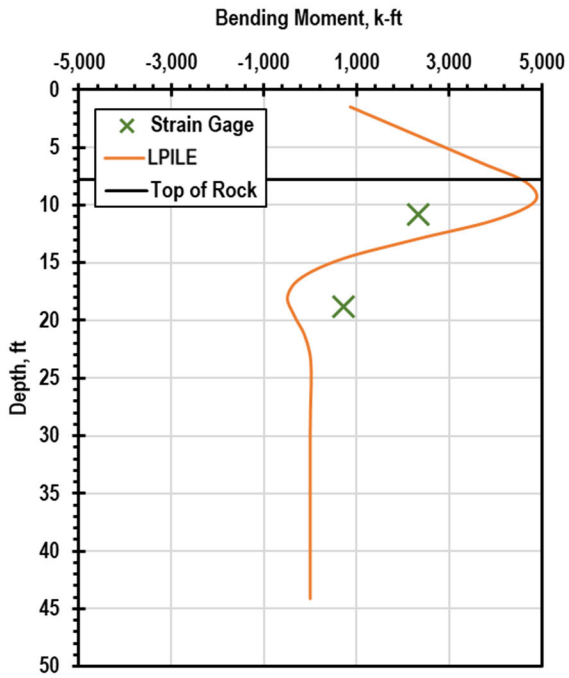

Edmond, T1 Retest, 613 kips

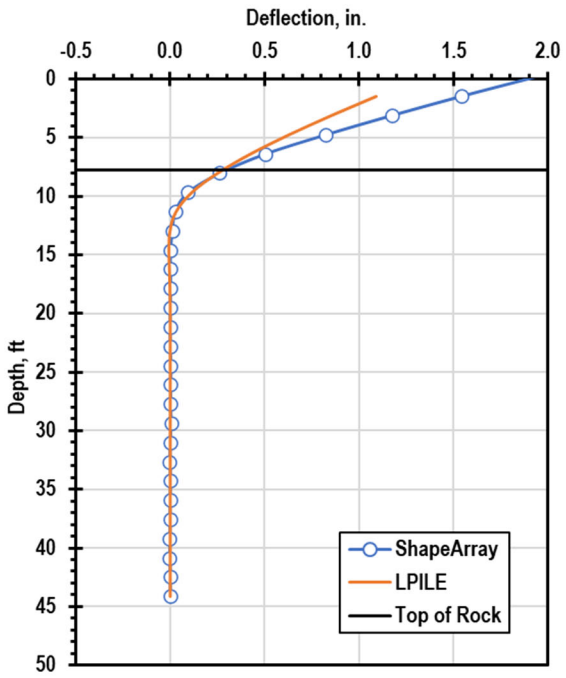

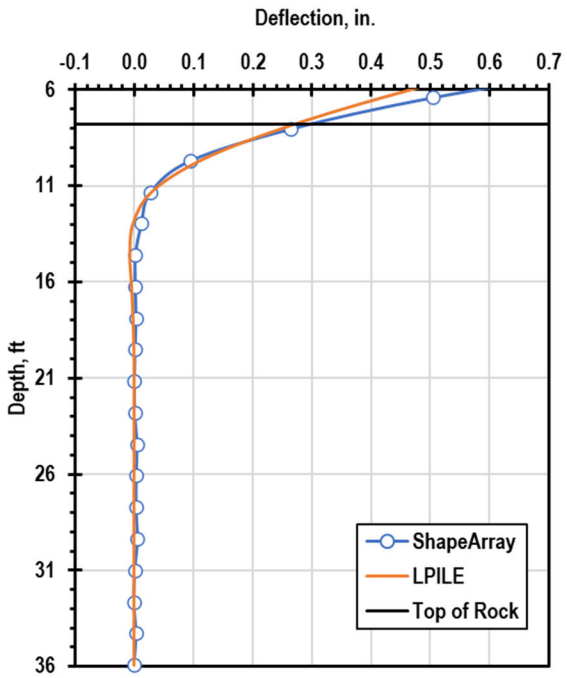

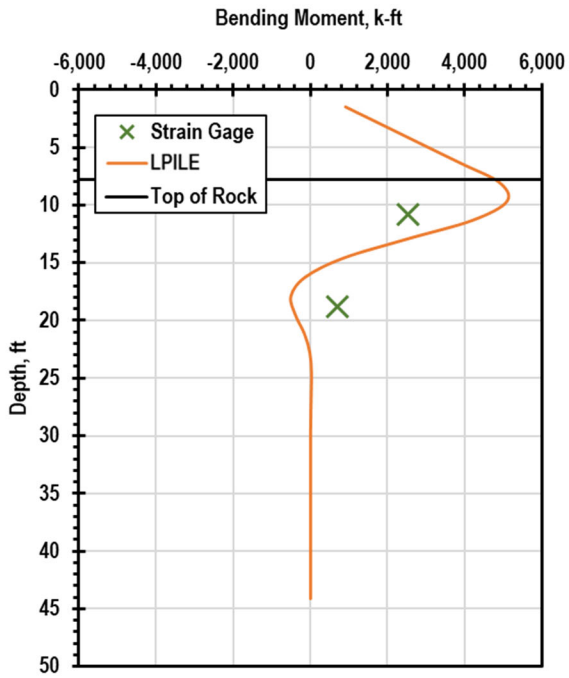

Edmond, T2 Retest, 117 kips

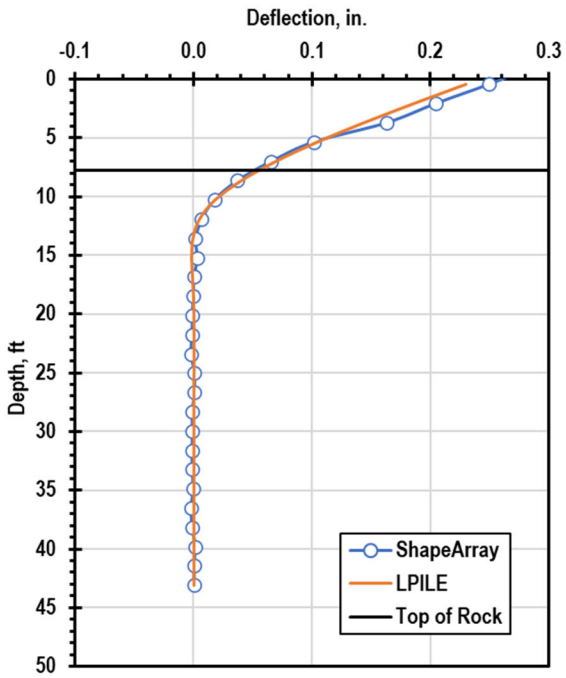

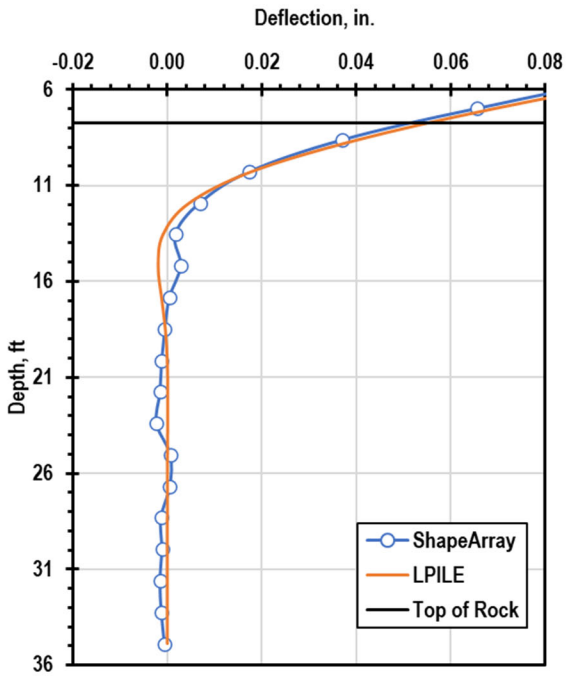

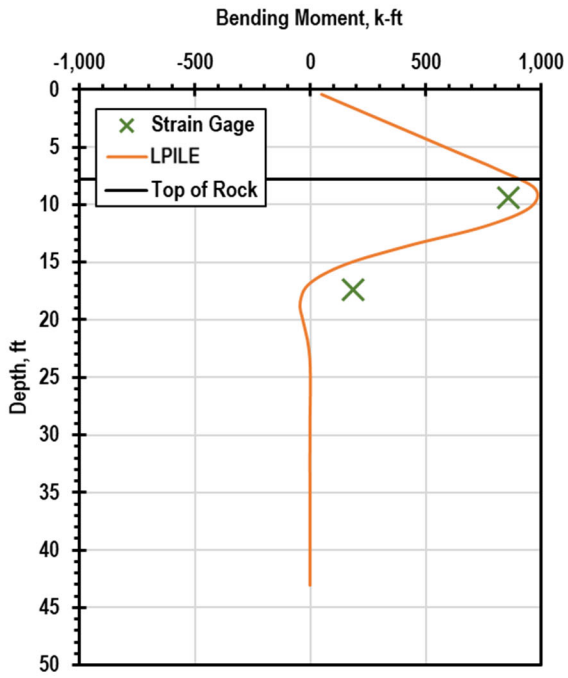

Edmond, T2 Retest, 234 kips

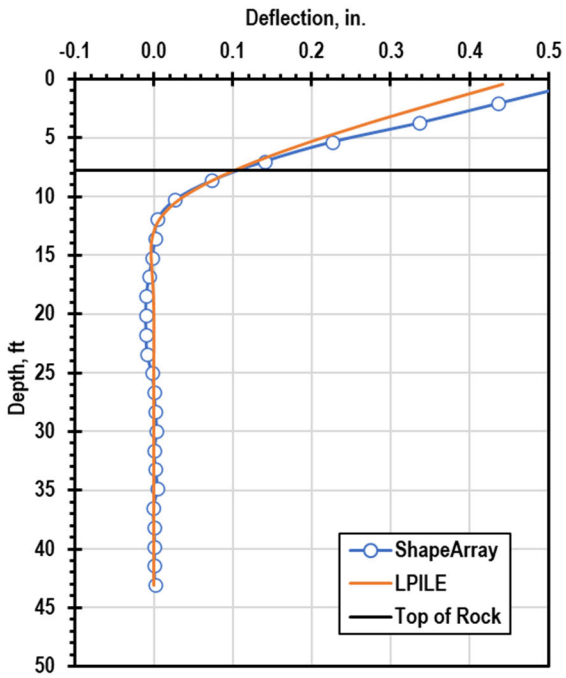

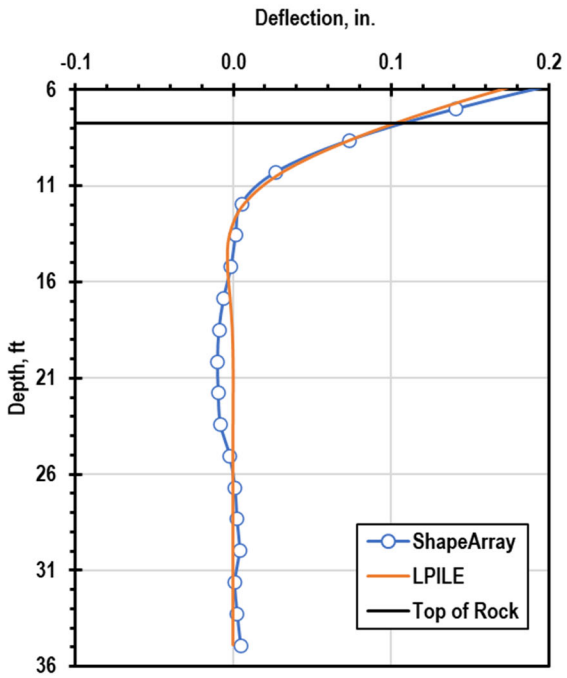

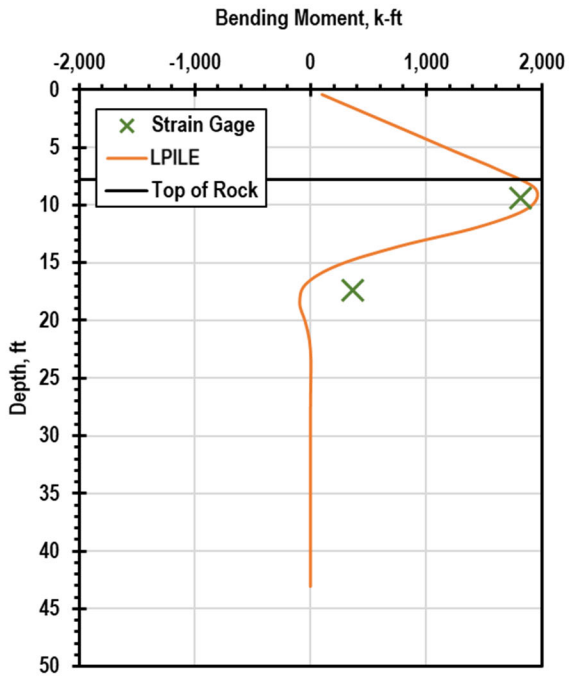

Edmond, T2 Retest, 351 kips

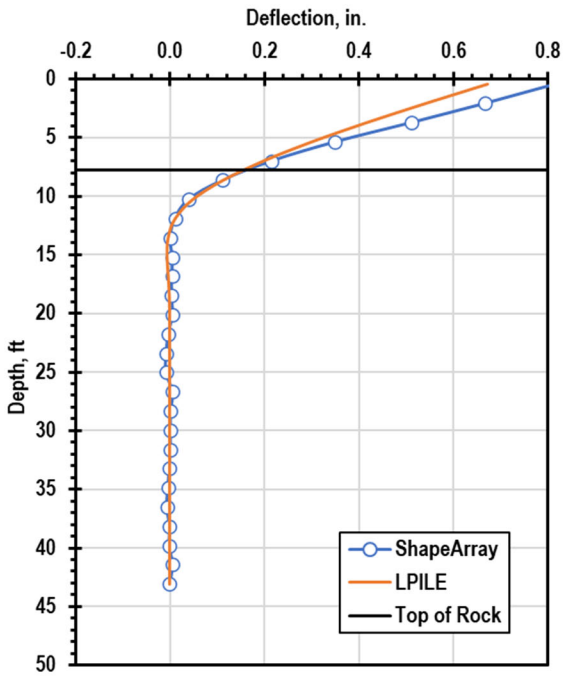

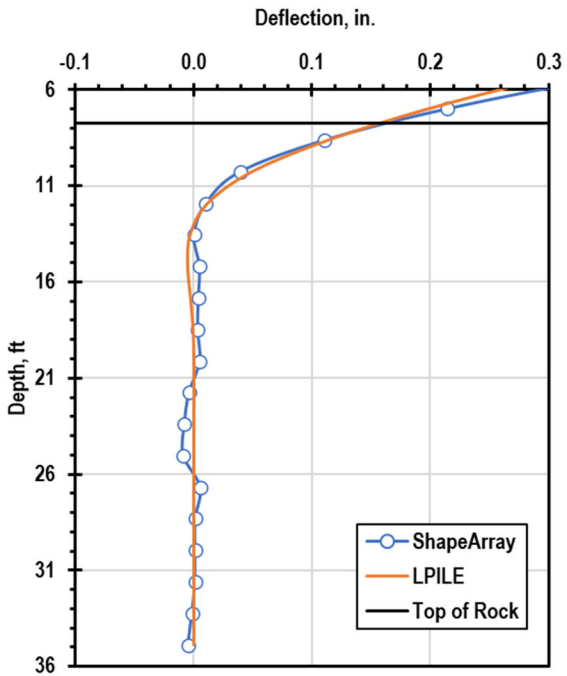

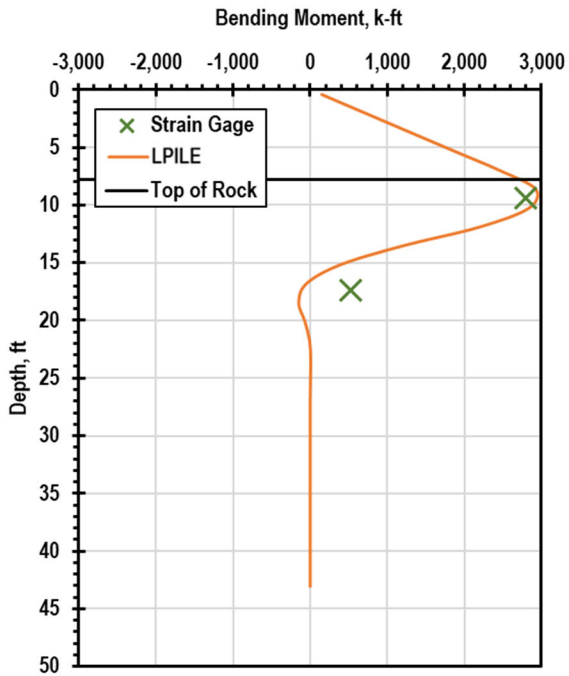

Edmond, T2 Retest, 467 kips

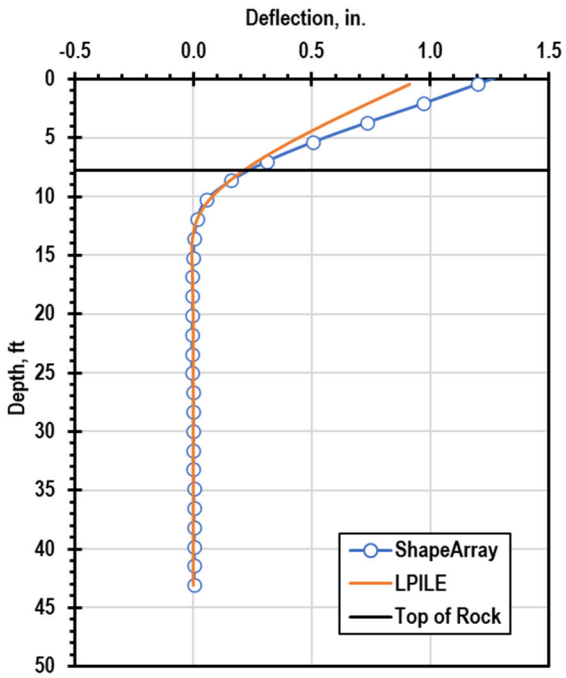

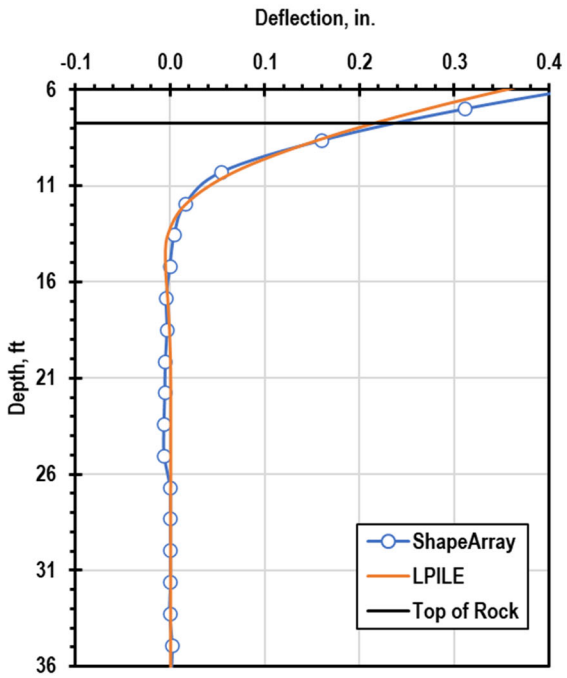

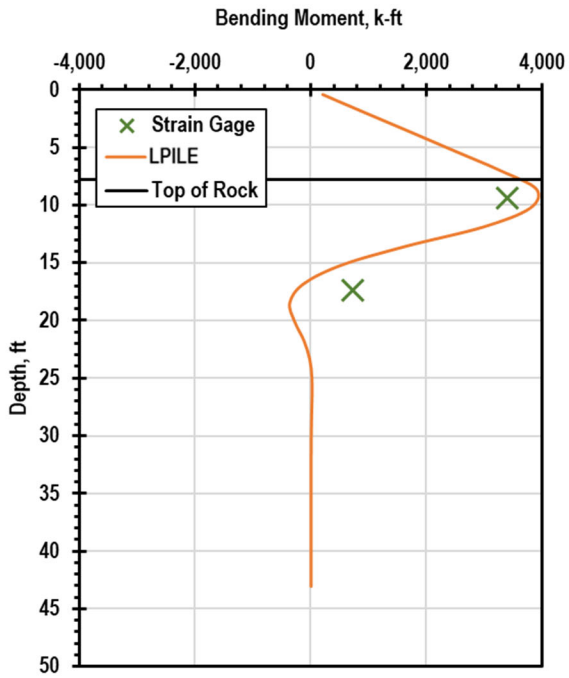

Edmond, T2 Retest, 584 kips

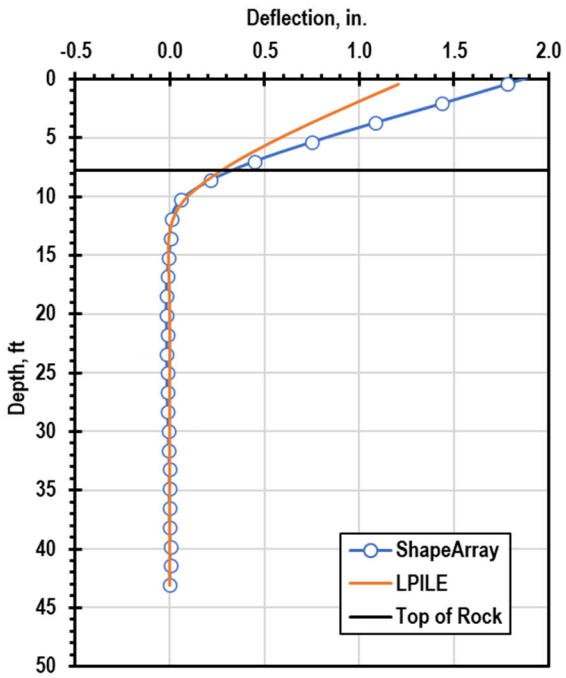

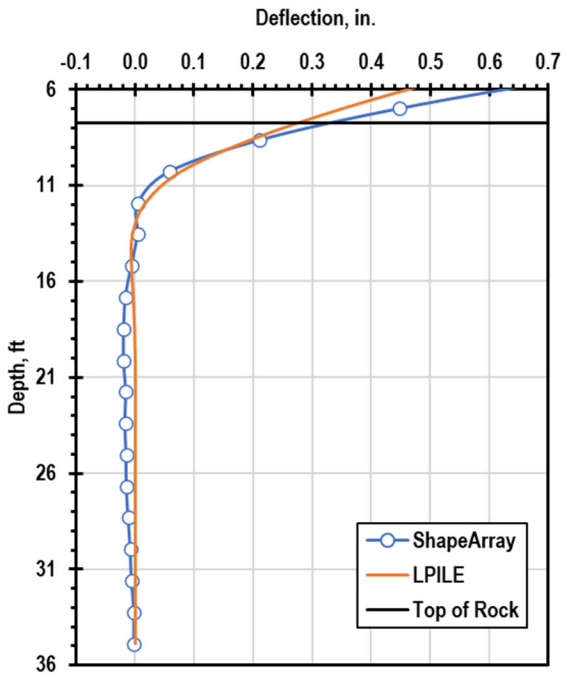

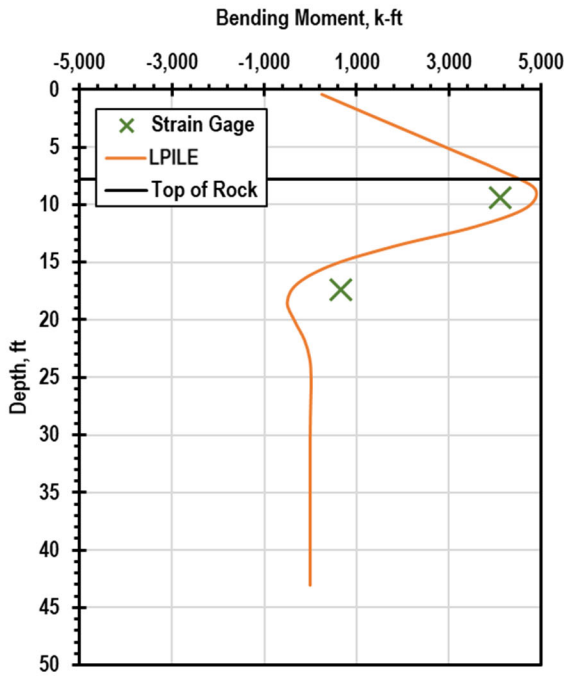

Edmond, T2 Retest, 613 kips

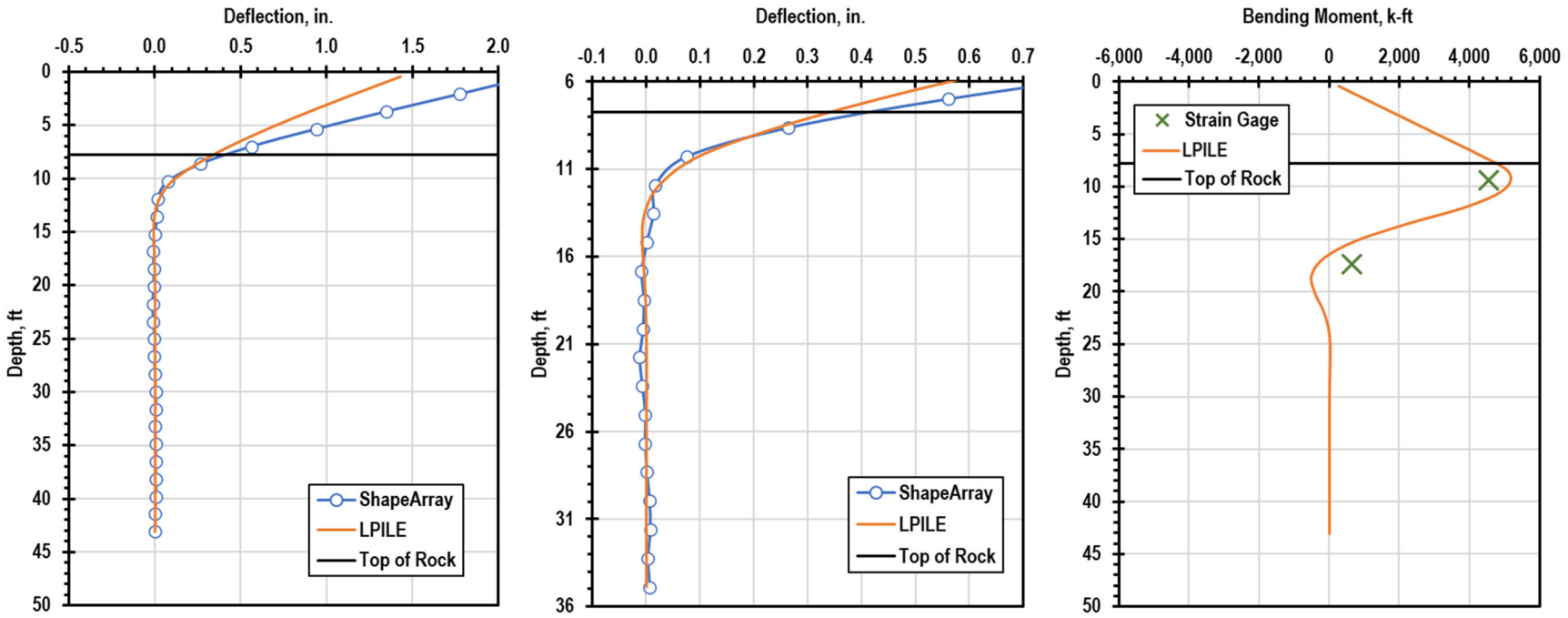

Edmond, T3 Retest, 117 kips

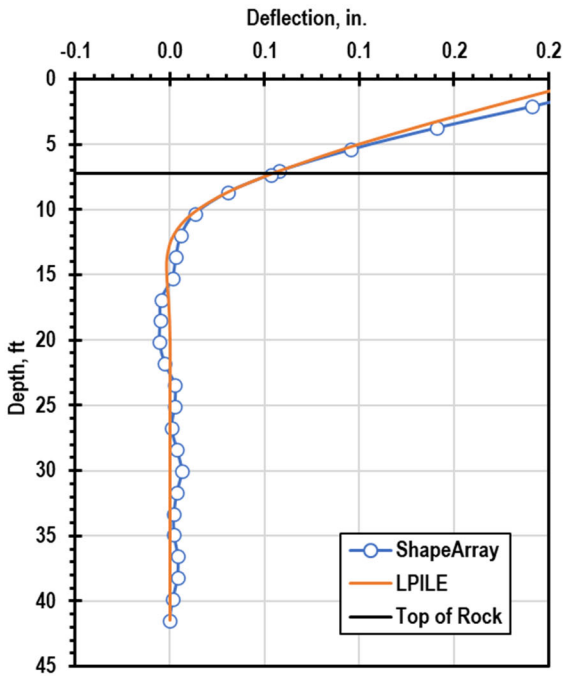

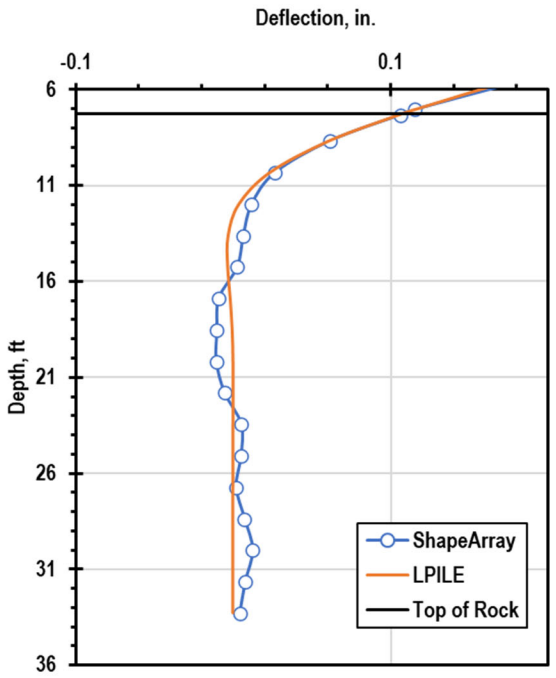

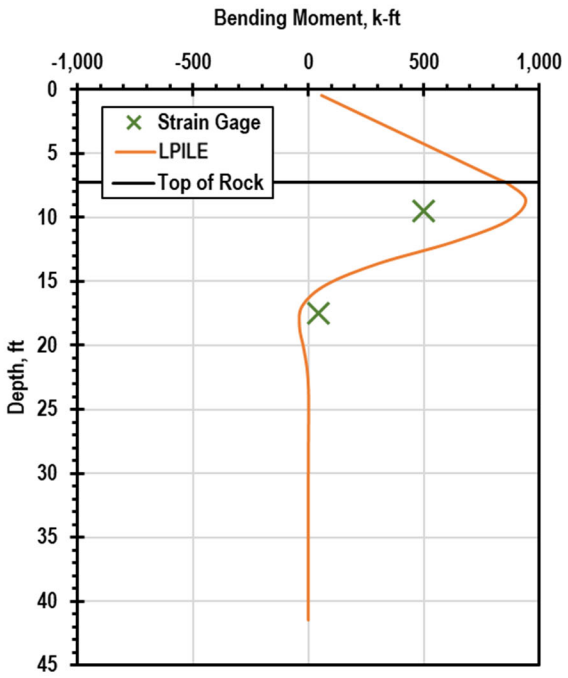

Edmond, T3 Retest, 234 kips

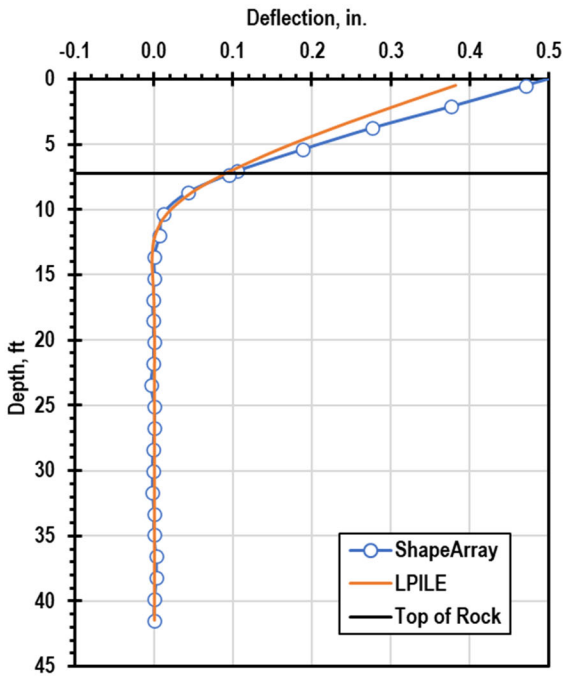

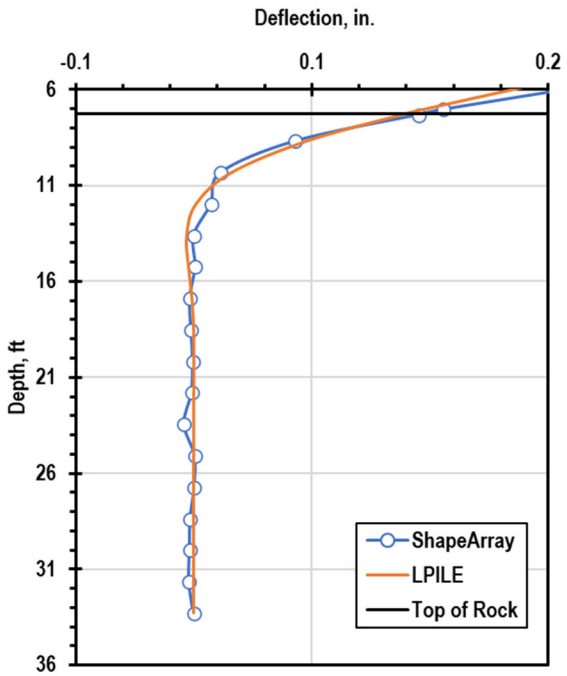

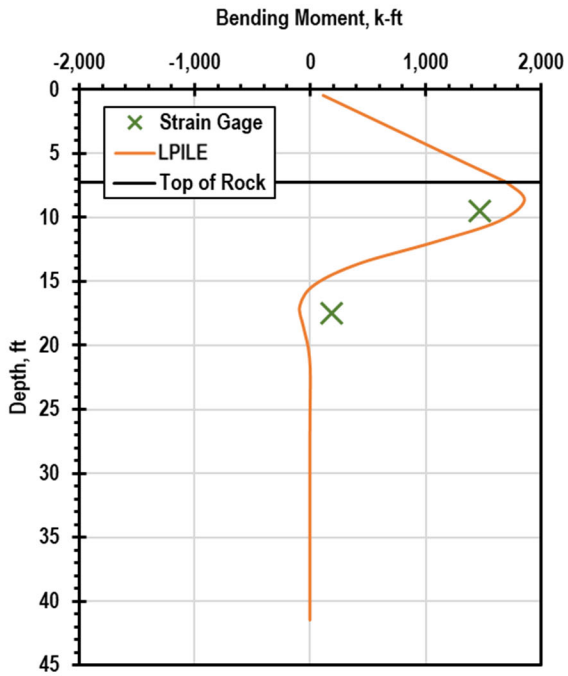

Edmond, T3 Retest, 351 kips

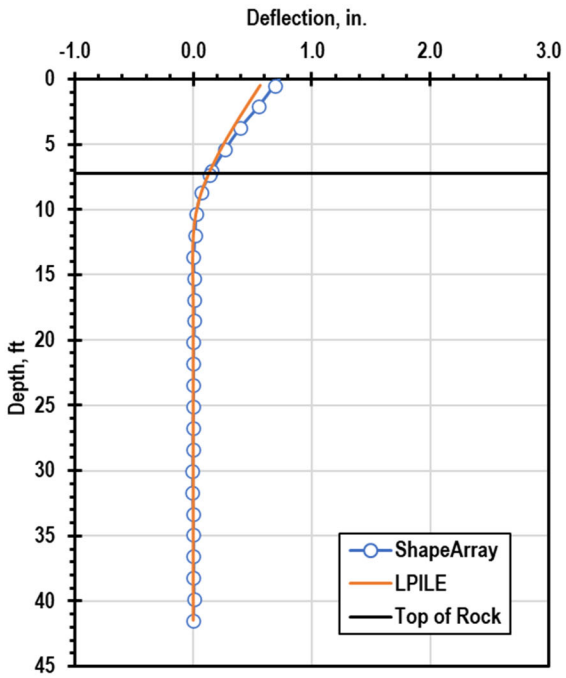

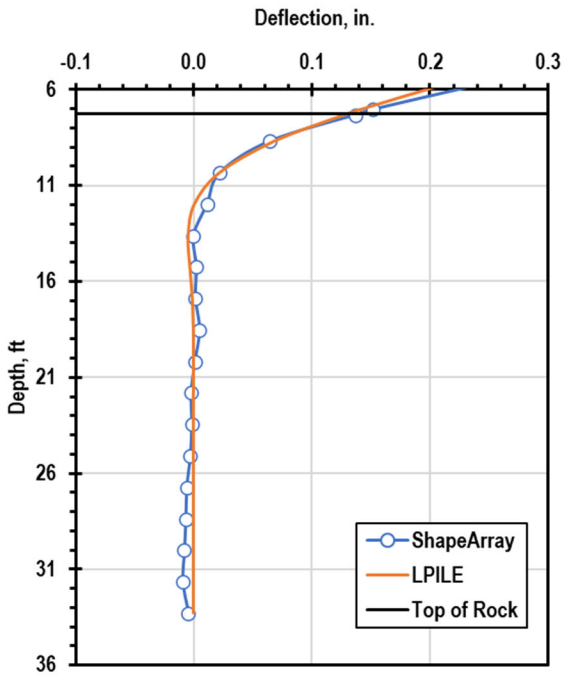

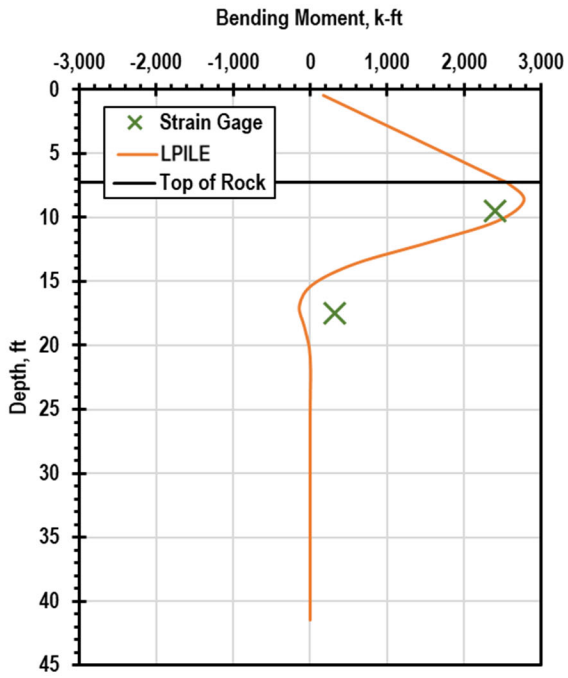

Edmond, T3 Retest, 467 kips

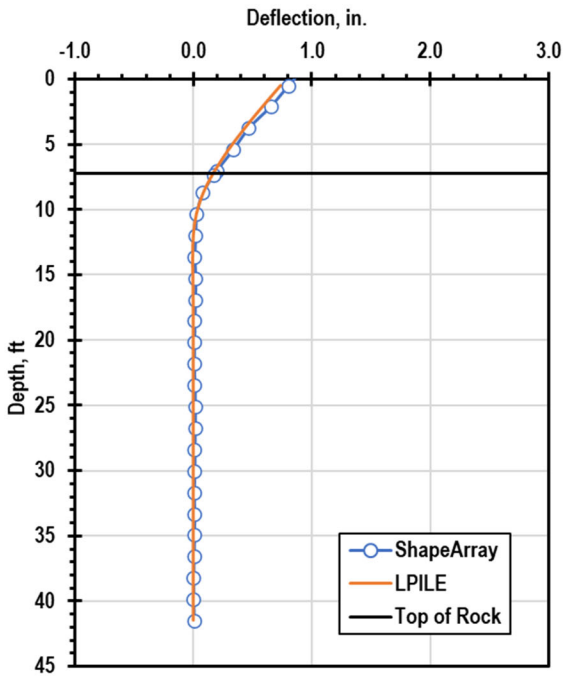

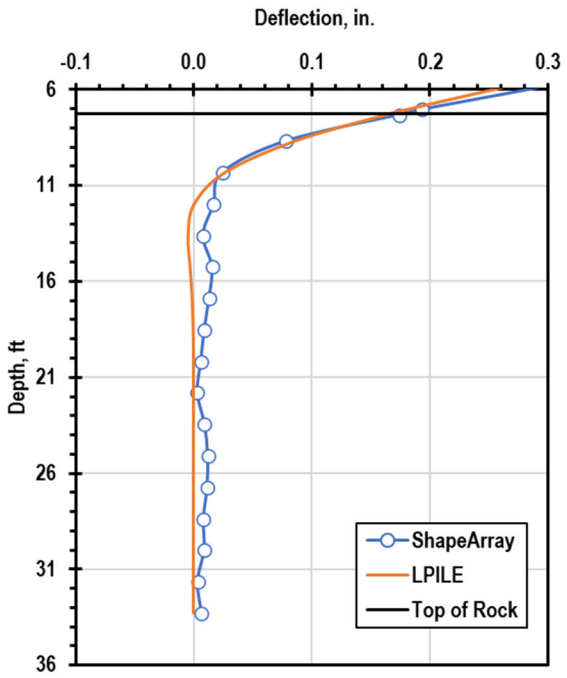

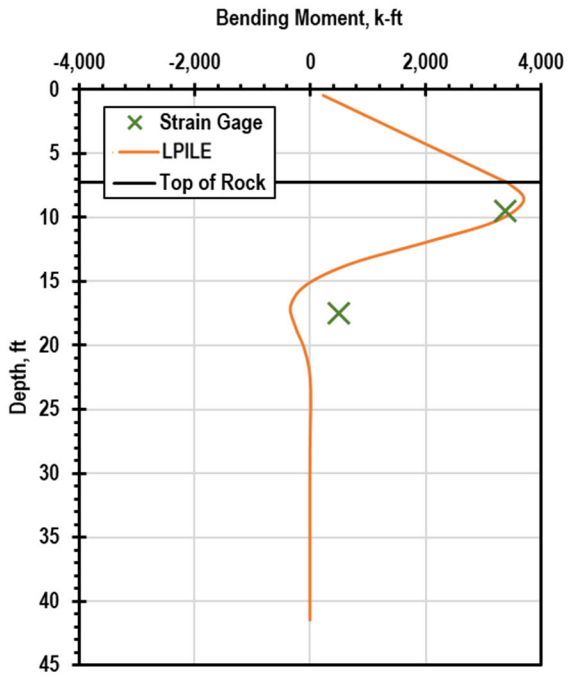

Edmond, T3 Retest, 584 kips

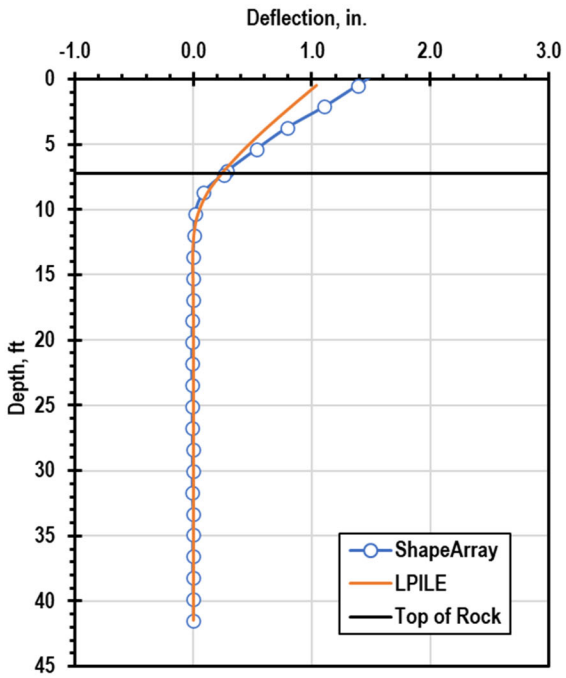

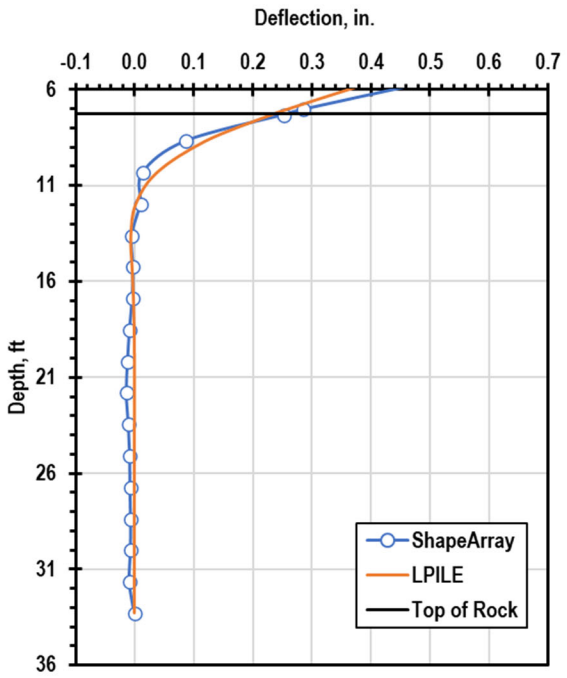

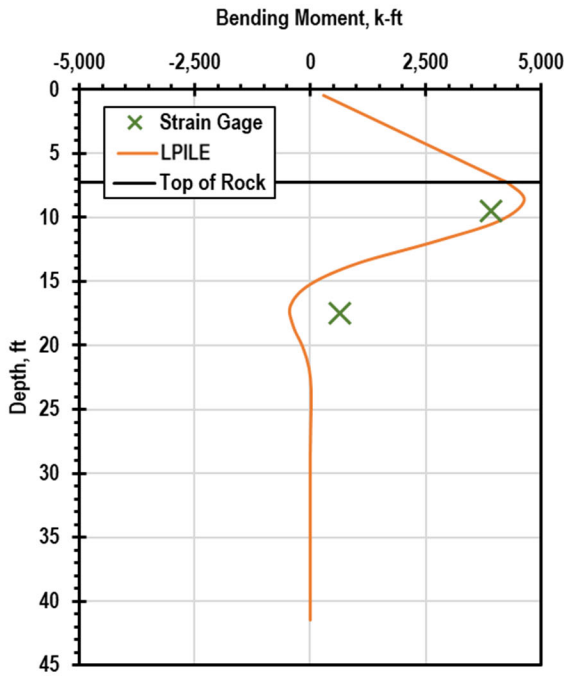

Edmond, T3 Retest, 643 kips

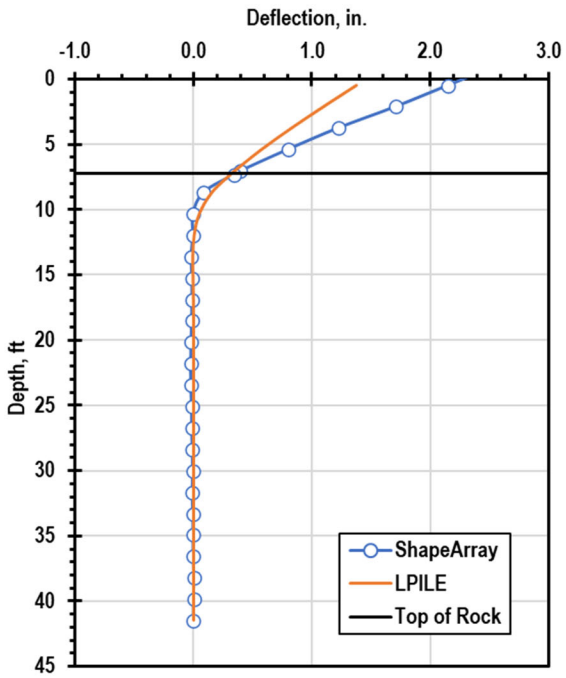

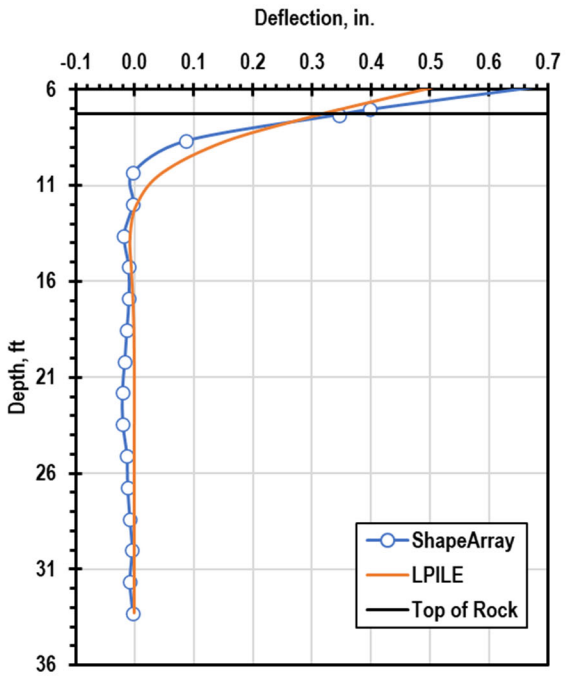

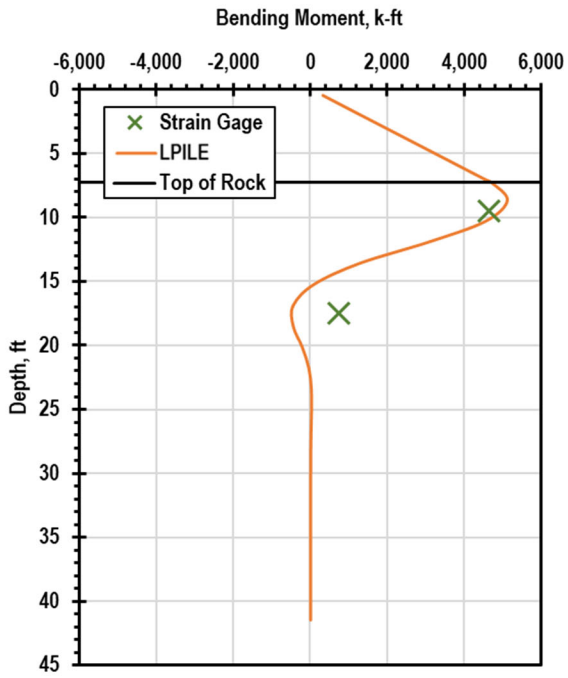

Edmond, T3 Retest, 672 kips

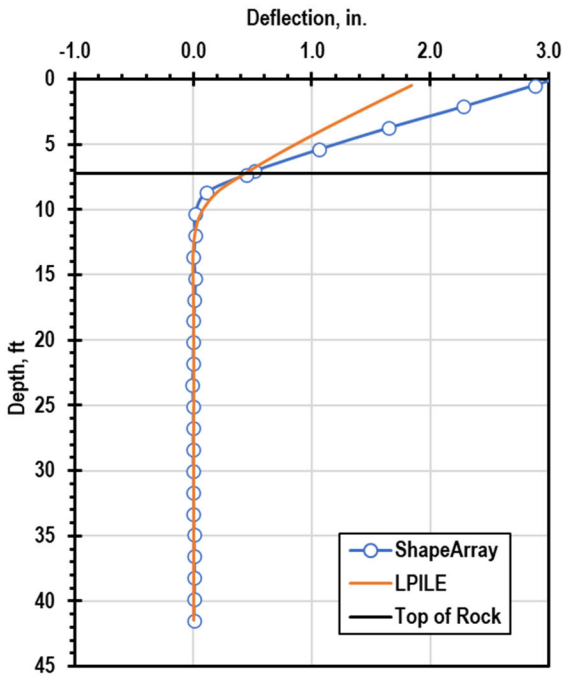

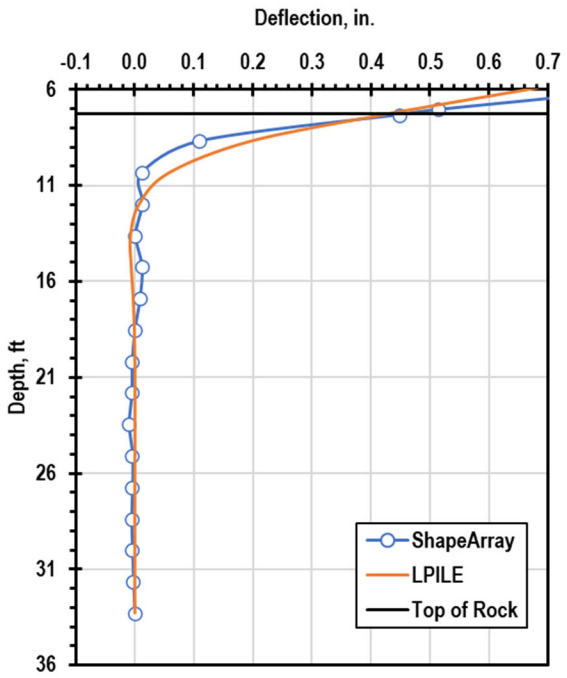

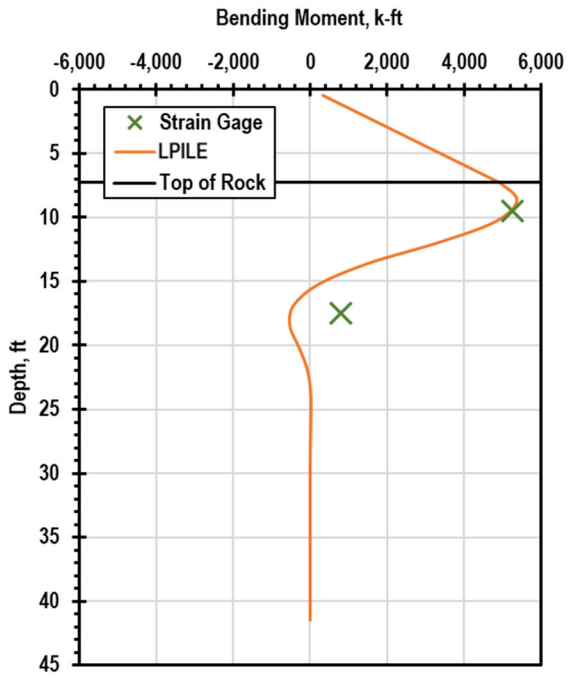

Edmond, T4 Retest, 117 kips

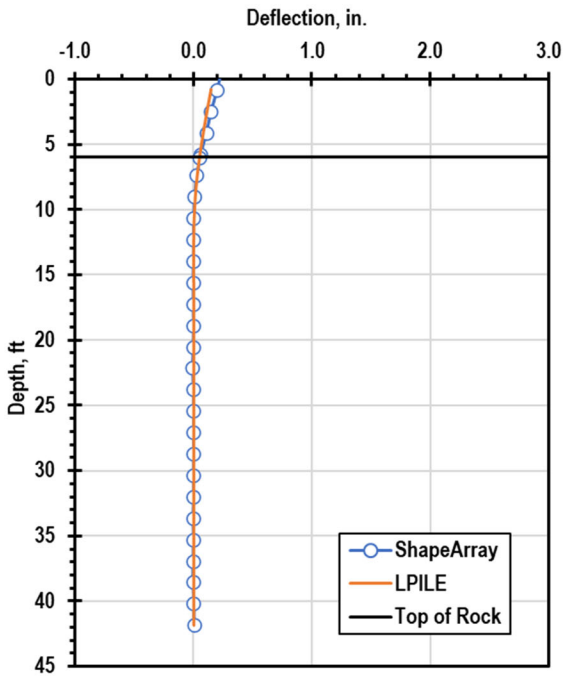

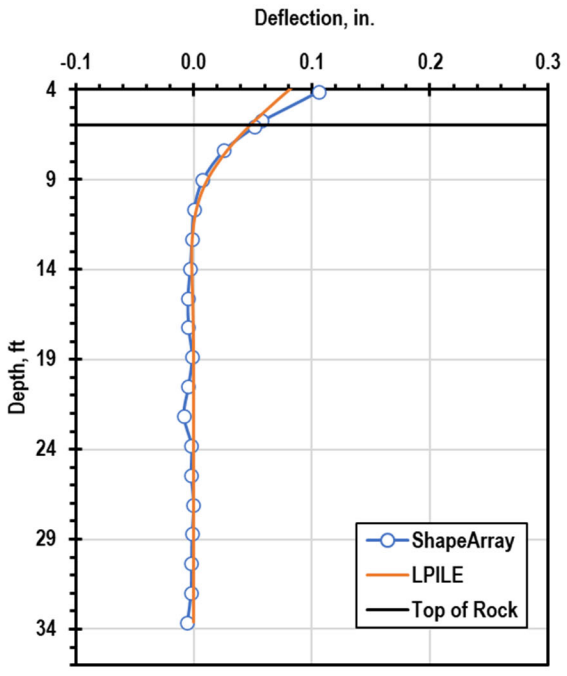

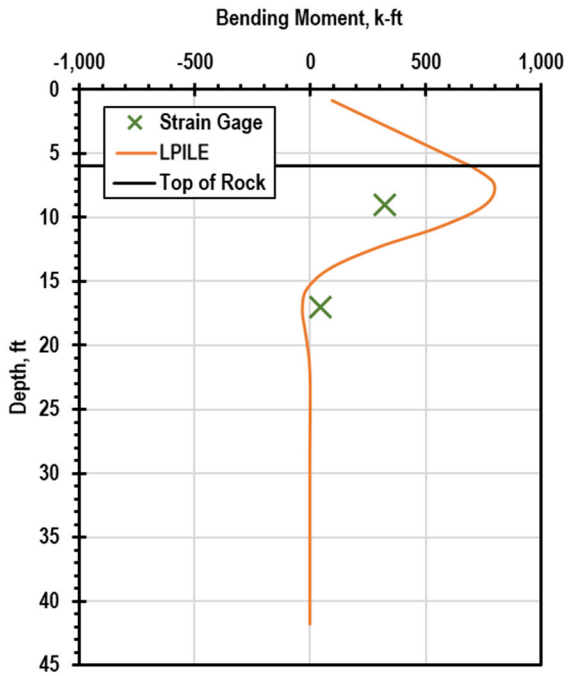

Edmond, T4 Retest, 234 kips

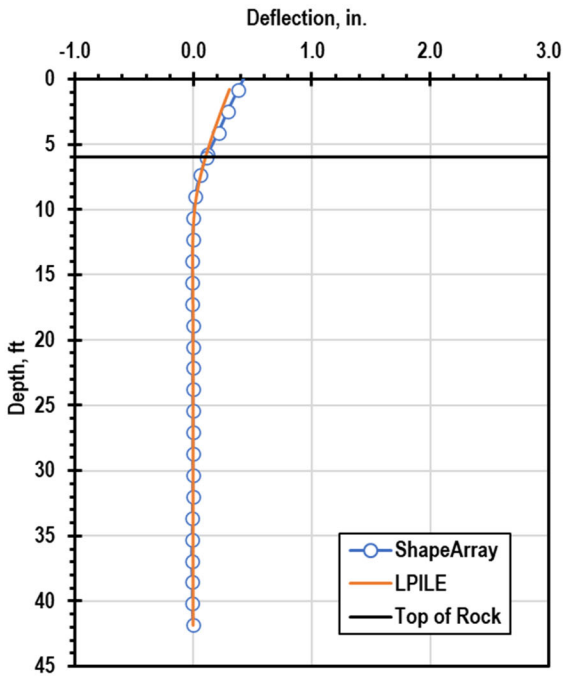

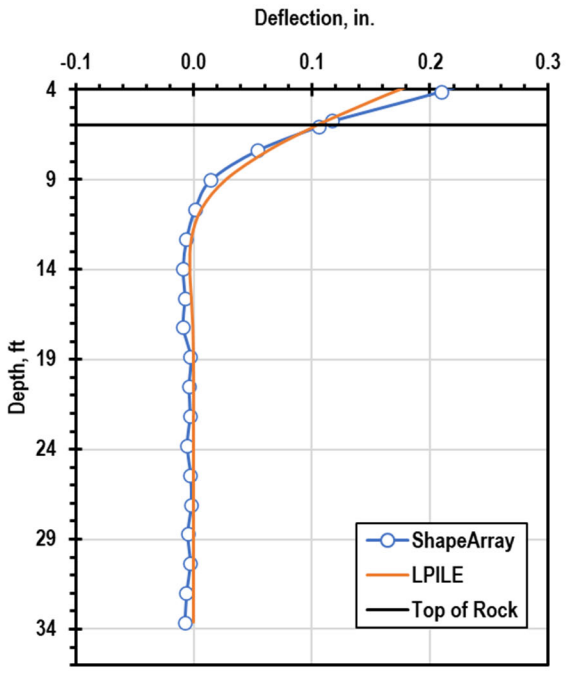

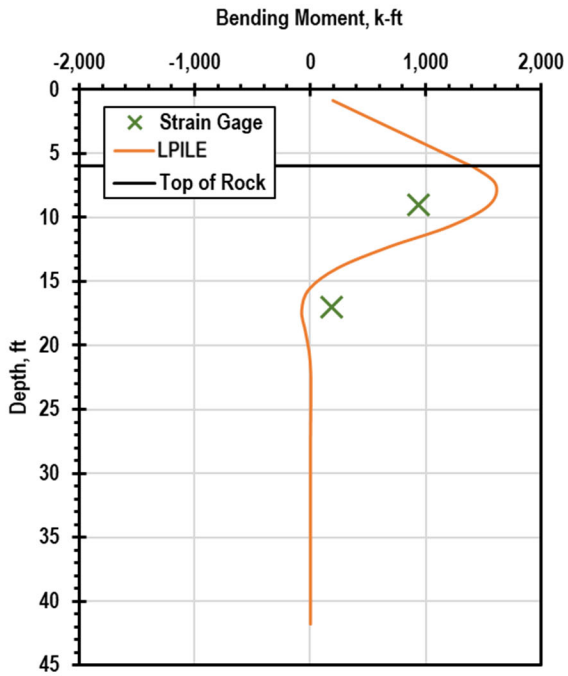

Edmond, T4 Retest, 351 kips

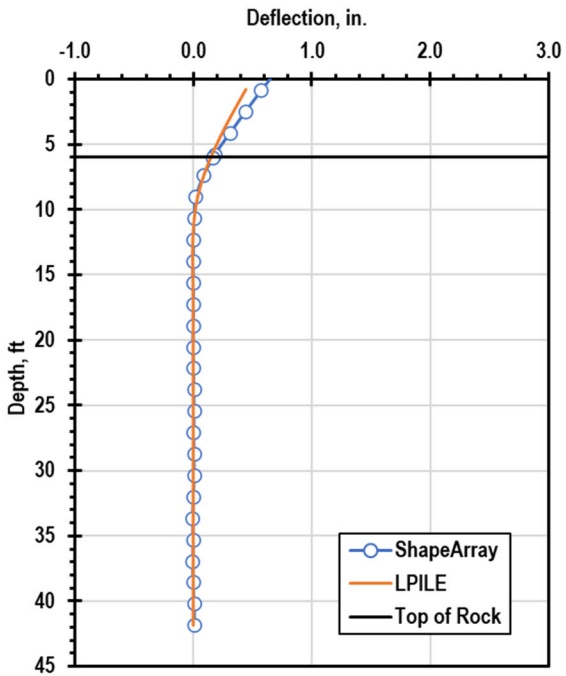

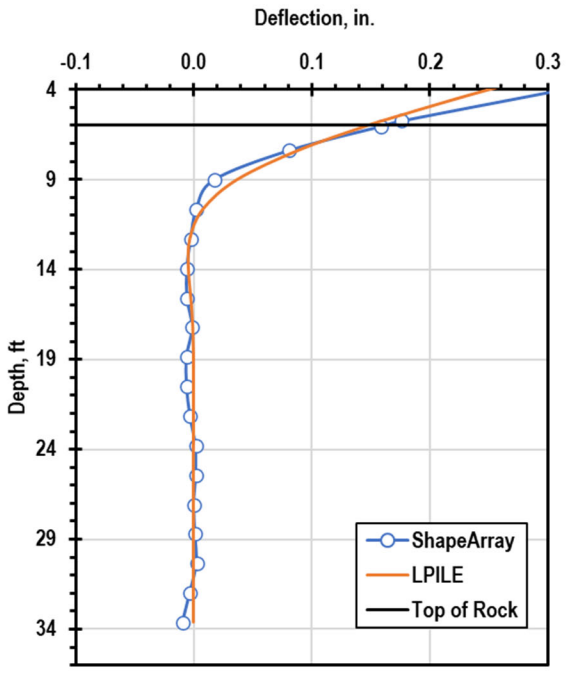

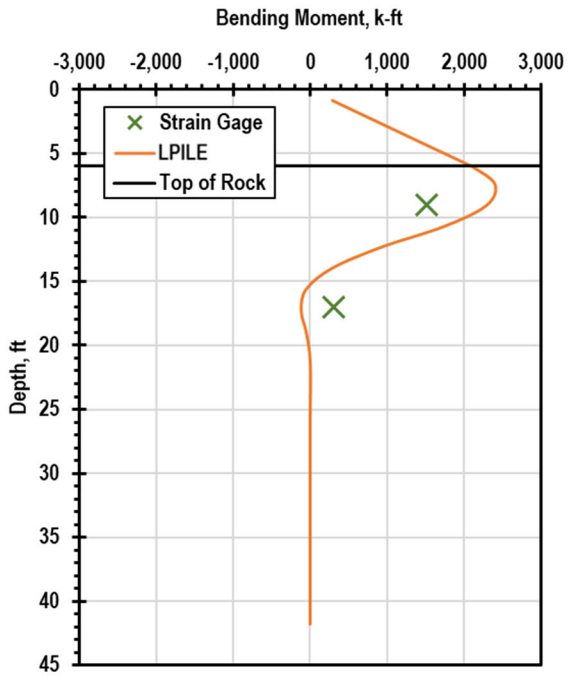

Edmond, T4 Retest, 467 kips

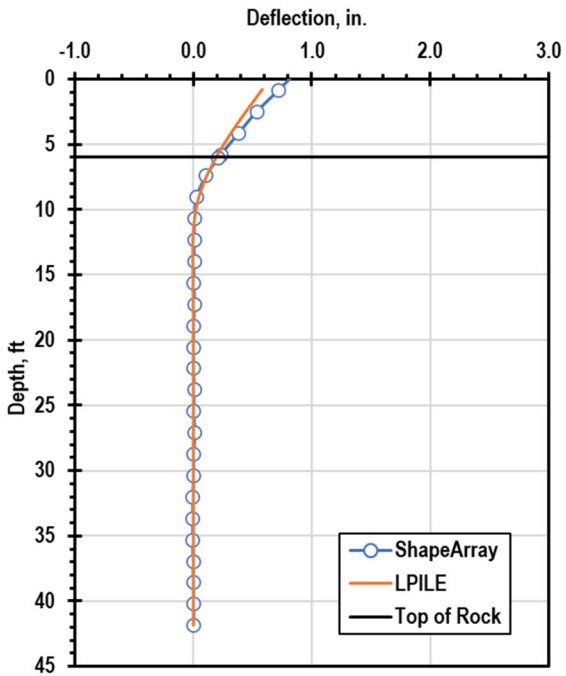

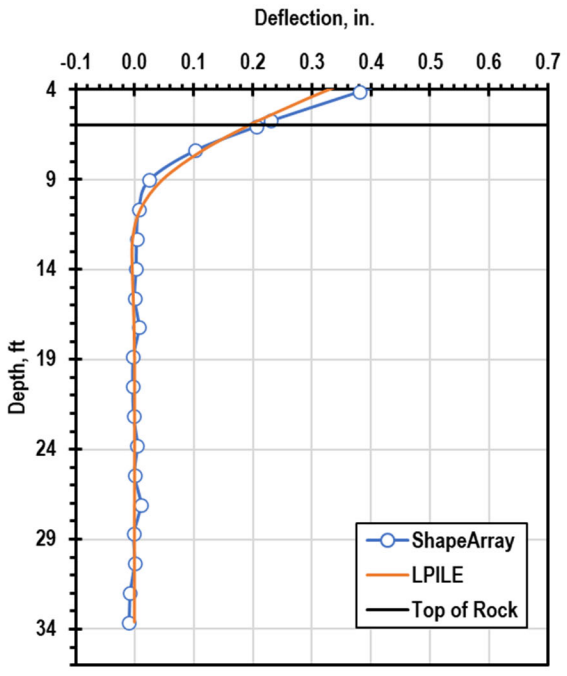

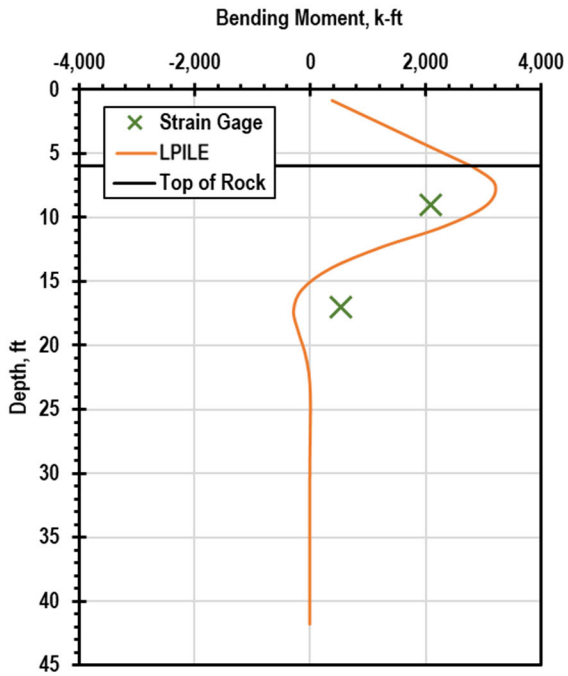

Edmond, T4 Retest, 584 kips

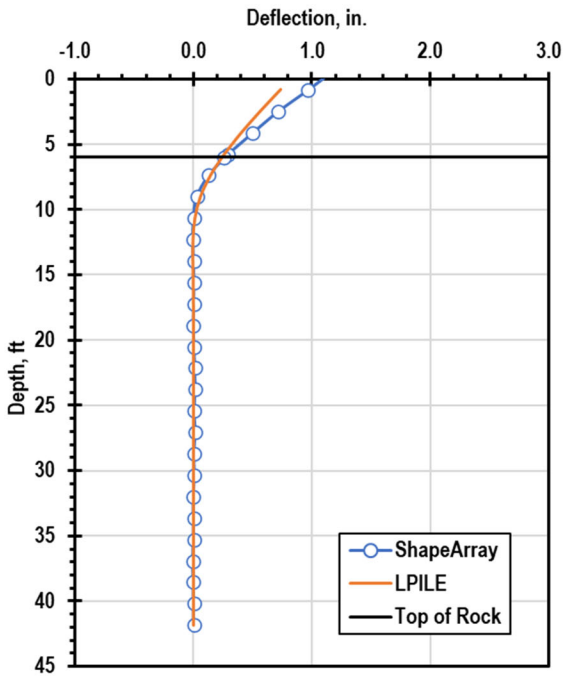

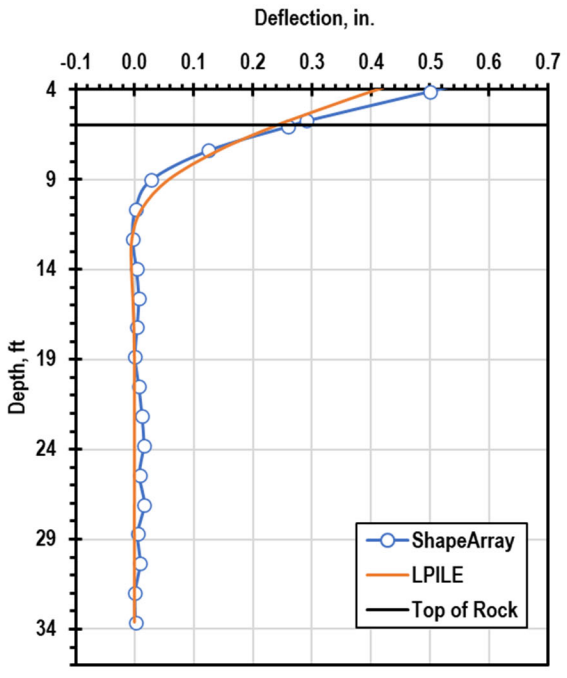

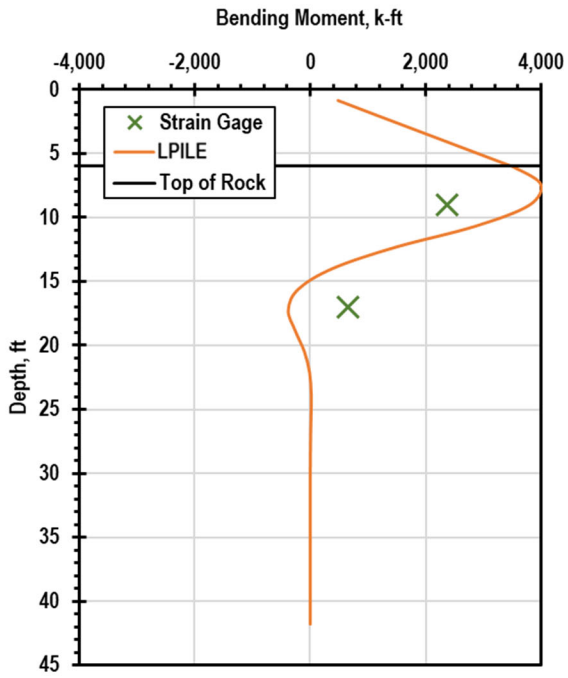

Edmond, T4 Retest, 643 kips

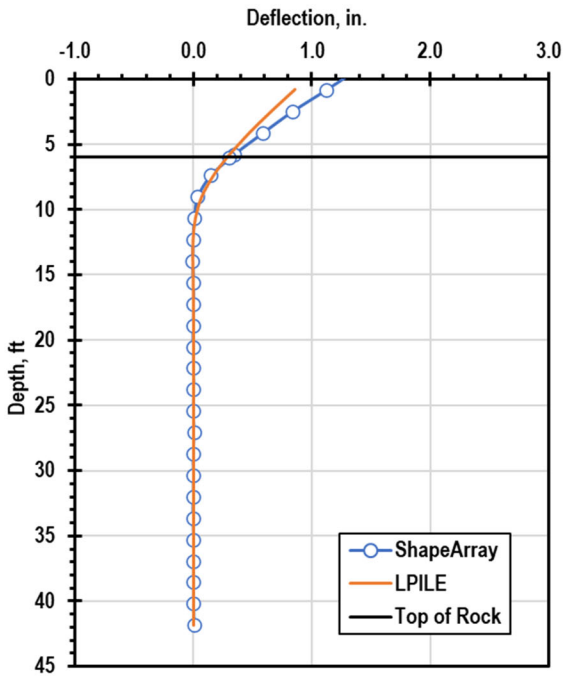

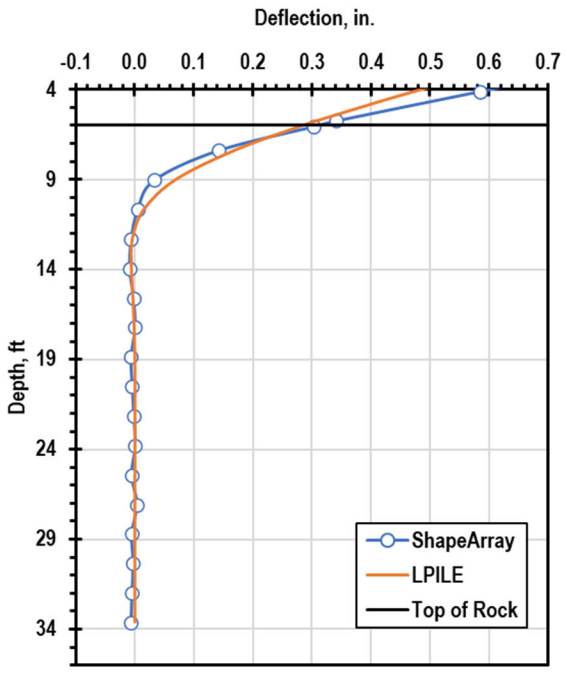

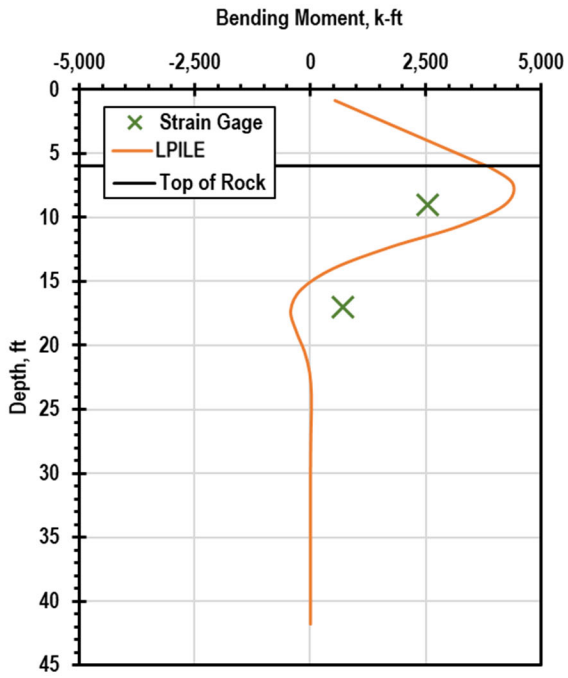

Edmond, T4 Retest, 672 kips

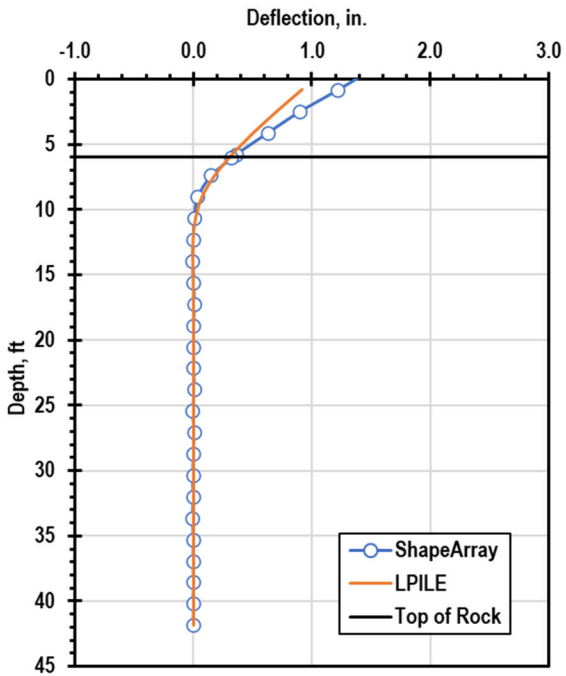

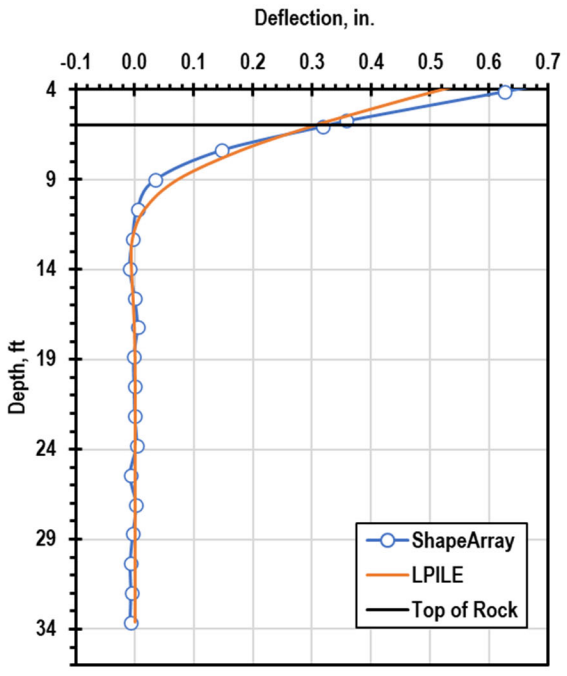

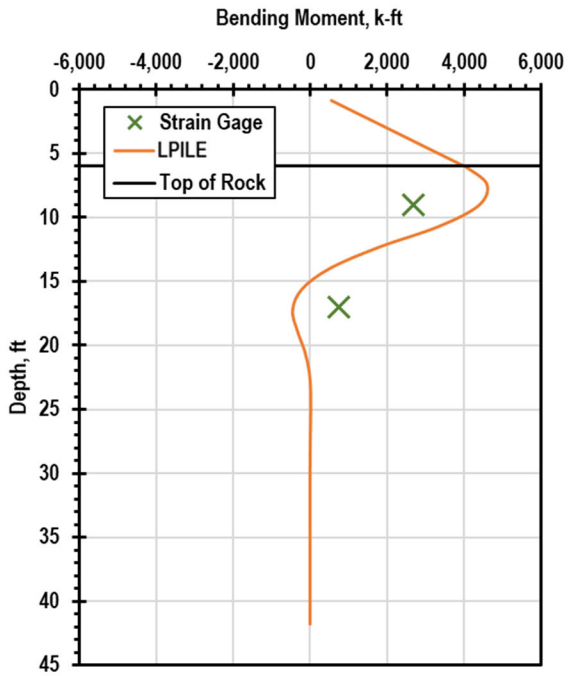

Minco, T1, 59 kips

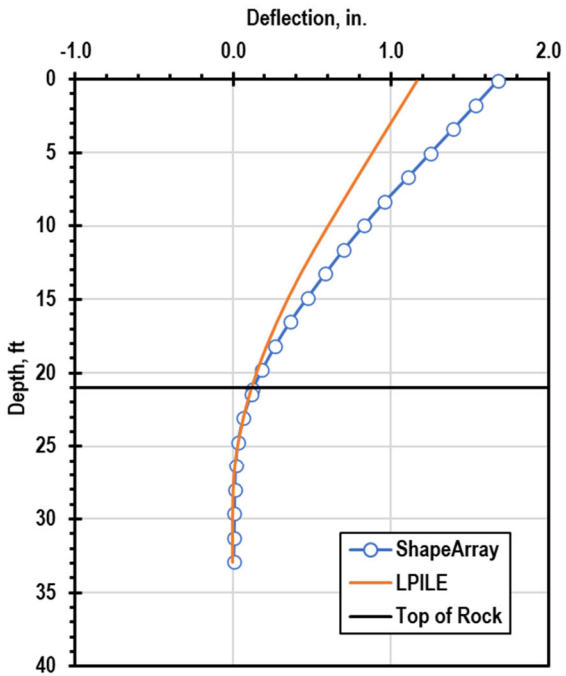

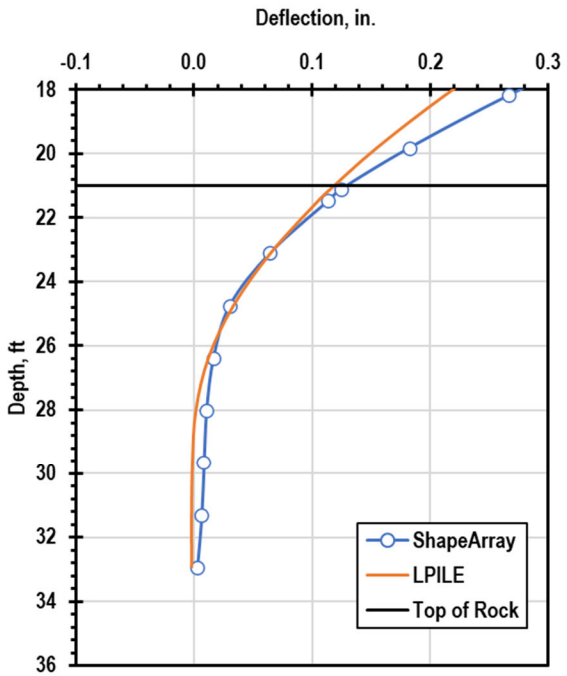

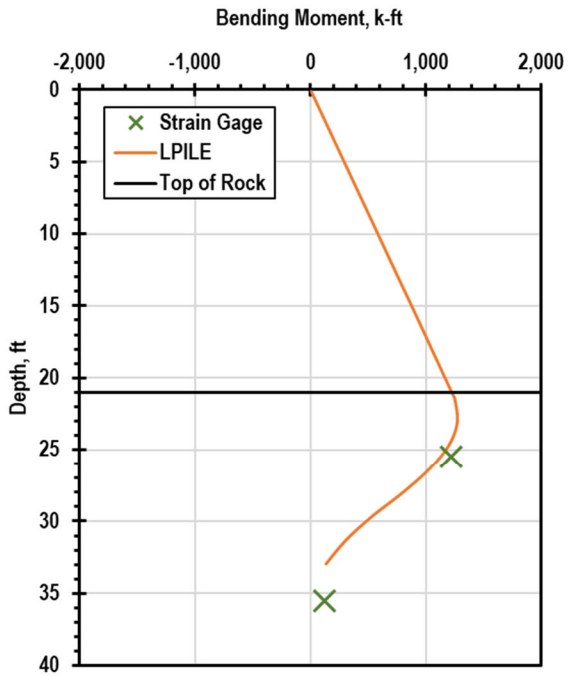

Minco, T1, 117 kips

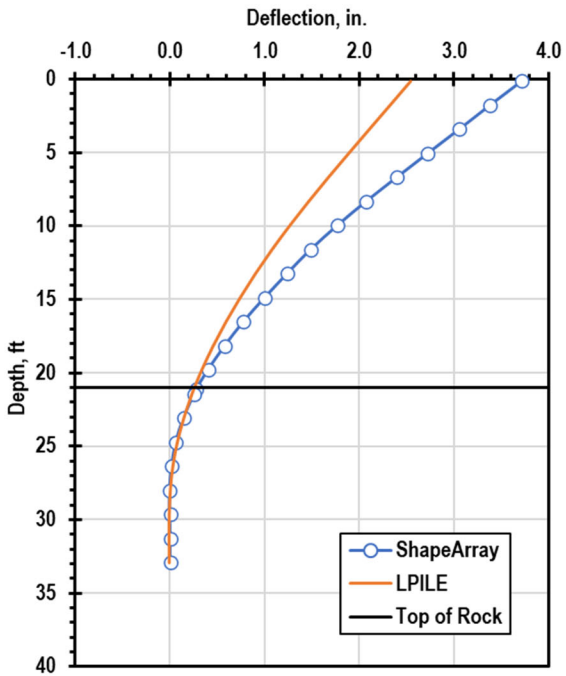

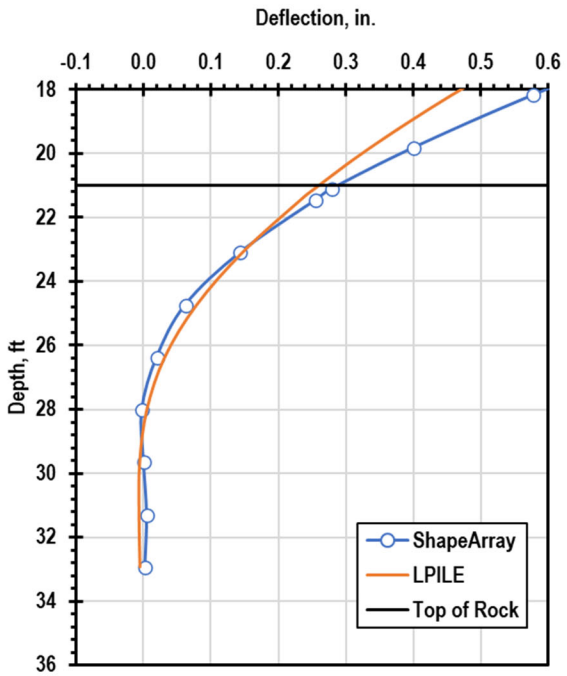

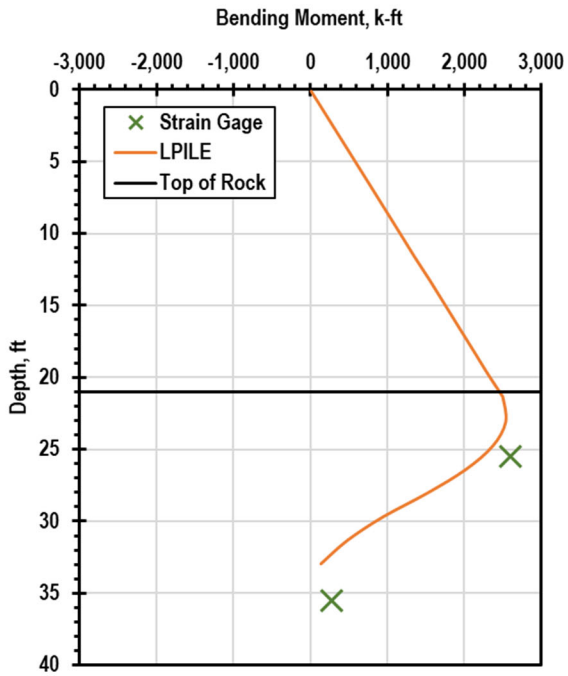

Minco, T1, 146 kips

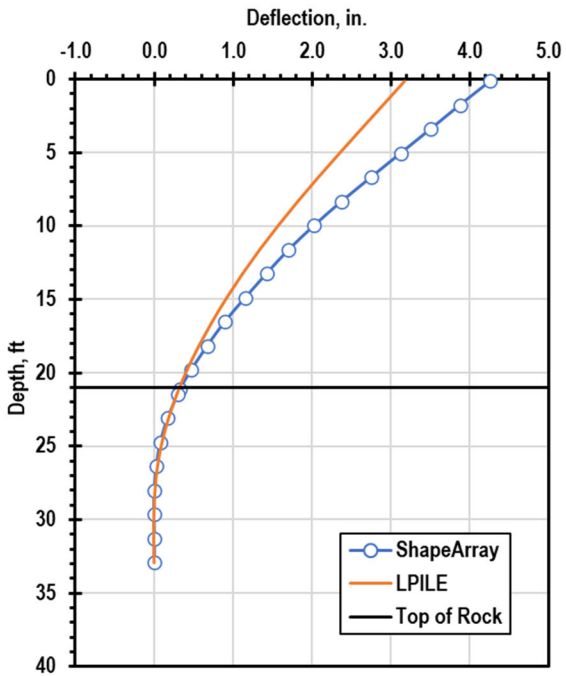

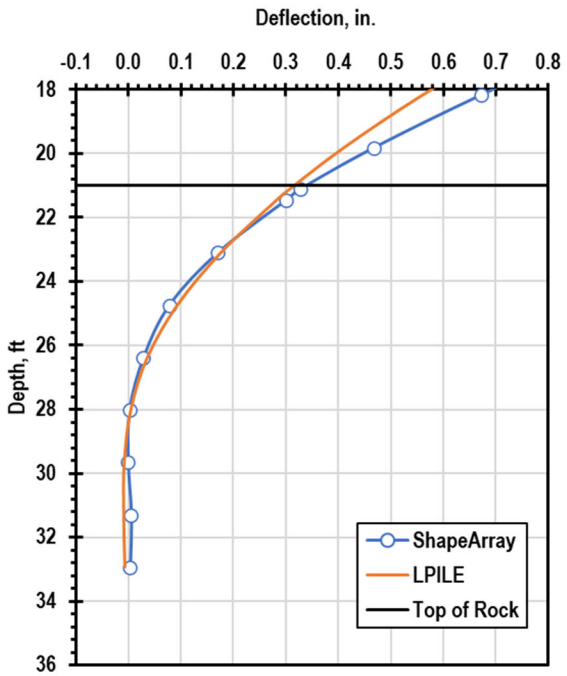

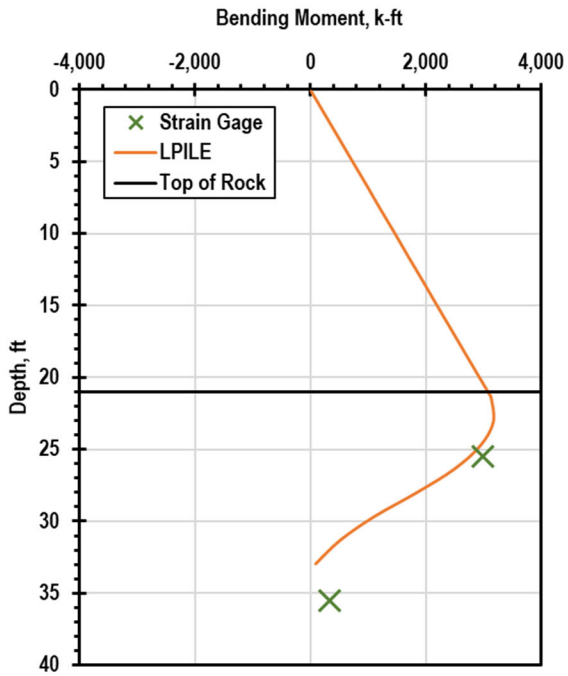

Minco, T1, 161 kips

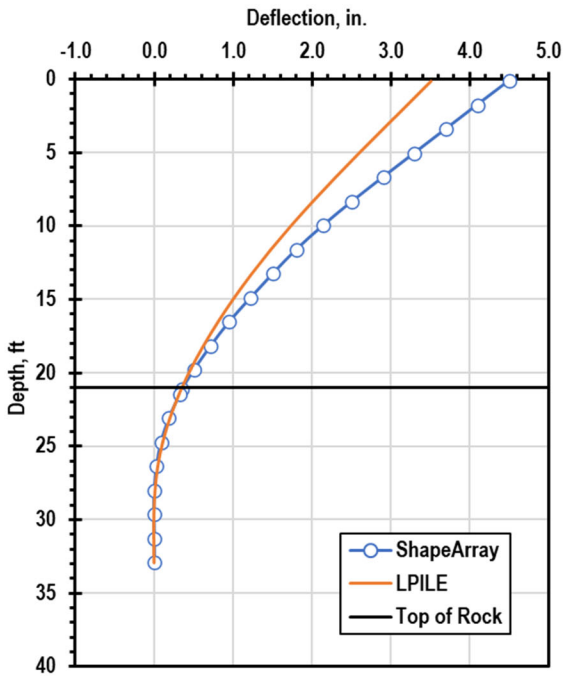

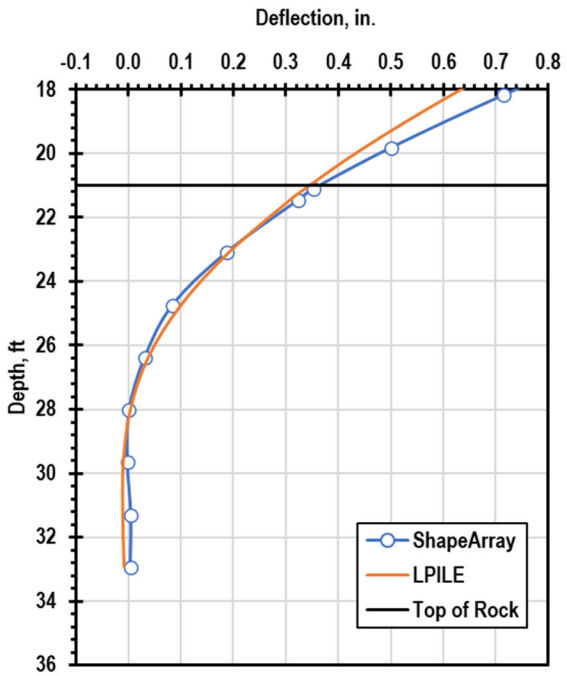

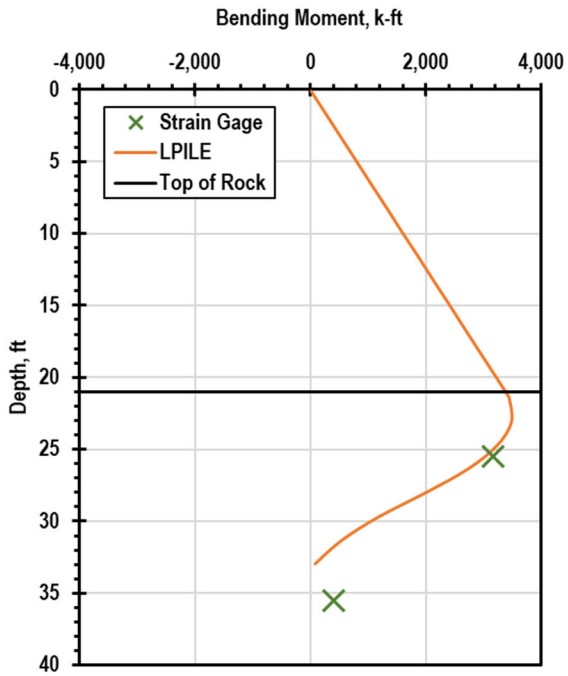

Minco, T1, 190 kips

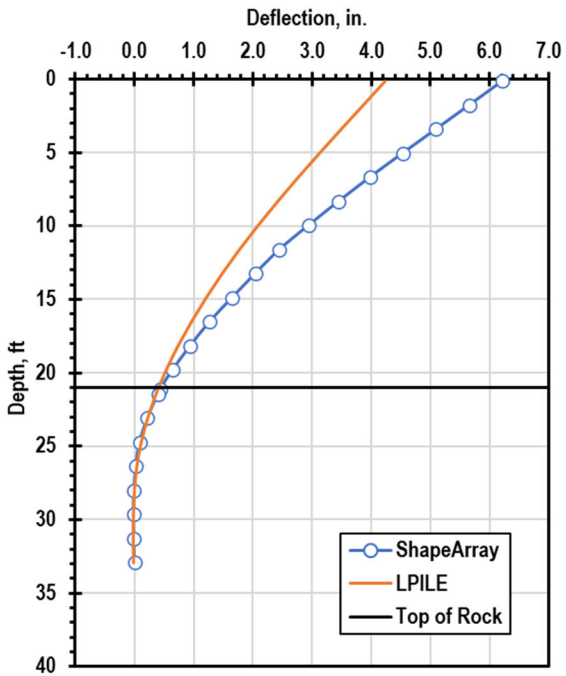

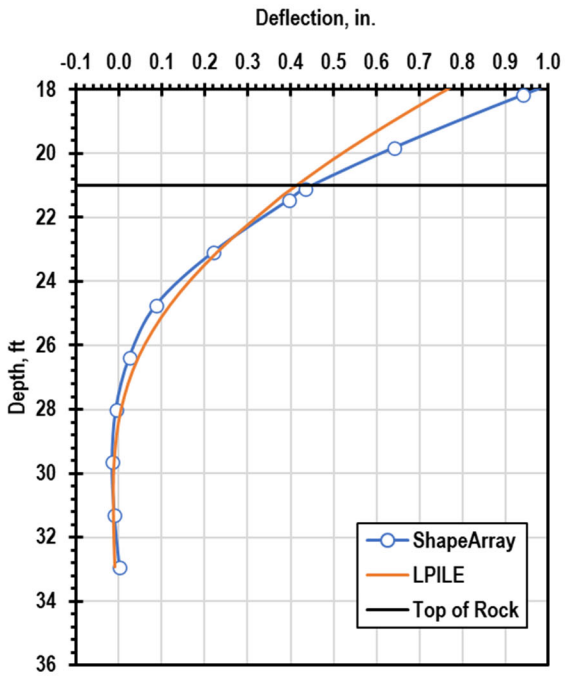

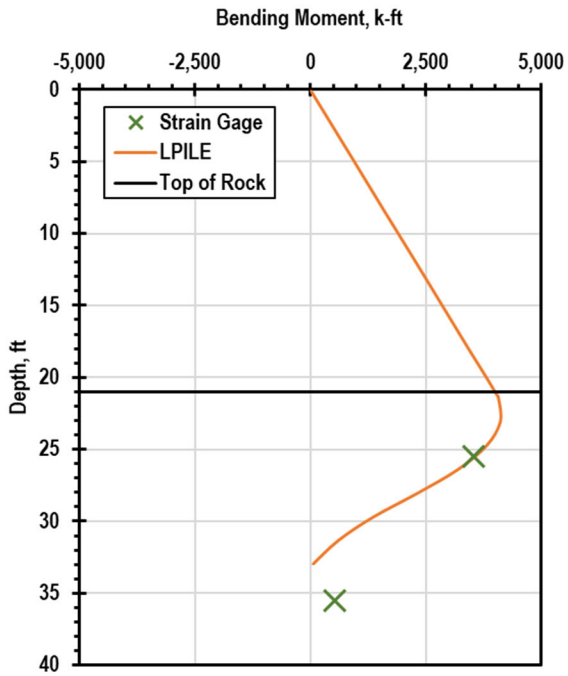

Minco, T1, 220 kips

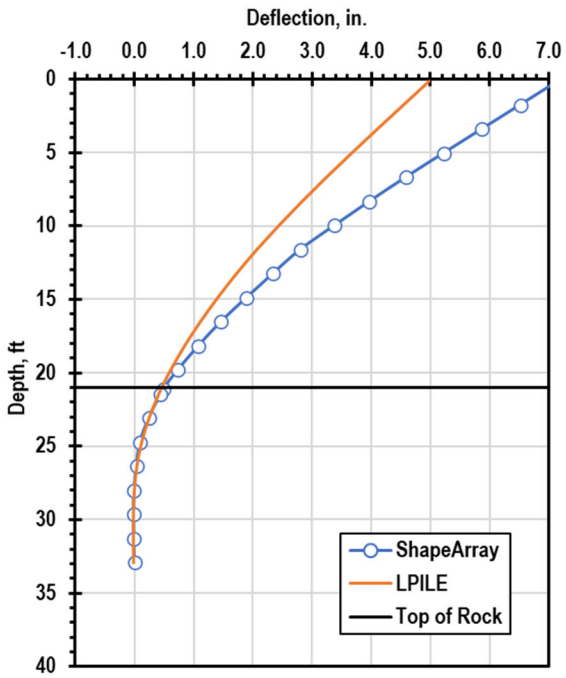

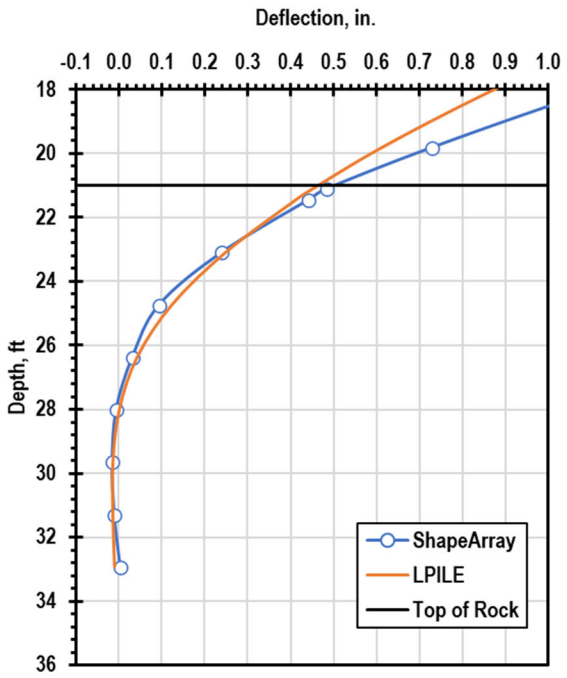

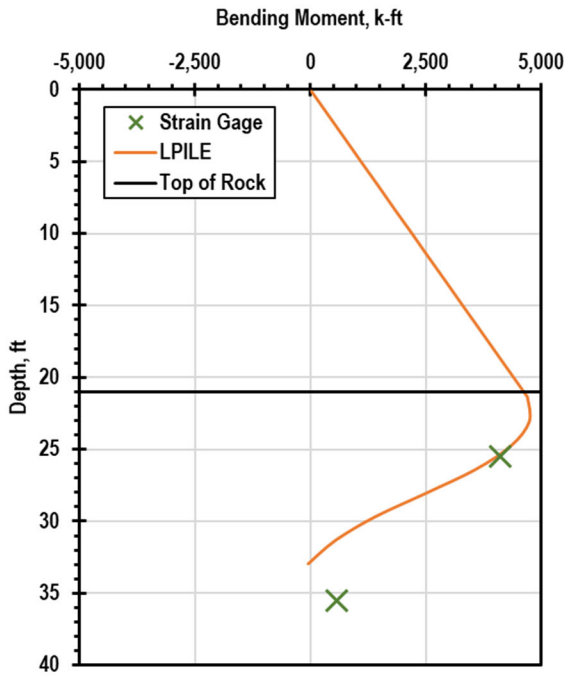

Minco, T2, 59 kips

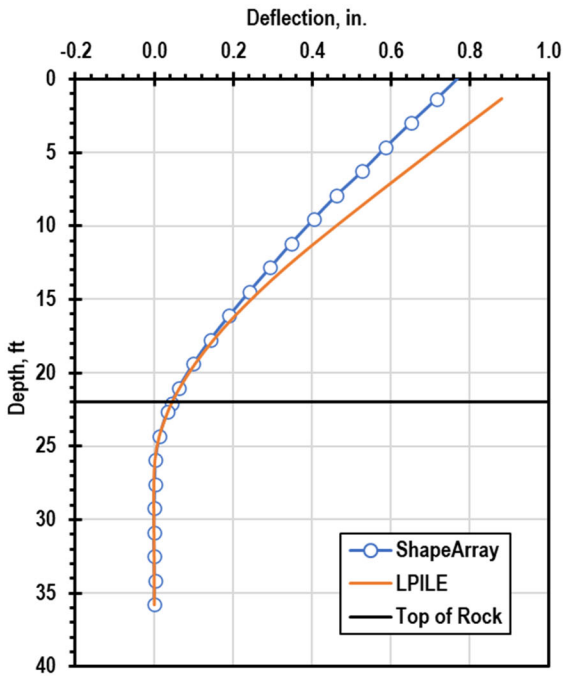

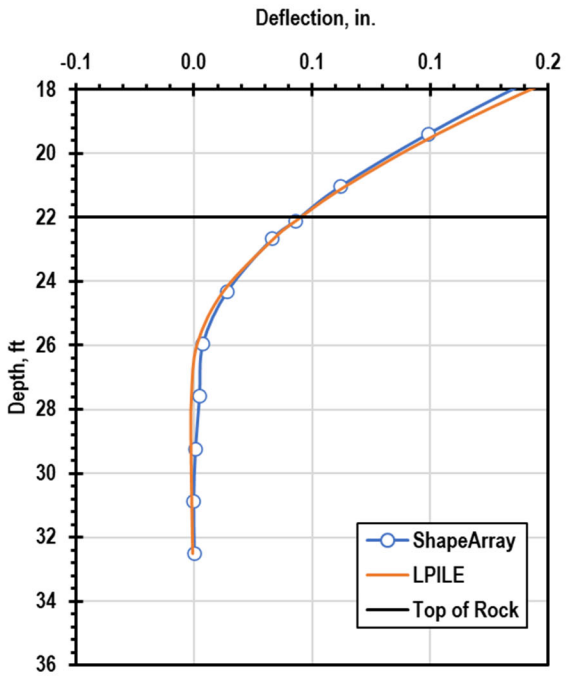

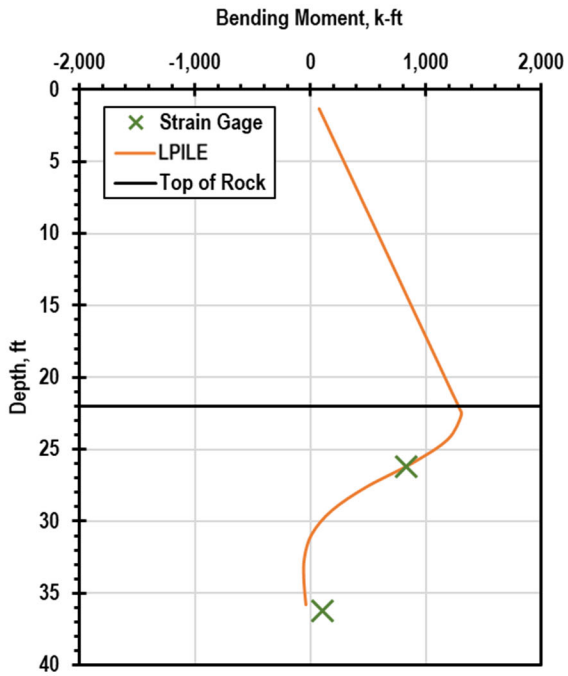

Minco, T2, 88 kips

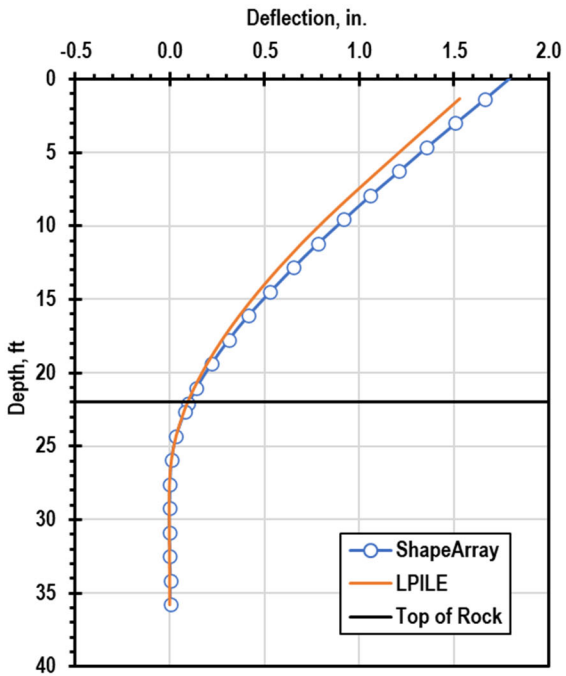

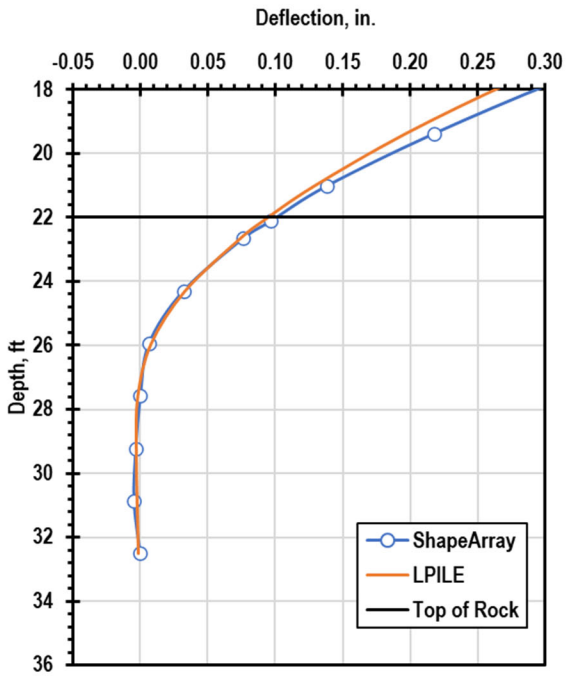

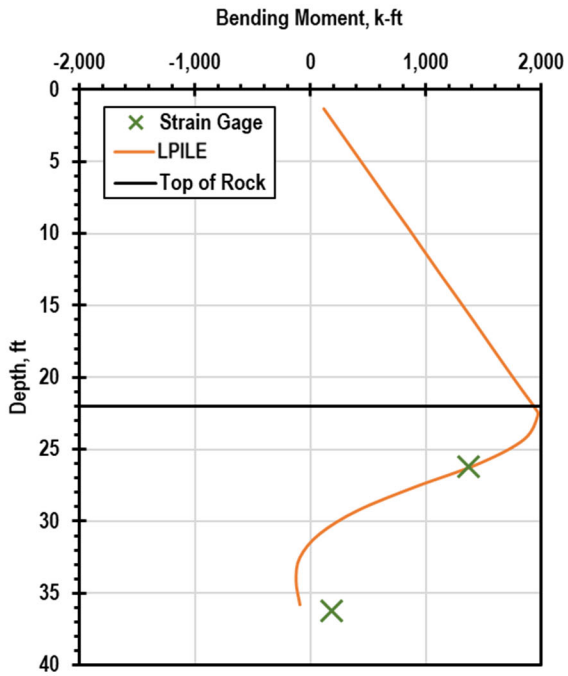

Minco, T2, 132 kips

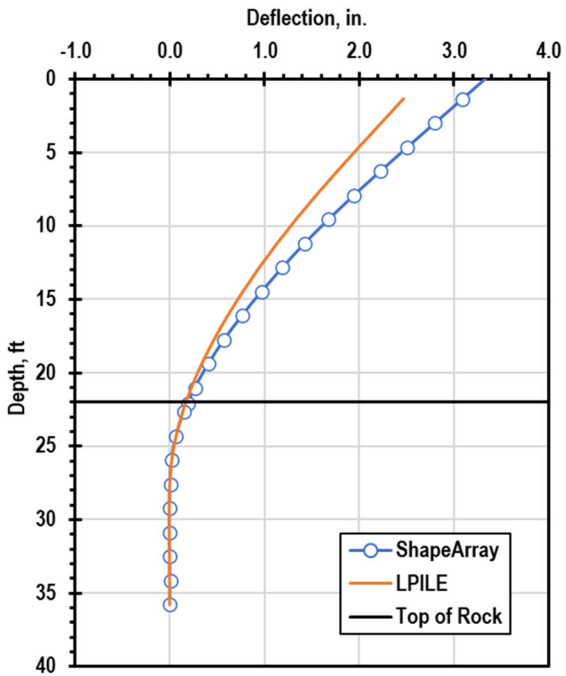

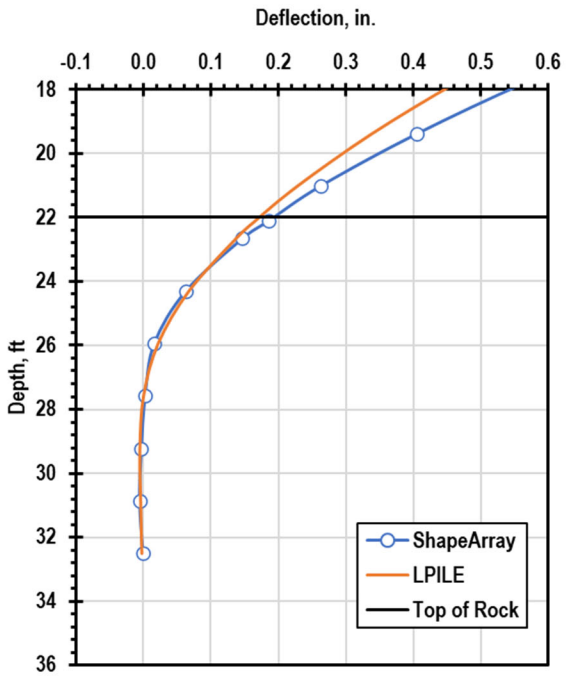

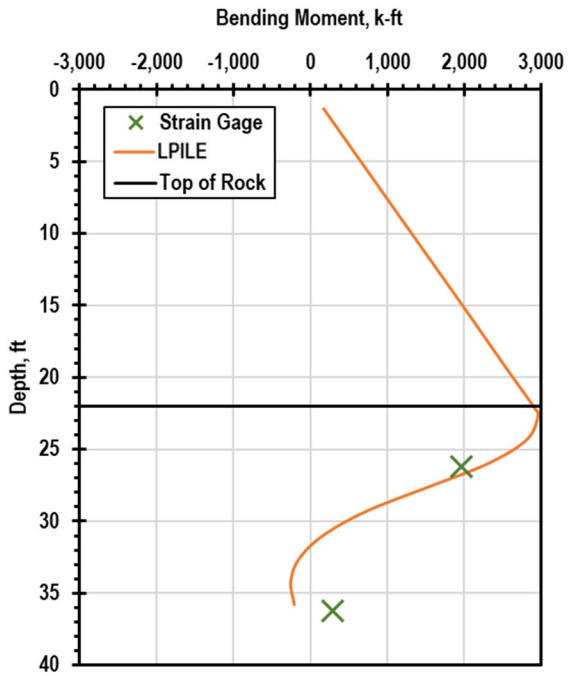

Minco, T2, 146 kips

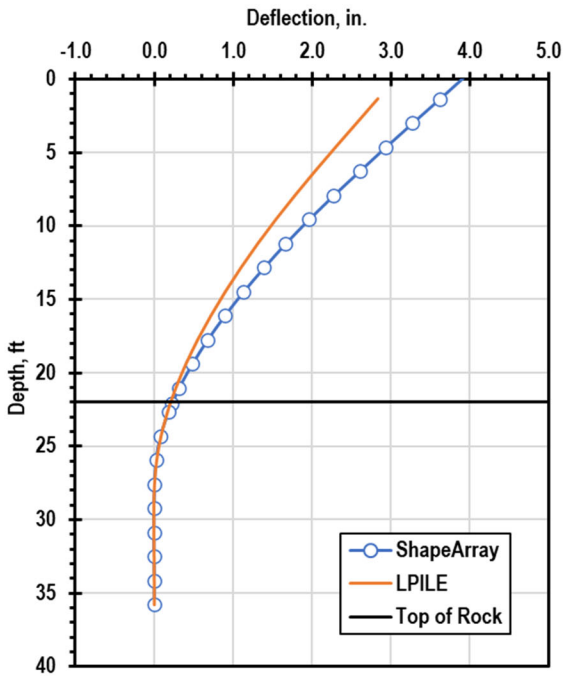

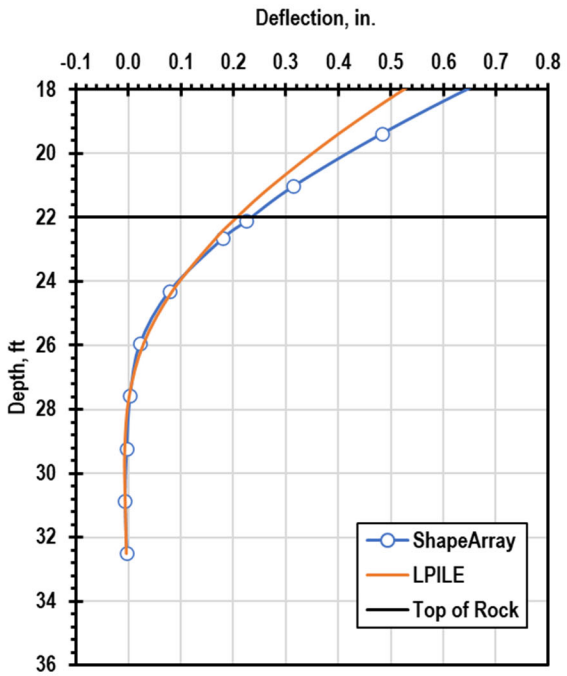

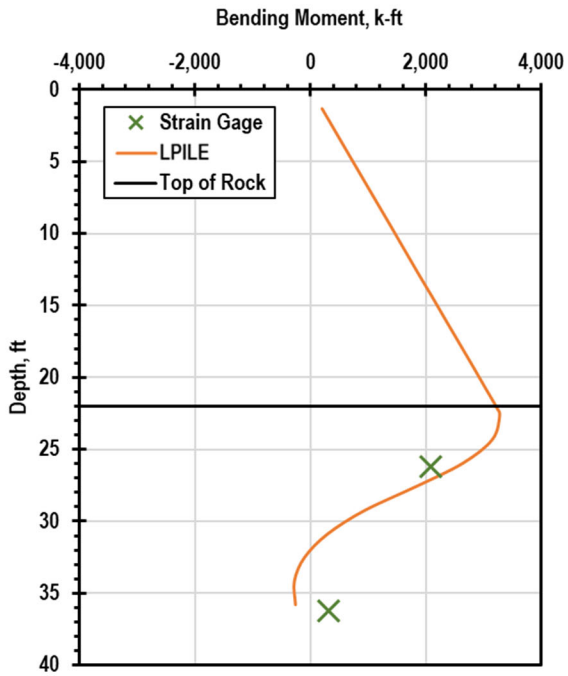

Minco, T2, 161 kips

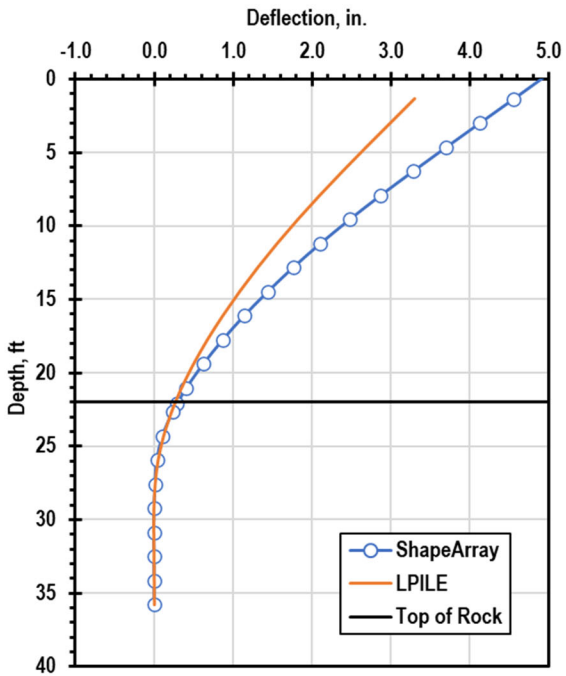

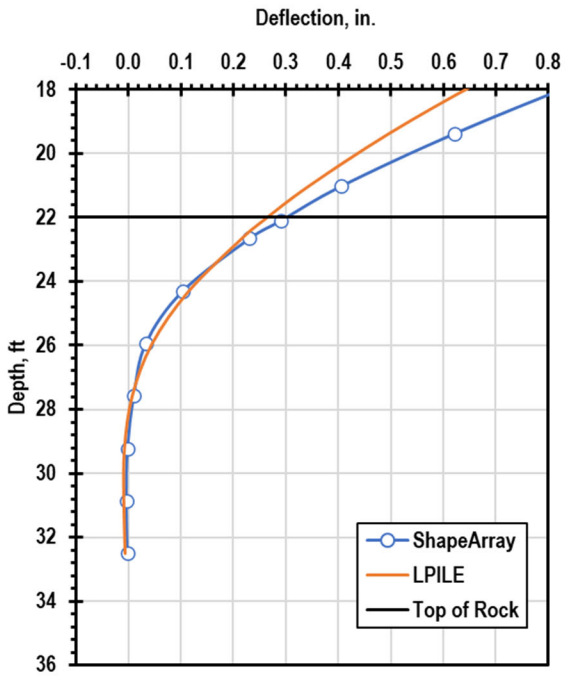

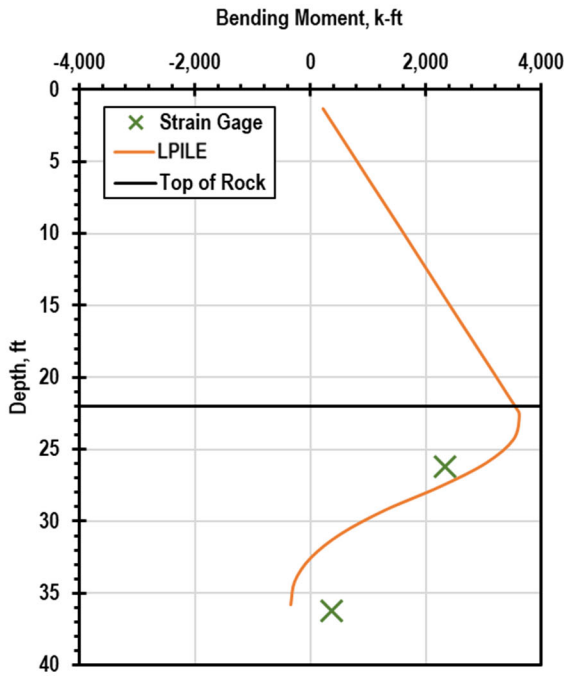

Minco, T2, 190 kips

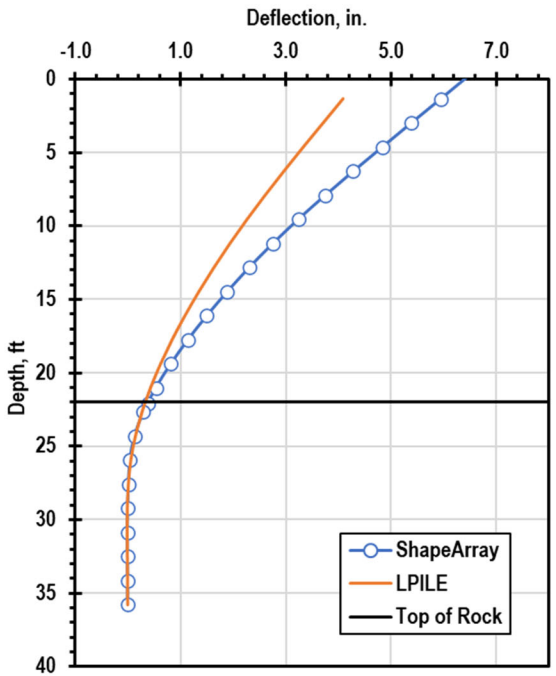

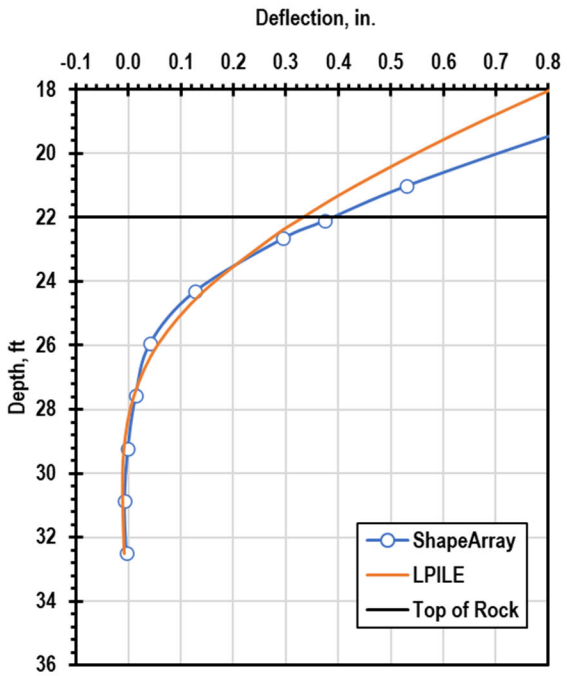

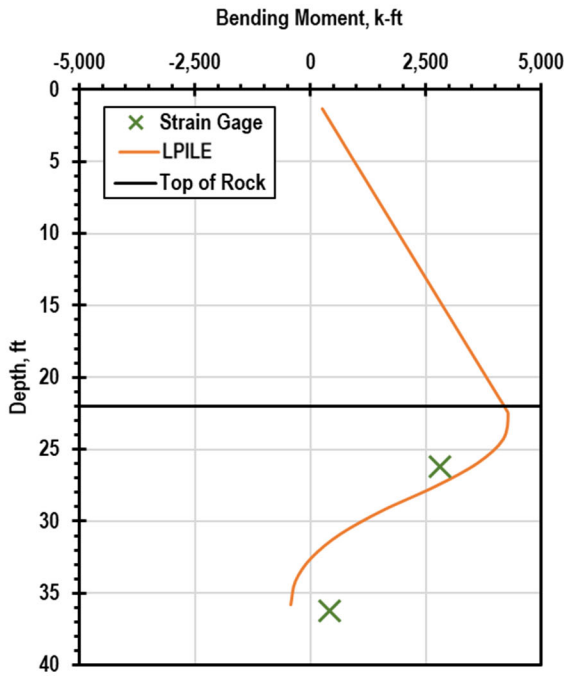

Minco, T2, 220 kips

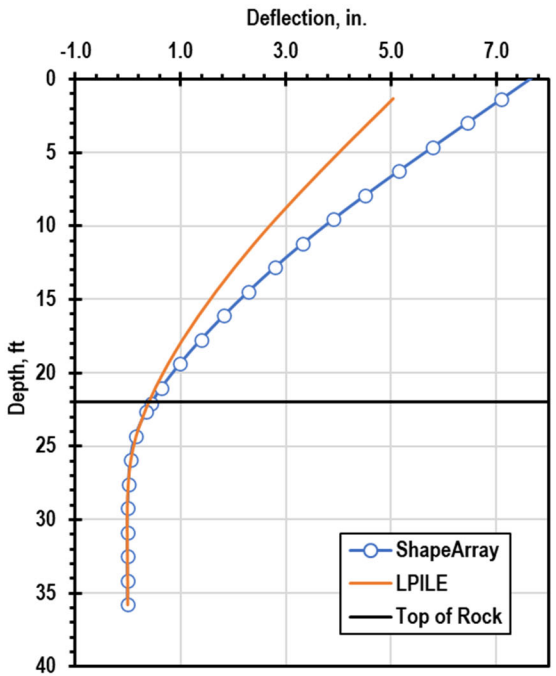

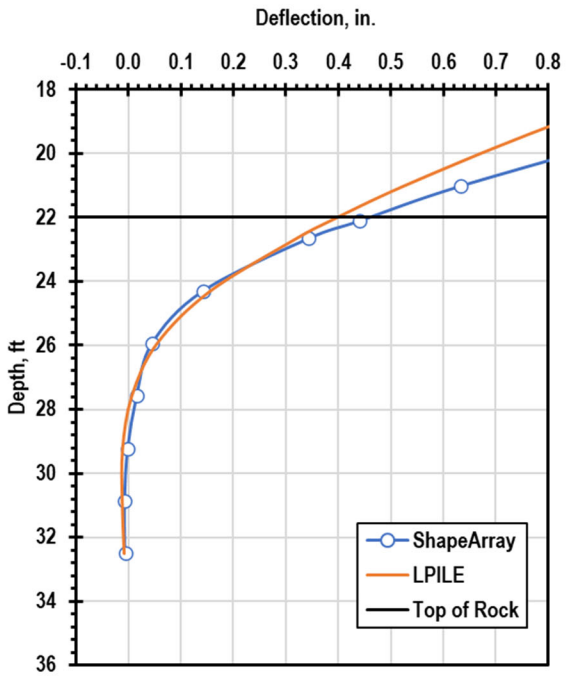

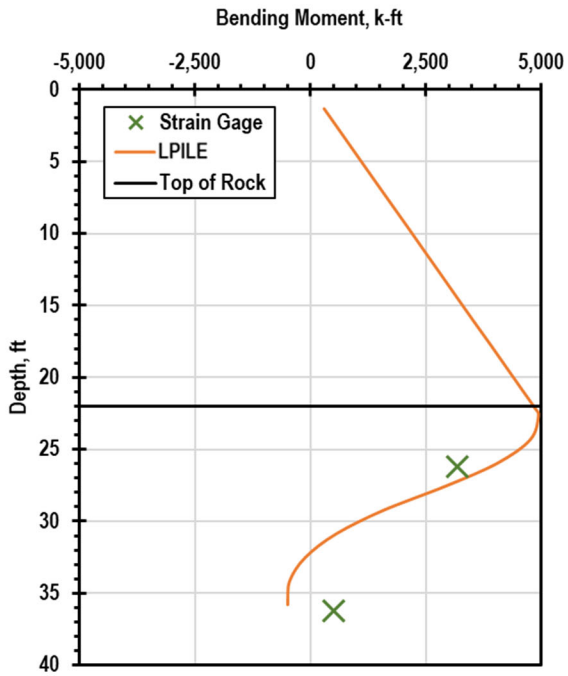

Minco, T3, 59 kips

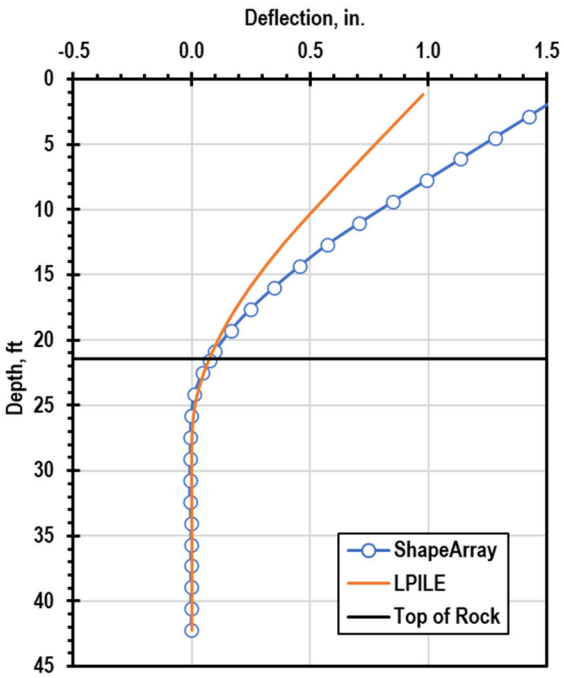

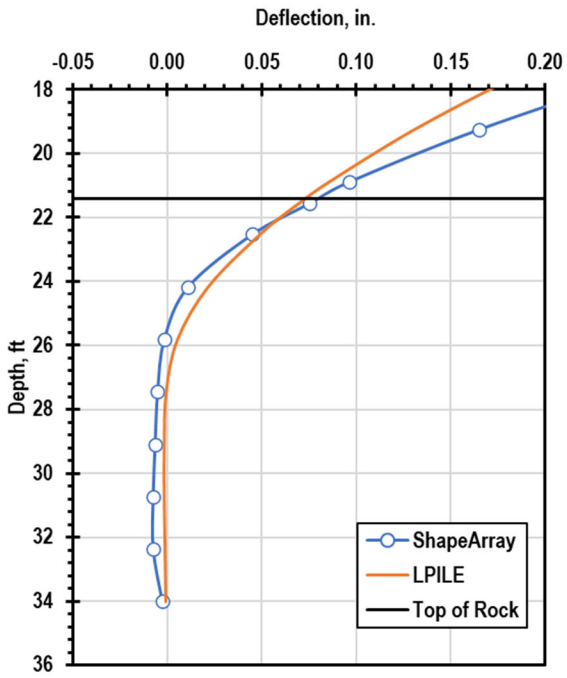

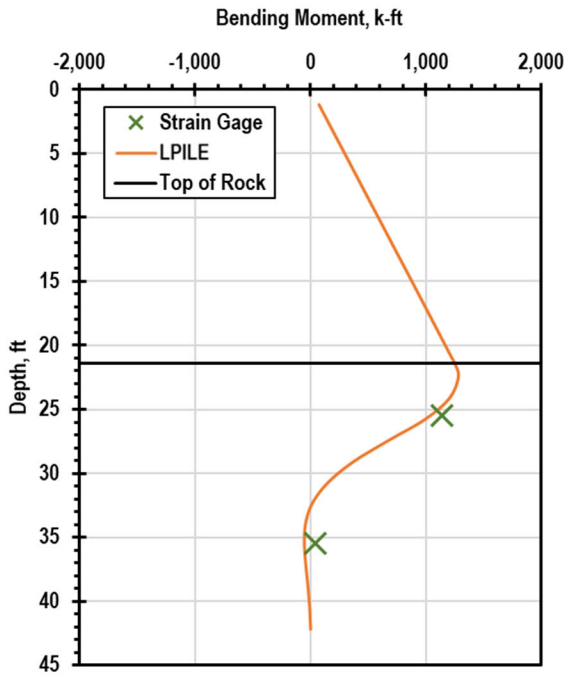

Minco, T3, 88 kips

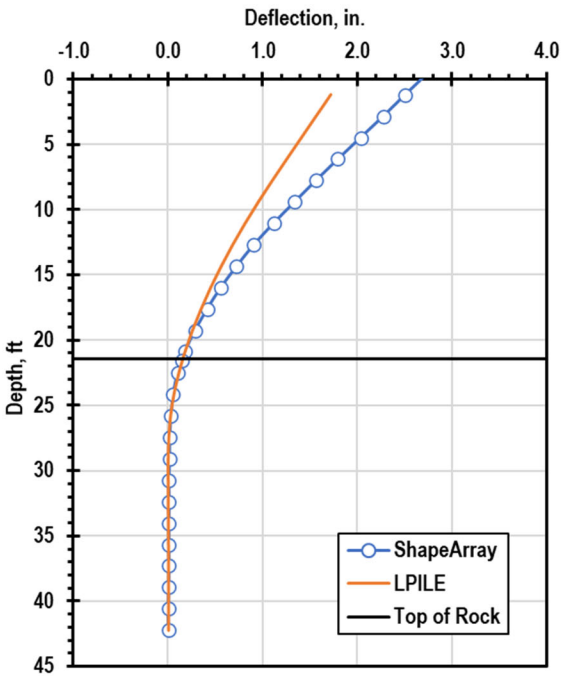

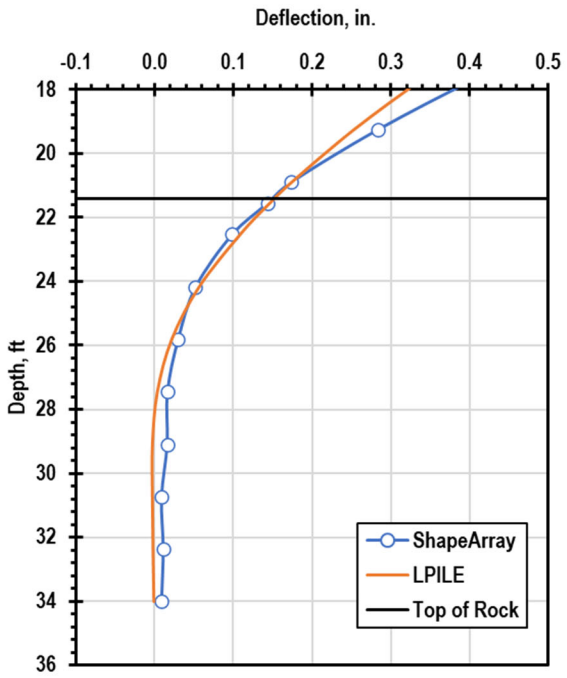

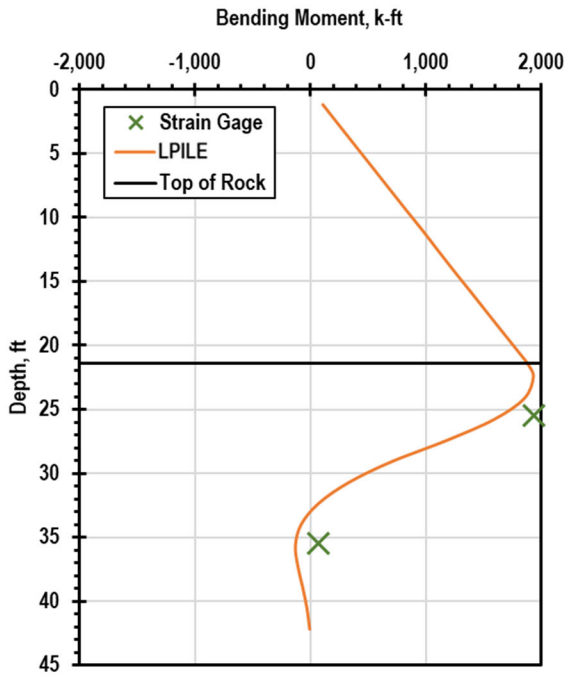

Minco, T3, 117 kips

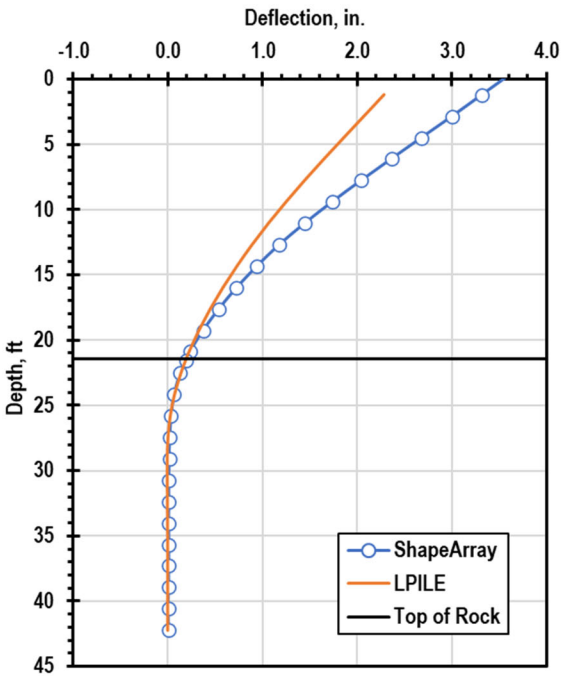

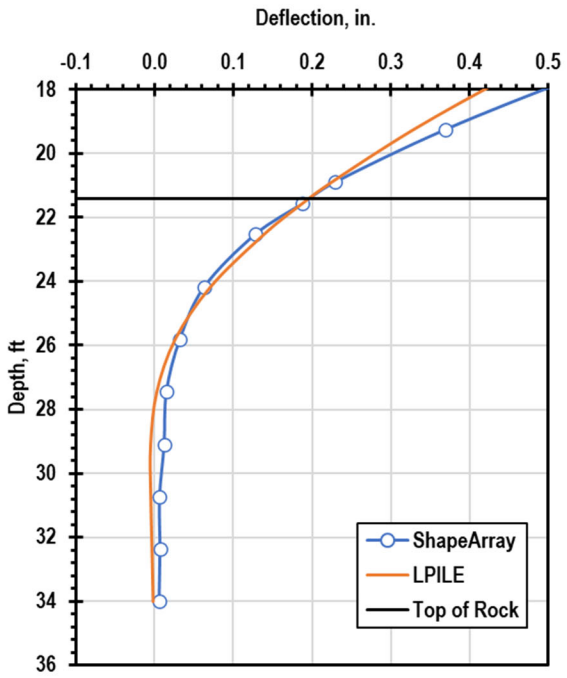

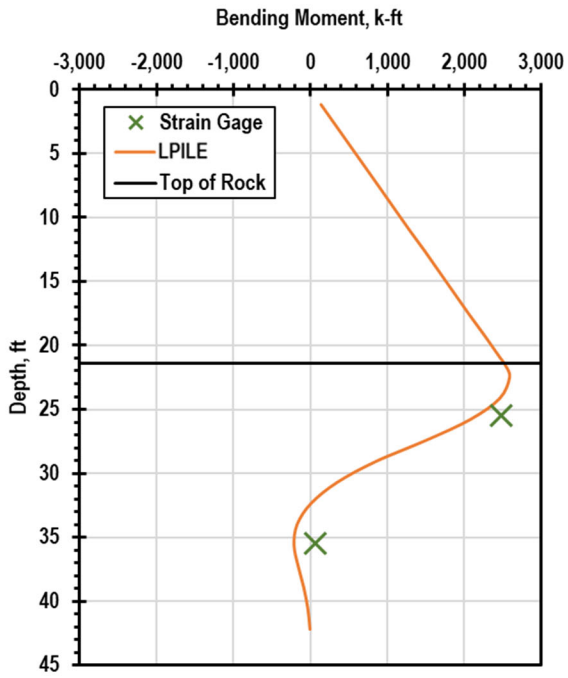

Minco, T3, 146 kips

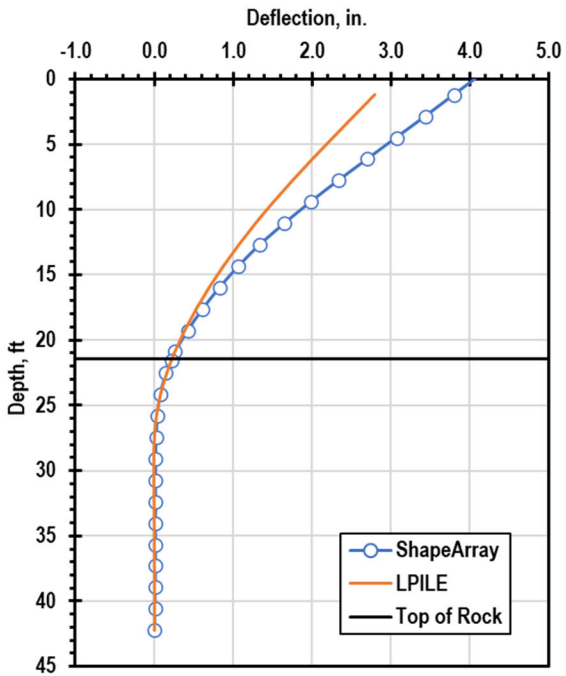

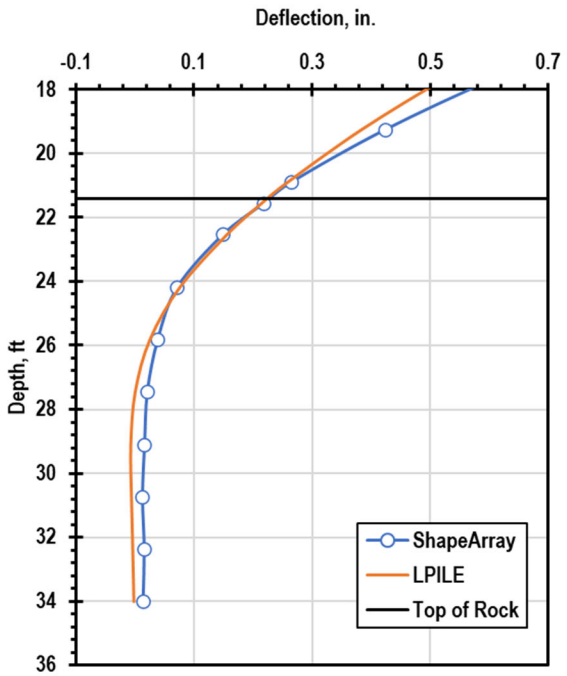

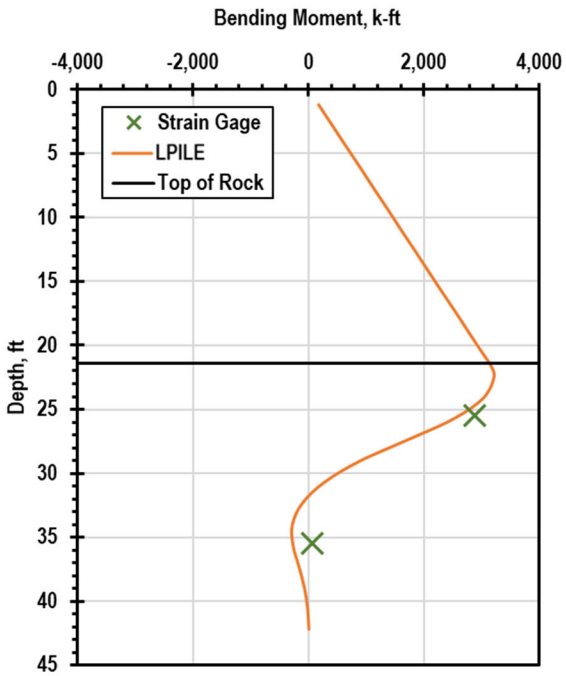

Minco, T3, 161 kips

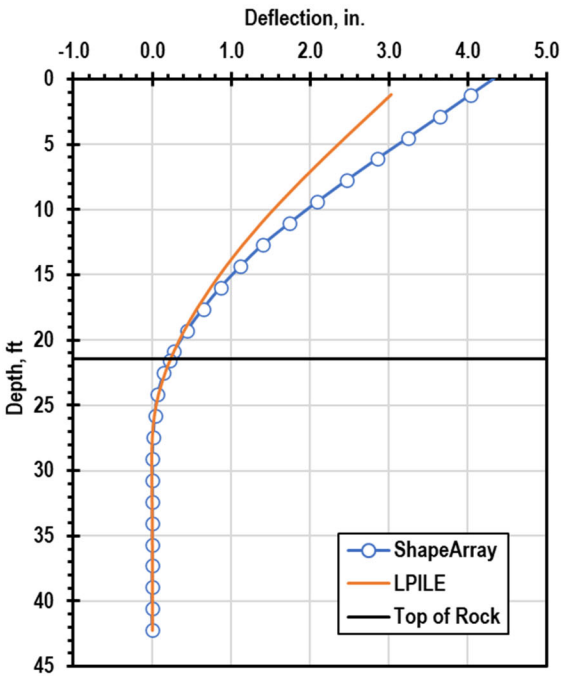

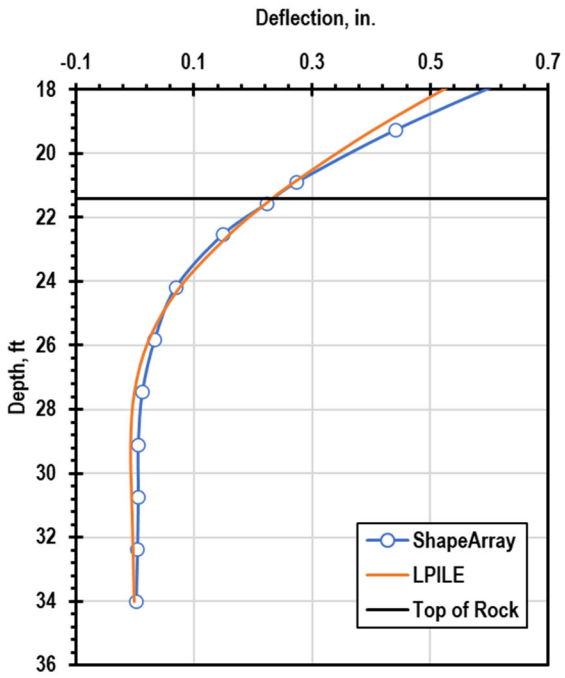

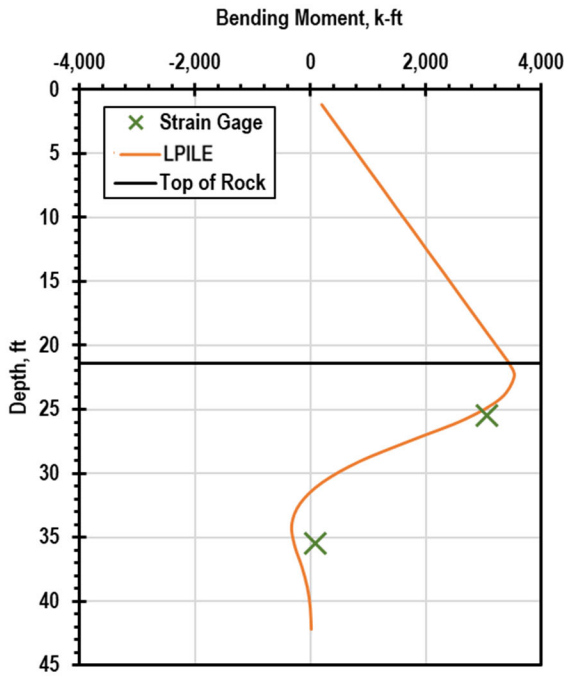

Minco, T3, 190 kips

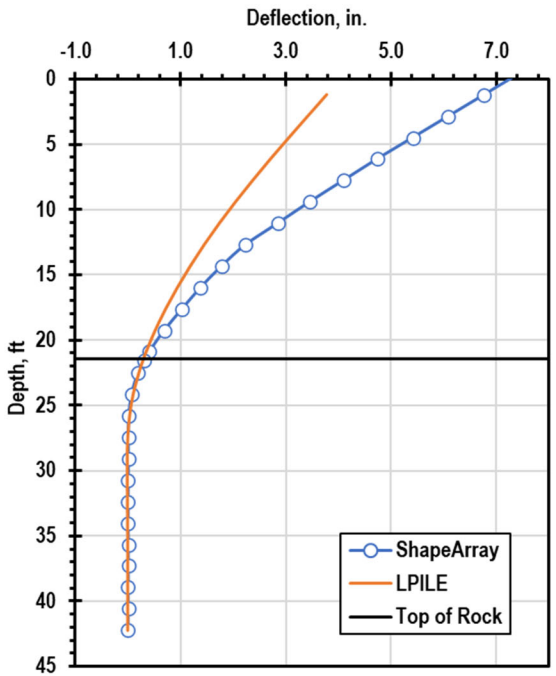

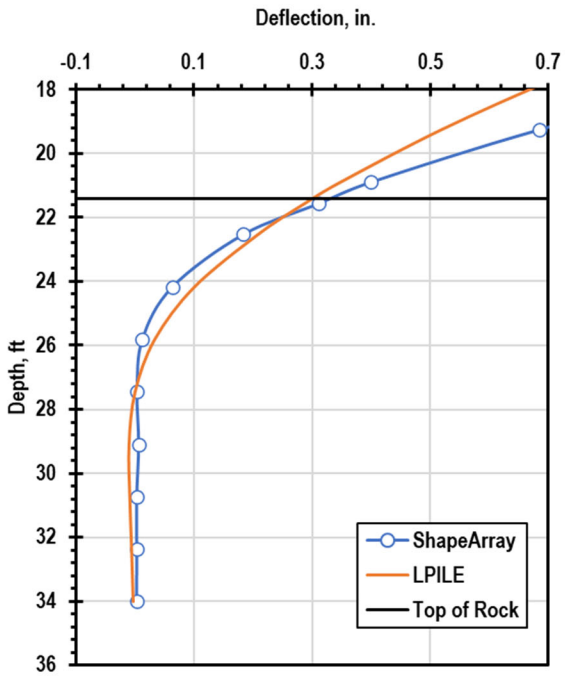

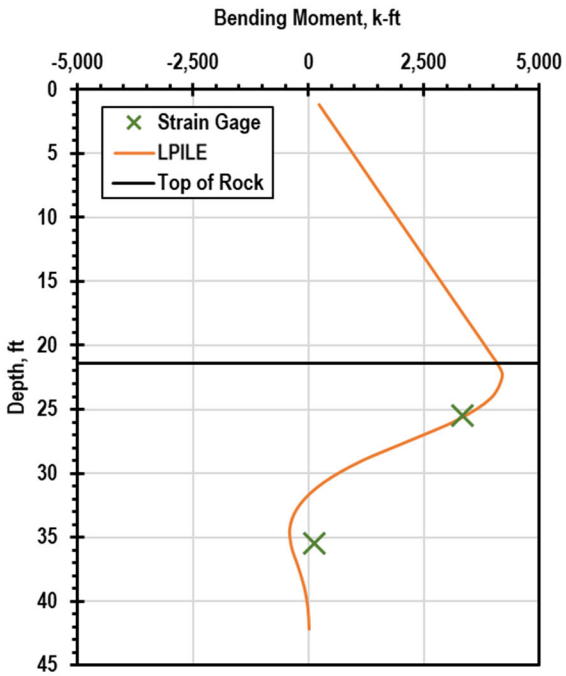

Minco, T3, 220 kips

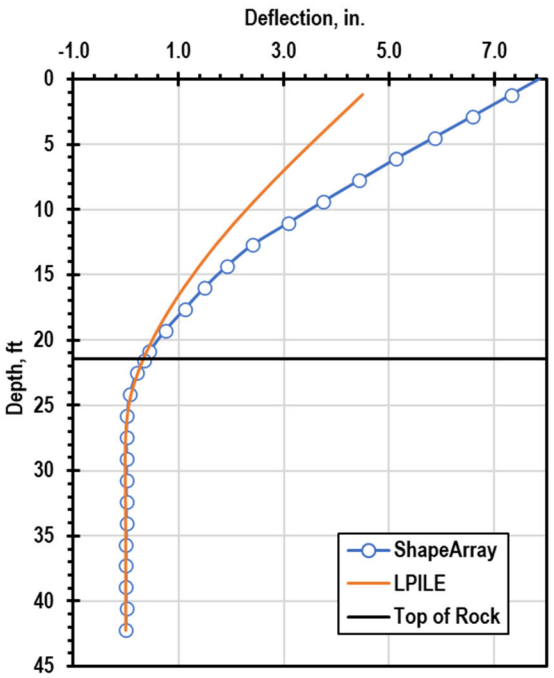

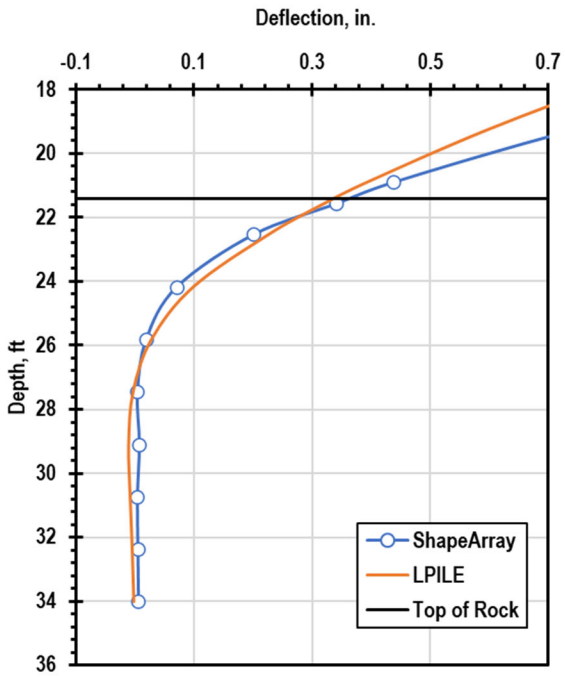

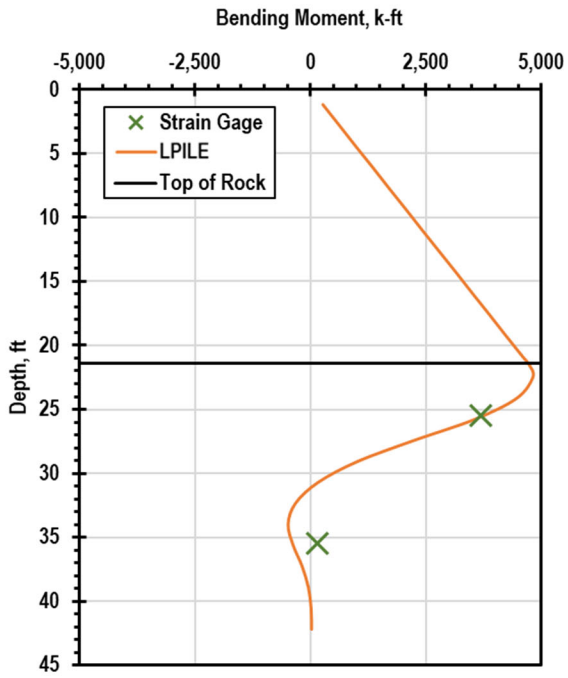

Minco, T4, 59 kips

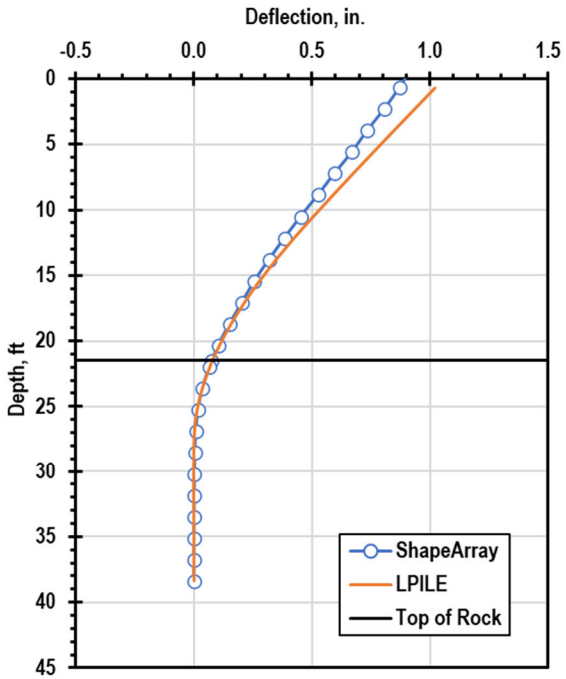

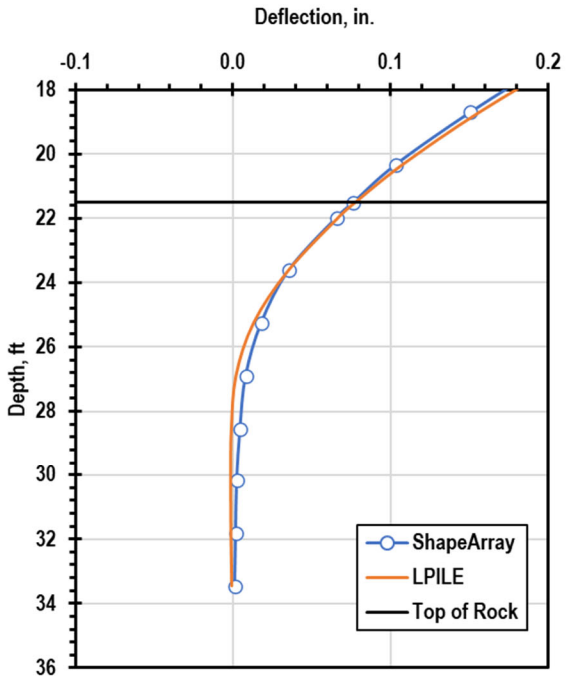

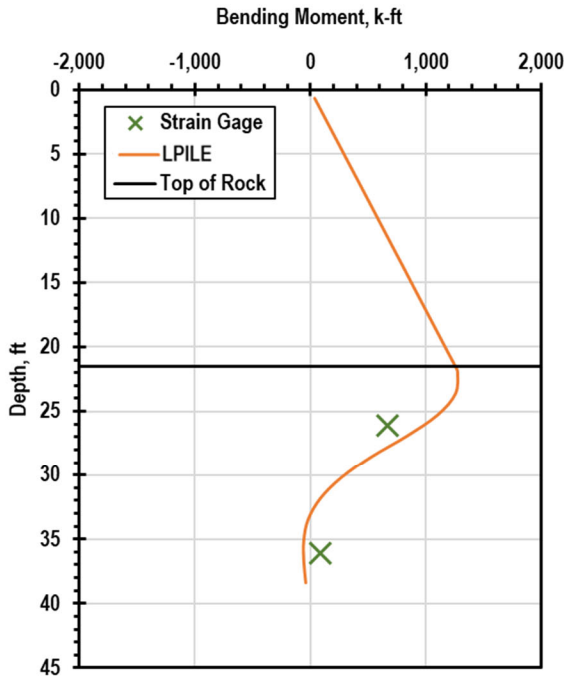

Minco, T4, 88 kips

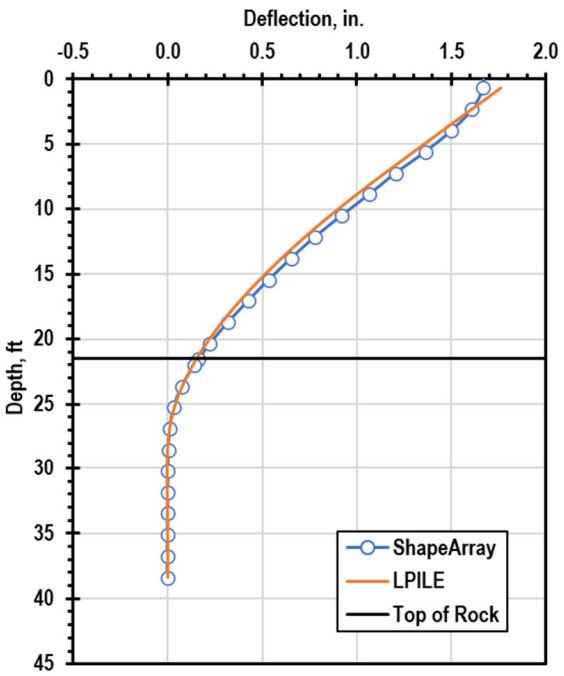

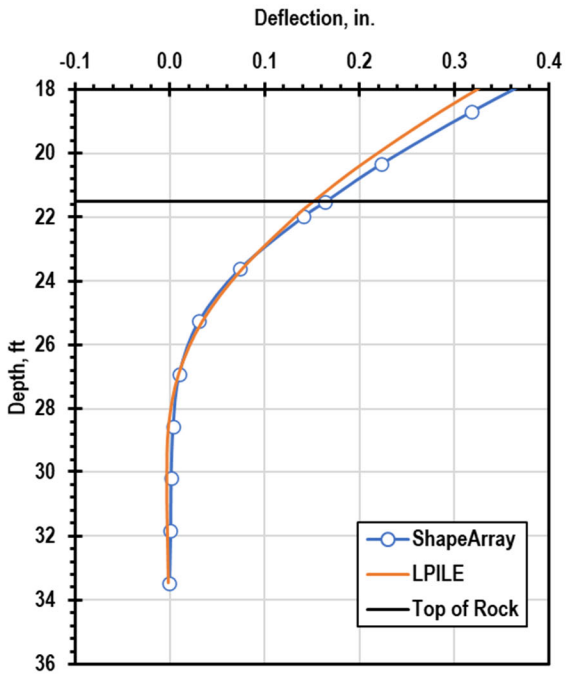

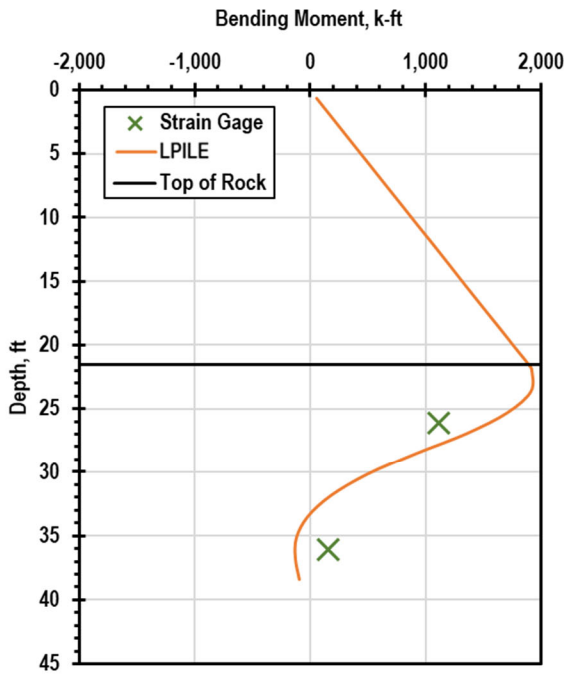

Minco, T4, 132 kips

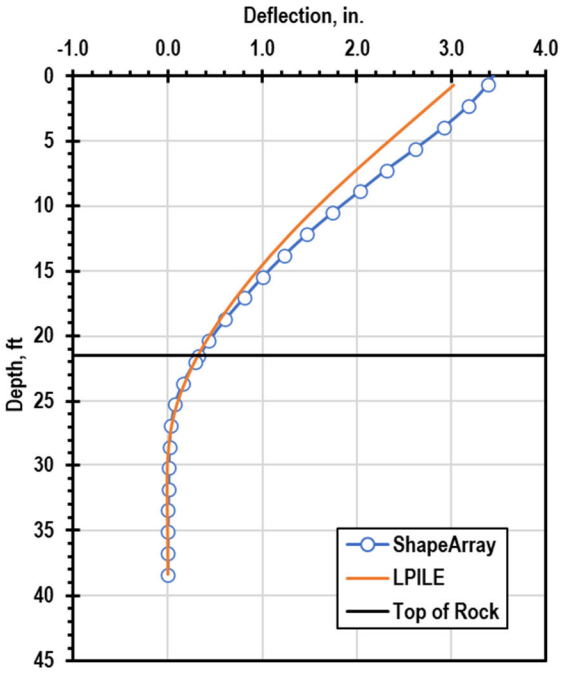

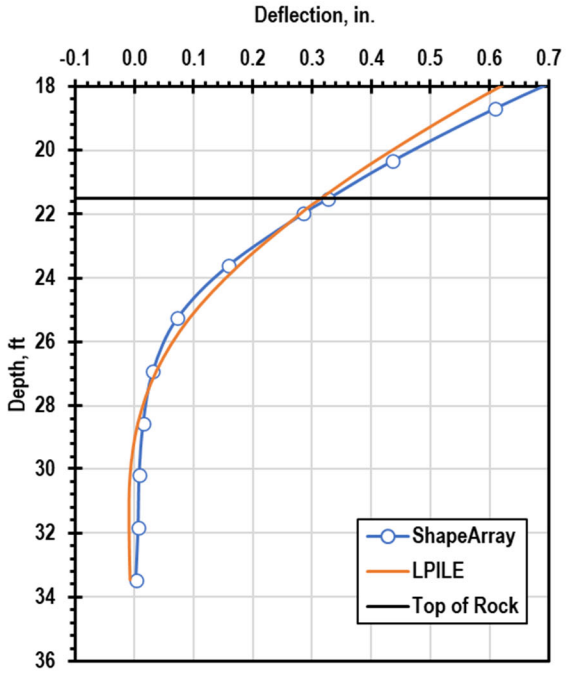

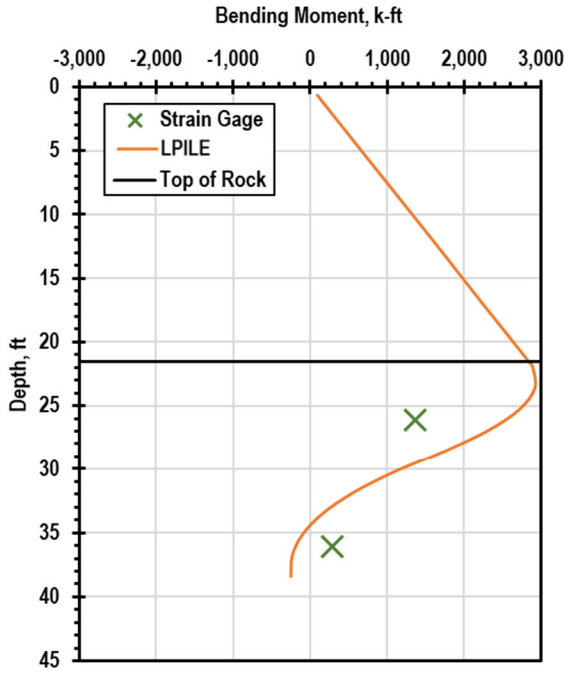

Minco, T4, 146 kips

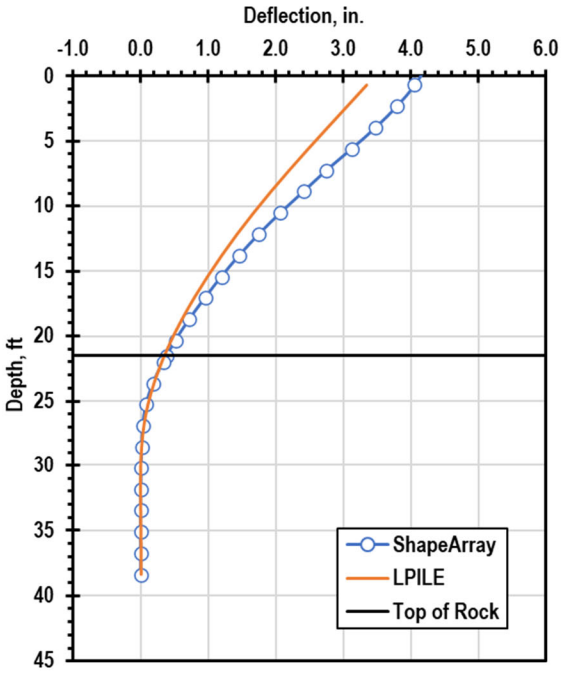

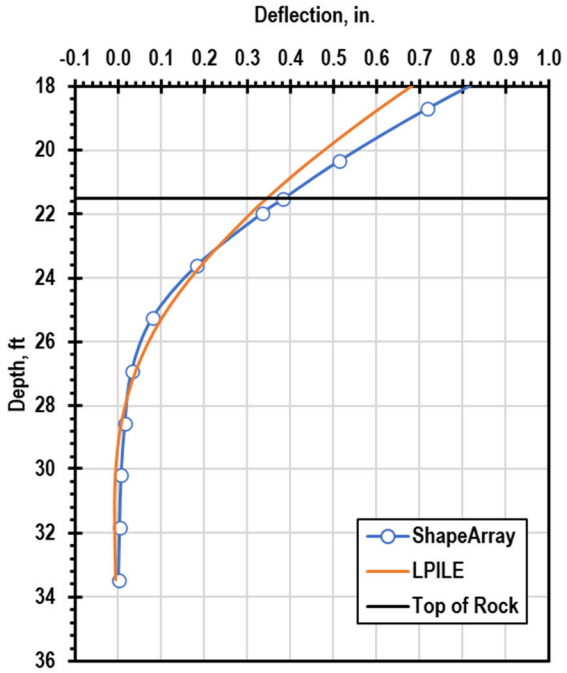

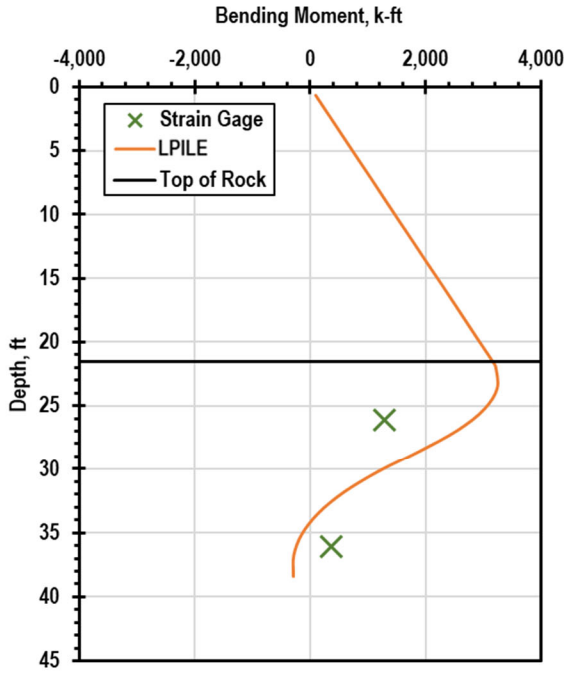

Minco, T4, 161 kips

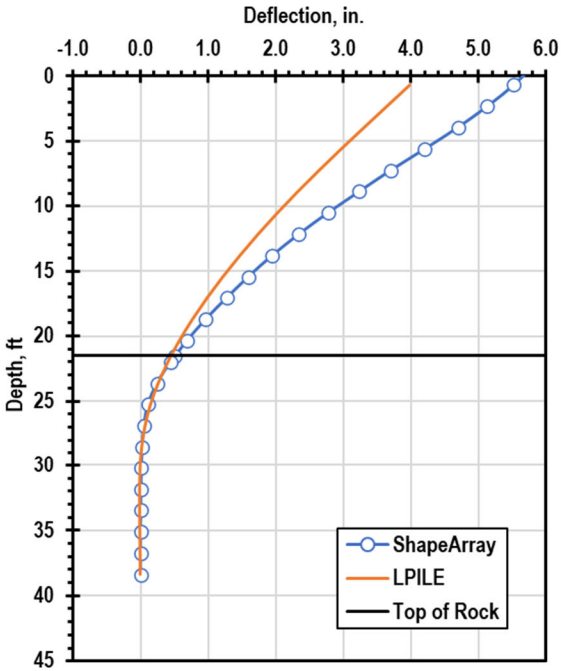

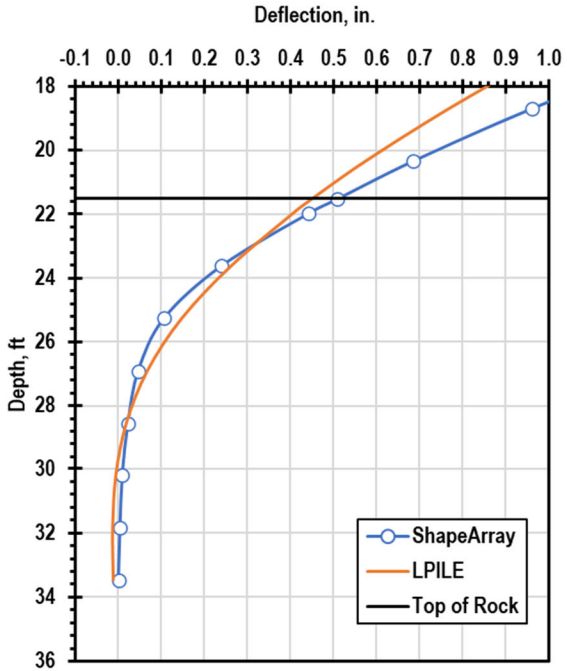

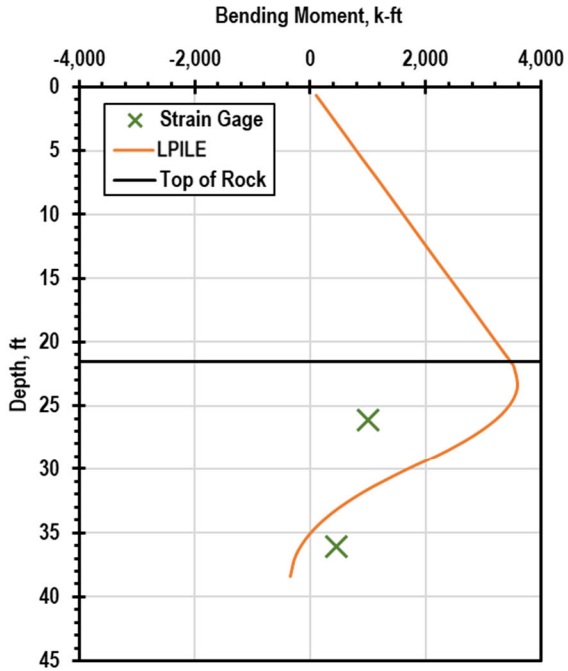

Minco, T4, 190 kips

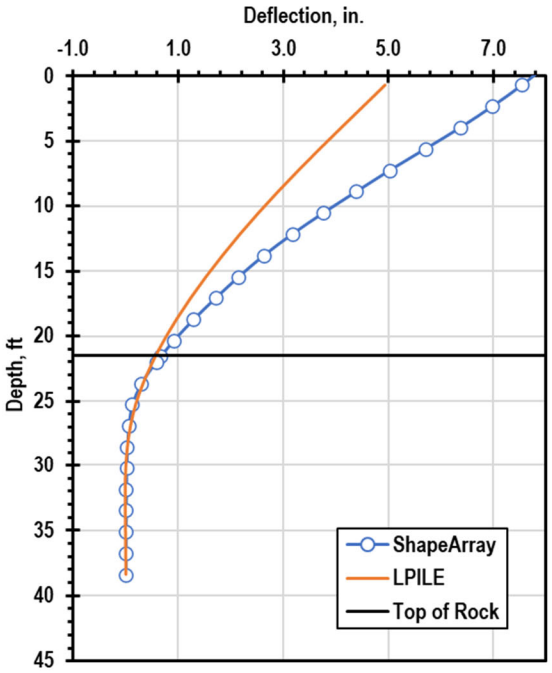

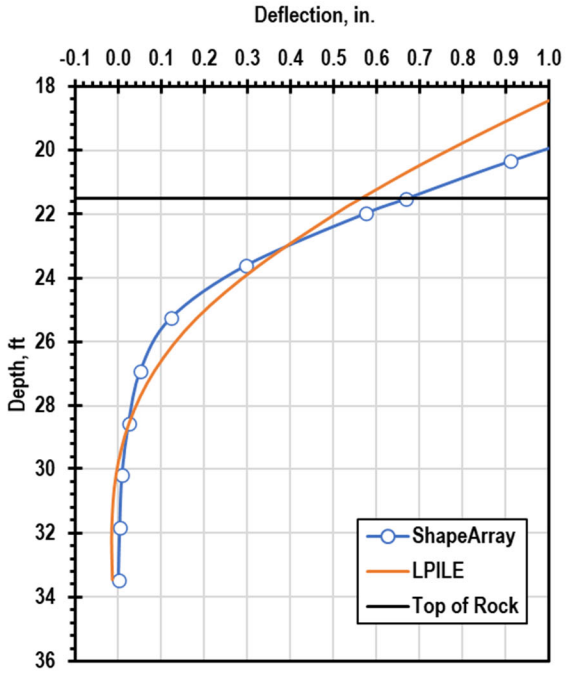

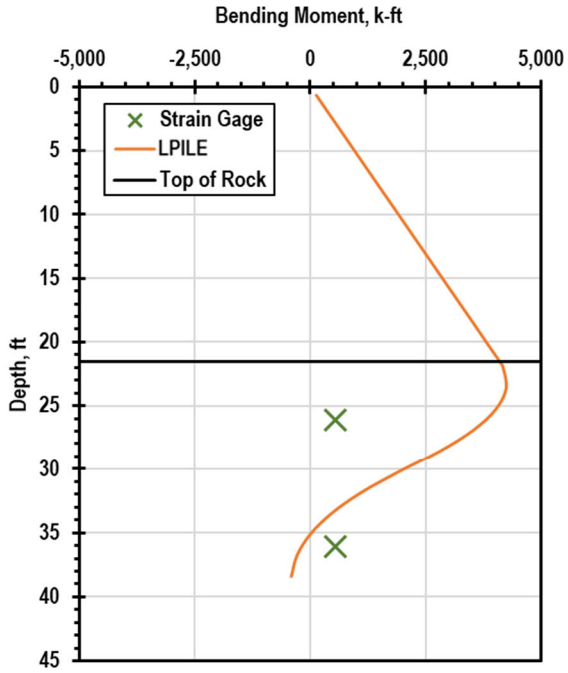

Appendix D – Fitted *p-y* Curves

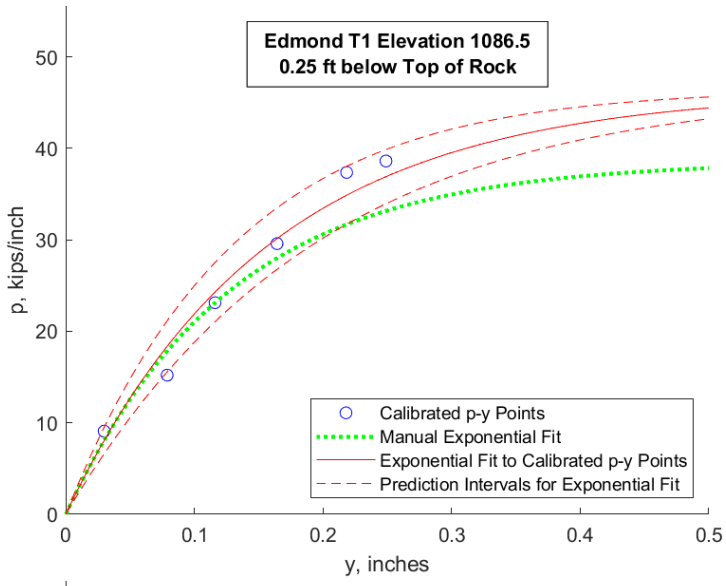
Edmond T1 Elevation 1086.5
0.25 ft below Top of Rock
p, kips/inch
y, inches
Calibrated p-y Points
Manual Exponential Fit
Exponential Fit to Calibrated p-y Points
Prediction Intervals for Exponential Fit

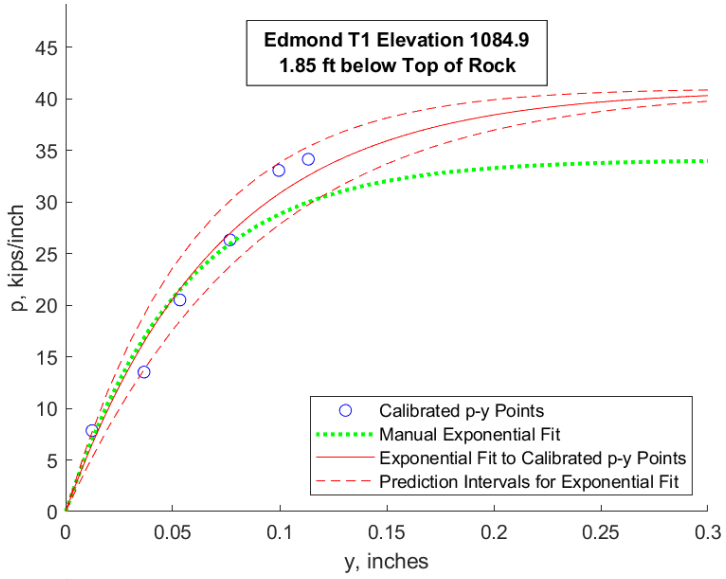
Edmond T1 Elevation 1084.9
1.85 ft below Top of Rock
p, kips/inch
y, inches
Calibrated p-y Points
Manual Exponential Fit
Exponential Fit to Calibrated p-y Points
Prediction Intervals for Exponential Fit

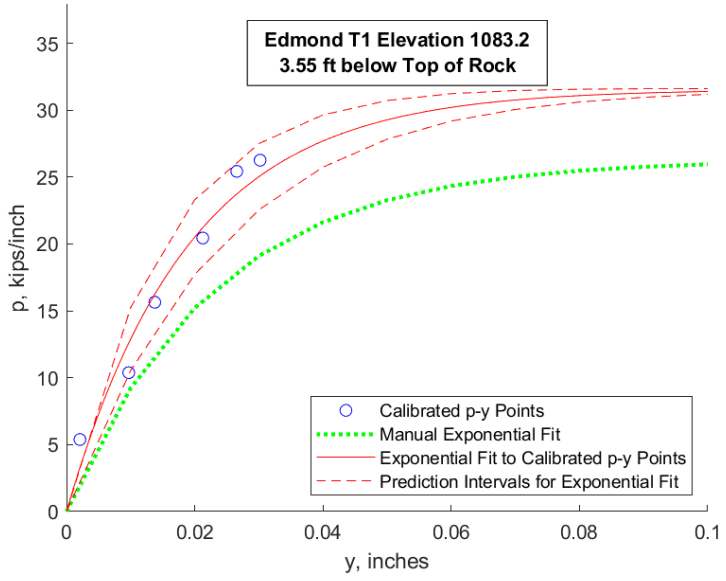
Edmond T1 Elevation 1083.2
3.55 ft below Top of Rock
p, kips/inch
y, inches
Calibrated p-y Points
Manual Exponential Fit
Exponential Fit to Calibrated p-y Points
Prediction Intervals for Exponential Fit

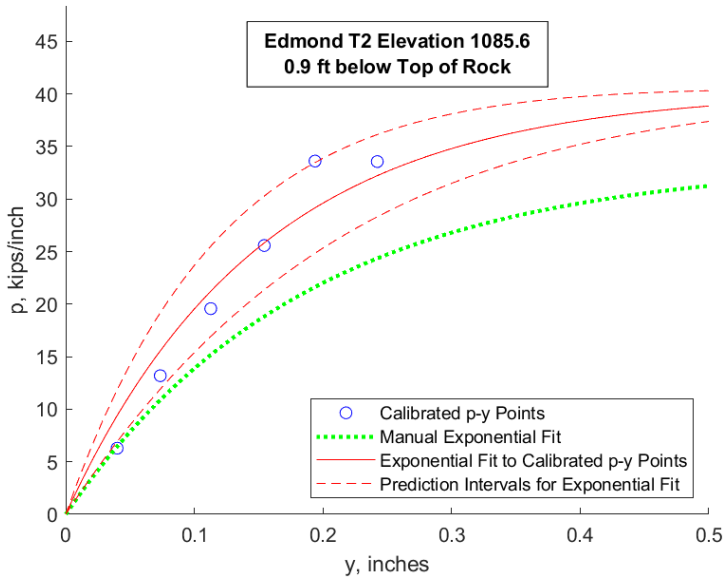
Edmond T2 Elevation 1085.6
0.9 ft below Top of Rock
p, kips/inch
y, inches
Calibrated p-y Points
Manual Exponential Fit
Exponential Fit to Calibrated p-y Points
Prediction Intervals for Exponential Fit

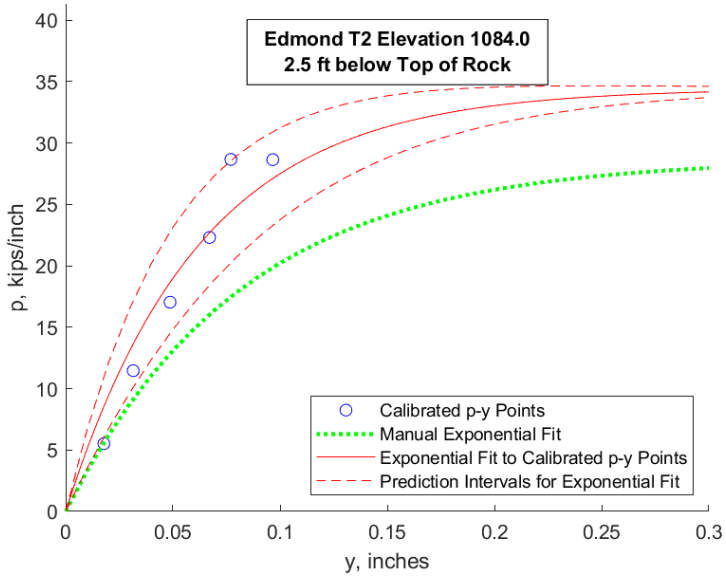
Edmond T2 Elevation 1084.0
2.5 ft below Top of Rock
p, kips/inch
y, inches
Calibrated p-y Points
Manual Exponential Fit
Exponential Fit to Calibrated p-y Points
Prediction Intervals for Exponential Fit

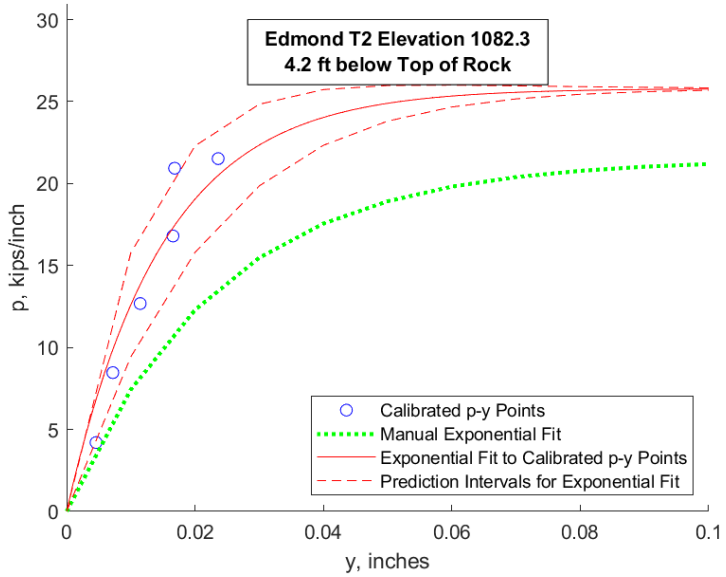
Edmond T2 Elevation 1082.3
4.2 ft below Top of Rock
p, kips/inch
y, inches
Calibrated p-y Points
Manual Exponential Fit
Exponential Fit to Calibrated p-y Points
Prediction Intervals for Exponential Fit

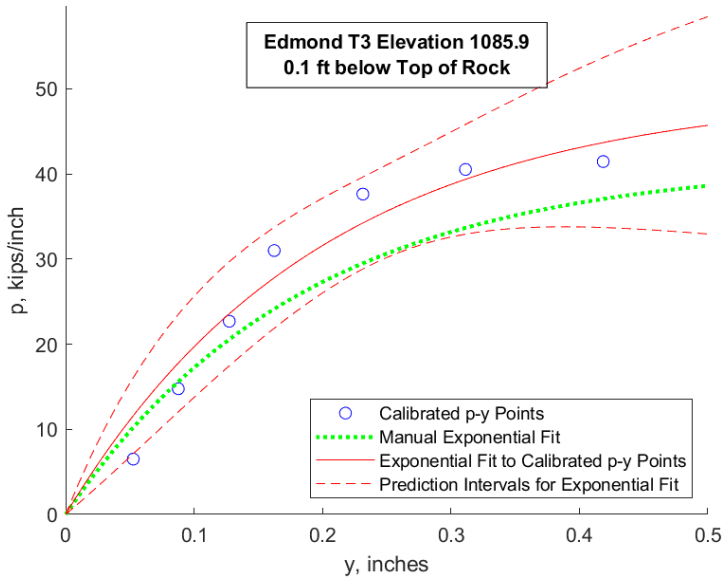
Edmond T3 Elevation 1085.9
0.1 ft below Top of Rock
p, kips/inch
y, inches
Calibrated p-y Points
Manual Exponential Fit
Exponential Fit to Calibrated p-y Points
Prediction Intervals for Exponential Fit

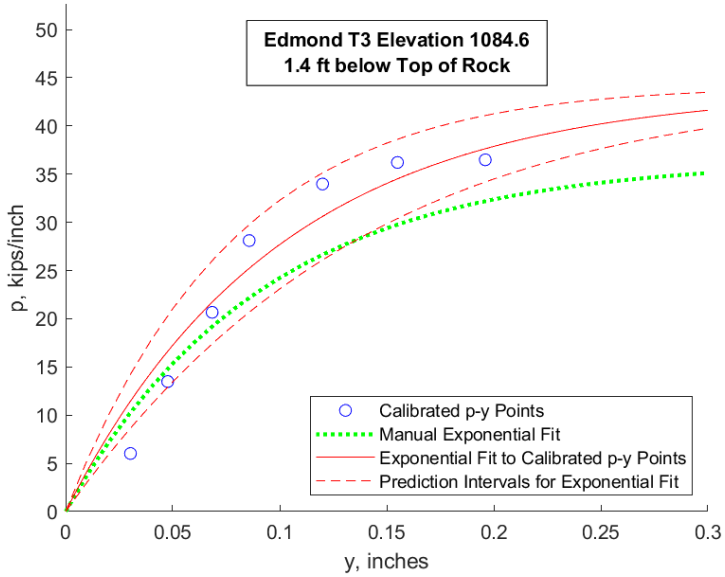
Edmond T3 Elevation 1084.6
1.4 ft below Top of Rock
p, kips/inch
y, inches
Calibrated p-y Points
Manual Exponential Fit
Exponential Fit to Calibrated p-y Points
Prediction Intervals for Exponential Fit

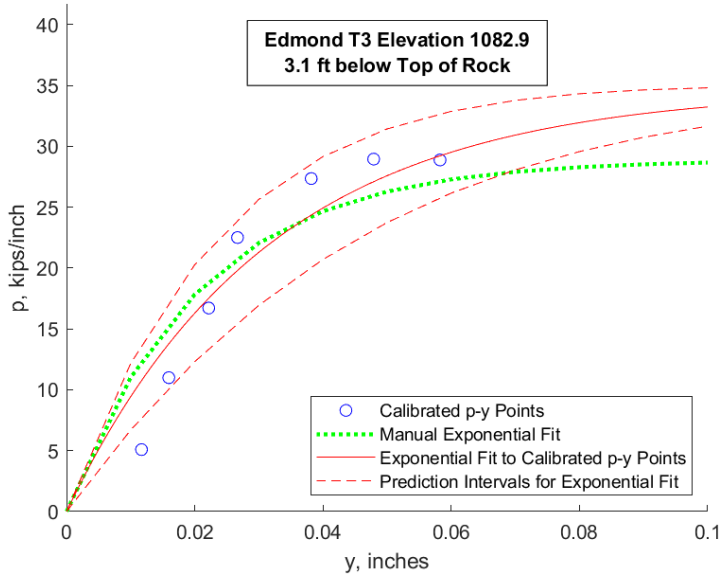
Edmond T3 Elevation 1082.9
3.1 ft below Top of Rock
p, kips/inch
y, inches
Calibrated p-y Points
Manual Exponential Fit
Exponential Fit to Calibrated p-y Points
Prediction Intervals for Exponential Fit

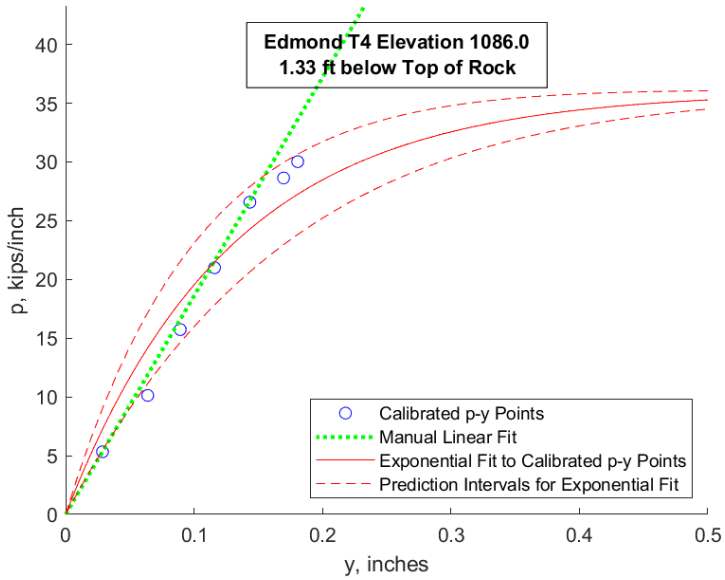
Edmond T4 Elevation 1086.0
1.33 ft below Top of Rock
p, kips/inch
y, inches
Calibrated p-y Points
Manual Linear Fit
Exponential Fit to Calibrated p-y Points
Prediction Intervals for Exponential Fit

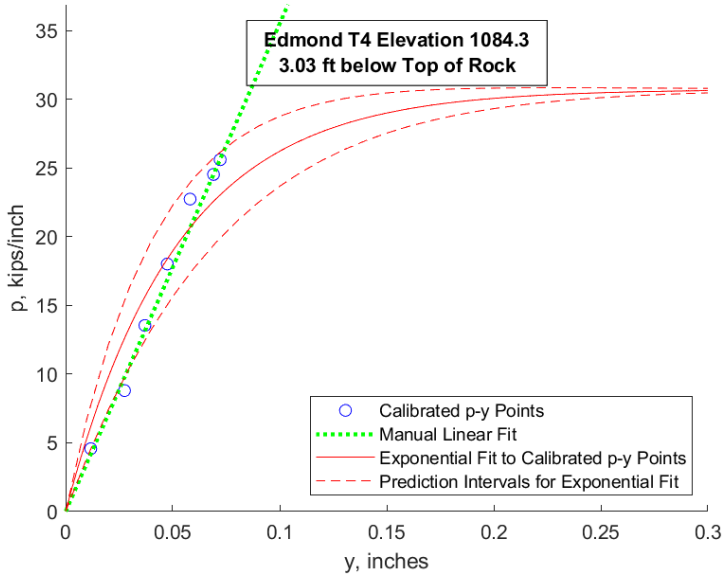
Edmond T4 Elevation 1084.3
3.03 ft below Top of Rock
p, kips/inch
y, inches
Calibrated p-y Points
Manual Linear Fit
Exponential Fit to Calibrated p-y Points
Prediction Intervals for Exponential Fit

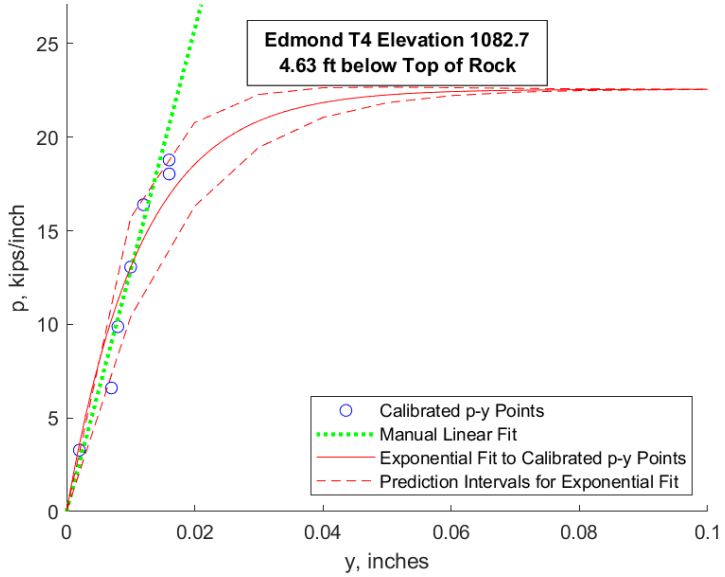
Edmond T4 Elevation 1082.7
4.63 ft below Top of Rock
p, kips/inch
y, inches
Calibrated p-y Points
Manual Linear Fit
Exponential Fit to Calibrated p-y Points
Prediction Intervals for Exponential Fit

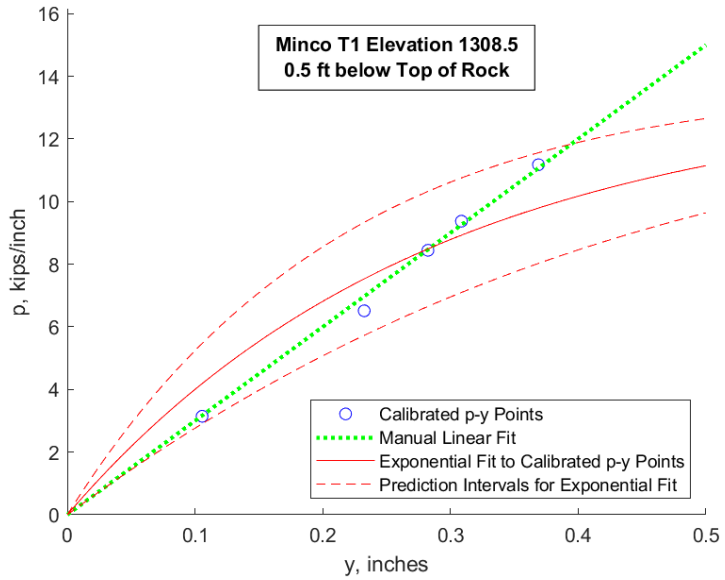
Minco T1 Elevation 1308.5
0.5 ft below Top of Rock
p, kips/inch
y, inches
Calibrated p-y Points
Manual Linear Fit
Exponential Fit to Calibrated p-y Points
Prediction Intervals for Exponential Fit

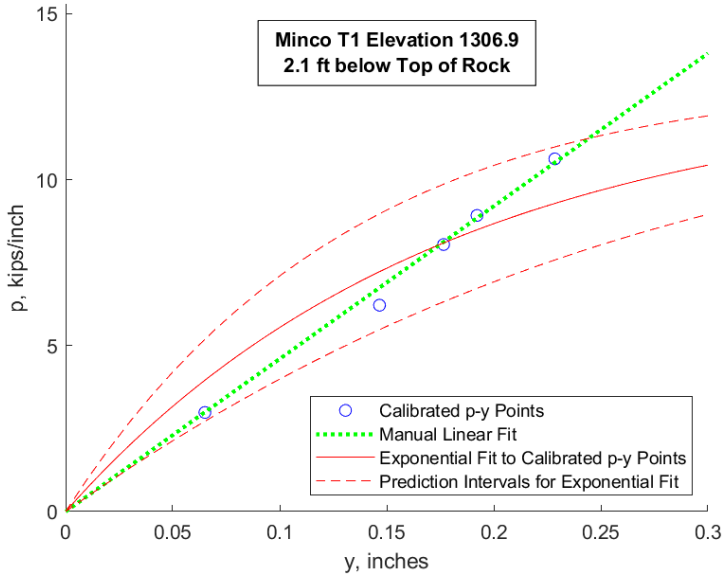
Minco T1 Elevation 1306.9
2.1 ft below Top of Rock
p, kips/inch
y, inches
Calibrated p-y Points
Manual Linear Fit
Exponential Fit to Calibrated p-y Points
Prediction Intervals for Exponential Fit

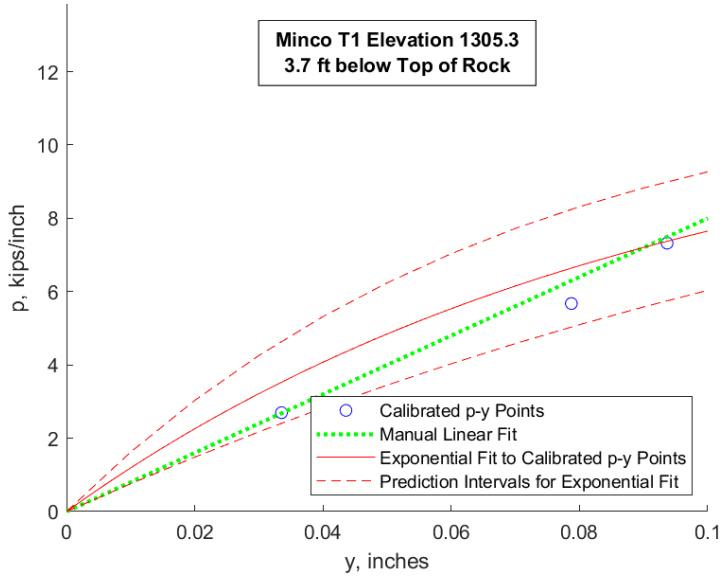
Minco T1 Elevation 1305.3
3.7 ft below Top of Rock
p, kips/inch
y, inches
Calibrated p-y Points
Manual Linear Fit
Exponential Fit to Calibrated p-y Points
Prediction Intervals for Exponential Fit

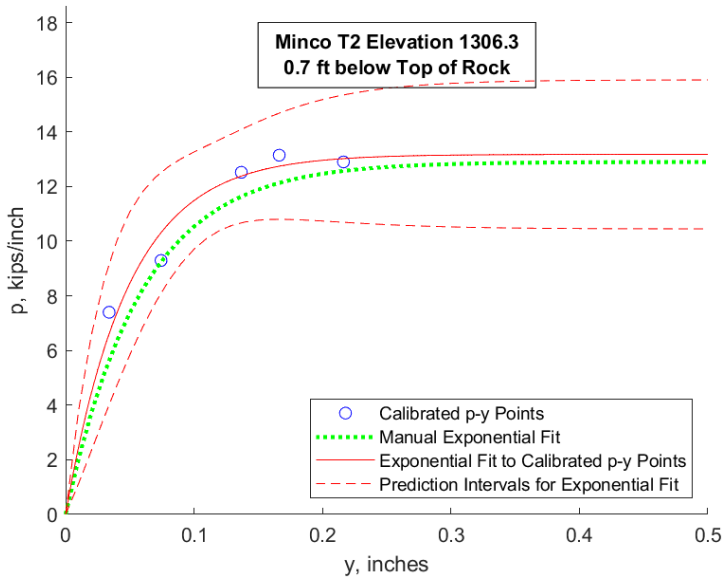
Minco T2 Elevation 1306.3
0.7 ft below Top of Rock
p, kips/inch
y, inches
Calibrated p-y Points
Manual Exponential Fit
Exponential Fit to Calibrated p-y Points
Prediction Intervals for Exponential Fit

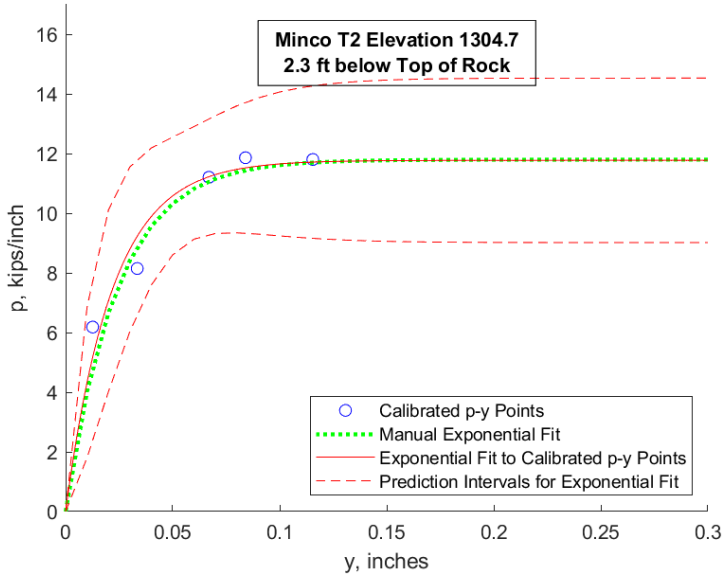
Minco T2 Elevation 1304.7
2.3 ft below Top of Rock
p, kips/inch
y, inches
Calibrated p-y Points
Manual Exponential Fit
Exponential Fit to Calibrated p-y Points
Prediction Intervals for Exponential Fit

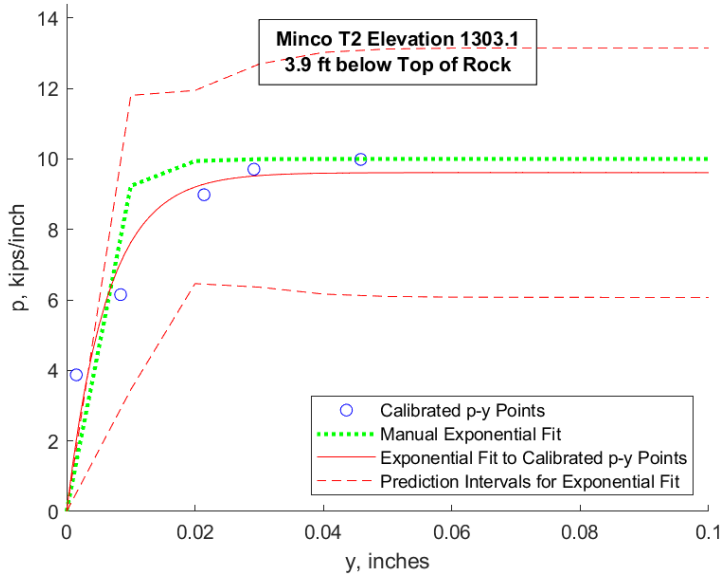
Minco T2 Elevation 1303.1
3.9 ft below Top of Rock
p, kips/inch
y, inches
Calibrated p-y Points
Manual Exponential Fit
Exponential Fit to Calibrated p-y Points
Prediction Intervals for Exponential Fit

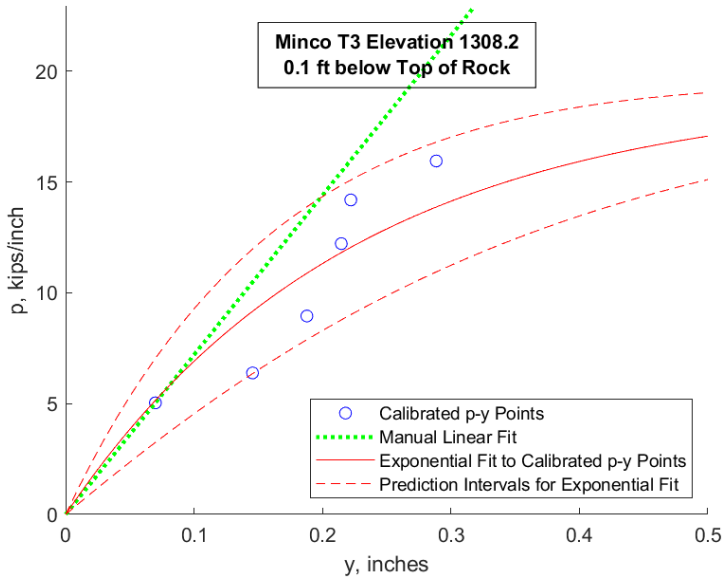
Minco T3 Elevation 1308.2
0.1 ft below Top of Rock
p, kips/inch
y, inches
Calibrated p-y Points
Manual Linear Fit
Exponential Fit to Calibrated p-y Points
Prediction Intervals for Exponential Fit

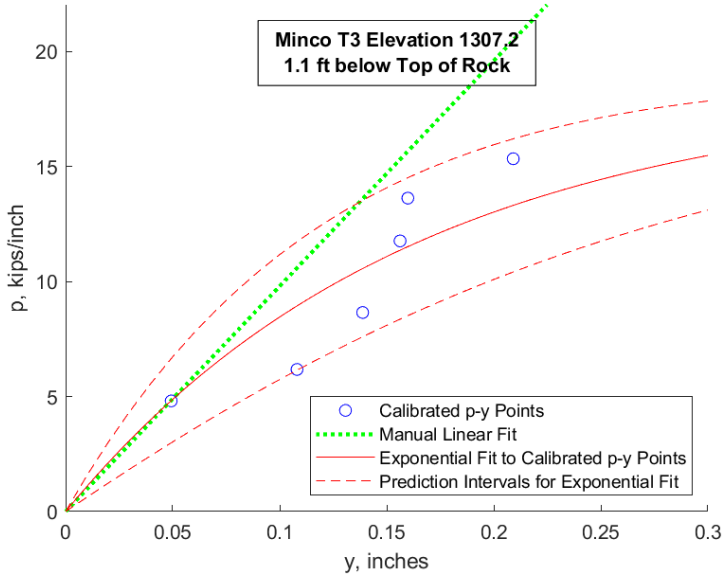
Minco T3 Elevation 1307.2
1.1 ft below Top of Rock
p, kips/inch
y, inches
Calibrated p-y Points
Manual Linear Fit
Exponential Fit to Calibrated p-y Points
Prediction Intervals for Exponential Fit

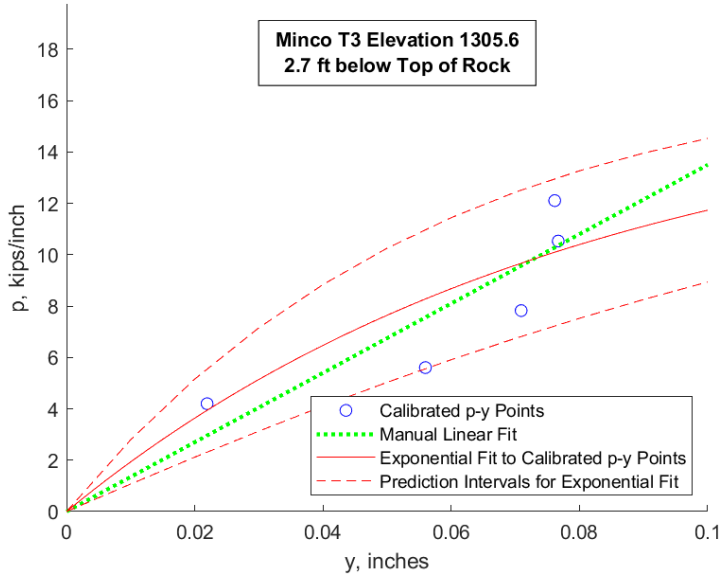
Minco T3 Elevation 1305.6
2.7 ft below Top of Rock
p, kips/inch
y, inches
Calibrated p-y Points
Manual Linear Fit
Exponential Fit to Calibrated p-y Points
Prediction Intervals for Exponential Fit

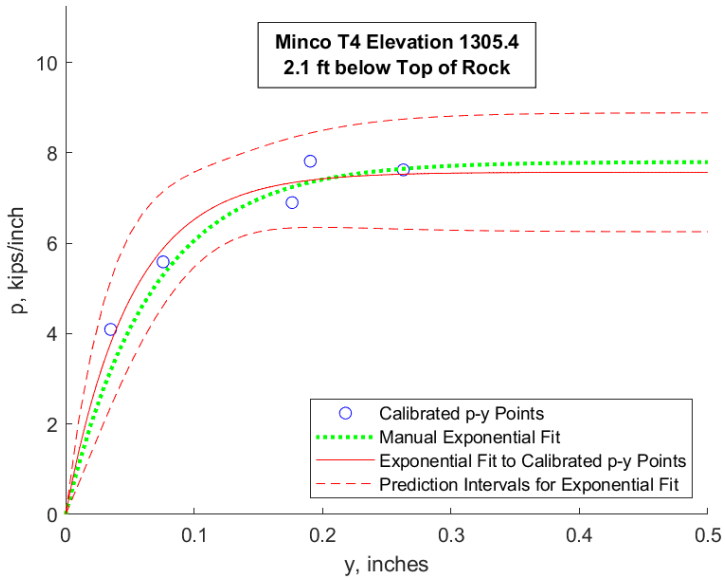
Minco T4 Elevation 1305.4
2.1 ft below Top of Rock
p, kips/inch
y, inches
Calibrated p-y Points
Manual Exponential Fit
Exponential Fit to Calibrated p-y Points
Prediction Intervals for Exponential Fit

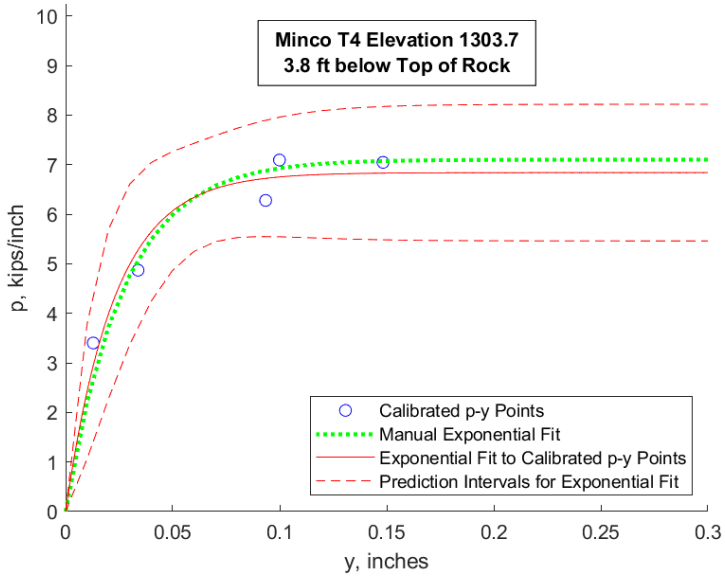
Minco T4 Elevation 1303.7
3.8 ft below Top of Rock
p, kips/inch
y, inches
Calibrated p-y Points
Manual Exponential Fit
Exponential Fit to Calibrated p-y Points
Prediction Intervals for Exponential Fit

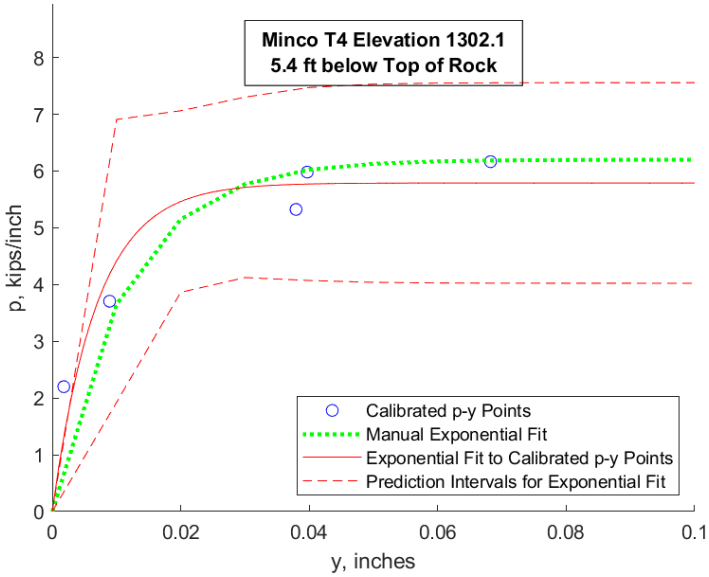
Minco T4 Elevation 1302.1
5.4 ft below Top of Rock
p, kips/inch
y, inches
Calibrated p-y Points
Manual Exponential Fit
Exponential Fit to Calibrated p-y Points
Prediction Intervals for Exponential Fit